

# Characterising 3D Small-scale Reconnection in Kinetic Simulations of Space Plasma Turbulence

*Jeffersson Andres Agudelo Rueda*

A dissertation submitted in partial fulfillment  
of the requirements for the degree of  
**Doctor of Philosophy**  
of  
**University College London.**

Mullard Space Science Laboratory  
Department of Space and Climate Physics  
University College London

July 18, 2022

I, Jeffersson Andres Agudelo Rueda, confirm that the work presented in this thesis is my own. Where information has been derived from other sources, I confirm that this has been indicated in the work.



# Abstract

Magnetic reconnection and turbulence are two of the most important and enigmatic phenomena in plasma physics. Although they have been widely studied individually in a wide range of configurations, the research about the links between turbulence and reconnection is still in its early stages. It is accepted that there is a bi-directional feedback between the two phenomena, and understanding it is crucial to solve the longstanding problem of energy dissipation in collisionless plasmas. In this thesis, I present my contribution to this research field. I use 3D fully kinetic particle-in-cell simulations to explore reconnection that occurs from the turbulent interaction of anisotropic fluctuations consistent with the plasma conditions in the solar wind. I characterise the turbulence in the simulation and propose a set of indicators to find reconnection sites in the simulation. I select one reconnection event and study its geometry, magnetic field configuration, and the associated particle flows. I also explore the profiles of plasma and magnetic-field fluctuations recorded along artificial-spacecraft trajectories passing near and through the reconnection region. Furthermore, I develop and apply a mathematical framework to explore the reversible and irreversible energy density transfer rates. I compare my results with previous studies of turbulent and laminar reconnection. The results presented in this thesis suggest that turbulent reconnection presents a complex three-dimensional problem, and the use of two-dimensional laminar or turbulent models to describe this type of reconnection does not accurately capture its energy transfer properties. Finally, I use my turbulent simulations for the preparation of a new multi-spacecraft mission concept (MagneToRE) to study the magnetic field topology in space plasmas.

# Impact statement

More than 99% of the visible matter in the universe is in plasma state. Most of the plasma in the universe, collisional or collisionless, exhibits turbulence. The energy of fluctuations at large scales cascades to smaller and smaller scales until the conditions for energy dissipation are achieved. Although we understand energy dissipation in collisional plasmas, collisionless energy dissipation is a highly active research field since there is no consensus about the mechanisms responsible for the energy dissipation. Among the extensive list of potential energy transfer mechanisms, magnetic reconnection is particularly important because it changes the magnetic field topology, it can transfer energy from the turbulent fields into the particles, and it occurs in a broad range of plasmas. Understanding the energy transfer across scales and the mechanisms responsible for the energy transfer is essential to illuminate our understanding of matter and energy across the universe. Although turbulence and reconnection have been studied extensively in two dimensions, the extension to the third dimension is still in its early stage due to the complexity of the problem and the computation limitations in the previous decades. Currently, the advent of High Performance Computing facilities is opening the road to address this question.

In this thesis, I explore the links between turbulence and reconnection by performing particle-in-cell simulations of anisotropic turbulence consistent with spacecraft observations in the solar wind. The main simulation that I present is one of the largest simulations of its kind at present. I study the characteristics and properties of three-dimensional magnetic reconnection that occur from a turbulent cascade. I propose new methods to explore turbulent reconnection and its energy transfer. This is an

important contribution towards answering the question of collisionless dissipation. These methods can be applied to in-situ measurements from spacecraft missions such as Parker Solar Probe and Solar Orbiter. This research has led me to gain a deep insight into the geometric properties associated with this three-dimensional turbulent reconnection, and into the fundamental differences with previous two-dimensional models. This work has received widespread international media attention and citations. I have also presented my results at several international conferences.

The future of space plasma physics exploration points towards multi-spacecraft missions. The turbulent simulations that I perform to study reconnection are a valuable tool for modelling and testing multi-spacecraft methods to study space plasmas. In this manuscript, I present part of my contribution to the development of the new mission concept MagneToRE. The mission concept has been accepted for further development under NASA's Heliophysics Flight Opportunities Studies (H-FOS) programme.

# Acknowledgements

To my family, especially my mom, Elizabeth, and my brother, Michael, to my girlfriend Sara and her family, I am truly grateful for you believing and trusting in me. To all my friends around the world who have ever listened to me talk about my tribulations and joys while sailing the turbulent waters of this research, I am immensely grateful for your support on this journey. To all the people in England, especially Sam and her family as well as Luisa and Shaun, whose warm welcome made this endeavour easier for me, thank you.

To my advisors, Daniel Verscharen, Rob Wicks, Andrew Walsh, and Christopher Owen, whose guidance has brought me where I am today. For all the fruitful discussions, patience, and encouragement, I am deeply thankful. To all the former and present members of the plasma group, who I have had the opportunity to work with, laugh and learn with, thank you very much! To everyone, I mean everyone, at MSSL, who makes this amazing laboratory such a unique place to unravel the secrets of space physics, I will always carry all the memories with me.

This work was supported by the European Space Agency's Networking/Partnering Initiative (NPI) programme and the Colombian programme Pasaporte a la Ciencia, Foco Sociedad - Reto 3 (Educación de calidad desde la ciencia, la tecnología y la innovación (CTel)), ICETEX (grant numbers 4000127929/19/NL/MH/mg and 3933061). This work was largely performed using the DiRAC Data Intensive service at Leicester (projects ACSP200 and ACSP224), operated by the University of Leicester IT Services, which forms part of the STFC DiRAC HPC Facility ([www.dirac.ac.uk](http://www.dirac.ac.uk)). The equipment was funded by BEIS capital funding via STFC

Capital Grants ST/K000373/1 and ST/R002363/1, and STFC DiRAC Operations Grant ST/R001014/1. DiRAC is part of the National e-Infrastructure.

“The family section is a community of everybody doing a different part, everybody being different. You know? And, in a household you learn about authority, right. You learn about order, you learn about selflessness, you learn about organisation, you learn about competition. That’s what a family gives you.” Keep on, Antiphon, Alfa Mist.

«“Look at that fire in the sky!” he cried, pointing to the sky in the middle of the wild storm. “That white fire leads us to the white whale!” . . . “Oh, great fire” shouted Ahab, “I burn with you! You light the way to the white whale! I am not afraid. ” . . . “Remember, you all swore to hunt the white whale with me, and we will hunt it! We are in this together and we will not turn back. No storm can stop me! No one can stop me!”» Captain Ahab, *Moby Dick* - Herman Melville.

“The melody of chaconne is just like the turbulence of life, from the first cry to the endless ups and downs. Music is truth, purity, love, beauty, and freedom.” Lucia Fox. Comment in Tomaso Antonio Vitali. Chaconne in G Minor for violin and piano.

# Contents

<b>1</b>	<b>Introduction</b>	<b>24</b>
<b>2</b>	<b>Plasma physics</b>	<b>31</b>
2.1	The Concept of Plasma . . . . .	31
2.2	From Kinetic to MHD . . . . .	34
2.2.1	Characteristic Parameters . . . . .	35
2.2.2	Single Fluid MHD . . . . .	37
2.3	Plasma Waves . . . . .	39
2.3.1	Plasma Wave Modes . . . . .	41
<b>3</b>	<b>Magnetic reconnection</b>	<b>45</b>
3.1	The General Concept of Magnetic Reconnection . . . . .	45
3.2	Magnetic Reconnection in 2D . . . . .	49
3.2.1	Hall MHD Reconnection . . . . .	55
3.2.2	Tearing Reconnection . . . . .	60
3.3	3D Magnetic Reconnection . . . . .	63
3.3.1	Laminar 3D Reconnection . . . . .	64
3.4	Observations of Reconnection in the Solar Wind . . . . .	66
<b>4</b>	<b>Turbulence in the Solar Wind</b>	<b>69</b>
4.1	Fluid Turbulence . . . . .	69
4.1.1	Nonlinear Energy Cascade, K41 . . . . .	70
4.2	Plasma Turbulence . . . . .	71

4.2.1	Elsässer Variables . . . . .	71
4.2.2	Nonlinear Energy Cascade, IK . . . . .	72
4.2.3	Nonlinear Energy Cascade, GS95 . . . . .	73
4.2.4	Nonlinear Energy Cascade and Dynamic Alignment . . . . .	74
4.2.5	Plasma Turbulence in the Solar Wind . . . . .	75
4.2.6	Kinetic Turbulence . . . . .	76
4.2.7	Turbulent 3D Reconnection . . . . .	77
<b>5</b>	<b>Simulation method: Particle In Cell Simulations</b>	<b>80</b>
5.1	Overview Particle-In-Cell Method . . . . .	80
5.1.1	Equation of Motion of the Quasi-Particles . . . . .	83
5.1.2	Method for Solving the Equations of Motion . . . . .	85
5.2	Initial Conditions to Simulate Anisotropic Turbulence . . . . .	88
5.3	Numerical Tests . . . . .	92
5.3.1	Evidence of Turbulence . . . . .	92
<b>6</b>	<b>Three-dimensional magnetic reconnection in particle-in-cell simulations of anisotropic plasma turbulence</b>	<b>101</b>
6.1	Introduction . . . . .	102
6.2	Simulation Setup . . . . .	103
6.3	Results . . . . .	104
6.3.1	Time Evolution and Formation of Current Structures . . . . .	104
6.3.2	Evidence of Turbulence in Our Simulation . . . . .	111
6.3.3	Reconnection Sites . . . . .	115
6.3.4	1D Trajectories Across the Reconnection Region . . . . .	123
6.4	Discussion and Conclusions . . . . .	131
<b>7</b>	<b>Energy transport during 3D small-scale reconnection driven by anisotropic turbulence using PIC simulations</b>	<b>136</b>
7.1	Introduction . . . . .	137
7.2	Energy Transfer and Transport . . . . .	138
7.2.1	Reconnection Event Overview . . . . .	142



7.3	Results . . . . .	145
7.3.1	Particle Agyrotropy in the Diffusion Region . . . . .	145
7.3.2	Energy Transfer and Transport . . . . .	148
7.3.3	Comparison with Damping and Heating Proxies . . . . .	154
7.4	Discussion and Conclusions . . . . .	154
<b>8</b>	<b>A method to reconstruct magnetic field from multi-spacecraft measurements in preparation of MagneToRE</b>	<b>159</b>
8.1	The Need of Multi-spacecraft Missions . . . . .	160
8.2	Case Study: Magnetic Field Reconstruction . . . . .	161
8.2.1	Reconstruction Method . . . . .	164
8.3	Results . . . . .	169
8.3.1	Magnetic Dipole . . . . .	169
8.3.2	Multiple Magnetic Dipoles . . . . .	171
8.3.3	Magnetic Flux-Rope . . . . .	171
8.3.4	Multiple Magnetic Flux-Ropes . . . . .	172
8.3.5	Turbulent Magnetic Field . . . . .	172
8.3.6	Goodness of the Reconstruction Method . . . . .	173
8.4	Discussion and Conclusions . . . . .	179
<b>9</b>	<b>Conclusions and Future Work</b>	<b>182</b>
	<b>Appendices</b>	<b>187</b>
<b>A</b>	<b>Second-order structure functions</b>	<b>187</b>
<b>B</b>	<b>Detailed Derivation of the Energy Equations</b>	<b>189</b>
B.1	Derivation of the Equations for the Energy Densities . . . . .	189
<b>C</b>	<b>A Framework to Study the Energy-density Transfer Using Fitted Moments from In-situ Data.</b>	<b>195</b>

# List of Figures

1.1	a) Sketch of the Archimedes spiral of a plasma stream, adapted from <a href="#">Dessler (1967)</a> . b) Ballerina skirt pattern of the heliospheric current sheet (HCS), adapted from <a href="#">Jokipii and Thomas (1981)</a> . c) Polar plots of the solar wind speed during solar minimum (top left) and solar maximum (top right). The distance from the center represents the magnitude of the speed. The red/blue colour marks the positive(outward)/negative(inward) interplanetary magnetic field. The background images are a composition of images taking by the Solar and Heliospheric Observatory (SOHO). Adapted from <a href="#">McComas et al. (2003)</a> . . . . .	26
2.1	a) Phase velocity diagram of the MHD modes for $v_A > c_s$ (a) and $v_A < c_s$ (b). Adapted from <a href="#">Baumjohann and Treumann (1997)</a> . . . .	43
3.1	a) Sketch of the frozen in theorem. The magnetic-field lines and the plasma parcels are couple to each other. b) Sketch of the magnetic field diffusion. The magnetic field diffuses in space as a function of time. Adapted from <a href="#">Baumjohann and Treumann (1997)</a> . . . . .	48

3.2	Sweet–Parker reconnection model. Oppositely directed magnetic fields $\mathbf{B}_0$ are convected with speed $\mathbf{v}_0$ . This forms a current sheet $\mathbf{J}$ directed out of the reconnection plane. The current sheet has length $2L$ and thickness $2\delta$ . A self-consistent uniform electric field $\mathbf{E}$ is directed out of the plane. The reconnected field $\mathbf{B}_{out}$ is convected away from the reconnection region at the speed $\mathbf{v}_{out}$ . Adapted from <a href="#">Somov (2012)</a> . . . . .	50
3.3	2D Hall MHD reconnection model. Unlike in SP, the diffusion region is divided between ion and electron diffusion regions. Poloidal (in plane) electron currents form and generate a characteristic quadrupole-like toroidal (out of the plane) magnetic field. Adapted from <a href="#">Sonnerup (1979)</a> . . . . .	57
3.4	The charge separation in the ion-diffusion region generates a poloidal electric field $\mathbf{E}_{pol}$ . Adapted from <a href="#">Uzdensky and Kulsrud (2006)</a> . . . .	58
3.5	Reconnection diffusion region. The dashed black lines define the reconnection separatrix. Within the ion diffusion region (gray area) ions are demagnetised and the ion flows (blue dashed lines) accelerate away of the reconnection ion-diffusion region. As magnetic field lines (continuous black lines) are convected to the central region, poloidal electron flows (red dashed lines) form to maintain quasi-neutrality. These flows generates the characteristic toroidal quadrupole-like magnetic field (green crosses and dots). Within the electron diffusion region (yellow area) electrons are demagnetised and accelerated out of the reconnection region. Adapted from <a href="#">Zweibel and Yamada (2016)</a> . . . .	59
3.6	Plasmoid chain formation. For large plasma size and high Lundquist number $S$ , the current sheet is unstable to tearing instability. Magnetic islands are formed while the current sheet is disrupted. Adapted from <a href="#">Ji and Daughton (2011)</a> . . . . .	61

- 3.7 2D magnetic reconnection phase diagram as a function of the Lundquist number and the plasma size. The orange vertical line marks the critical plasma size  $\lambda_c$ . The horizontal green line marks the critical Lundquist number  $S_c$ . The diagonal black line marks the transition from multiple X-line collisionless reconnection to the hybrid phase. The blue diagonal line marks the transition from multiple X-line collisional reconnection to the hybrid phase. In the hybrid phase, collisional and collisionless reconnection can proceed with single and multiple X-lines. The orange square shows the range of plasma size and Lundquist number that can be studied by laboratory experiments and numerical simulations. Adapted from [Ji et al. \(2019\)](#). . . . . 63
- 3.8 Left: In the neighbourhood of a null point, hyperbolic magnetic field lines converge to the spine line and spread out, forming a fan-like structure. The spine-fan configuration can collapse and form current sheets. Right: In the absence of magnetic null points, the intersection of spine-fan structures define the so-called separator. Separators can collapse as well. Adapted from [Pontin \(2011\)](#). . . . . 65
- 3.9 Idealised 2D projection of an exhaust region. The continuous black (red) lines and arrows represent the reconnecting (reconnected) magnetic field. The dashed red lines and arrows represent the rotational discontinuities associated with the reconnection region and the dash-dotted line illustrate a representative spacecraft trajectory. Adapted from [Gosling \(2012\)](#). . . . . 67
- 4.1 Power spectral density of magnetic field fluctuations. The vertical dashed lines corresponds to the frequencies associated, through the Taylor hypothesis, with spatial variations at different scales in the spacecraft frame. Adapted from [Verscharen et al. \(2019\)](#). . . . . 75

- 4.2 In the laminar SP model, the aspect ratio ( $\Delta/L$ ) is defined by the size of the current sheet. In the presence of pre-existing turbulence, the magnetic field lines wander and change the effective width  $\Delta$  of the reconnection region. This change increases the aspect ratio and thus the reconnection rate. Adapted from [Lazarian et al. \(2020\)](#). . . . 78
- 5.1 First three standard b-splines functions. Adapted from [Lapenta \(2012\)](#). 82
- 5.2 Yee grid unit cell. The magnetic field components are calculated on the cell faces. The components of the electric field and the electric current density are calculated on the edges of the cell. The charge density is calculate on the corners of the cell. Adapted from [Germaschewski et al. \(2016\)](#). . . . . 87
- 5.3 Leap-frog algorithm. The position, the electric field and the charge density are calculated at integer times. The momentum, the magnetic field and the electric current density are calculated at half time steps between the integer time steps. Adapted from [Germaschewski et al. \(2016\)](#). . . . . 87
- 5.4 Perpendicular one-dimensional reduced power spectral density of the magnetic field fluctuations  $P_{1D\perp}^B$  (top) and of the ion velocity fluctuations  $P_{1D\perp}^{v_i}$  (bottom) for the test runs s1 ( $v_{A,i}/c = 0.06$ ; black), s2 ( $v_{A,i}/c = 0.08$ ; red) and s3 ( $v_{A,i}/c = 0.1$ ; orange) at  $t = t_R$ . The vertical dashed lines from left to right indicate  $k_{\perp}d_i = 1$ ,  $k_{\perp}d_e = 1$ ,  $k_{\perp}\lambda_{Ds3} = 1$ ,  $k_{\perp}\lambda_{Ds2} = 1$  and  $k_{\perp}\lambda_{Ds1} = 1$ . . . . . 95
- 5.5 Perpendicular one-dimensional reduced power spectral density of the magnetic field fluctuations  $P_{1D\perp}^B$  (top) and the ion velocity fluctuations  $P_{1D\perp}^{v_i}$  (bottom) for the test runs s4 ( $ppc = 50$ ; black), s3 ( $ppc = 100$ ; red), s5 ( $ppc = 150$ ; orange), s6 ( $ppc = 200$ ; blue), s7 ( $ppc = 250$ ; gray) and s6 ( $ppc = 300$ ; pink) at  $t = t_R$ . The vertical dashed lines from left to right indicate  $k_{\perp}d_i = 1$ ,  $k_{\perp}d_e = 1$ ,  $k_{\perp}\lambda_D = 1$ . 96

- 5.6 Perpendicular one-dimensional reduced power spectral density of the magnetic field fluctuations  $P_{1D\perp}^B$  (top) and the ion velocity fluctuations  $P_{1D\perp}^{v_i}$  (bottom) for the test runs s9 ( $m_i/m_e = 1$ ; black), s10 ( $m_i/m_e = 10$ ; red), s1 ( $m_i/m_e = 100$ ; orange), s13 ( $m_i/m_e = 200$ ; blue), s15 ( $m_i/m_e = 300$ ; gray), s16 ( $m_i/m_e = 400$ ; pink) and s17 ( $m_i/m_e = 500$ ; purple) at  $t = t_R$ . The vertical dashed lines from left to right indicate  $k_\perp d_i = 1$ ,  $k_\perp d_{es1} = 1$ ,  $k_\perp d_{es13} = 1$ ,  $k_\perp d_{es17} = 1$  and  $k_\perp \lambda_D = 1$ . . . . . 97
- 6.1 Time evolution of the rms of the current density  $\mathbf{J}$  (blue), magnetic field  $\mathbf{B}$  (black), and ion velocity  $\mathbf{v}_i$  (red). The vertical dashed line marks the time  $t_R = 120/\omega_{pi}$  at which  $J^{rms}$  begins to decrease. . . . 105
- 6.2 3D rendering of the transverse magnetic field magnitude  $|\mathbf{B}_{xy}| = \sqrt{B_x^2 + B_y^2}$  at  $t = 0$  (a) and  $t = t_R$  (b). The colour bar ranges from the minimum magnitude (black) to the maximum magnitude (yellow) throughout the simulation domain at  $t = t_R$ . We use the same colour bar in both panels for a direct comparison. The initial background magnetic field is directed along  $z$ -direction. At the initial time, the fluctuations are anisotropic and elongated along the  $z$ -direction. At  $t = t_R$ , small-scale magnetic eddies have formed and interact non-linearly with each other. The eddies present varying cross section diameters  $L_D$  and lengths  $L_\parallel$ . . . . . 106
- 6.3 Panels (a) and (b): Probability distribution functions of elongations  $L_\parallel$  (top), cross section diameters  $L_D$  (middle), and aspect ratios  $L_\parallel/L_D$  (bottom) of the magnetic structures at  $t = 0$  (a) and  $t = t_R$  (b). Panel (c): Scaling between  $L_\parallel$  and  $L_D$  at  $t = 0$ . The black dashed line shows a linear fit. Panel (d): Scaling between  $L_\parallel$  and  $L_D$  of the large-scale population (orange) and small-scale population (blue) at  $t = t_R$ . The top black dashed line shows a linear fit to the former while the bottom red dashed line shows a linear fit to the latter. . . . 107

- 6.4 Visualisations of the simulation domain at  $t = t_R$ . (a) 3D rendering of the magnetic-field component  $B_z$ . Blue represents negative, red positive and white zero values of  $B_z$ . The eddies' centres present different values of  $B_z$  with either positive or negative polarity. (b) 3D rendering of the magnitude of the current density  $|\mathbf{J}|$  from the same vantage point as (a). The colour represents in blue (red) the smallest (largest) values of  $|\mathbf{J}|$ . Filaments of intense current density are aligned with the eddies' centres. Current filaments and extended current-sheet-like structures are mainly elongated along the  $z$ -direction. 108
- 6.5 Isocontours of  $\log_{10} P_{2D}^{\mathbf{B}}$  of the fluctuating magnetic field as a function of  $k_{\parallel}$  and  $k_{\perp}$  at different time-steps. The dashed lines provide a reference for the scaling of  $k_{\perp}$  and  $k_{\parallel}$ . The horizontal (vertical) dashed line marks  $k_{\perp} d_e = 1$  ( $k_{\parallel} d_i = 1$ ). At  $t = 0$ , the spectrum shows the modes of our initialisation and their Fourier harmonics. At  $t = 12/\omega_{pi}$ , the cascade in the perpendicular direction (vertical axis) has proceeded beyond electron scales ( $k_{\perp} d_i \geq 10$ ). At  $t = t_R$ , although the perpendicular cascade has not proceeded significantly further, the cascade in the parallel direction (horizontal axis) has reached the kinetic range ( $k_{\parallel} d_i \approx 1$ ) up to ion scales but not to electron scales. At  $t = 240/\omega_{pi}$  the distribution has not considerably changed compared to  $t = t_R$ . . . 113
- 6.6 (a) Perpendicular and (b) parallel reduced one-dimensional power spectral densities  $P_{1D_{\parallel,\perp}}^B$  (black),  $P_{1D_{\parallel,\perp}}^{v_i}$  (red), and  $P_{1D_{\parallel,\perp}}^{n_i}$  (blue) at  $t = t_R$ . The vertical dashed lines indicate  $k_{\parallel,\perp} d_i = 1$ ,  $k_{\parallel,\perp} d_e = 1$ , and  $k_{\parallel,\perp} \lambda_D = 1$ . . . . . 114

- 6.7 Reconnection indicators projected onto a 2D cut in the  $zx$ -plane at  $y = 21d_i$ . (a) Indicator C1: Isosurfaces of  $|\mathbf{J}| = \langle |\mathbf{J}| \rangle + 3(|\mathbf{J}|)^{rms}$  (light blue). (b) Indicator C2: Isosurfaces of  $|\mathbf{v}_{i,e}| = \langle \mathbf{v}_{i,e} \rangle + 3(\mathbf{v}_{i,e})^{rms}$  for ions (green) and for electrons (purple). (c) Indicator C3: Isosurfaces of  $T_{i,e} = \langle T_{i,e} \rangle + 3(T_{i,e})^{rms}$  for ions (gold) and for electrons (pink). (d) Indicator C4: Isosurfaces of  $\mathbf{J} \cdot \mathbf{E} = \langle \mathbf{J} \cdot \mathbf{E} \rangle \pm 3(\mathbf{J} \cdot \mathbf{E})^{rms}$  for positive  $\mathbf{J} \cdot \mathbf{E}$  (red) and negative  $\mathbf{J} \cdot \mathbf{E}$  (blue). (e) Indicator C5: Isosurfaces of  $E_{\parallel} = \langle |E_{\parallel}| \rangle \pm 2(|E_{\parallel}|)^{rms}$  for positive  $E_{\parallel}$  (orange) and negative  $E_{\parallel}$  (blue). Panel (f) shows, on top of the isosurfaces related to indicators C1 through C4, magnetic field lines colour-coded with  $|\mathbf{B}|$ . The magnetic field lines suggest the reconnection of a twisted flux rope with an adjacent flux rope. The white sphere of radius  $1d_i$  at  $(z, x) = (77, 13.5)d_i$  in panel (f) is a reference point that marks the position of a reconnection site. In panel (f), we also indicate the regions  $R_1$  and  $R_2$  defined in the text. . . . . 119
- 6.8 Streamlines of the ion and electron bulk velocities over 2D cuts of the simulation plane showing  $J_z$ . (a) and (b) view over the  $xy$ -plane in which the  $x$ -direction points downward and the  $y$ -direction points towards the right-hand side. (c) and (d) view over the  $zx$ -plane in which the  $x$ -direction points downward and the  $z$ -direction points towards the left-hand side. (a) and (c) show ion bulk velocity streamlines colour-coded with  $v_{ix}$ . (b) and (d) show electron velocity streamlines colour-coded with  $v_{ez}$ . The arrows indicates the direction of the ion bulk motion and of the electron bulk motion. . . . . 122
- 6.9 Trajectories of an artificial spacecraft crossing our simulation domain. (a) Trajectory  $T1$ . The spacecraft moves from the top-left corner to the bottom-right corner. This trajectory crosses a region that we identify as a reconnection exhaust. (b) Trajectories  $T2$  and  $T3$  are parallel to each other. The former crosses through the reconnection site while the latter passes right outside of the reconnection site. . . . 124



6.10	Plasma and magnetic-field fluctuations associated with our trajectories $T1$ and $T2$ . . . . .	127
7.1	Spatial context of the reconnection event within the simulation domain. Panel a) shows a volume rendering of $ \mathbf{J} $ . Panel b) shows the 3D magnetic field lines colour-coded with $ \mathbf{B} $ . On the vertical cuts in panel b), we show $J_z$ . Panel c) shows the magnetic field lines in the $xy$ -plane. The black contours show in-plane magnetic-field lines. The green square highlights the size and position of the region for the energy analysis. . . . .	143
7.2	2D cuts in the $rp$ -plane at simulation time $t = 120\omega_{pi}^{-1}$ . a) Magnetic field magnitude $ \mathbf{B} /B_0$ . The black contours represent the in-plane magnetic-field lines, and the black stars represent two x-points. b) Out-of-plane component of the magnetic field, $(B_a - B_0)/B_0$ . The black arrows in this panel represent the in-plane magnetic vectors ( $\mathbf{B}_{rp}$ ). c) Out-of-plane electron speed $u_{a,e}/V_{A,i}$ . The black arrows in this panel represent the in-plane electron velocity vectors ( $\mathbf{v}_{rp,e}/V_{A,i}$ ). d) Out-of-plane ion speed $u_{a,i}/V_{A,i}$ . The black arrows in this panel represent the in-plane ion velocity vectors ( $\mathbf{v}_{rp,i}$ ). In all panels, the black square outlines the diffusion region. . . . .	144
7.3	2D cuts of the pressure tensor components in the $rp$ -plane at the simulation time $t = 120\omega_{pi}^{-1}$ . a) Electron scalar pressure $p_e/p_0$ . Off-diagonal components of the electron pressure tensor: b) $\Pi_{ra,e}/p_0$ , c) $\Pi_{pa,e}/p_0$ , and d) $\Pi_{pr,e}/p_0$ . e) Ion scalar pressure $p_i/p_0$ . Off-diagonal components of the ion pressure tensor: f) $\Pi_{ra,i}/p_0$ , g) $\Pi_{pa,i}/p_0$ , and h) $\Pi_{ra,i}/p_0$ . . . . .	147

- 7.4 Magnification of the region delimited by the black square in Figure 7.2 in the  $rp$ -plane at the simulation time  $t = 120\omega_{pi}^{-1}$ . a) Electron scalar pressure  $p_e$ . Off-diagonal components of the electron pressure tensor: b)  $\Pi_{ra,e}$ , c)  $\Pi_{pa,e}$ , and d)  $\Pi_{pr,e}$ . Panel e) shows a sketch of the patterns of the scalar pressure emerging in 2D simulations of reconnection, and f) to h) show sketches of the off-diagonal terms of the electron pressure based on 2D Harris current sheet reconnection without guide field (Yin et al., 2001). . . . . 148
- 7.5 2D cuts in the  $rp$ -plane at the simulation time  $t = 120\omega_{pi}^{-1}$ . Panels a) to e): kinetic power density terms for electrons. Panels f) to j): thermal power density terms for electrons. All quantities are normalised to  $\Delta\varepsilon_0 = \omega_{pi}m_i v_{A,i}^2$ . . . . . 150
- 7.6 1D cuts of the power density terms along the  $\hat{p}$ -direction at  $r = 5.58d_i$  and at the simulation time  $t = 120\omega_{pi}^{-1}$ . a) Kinetic power density terms in Eq. (7.5). b) Thermal power density terms in Eq. (7.8). The vertical dashed line represents the crossing of the x-point  $r = 5.8d_i$  and  $p = 6.6d_i$ . . . . . 153
- 7.7 Damping and heating proxies at the simulation time  $t = 120\omega_{pi}^{-1}$ . 2D cuts in the  $rp$ -plane of a) The Zenitani parameter for electrons  $D_{ze}$ . b) Diagonal part of the strain-pressure interaction  $p\theta_e$ . c) Off-diagonal part of the strain-pressure interaction  $Pi-D_e$ . d) 1D cut of these terms like in Figure 7.6. . . . . 155
- 8.1 Representation of the macroscales (left), mesoscales (middle) and microscales (right) in the interplanetary magnetic field (IMF) and of the scales covered by multi-spacecraft missions past/present (solid) and future (dashed). Adapted from Maruca et al. (2021) . . . . . 162
- 8.2 Synthetic data set designed to test the reconstruction method. Magnetic field lines for a) a dipole, b) multiple dipoles, c) a flux-rope, and d) multiple flux-rope. The magnetic-field lines are colour-coded with  $|\mathbf{B}|$  in logarithmic scale. . . . . 165

8.3	Magnetic field magnitude $ \mathbf{B} $ on the surface of the simulation domain in the turbulence case. The magnetic field shows elongated structures such as null regions (dark patches) and intense magnetic field regions (orange patches). . . . .	166
8.4	Spacecraft configurations a) C1: 4 spacecraft, b) C2: 8 spacecraft, c) C3: 16 spacecraft, and d) C4: 24 spacecraft in the $xy$ -plane. Each bundle of arrows represents a point in the plane perpendicular to the direction of the spacecraft motion in the $\hat{z}$ -direction. The arrows show the direction of the magnetic field at each point along the trajectory. . . . .	168
8.5	a) Magnetic field lines of the synthetic magnetic dipole. b) Reconstructed magnetic field for C1. c) Reconstructed magnetic field for C2. d) Reconstructed magnetic field for C3. The magnetic field lines are colour-coded with $ \mathbf{B} $ on a logarithmic scale. . . . .	170
8.6	Magnetic field lines. a) Synthetic multiple magnetic dipoles. b) Reconstructed magnetic field of the multiple dipoles for C4. The magnetic field lines are colour-coded with $ \mathbf{B} $ on a logarithmic scale. . . . .	171
8.7	Magnetic field lines. a) Synthetic magnetic flux-rope. b) Reconstructed magnetic field of the flux-rope for C4. The magnetic field lines are colour-coded with $ \mathbf{B} $ on a logarithmic scale. . . . .	173
8.8	Magnetic field lines. a) Synthetic multiple magnetic flux-ropes. b) Reconstructed magnetic field of the multiple magnetic flux-ropes for C4. The magnetic field lines are colour-coded with $ \mathbf{B} $ on a logarithmic scale. . . . .	174
8.9	Magnetic field lines of the turbulence simulation data set designed to test the reconstruction method. a) Magnetic field lines of the synthetic input data. b) Reconstructed magnetic field lines for C2. c) Reconstructed magnetic field lines for C3. c) Reconstructed magnetic field lines for C4. The magnetic field lines are colour-coded with $ \mathbf{B} $ on a linear scale. . . . .	175

8.10	Point-wise error distribution for (a) the magnetic dipole, (b) multiple magnetic dipoles, (c) the magnetic flux-rope, and (d) multiple magnetic flux-ropes. The counts are normalised to the total number of counts $N_c$ . . . . .	177
8.11	Point-wise relative direction distribution for (a) the magnetic dipole, (b) multiple magnetic dipoles, (c) the magnetic flux-rope, and (d) multiple magnetic flux-ropes. . . . .	177
8.12	(a) Point-wise error distribution for the turbulence simulation. (b) Point-wise relative direction distribution for the turbulence simulation.	178
A.1	Second-order structure functions of the magnetic fluctuation $\mathbf{b}$ in the $r_\perp, r_\parallel$ -plane as $\log_2 F2b$ at $t = 0/\omega_{pi}$ (a), $t = 12/\omega_{pi}$ (b), $t = t_R$ (c), and $t = 240/\omega_{pi}$ (d). At $t = 0$ , while the magnetic energy is distributed across multiple perpendicular scales, it is mainly stored at large parallel scales. At $t = t_R$ , the magnetic energy is distributed across multiple parallel scales. . . . .	188

# List of Tables

2.1	Characteristic length and time scales at 1 au. Adapted from <a href="#">Verscharen et al. (2019)</a> . . . . .	37
5.1	Simulation test runs. . . . .	93
6.1	Number of events in our simulation domain at time $t = t_R$ fulfilling each of our criteria for reconnection. . . . .	118
8.1	Parameters to estimate the goodness of the reconstruction method. .	179

## Chapter 1

# Introduction

The sun is a highly dynamic system in which the pull between plasma pressure and magnetic pressure is constantly evolving. The Sun's magnetic field expands beyond the interplanetary space forming the so-called heliosphere until the boundary between the interstellar medium (magnetopause) is reached. The convection and magnetic bouyancy of the magnetic field below the solar surface produces magnetic arcades ([Magara, 2004](#); [Vargas Domínguez et al., 2012](#)) who retain the plasma. However, the complex non-linear interaction between magnetic structures on the surface leads to the onset of explosive events that release plasma radially outwards at supersonic speeds. This stream of plasma particles, the so-called solar wind, was first predicted by Parker [Parker \(1958\)](#) inspired by comet tail observations ([Biermann and Schlüter, 1951](#)). As the solar wind expands into the heliosphere, the rotation of the Sun drags the Sun's magnetic field forming an the plasma follows an Archimedes spiral Figure 1.1a. Likewise, the solar wind stretches away the magnetic field and the precession of Sun's magnetic dipole generate a characteristic heliospheric current sheet (HCS) that resembles a ballerina skirt pattern 1.1b.

The solar wind is a low-collisionality plasma produced in the solar corona ([Marsch, 2006](#)). Although it is still not clear what the specific source regions of the solar wind are, two main types of streams have been identified, both originating in the solar corona ([Srivastava and Schwenn, 2000](#); [Feldman et al., 2005](#); [McComas et al., 2003](#)): the slow and the fast wind. The former has a speed ranging from 300 km/s

to 500 km/s and a minimum proton temperature  $\sim 5 \times 10^4$  K whilst the latter has a speed in the range from 500 km/s to 800 km/s and a proton temperature in the range  $\sim 5 - 8 \times 10^5$  K at 1 au (Marsch et al., 1982; Marsch, 2006). Ulysses spacecraft measurements of velocity and density show that during solar minimum the fast/slow wind is largely restricted to high/low heliospheric latitudes Figure 1.1c. During solar maximum, coronal holes, which are the sources of fast wind (Krieger et al., 1973), move to lower latitudes mixing the sources of fast and slow wind.

The solar wind expands across the solar system exhibiting spatial and temporal variations in composition, density, velocity, and temperature as well as in the electric and magnetic fields. The solar wind shows a non-adiabatic temperature profile with distance from the Sun (Gazis and Lazarus, 1982; Cranmer, 2009, 2012) which suggests the presence of local heating and particle-acceleration mechanisms (Goldstein et al., 2015). The observed velocity distribution functions of the solar wind species often exhibit non-thermal features (e.g., Marsch et al., 1982; Feldman et al., 1975, 1978; McComas et al., 1992).

In the solar wind, the magnetic-field fluctuations exhibit a power-law distribution of the magnetic energy across a large range of spatial scales from about 0.1 au to sub-proton scales (Coleman Jr, 1968; Marsch and Tu, 1990) which indicates the presence of turbulence in the solar wind. The transport of energy between scales is known as the energy cascade. At sub-proton scales, kinetic dissipation mechanisms become important, particles are energised and the entropy of the system irreversibly increases (Tatsuno et al., 2009; Eyink, 2018; Verscharen et al., 2019). The nature of the fluctuations at sub-proton scales and the properties of the plasma determine whether the turbulent energy is mainly dissipated by ions or whether it cascades to electron scales at which it is ultimately dissipated in the form of electron heating. In the theoretical framework of wave turbulence, the energy-transfer mechanisms are classified into two main categories: resonant heating such as Landau damping and ion-cyclotron damping (Marsch et al., 2003; Kasper et al., 2008), and non-resonant heating such as stochastic heating (Chandran et al., 2010, 2013). In this framework, turbulent fluctuations with polarisation properties consistent with kinetic Alfvén

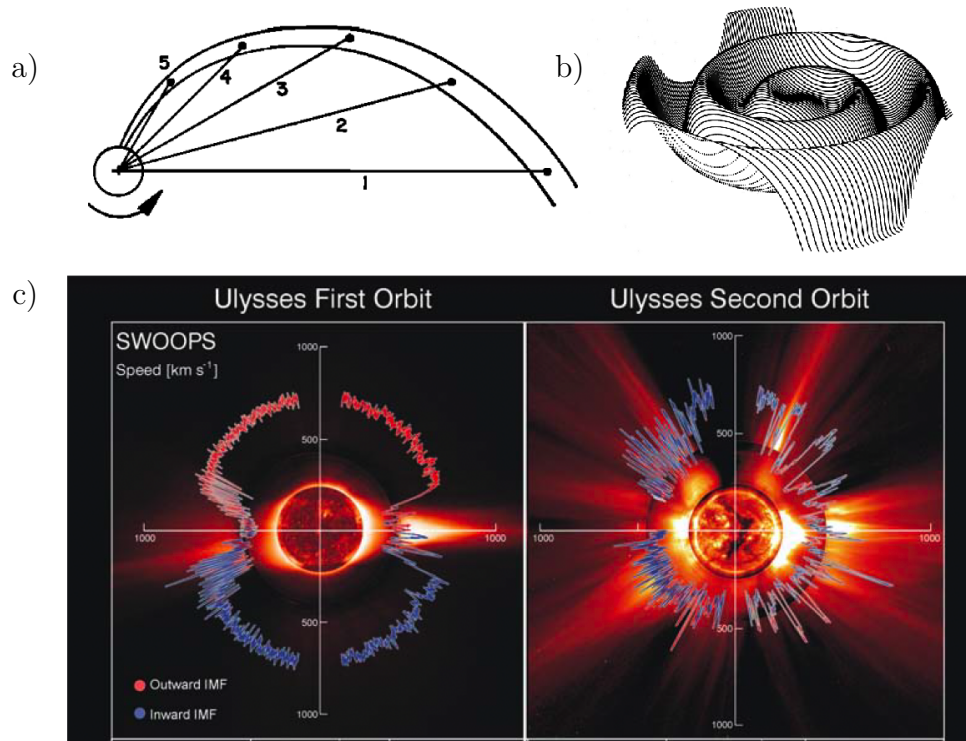


**Figure 1.1:** a) Sketch of the Archimedes spiral of a plasma stream, adapted from [Dessler \(1967\)](#). b) Ballerina skirt pattern of the heliospheric current sheet (HCS), adapted from [Jokipii and Thomas \(1981\)](#). c) Polar plots of the solar wind speed during solar minimum (top left) and solar maximum (top right). The distance from the center represents the magnitude of the speed. The red/blue colour marks the positive(outward)/negative(inward) interplanetary magnetic field. The background images are a composition of images taking by the Solar and Heliospheric Observatory (SOHO). Adapted from [McComas et al. \(2003\)](#)

waves (KAWs) and whistler waves are often invoked as the mechanisms that carry the turbulent cascade to electron scales. In general, observations more often find evidence for KAW-like fluctuations than for whistler-wave-like fluctuations ([Smith et al., 2011](#); [Salem et al., 2012](#); [Podesta and TenBarge, 2012](#); [Podesta, 2013](#); [Roberts et al., 2013](#); [Goldstein et al., 2015](#)).

Another mechanism proposed to carry the turbulent cascade to sub-proton scales is magnetic reconnection ([Sundkvist et al., 2007](#); [Franci et al., 2017](#); [Loureiro and Boldyrev, 2020](#)). Magnetic reconnection is a process in which particles are heated and accelerated while the magnetic field topology changes. It takes place when magnetic structures form a region in which the frozen-in condition is locally broken allowing the exchange of particles between the magnetic structures and leading to



a change in the magnetic connectivity (Hesse and Schindler, 1988; Pontin, 2011). Magnetic reconnection is a multiscale phenomenon that appears in both space and laboratory plasmas under conditions reaching from fully collisional to effectively collisionless. It has been predicted to occur in coronal mass ejections, solar flares, explosive events in planetary magnetospheres, accretion discs, star-formation regions, fusion plasmas, and in the solar wind (see Priest and Forbes, 2007; Zweibel and Yamada, 2009, and references therein). In the solar wind, reconnection events are characterised by streams of particles associated with Alfvénic disturbances and magnetic-field rotations (Gosling et al., 2005; Davis et al., 2006; Gosling et al., 2006; Phan et al., 2006, 2009; Gosling, 2012; Phan et al., 2020). These structures are interpreted as the so-called “exhaust regions” of reconnection events.

Although magnetic reconnection has been studied for over 60 years, there is still no consensus in terms of a complete theory to describe magnetic reconnection at all scales involved. The problem is rooted in the fact that the range of spatial ( $L$ ) and temporal ( $\tau$ ) scales involves fluid-like behaviour at  $L \gg \rho_i, d_i$ , where  $\rho_i$  is the ion gyroradius and  $d_i$  is the ion inertial length, as well as kinetic behaviour and energy dissipation at sub-proton scales,  $L \lesssim \rho_i, d_i$ . In addition, since plasmas are often in a turbulent state, the presence of a turbulent field alters the onset and evolution of reconnection events (Matthaeus and Lamkin, 1986; Strauss, 1988; Lazarian and Vishniac, 1999; Kim and Diamond, 2001; Servidio et al., 2011; Boldyrev and Loureiro, 2017; Adhikari et al., 2020b; Loureiro and Boldyrev, 2020). Unlike in collisional plasmas, in the solar wind, the heating and energy dissipation cannot be attributed to the viscous interaction due to binary particle collisions nor to any process that depends directly on collisions, such as the collisional electric resistivity for instance. To understand the mechanisms of energy dissipation and plasma heating in the solar wind, it is necessary to study the energy partition at small scales where particle energisation occurs and the free energy is removed from the system in an irreversible way increasing the entropy.

Turbulence, plasma instabilities, and magnetic reconnection are phenomena that can generate the necessary conditions for energy dissipation in collisionless plasmas

(e.g., [Kiyani et al., 2015](#); [Li et al., 2016](#); [Matthaeus et al., 2020](#)). Nonetheless, the partition of energy between the electromagnetic fields and the plasma particles as well as the dissipation of energy through the different channels is still under debate. The plasma-physics processes responsible for this heating are not fully understood.

Important progress has been made to understand heating and energy dissipation (e.g., [Gary, 1999](#); [Howes et al., 2017](#); [Klein et al., 2017](#); [Matthaeus et al., 2020](#)). Landau damping, ion-cyclotron damping, and stochastic heating are considered collisionless dissipation mechanisms that transfer energy from the electromagnetic field to the plasma particles ([Marsch et al., 2003](#); [Kasper et al., 2008](#); [Chandran et al., 2010, 2013](#)). The dissipation occurs predominantly in intermittent structures which form in plasma turbulence ([Matthaeus et al., 1999](#); [Kiyani et al., 2015](#)).

The use of numerical simulations has been proven to be an invaluable tool to test existing theories over a wide range of parameters. Moreover, using simulations, we self-consistently explore nonlinear problems which lie beyond analytical theory. Simulations expand our knowledge regarding magnetic reconnection processes in 2D ([Birn et al., 2001](#); [Shay et al., 2001](#); [Servidio et al., 2009](#); [Loureiro et al., 2009](#); [Servidio et al., 2010b](#); [Bessho et al., 2017](#)) and in 3D ([Hesse et al., 2001b](#); [Pritchett and Coroniti, 2001](#); [Lapenta, 2003](#); [Lapenta et al., 2006](#); [Kowal et al., 2009](#); [Daughton et al., 2011](#); [Pritchett, 2013](#); [Baumann et al., 2013](#); [Liu et al., 2013](#); [Muñoz and Büchner, 2018](#)). The use of high-performance computing facilities and the increasing computational capabilities facilitate the study of plasmas from first principles using particle-in-cell (PIC) simulations ([Lapenta, 2012](#); [Germaschewski et al., 2016](#)). These simulations are able to resolve proton and electron scales and to account for phenomena that only reveal themselves using kinetic theory. For instance, electron-kinetic effects can affect ion-scale processes ([Told et al., 2016](#)) even in linear theory. These effects may be even enhanced in nonlinear processes. Currently, full PIC simulations are unable to cover the whole range of scales involved in natural plasma turbulence and reconnection since they are expensive in terms of computing memory and require small time steps to satisfy stability criteria. However, their ability to model the physics behind the energy partition at small scales makes PIC the most

appropriate method to address sub-proton and electron-scale phenomena as well as collisionless energy dissipation.

The main aim of this study is *to identify and quantify the role of reconnection in the turbulent cascade as a dissipation channel*. To do this, we perform 3D fully kinetic simulations using the Plasma Simulation Code (PSC [Germaschewski et al., 2016](#)) which is an explicit PIC code. We simulate anisotropic Alfvénic turbulence in the solar wind which has been widely observed ([Bavassano and Bruno, 1989](#); [Grappin et al., 1991](#); [Chen et al., 2012](#); [Wicks et al., 2011](#); [Chen et al., 2011](#)). Although, the role of reconnection in the small-scale turbulent cascade has been studied previously ([Franci et al., 2017](#); [Boldyrev and Loureiro, 2017](#); [Cerri and Califano, 2017](#)), it is still unclear how 3D reconnection proceeds in the turbulent solar wind and how energy is dissipated through magnetic reconnection. Therefore, we study the formation of electric current structures and the spontaneous onset of magnetic reconnection as part of the turbulent cascade in a 3D geometry. We also define a set of indicators of reconnection, taking into account the differences and similarities between 2D and 3D reconnection. Once we identify reconnection sites in the simulation, we determine the percentage of energy exchange from the electromagnetic fields to the plasma particles through magnetic reconnection. In this way, by determining the amount of reconnection events in our simulation domain, we will be able to quantify the particle acceleration due to reconnection as well as the dissipation owing to heating mechanisms that can be triggered due to magnetic reconnection.

Having stated the aim of this thesis and the open questions that we want to address, following [Baumjohann and Treumann \(1997\)](#); [Klimontovich \(1997\)](#), I introduce the concept of plasma and the essential mathematical description that we use to describe plasmas in Chapter 2. In Chapter 3, I present the concept of magnetic reconnection as well as the basic models and properties of magnetic reconnection. Then, in Chapter 4, I introduce the models of plasma turbulence and discuss the characteristic features of plasma turbulence that are important for our study.

In Chapter 5, I introduce the simulation method that we use to study the occurrence

of reconnection in a turbulent cascade and present a set of tests which allows us to estimate the best simulation parameters to use. In Chapter 6, I introduce our results characterising the turbulent simulations and the geometry of the reconnection events that occur in our simulation domain. We visualise the role of turbulence as a mechanism to create magnetic reconnection.

In Chapter 7, I present the results of our second work in which we develop a framework to study the energy density transfer rate associated with magnetic reconnection in plasma turbulence. This allows us to explore and quantify the role of magnetic reconnection as an energy transfer mechanism in turbulent plasmas.

Afterwards, in Chapter 8, I introduce a new method to reconstruct the magnetic field geometry from multi-point measurements. This is part of my contribution to the MagneToRE mission concept ([Maruca et al., 2021](#)). Finally, in Chapter 9, I present the conclusions and perspectives for future work derived from our research.

## Chapter 2

# Plasma physics

In this chapter I introduce the basic plasma physics that is essential for my project. I begin with the definition of a plasma from a kinetic description and explain the parameters often used to characterise plasmas. Then, I introduce the single-fluid magnetohydrodynamic equations. Finally, I introduce wave modes that exist in plasmas.

### 2.1 The Concept of Plasma

A plasma is an overall quasi-neutral gas consisting of charged particles that respond to electric  $\mathbf{E}$  and magnetic  $\mathbf{B}$  fields. A plasma consists of electrons of mass  $m_e$ , charge  $q_e = -e$  and ions of mass  $m_i$  and charge  $q_i = Ze$ , where  $e$  is the elemental charge and  $Z$  is the atomic charge number. The electromagnetic fields add forces and drifts that considerably change the motions of the charged particles compared to the neutral case. In general, the equations of motion of a plasma particle of species  $s$  are

$$\frac{d\mathbf{x}_s}{dt} = \mathbf{v}_s, \quad (2.1)$$

$$\frac{d\mathbf{v}_s}{dt} = \frac{q_s}{m_s}(\mathbf{E}_m + \mathbf{v}_s \times \mathbf{B}_m), \quad (2.2)$$

where  $\mathbf{E}_m$  and  $\mathbf{B}_m$  are the microscopic electric and magnetic fields acting on the particle with velocity  $\mathbf{v}_s$ , charge  $q_s$  and mass  $m_s$ . Although a description of the

plasma evolution based on the individual particle motion is exact, it is not feasible given the large number of particles ( $\gtrsim 10^{23}$ ) in a typical plasma. Instead, the dynamics of the plasma species  $s = i, e$  is approached by looking at the evolution of the distribution function  $F_s(\mathbf{x}, \mathbf{v}, t)$  in phase space  $(\mathbf{x}, \mathbf{v})$ . In Eq. (2.2),  $\mathbf{E}_m$  and  $\mathbf{B}_m$  evolve according to the Maxwell's equations

$$\nabla \cdot \mathbf{E}_m = \frac{\rho_m}{\epsilon_0}, \quad (2.3)$$

$$\nabla \cdot \mathbf{B}_m = 0, \quad (2.4)$$

$$\frac{\partial \mathbf{E}_m}{\partial t} = c^2 \nabla \times \mathbf{B}_m - \frac{\mathbf{J}_m}{\epsilon_0}, \quad (2.5)$$

$$\frac{\partial \mathbf{B}_m}{\partial t} = -\nabla \times \mathbf{E}_m, \quad (2.6)$$

where  $c$  is the speed of light and  $\epsilon_0$  is the vacuum electric permittivity. In Eq. (2.3)

$$\rho_m(\mathbf{x}, t) = \sum_s q_s \int F_s(\mathbf{x}, \mathbf{v}, t) d^3v \quad (2.7)$$

is the microscopic charge density. In Eq. (2.5),

$$\mathbf{J}_m(\mathbf{x}, t) = \sum_s q_s \int F_s(\mathbf{x}, \mathbf{v}, t) \mathbf{v} d^3v \quad (2.8)$$

is the microscopic current density. The equation that governs the evolution of  $F_s$ , based on Eqs.(2.1) and (2.2), is the Klimontovich–Dupree equation:

$$\frac{\partial F_s}{\partial t} + \mathbf{v} \cdot \nabla_x F_s + \frac{q_s}{m_s} (\mathbf{E}_m + \mathbf{v} \times \mathbf{B}_m) \cdot \nabla_v F_s = 0. \quad (2.9)$$

If we take an ensemble average  $\langle \dots \rangle$  of Eq. (2.9) and define the following quantities as  $f_s = \langle F_s \rangle$ ,  $\mathbf{E} = \langle \mathbf{E}_m \rangle$ ,  $\mathbf{B} = \langle \mathbf{B}_m \rangle$ , where the fluctuations of these quantities are statistical ensembles with  $\langle \delta F_s \rangle = \langle \delta \mathbf{E} \rangle = \langle \delta \mathbf{B} \rangle = 0$ , the equation of evolution of the phase space averaged distribution function  $f_s$  can be simplified to the kinetic equation

$$\frac{\partial f_s}{\partial t} + \mathbf{v} \cdot \nabla_x f_s + \frac{q_s}{m_s} (\mathbf{E} + \mathbf{v} \times \mathbf{B}) \cdot \nabla_v f_s = -\frac{q_s}{m_s} \langle (\delta \mathbf{E} + \mathbf{v} \times \delta \mathbf{B}) \cdot \nabla_v \delta F_s \rangle, \quad (2.10)$$

where  $f_s(\mathbf{x}, \mathbf{v}, t)$  is the coarse-grained distribution function which represents the probability of finding a particle in an element  $d\mathbf{x}d\mathbf{v}$  of phase space under the effect of averaged electric and magnetic fields. These fields are averaged over small Coulomb potentials of single particles in the ensemble. From now on, we refer to  $f_s(\mathbf{x}, \mathbf{v}, t)$  simply as the distribution function. If the second-order interactions on the right-hand side of Eq. (2.10) are dropped, the equation becomes the Vlasov equation

$$\frac{\partial f_s}{\partial t} + \mathbf{v} \cdot \nabla_{\mathbf{x}} f_s + \frac{q}{m} (\mathbf{E} + \mathbf{v} \times \mathbf{B}) \cdot \nabla_{\mathbf{v}} f_s = 0. \quad (2.11)$$

Eq. (2.11) describes the evolution of the particle species  $s$  in a collisionless plasma. If the initial  $f_s$  and the initial fields  $\mathbf{E}$  and  $\mathbf{B}$  are known, the plasma dynamics can be studied using Eq. (2.11) and Maxwell's equations (2.3) through (2.6). This is known as the kinetic approach. However, there are cases in which it is not feasible to study the plasma evolution directly from  $f_s$  but from macroscopic quantities derived from  $f_s$ . One such approach is known as magnetohydrodynamics (MHD).

In multifluid MHD, the macroscopic quantities that describe the evolution of the plasma are the density

$$n_s = \int f_s(\mathbf{x}, \mathbf{v}, t) d^3v, \quad (2.12)$$

the bulk velocity  $\mathbf{u}_s$

$$\mathbf{u}_s = \frac{1}{n_s} \int \mathbf{v} f_s(\mathbf{x}, \mathbf{v}, t) d^3v, \quad (2.13)$$

the pressure tensor

$$\overline{\mathbf{P}}_s = m_s \int (\mathbf{v} - \mathbf{u}_s)(\mathbf{v} - \mathbf{u}_s) f_s(\mathbf{x}, \mathbf{v}, t) d^3v, \quad (2.14)$$

where  $(\mathbf{v} - \mathbf{u}_s)(\mathbf{v} - \mathbf{u}_s)$  is a dyadic product, the scalar temperature

$$T_s = \frac{m_s}{3k_b n_s} \int (\mathbf{v} - \mathbf{u}_s) \cdot (\mathbf{v} - \mathbf{u}_s) f_s(\mathbf{x}, \mathbf{v}, t) d^3v, \quad (2.15)$$

where  $k_B$  is the Boltzmann constant, the heat flux tensor

$$\overline{\overline{\mathbf{Q}}}_s = m_s \int (\mathbf{v} - \mathbf{u}_s)(\mathbf{v} - \mathbf{u}_s)(\mathbf{v} - \mathbf{u}_s) f_s(\mathbf{x}, \mathbf{v}, t) d^3v, \quad (2.16)$$

and the heat flux vector

$$\mathbf{h}_s = \frac{m_s}{2} \int (\mathbf{v} - \mathbf{u}_s) \cdot (\mathbf{v} - \mathbf{u}_s)(\mathbf{v} - \mathbf{u}_s) f_s(\mathbf{x}, \mathbf{v}, t) d^3v. \quad (2.17)$$

## 2.2 From Kinetic to MHD

The equations that describe the evolution of the macroscopic quantities are derived by taking velocity moments of Eq. (2.11). Thus, the zeroth moment leads to the continuity equation

$$\frac{\partial n_s}{\partial t} + \nabla \cdot (n_s \mathbf{u}_s) = 0, \quad (2.18)$$

the first moment yields the momentum equation

$$\frac{\partial(n_s \mathbf{u}_s)}{\partial t} + \nabla \cdot (n_s \mathbf{u}_s \mathbf{u}_s) + \frac{1}{m_s} \nabla \cdot \overline{\mathbf{P}}_s - \frac{q_s}{m_s} n_s (\mathbf{E} + \mathbf{u}_s \times \mathbf{B}) = 0, \quad (2.19)$$

and the second moment leads to the energy equation

$$\frac{3}{2} n_s k_B \left( \frac{\partial T_s}{\partial t} + \mathbf{u}_s \cdot \nabla T_s \right) + p_s \nabla \cdot \mathbf{u}_s = -\nabla \cdot \mathbf{h}_s - (\overline{\mathbf{P}}_s^s \cdot \nabla) \cdot \mathbf{u}_s. \quad (2.20)$$

Since each moment of the Vlasov equation includes a new high-order quantity, another higher-order equation is required to close the system. This is known as the closure problem (Chew et al., 1956; Chust and Belmont, 2006). To close the system and considering different scenarios for the plasma, it is a common approach to define an equation of state. For instance, in isotropic plasmas, i.e.,  $\overline{\mathbf{P}}_s = p_s \mathbf{I}$ , where  $\mathbf{I}$  is the unitary matrix and

$$p_s = \sum P_{ii,s}/3 \quad (2.21)$$



is the scalar pressure, the equation of state that closes the system is

$$p_s = p_{s0} \left( \frac{n_s}{n_{s0}} \right)^\gamma, \quad (2.22)$$

where  $p_{s0}$  and  $n_{s0}$  are constant initial values and  $\gamma = C_p/C_V$  is the adiabatic index which represents the ratio between the specific heats at constant pressure  $C_p$  and at constant volume  $C_V$ . In more general scenarios, the index  $\gamma$  is also known as the polytropic index. In isobaric conditions (constant pressure)  $\gamma = 0$ . In adiabatic conditions (no heat transfer)  $\gamma = 5/3$ . In isothermal conditions (constant temperature),  $\gamma = 1$ , and in isometric conditions (constant density),  $\gamma = \infty$ .

If the plasma cannot be considered isotropic, a possible fluid closure is based on the double-adiabatic invariants, also known as the Chew-Goldberger-Low (CGL) invariants ([Chew et al., 1956](#)):

$$\frac{d}{dt} \left( \frac{p_{s,\perp}}{n_s B} \right) = 0 \quad (2.23)$$

and

$$\frac{d}{dt} \left( \frac{p_{s,\parallel} B^2}{n_s^3} \right) = 0, \quad (2.24)$$

where  $p_{s,\parallel}$  and  $p_{s,\perp}$  are the pressures parallel and perpendicular to the magnetic field  $\mathbf{B}$  and  $B = |\mathbf{B}|$  is the magnetic field strength. Equations (2.23) and (2.24) can be used to close the system of equations and to model the evolution of a multi-fluid plasma.

### 2.2.1 Characteristic Parameters

The characteristic length parameters used to describe plasmas are:

- The characteristic size of the system  $L$ . In the solar wind,  $L$  is similar to the size of the inner heliosphere.

- The inertial length of the species  $s$

$$d_s = \frac{c}{\omega_{ps}}, \quad (2.25)$$

where

$$\omega_{ps} = \sqrt{\frac{n_s q_s^2}{m_s \epsilon_0}} \quad (2.26)$$

is the plasma frequency. The inertial length is the distance associated to the exponential decay of electromagnetic fluctuations with frequency  $\omega \leq \omega_{ps}$  in the plasma.

- The gyroradius

$$\rho_s = \frac{m_s v_{\perp,s}}{q_s B}, \quad (2.27)$$

$v_{\perp,s}$  is the component of the particle's speed in the plane perpendicular to the magnetic field. The gyroradius is associated with the gyration motion of the particle around the magnetic field with the gyrofrequency

$$\Omega_s = \frac{qB}{m_s}. \quad (2.28)$$

- The Debye length

$$\lambda_{D_s} = \sqrt{\frac{\epsilon_0 k_B T_s}{n_s q_s^2}}. \quad (2.29)$$

The Debye length is the distance over which thermal fluctuations of particles are balanced with the Coulomb potential such that the plasma remains quasi-neutral on scales  $\gtrsim \lambda_{D_s}$ .

The characteristic values of these parameters in the solar wind, at 1 au ( $1.49 \times 10^8$  km), are shown in table 2.1 where the periods are calculated as  $\Pi_{\Omega_s} = 2\pi/\Omega_s$  and  $\Pi_{\omega_{ps}} = 2\pi/\omega_{ps}$ . It is worth noting that, owing to the low density of the solar wind

$L$	1 au	characteristic size of the system
$d_i$	140 km	proton inertial length
$\rho_i$	160 km	proton gyroradius
$d_e$	3 km	electron inertial length
$\rho_e$	2 km	electron gyroradius
$\lambda_i, \lambda_e$	12 m	proton and electron Debye lengths
$\Pi_{\Omega_i}$	26 s	proton gyroperiod
$\Pi_{\Omega_e}$	14 ms	electron gyroperiod
$\Pi_{\omega_{pi}}$	3 ms	proton plasma period
$\Pi_{\omega_{pe}}$	70 $\mu$ s	electron plasma period

**Table 2.1:** Characteristic length and time scales at 1 au. Adapted from [Verscharen et al. \(2019\)](#)

at 1 au,  $n_s \sim 5 \text{ cm}^{-3}$ , the proton collisional mean free path  $\lambda_{mfp,i}$  is  $\sim 3$  au. Hence, particle collisions are extremely low and a collisionless description, Eq. (2.11), is suitable to study the plasma dynamics.

### 2.2.2 Single Fluid MHD

The MHD approach describes low frequency phenomena, i.e.,  $\omega \ll \omega_{ps}$  and  $\lambda \gg d_s$ . In single-fluid MHD, the plasma is considered a highly-conducting and quasi-neutral single-component fluid ( $n = n_i = n_e$ ) where the charge density is defined as

$$\rho_c = \sum_s q_s n_s. \quad (2.30)$$

For a quasi-neutral fluid,  $\rho_c \approx 0$ . The electric current density is defined as

$$\mathbf{J} = \sum_s q_s n_s \mathbf{u}_s, \quad (2.31)$$

and the fluid density is defined as

$$n = \frac{\sum_s m_s n_s}{\sum_s m_s}. \quad (2.32)$$

The mass of a fluid volume is

$$m = \frac{n_i m_i + n_e m_e}{n_i + n_e}, \quad (2.33)$$

and

$$\mathbf{u} = \frac{m_e n_e \mathbf{u}_e + m_i n_i \mathbf{u}_i}{m_e n_e + m_i n_i}, \quad (2.34)$$

is the fluid velocity. Multiplying the continuity equation Eq. 2.18 for each species  $s$  with its respective mass  $m_s$  and adding them, we obtain the continuity equation for the fluid

$$\frac{\partial n}{\partial t} + \nabla \cdot (n \mathbf{u}) = 0, \quad (2.35)$$

In addition, by adding the momentum equation Eq. 2.19 for ions and electrons we obtain the momentum equation for the fluid

$$\frac{\partial(nm\mathbf{u})}{\partial t} + \nabla \cdot (nm\mathbf{u}\mathbf{u}) = -\nabla \cdot \bar{\mathbf{P}} + \mathbf{J} \times \mathbf{B} = 0, \quad (2.36)$$

where  $\bar{\mathbf{P}} = \bar{\mathbf{P}}_e + \bar{\mathbf{P}}_i$ . Another important equation in MHD theory is the generalised Ohm's law

$$\mathbf{E} + \mathbf{u} \times \mathbf{B} = \eta \mathbf{J} + \frac{1}{nq} \mathbf{J} \times \mathbf{B} - \frac{1}{nq} \nabla \cdot \bar{\mathbf{P}}_e + \frac{m_e}{nq^2} \frac{\partial \mathbf{J}}{\partial t}, \quad (2.37)$$

where  $\eta$  is the electric resistivity and  $\bar{\mathbf{P}}_e$  is the electron pressure. If the right-hand side of Eq. (2.37) is identically zero, the plasma is considered as *ideal* and it is attached to the magnetic field. Thus, convected magnetic field structures carry plasma particles without diffusion and vice-versa (see section 3.1). The equation (2.37) takes into account that the mass of electrons is considerably smaller than the ion's mass, i.e.,  $m_i/m_e \gg 1$ . Thus, the contribution of the ion pressure  $\bar{\mathbf{P}}_i$  and the ion velocity  $\mathbf{u}_i$  are negligible. For details on how to calculate this expression see [Baumjohann and Treumann \(1997\)](#) section 7.3. The generalised Ohm's law is important for the Hall MHD theory that is used to describe reconnection as I will briefly show in subsection 3.2.1.

## 2.3 Plasma Waves

In plasmas, in addition to the density and velocity perturbations, the electric and magnetic field perturbations generate a rich variety of propagating and non-propagating normal modes of these systems. This is mostly due to the additional restoring forces acting on both the plasma particles and the electromagnetic fields in comparison to neutral gases. To describe the perturbations from linear theory (Baumjohann and Treumann, 1997; Brambilla, 1998), consider a physical quantity

$$\mathbf{A}(\mathbf{x}, t) = \mathbf{A}_0 + \delta\mathbf{A}(\mathbf{x}, t) \quad (2.38)$$

which depends on the position  $\mathbf{x}$  and time  $t$ . The term  $\delta\mathbf{A}(\mathbf{x}, t)$  represents the fluctuating perturbations around the equilibrium state  $\mathbf{A}_0$ . We assume that  $|\delta\mathbf{A}(\mathbf{x}, t)| \ll |\mathbf{A}_0|$  and that the perturbation has the form of a plane wave with a wavelength  $\lambda$ . We then find

$$\delta\mathbf{A}(\mathbf{x}, t) = \text{Re} \left[ \tilde{\mathbf{A}}(\mathbf{k}, \omega) e^{i\mathbf{k} \cdot \mathbf{x} - i\omega t} \right], \quad (2.39)$$

where  $\mathbf{k}$  is the real wave-vector and  $\omega = \omega_r + i\gamma$  is the complex frequency. The term

$$\tilde{\mathbf{A}}(\mathbf{k}, \omega) = \int_{-\infty}^{\infty} \mathbf{A}(\mathbf{x}, t) e^{i\mathbf{k} \cdot \mathbf{x} - i\omega t} d\mathbf{x} dt \quad (2.40)$$

is the complex Fourier amplitude of  $\mathbf{A}(\mathbf{x}, t)$  in Fourier space. The components of the wave vector are the wave numbers  $k_j = 2\pi/\lambda_j$ . The real frequency  $\omega_r$  corresponds to the real part of  $\omega$ , and  $\gamma$  corresponds to the imaginary part of  $\omega$ , which is the linear damping/growth rate. The two velocities for a plane wave are the phase velocity

$$\mathbf{v}_{ph} = \frac{\omega \mathbf{k}}{k^2} \quad (2.41)$$

and the group velocity

$$\mathbf{v}_{gr} = \frac{\partial \omega}{\partial \mathbf{k}}, \quad (2.42)$$

where the  $\mathbf{v}_{ph}$  is the velocity of the wave front and  $\mathbf{v}_{gr}$  is the velocity of the energy flow carried by the wave. According to Eqs. (2.38) and (2.39), the electric and magnetic fields can be expressed as

$$\mathbf{E} = \text{Re} \left[ \tilde{\mathbf{E}}(\mathbf{k}, \omega) e^{(i\mathbf{k} \cdot \mathbf{x} - i\omega t)} \right] \quad (2.43)$$

and

$$\mathbf{B} = \mathbf{B}_0 + \text{Re} \left[ \tilde{\mathbf{B}}(\mathbf{k}, \omega) e^{(i\mathbf{k} \cdot \mathbf{x} - i\omega t)} \right], \quad (2.44)$$

where the background electric field  $\mathbf{E}_0$  is neglected. In Fourier space,  $\partial/\partial t \rightarrow -i\omega$  and  $\nabla \rightarrow i\mathbf{k}$ . Thus, according to Eqs. (2.43) and (2.44), Maxwell's equations (2.3) through (2.6) can be expressed as

$$\mathbf{k} \cdot \tilde{\mathbf{E}} = -i \frac{\tilde{\rho}_c}{\epsilon_0}, \quad (2.45)$$

$$\mathbf{k} \cdot \tilde{\mathbf{B}} = 0, \quad (2.46)$$

$$\mathbf{k} \times \tilde{\mathbf{B}} + \frac{\omega}{c^2} \tilde{\mathbf{E}} = -i\tilde{\mathbf{J}}\mu_0, \quad (2.47)$$

$$\mathbf{k} \times \tilde{\mathbf{E}} - \omega\tilde{\mathbf{B}} = 0, \quad (2.48)$$

where  $\mu_0 = 1/(\epsilon_0 c^2)$  is the vacuum magnetic permeability. The left-hand sides of Eqs. (2.45) through (2.48) contain the interactions between the electric and magnetic fields whereas the right-hand sides contain the interaction of the fields with the particles. The fluctuations quantified by  $\tilde{\mathbf{J}}$  are correlated with  $\tilde{\mathbf{E}}$  through

$$\tilde{\mathbf{J}} = \bar{\sigma}(\mathbf{k}, \omega) \cdot \tilde{\mathbf{E}}, \quad (2.49)$$

where  $\bar{\sigma}(\mathbf{k}, \omega)$  is the so-called conductivity tensor. Taking the cross product of  $\mathbf{k}/\omega$  with Eq. (2.48) and substituting it along with Eq. (2.49) into Eq. (2.47) we obtain the expression

$$\left[ \left( k^2 - \frac{\omega^2}{c^2} \right) \bar{\mathbf{I}} - \mathbf{k}\mathbf{k} - i\omega\mu_0\bar{\sigma}(\mathbf{k}, \omega) \right] \cdot \tilde{\mathbf{E}}(\mathbf{k}, \omega) = 0, \quad (2.50)$$

where we have used the identity  $\mathbf{k} \times \mathbf{k} \times \mathbf{E} = (\mathbf{k}\mathbf{k} - k^2\bar{\mathbf{I}}) \cdot \mathbf{E}$ . Defining the dielectric tensor

$$\bar{\epsilon}(\mathbf{k}, \omega) = \bar{\mathbf{I}} + \frac{i}{\omega\epsilon_0} \bar{\sigma}(\mathbf{k}, \omega), \quad (2.51)$$

Eq (2.50) can be expressed as

$$\left[ \frac{k^2 c^2}{\omega^2} \left( \frac{\mathbf{k}\mathbf{k}}{k^2} - \bar{\mathbf{I}} \right) + \bar{\epsilon}(\mathbf{k}, \omega) \right] \cdot \tilde{\mathbf{E}}(\mathbf{k}, \omega) = 0. \quad (2.52)$$

The wave modes that can be excited in a plasma are described by the relation between  $\mathbf{k}$  and  $\omega$  that depends on the plasma properties captured by  $\bar{\epsilon}(\mathbf{k}, \omega)$ . The non-trivial solutions of Eq (2.52) require that

$$\text{Det} \left[ \frac{k^2 c^2}{\omega^2} \left( \frac{\mathbf{k}\mathbf{k}}{k^2} - \bar{\mathbf{I}} \right) + \bar{\epsilon}(\mathbf{k}, \omega) \right] = 0. \quad (2.53)$$

Eq. (2.53) is the so-called dispersion relation. The solution of this equation requires to know the dielectric tensor. The functional form of  $\bar{\epsilon}(\mathbf{k}, \omega)$  depends on the model used to describe the plasma (Gary and Gary, 1993; Baumjohann and Treumann, 1997). The explicit calculation of  $\bar{\epsilon}$  is beyond the scope of this manuscript. Instead, we discuss the wave modes as known solutions of Eq. (2.53) that are excited in plasmas and that are relevant for this study.

### 2.3.1 Plasma Wave Modes

The most important plasmas modes that are excited at large scales ( $kd_i \ll 1$  and  $k\rho_i \ll 1$ ) are the non-compressive Alfvénic (Alfvén, 1942) and compressive modes. In the solar wind, the more relevant mode for this study is the Alfvén mode due to the majority of the turbulent fluctuations in space plasmas is the Alfvén mode (Tu and Marsch, 1995; Bruno and Carbone, 2013). The magnetic energy associated with compressive modes is around 2%-10% of the magnetic energy associated with Alfvén modes (Chen, 2016). The Alfvén waves correspond to magnetic perturbations  $\delta\mathbf{B}$  perpendicular to the background magnetic field  $\mathbf{B}_0$  and to  $\mathbf{k}$ . The perturbation propagates along  $\mathbf{B}_0$ . For this mode, the restoring force is the magnetic tension.

The linear dispersion relation is

$$\omega_r = \pm |k_{\parallel}| v_A, \quad (2.54)$$

where  $k_{\parallel}$  is the wave-number parallel to  $\mathbf{B}_0$  and  $v_A = |\mathbf{B}_0|/\sqrt{nm\mu_0}$  is the Alfvén speed. The perturbations  $\delta\mathbf{B}$  are (anti-)correlated with the perturbations  $\delta\mathbf{u}$  in the plasma velocity  $\mathbf{u}$  through the polarisation relation

$$\frac{\delta\mathbf{B}}{|\mathbf{B}_0|} = \mp \frac{\delta\mathbf{u}}{v_A}, \quad (2.55)$$

where the sign  $-(+)$  indicates the perturbation is propagating in the direction parallel (anti-parallel) to the magnetic field  $\mathbf{B}_0$ . This type of fluctuations are routinely measured in the solar wind (Unti and Neugebauer, 1968; Belcher et al., 1969; Velli and Pruneti, 1997; Podesta and TenBarge, 2012). Parallel-propagating Alfvén waves are left-circularly polarized (Verscharen et al., 2019) and can be resonantly damped by resonant ions with parallel speed

$$v_r = \frac{\omega_r - l\Omega_i}{k_{\parallel}}, \quad (2.56)$$

where  $l$  is an integer number. Another family of modes that are excited at large scales are magnetosonic modes. The dispersion relation for these modes is

$$\omega_{ms}^2 = \frac{k^2}{2} \left\{ c_{ms}^2 \pm \left[ (v_A^2 - c_s^2)^2 + 4v_A^2 c_s^2 \frac{k_{\perp}^2}{k^2} \right]^{1/2} \right\} \quad (2.57)$$

where  $c_s^2 = \gamma k_B T / m_i$  is the sound speed and  $c_{ms}^2 = c_s^2 + v_A^2$  is the magnetosonic speed. The positive/negative sign is for the fast/slow magnetosonic mode. The fast mode propagates into the perpendicular direction with phase velocity  $v_{ph,f\perp} = c_{ms}$  whereas the slow mode does not propagate into the perpendicular direction. The propagation into the parallel direction depends on the relation between  $v_a$  and  $c_s$ . In the case  $v_A > c_s$ , the fast mode propagates with speed  $v_{ph,f\parallel} = v_a$  and the slow mode propagates with phase speed  $v_{ph,s\parallel} = c_s$ . In the opposite case,  $v_A < c_s$  the fast



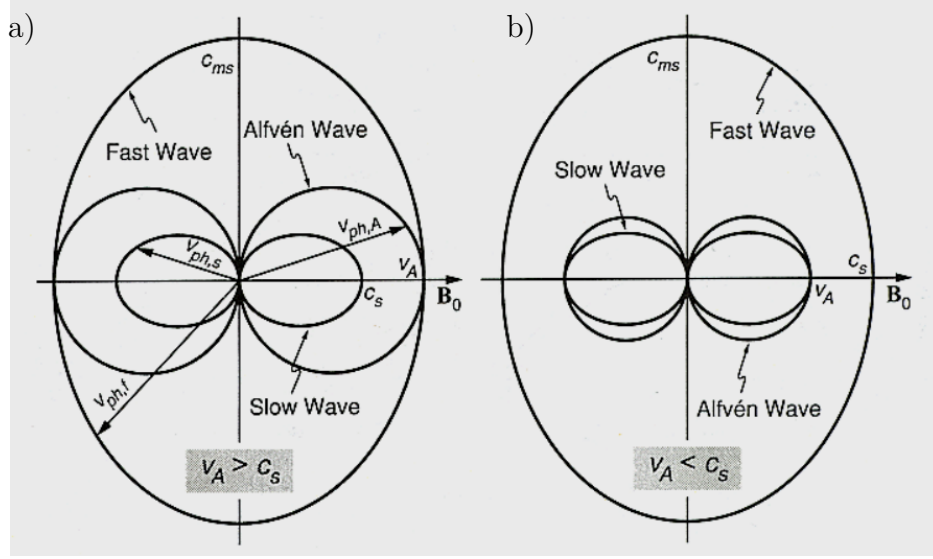


**Figure 2.1:** a) Phase velocity diagram of the MHD modes for  $v_A > c_s$  (a) and  $v_A < c_s$  (b). Adapted from [Baumjohann and Treumann \(1997\)](#)

mode propagates with phase speed  $v_{ph,f\parallel} = c_s$  while the slow mode propagates with phase speed  $v_{ph,s\parallel} = v_A$ . Figure 3.7 shows a phase velocity diagram that summarizes these relations.

Returning to the Alfvén mode, the dispersion relation for Alfvén waves, at low frequencies ( $\omega_r \ll \Omega_i$ ), splits into two branches at small-scales ( $kd_i \gtrsim 1$  and  $k\rho_i \gtrsim 1$ ): kinetic Alfvén waves (KAW) and ion-cyclotron waves. *i*) Kinetic Alfvén waves (KAW) exist at  $k_\perp \rho_i \gtrsim 1$  and  $k_\perp \gg k_\parallel$ , are right-hand polarised oblique-propagating modes ([Hollweg, 1999](#); [Howes et al., 2006](#); [Schekochihin et al., 2009](#)). They are compressive. The fluctuations in density  $\delta n$  and in the parallel magnetic field  $\delta B_\parallel$  generate fluctuations in the parallel electric field  $\delta E_\parallel$ . *ii*) Ion-cyclotron waves exist at  $k_\parallel \rho_i \gtrsim 1$  and  $k_\perp \ll k_\parallel$ . They are left-hand polarised quasi-parallel propagating modes ([Verscharen et al., 2012](#)). At high frequencies ( $\omega_r \gg \Omega_i$ ), the family of fast-magnetosonic whistler (FM/W) waves exist. This includes whistler waves, lower-hybrid waves and kinetic magnetosonic waves. The quasi-parallel propagating mode, also known as the R-mode, is right-handed in polarisation and can resonate with electrons ([Verscharen et al., 2012](#)). The R-mode connects with the Alfvén mode at large scales. In oblique propagation and at  $kd_i \gg 1$ , the FM/W branch becomes the dispersive whistler mode, whereas in quasi-perpendicular propagation, it becomes

the lower-hybrid mode ([Verscharen et al., 2019](#)).

## Chapter 3

# Magnetic reconnection

In this chapter, I review the general concept of magnetic reconnection. Then, I cover the models in two dimensions starting with the Sweet–Parker model, on which I put special emphasis due to its pedagogic values. I then continue with the Hall-MHD reconnection model and follow on with the tearing reconnection model. Afterwards I present a general discussion of three-dimensional magnetic reconnection and finish by commenting on the observation of magnetic reconnection in the solar wind.

### 3.1 The General Concept of Magnetic Reconnection

Since plasma particles gyrate around magnetic field, they are bounded to the magnetic-field lines as long as there is no electric resistivity (ideal plasmas) or as long as there are no strong gradients in the magnetic field. Under this conditions the plasma is “frozen” onto the magnetic field. As a consequence, if an external force modifies the magnetic topology, for instance by bending the magnetic field lines (see Figure 3.1a), the motion of the plasma particles is modified accordingly. Likewise, if the external force acts on the plasma particles, the magnetic-field lines are also modified. This is known as the “frozen-in theorem”. Therefore, any change in the magnetic field is associated with a convective motion of the plasma. The equation that describes this behavior is the ideal induction equation

$$\frac{\partial \mathbf{B}}{\partial t} - \nabla \times (\mathbf{u} \times \mathbf{B}) = 0. \quad (3.1)$$

which follows from inserting the electric field

$$\mathbf{E} = -\mathbf{u} \times \mathbf{B} \quad (3.2)$$

into Faraday's law Eq. (2.6)

$$\frac{\partial \mathbf{B}}{\partial t} + \nabla \times \mathbf{E} = 0, \quad (3.3)$$

where  $\mathbf{u}$  is the bulk velocity of the particles. Integrating Eq. 3.5 on a surface area  $S$

$$\frac{\partial}{\partial t} \int_S \mathbf{B} \cdot d\mathbf{S} = \int_S \nabla \times (\mathbf{u} \times \mathbf{B}) \cdot d\mathbf{S}, \quad (3.4)$$

$$\frac{\partial \phi_B}{\partial t} = 0, \quad (3.5)$$

where  $\phi_B$  is the magnetic flux through the surface area  $S$ . Thus, the magnetic flux remains constant.

On the contrary, if the plasma is non-ideal, i.e., there is a source of resistivity, the equation that represents this behavior is the non-ideal induction equation

$$\frac{\partial \mathbf{B}}{\partial t} = \nabla \times (\mathbf{u} \times \mathbf{B}) - \nabla \times \mathbf{R}, \quad (3.6)$$

which follows from inserting the generalized Ohm's law, Eq. (2.37)

$$\mathbf{E} + \mathbf{u} \times \mathbf{B} = \mathbf{R}, \quad (3.7)$$

into Faraday's law Eq. (2.6). The term  $\mathbf{R}$  represents any non-ideal contributions. In the particular case of resistive MHD, the dominant term on the right-hand side of Eq. (2.37) is  $\eta \mathbf{J}$ . Thus,  $\mathbf{R} = \eta \mathbf{J}$  and Eq. (3.6) can be written as

$$\frac{\partial \mathbf{B}}{\partial t} = \nabla \times (\mathbf{u} \times \mathbf{B}) + \frac{\eta}{\mu_0} \nabla^2 \mathbf{B}, \quad (3.8)$$

where the displacement current term in Ampère's law, Eq. (2.5), is neglected. From Eq. (3.8), whenever  $\eta$  or  $\nabla^2 \mathbf{B}$  are so large that the first and second terms on the right side of Eq. (3.8) are comparable, the frozen-in condition is locally broken. Therefore, magnetic field not only advects according to Eq. (3.5) but also diffuses locally (see Figure 3.1b), allowing for a reconfiguration of magnetic topology ([Axford, 1984](#); [Wilmot-Smith et al., 2005](#)).

This behavior can be expressed in term of the diffusion time  $\tau_{diff} \sim \mu_0 L^2 / \eta$  and convective time  $\tau_{con} \sim L / u$ . The ratio between these two times is the magnetic Reynolds number ( $Re_m$ ):

$$Re_m = \frac{Lu\mu_0}{\eta}. \quad (3.9)$$

For large  $Re_m$ , the convective motion of the magnetic field dominates the evolution of the plasma flow and any magnetic field diffusion is negligible.

A fundamental feature of magnetic reconnection, regardless of the theory used to describe it, is that it is a non-linear process which leads to the merging and recon-

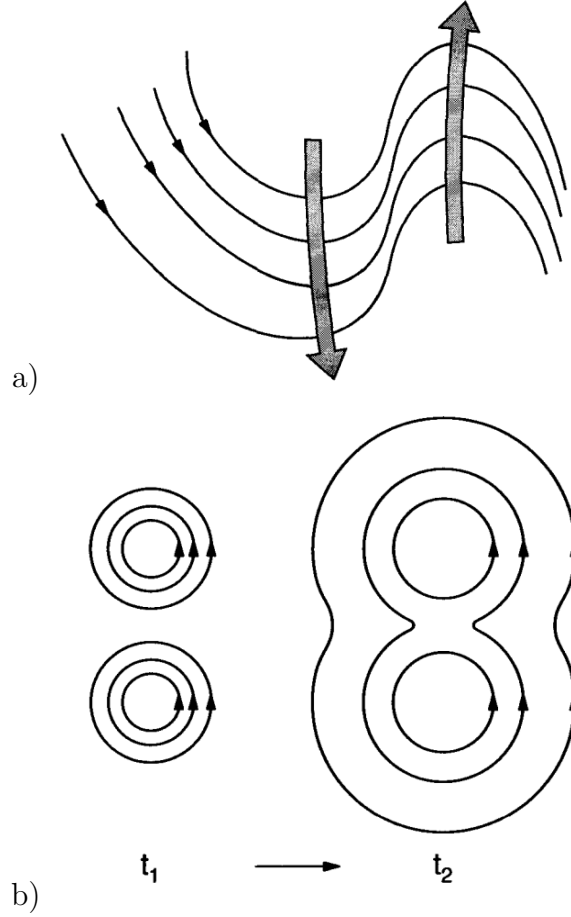


**Figure 3.1:** a) Sketch of the frozen-in theorem. The magnetic-field lines and the plasma parcels are couple to each other. b) Sketch of the magnetic field diffusion. The magnetic field diffuses in space as a function of time. Adapted from [Baumjohann and Treumann \(1997\)](#)

figuration of magnetic field structures which otherwise would experience convection but not diffusion. This mechanism changes the topology of the magnetic field and mixes plasmas from different, otherwise separated magnetic environments. In order for reconnection to occur, plasma and magnetic field within a local region, the so-called *diffusion region* must move independently of each other. Whenever this happens, the magnetic field is not bound to the particles and vice-versa which means that the frozen-in condition, Eq. 3.5, is locally broken and the ideal single fluid approach (section 2.2.2) is no longer valid at the diffusion region. Thus, magnetic reconnection is a process that depends highly on the diffusion of the magnetic field. This is true no matter which theory is used to describe the process. However, there are several discrepancies about reconnection rates, plasma parameters dependen-

cies, and energy transport between the predictions from early steady-state models (Parker, 1957; Sweet, 1958; Dungey, 1961), from the most recent turbulent models (Eyink, 2015; Huang and Bhattacharjee, 2016; Lazarian et al., 2020) and from observations made in different regimes in the solar wind (Gosling, 2012; Lalescu et al., 2015). Despite these discrepancies, we will first introduce the 2D case to give an idea about the concept of the reconnection process and then talk about the theories in 3D geometry and the role of turbulence in magnetic reconnection.

### 3.2 Magnetic Reconnection in 2D

The study of magnetic reconnection has been motivated as a way to explain explosive events (i.e., flares) in the Sun. It was first discussed by Parker (1957); Sweet (1958) and Dungey (1961) as a particle acceleration process in the vicinity of magnetic null points in solar flares and later as a steady-state magnetic merging process by Vasyliunas (1975). The Sweet–Parker model of 2D reconnection is based on the conservation of mass, momentum, energy and magnetic flux for an incompressible, resistive and steady-state MHD flow. As a 2D geometry is assumed, there are no variations along  $\hat{y}$ , i.e.,  $\partial/\partial y = 0$ . Because of the steady-state assumption, there are no temporal variations either, i.e.,  $\partial/\partial t = 0$ .

In this model, oppositely directed magnetic fields in a laminar setup approach each other. As they are convected in a converging pattern, a current sheet forms to sustain the gradient of the magnetic field. Thus, we consider a current sheet of length  $2L$  along  $\hat{x}$  and thickness  $\delta$  along  $\hat{z}$ , see Figure 3.2, where  $\mathbf{v}_0$  ( $\mathbf{v}_{out}$ ) and  $\mathbf{B}_0$  ( $\mathbf{B}_{out}$ ) are the inflow (outflow) plasma speed and magnetic field strength respectively.

Since particles enter the current sheet with speed  $v_0$  through  $2L$  and leave the current sheet with speed  $v_{out}$  and through  $2\delta$ , the mass conservation

$$\nabla \cdot (\rho \mathbf{u}) = \oint \rho \mathbf{u} \cdot d\mathbf{A} = -4\rho v_0 L + 4\rho v_{out} \delta = 0, \quad (3.10)$$

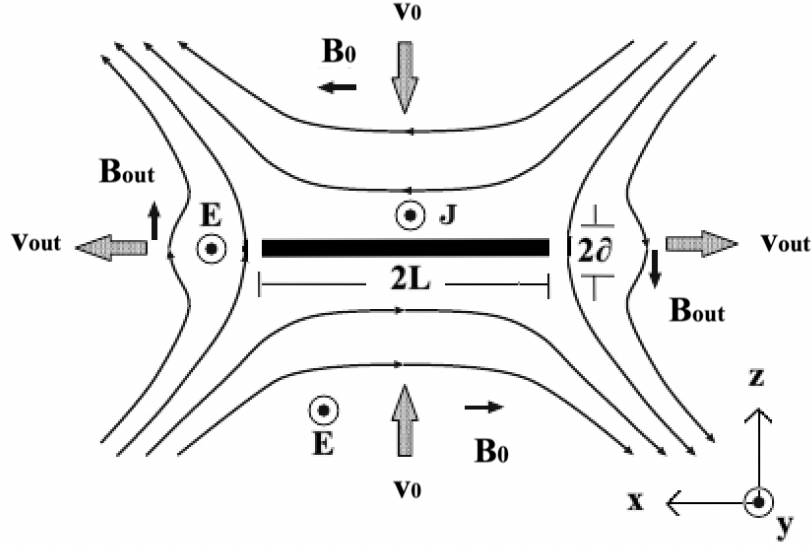


**Figure 3.2:** Sweet–Parker reconnection model. Oppositely directed magnetic fields  $\mathbf{B}_0$  are convected with speed  $\mathbf{v}_0$ . This forms a current sheet  $\mathbf{J}$  directed out of the reconnection plane. The current sheet has length  $2L$  and thickness  $2\delta$ . A self-consistent uniform electric field  $\mathbf{E}$  is directed out of the plane. The reconnected field  $\mathbf{B}_{out}$  is convected away from the reconnection region at the speed  $\mathbf{v}_{out}$ . Adapted from [Somov \(2012\)](#)

where the factor 2 accounts for the symmetry in the mass flow, leads to

$$v_0 L = v_{out} \delta, \quad (3.11)$$

where  $\rho$  is the mass density of the plasma and  $A$  defines the surface area of the current sheet. If there is a diffusion region between the magnetic field lines in which the electric resistivity is high enough to break down the frozen-in condition, the particles moving along with the field lines de-magnetize and join the particles associated with the field lines on the other side of the current sheet. To illustrate this, we consider Ohm’s law outside the current sheet, the electric field

$$E_y = (\mathbf{v}_0 \times \mathbf{B}_0)_y = (v_0 B_0). \quad (3.12)$$

Ohm’s law within the current sheet, where the speed of the plasma is zero, i.e., in



the so-called stagnation point, leads to

$$E_y = \eta J_y. \quad (3.13)$$

Using the Ampère's law and considering the curl of  $\mathbf{B}$  over a distance  $\delta$

$$\nabla \times \mathbf{B}_0 = \mu_0 \mathbf{J}, \quad (3.14)$$

leads to an expression for the current

$$J_y = \frac{B_0}{\delta \mu_0}. \quad (3.15)$$

Combining Eq. (3.15) with Eq. (3.13), we find

$$E_y = \eta \frac{B_0}{\delta \mu_0}. \quad (3.16)$$

This expression, along with Eq. (3.12), gives us  $v_0 = \eta/\delta \mu_0$  which, along with Eq. (3.11), leads to

$$v_0^2 = v_{out} \frac{\eta}{L \mu_0}, \quad (3.17)$$

linking the inflow speed with the outflow speed. In the equation of motion for the steady-state plasma, neglecting any variation in pressure,

$$\nabla \cdot (\rho \mathbf{u} \mathbf{u}) = \rho \mathbf{E} + \mathbf{J} \times \mathbf{B}, \quad (3.18)$$

the second term on the right-hand side, the Lorentz term, accelerates the particles in the stagnation region to the speed  $v_{out}$  over the distance  $L$ . Thus, taking the  $x$  component of Eq. (3.18) we get

$$\rho(\mathbf{u} \cdot \nabla) u_x = (\mathbf{J} \times \mathbf{B})_x, \quad (3.19)$$

and thus, under our geometric simplifications,

$$\frac{\rho v_{out}^2}{L} = J_y B_{out} = \frac{B_0}{\delta \mu_0} B_{out}. \quad (3.20)$$

Taking the conservation of magnetic flux across the surface  $A$ , as magnetic flux is convected in and out of the current sheet,

$$\oint \mathbf{B} \cdot d\mathbf{A} = -4\rho B_0 \delta + 4\rho B_{out} L = 0, \quad (3.21)$$

so that

$$B_0 \delta = B_{out} L. \quad (3.22)$$

By replacing Eq. (3.22) into Eq. (3.20), this leads us to

$$v_{out}^2 = \frac{B_0^2}{\rho \mu_0}, \quad (3.23)$$

which is the square of the Alfvén speed  $v_A = B_0 / \sqrt{\mu_0 \rho}$  associated with the reconnecting magnetic field. Thus, according to the SP, plasma particles leave the reconnection region at the Alfvén speed. As particles are frozen into the pre-reconnection magnetic field lines, they move with the convection speed  $v_0$  into current sheet. Since a steady-state is considered, the conduction electric field  $\mathbf{E}$  induced by this flow and magnetic field pattern generates a self-consistent  $\mathbf{E} \times \mathbf{B}$  drift

$$\mathbf{v}_d = \frac{\mathbf{E} \times \mathbf{B}}{|\mathbf{B}|^2}. \quad (3.24)$$

This drift bends the field lines, thus increases the magnetic tension, and is the responsible for the “dragging” of the magnetic field lines closer to the current sheet as long as the particles continue to be magnetised (outside of the diffusion region). Since outside the diffusion region the frozen-in condition is valid again, the reconnected field lines are then expelled out of the region along with the plasma particles.

When the velocity  $v$  is equal to the Alfvén speed, the magnetic Reynolds number

Eq. 3.9 is known as the Lundquist number

$$S = \frac{Lv_A\mu_0}{\eta}, \quad (3.25)$$

This number is fundamental to characterize the behaviour of reconnection in plasmas. For instance, by replacing  $v_{out}$  with  $v_A$  in Eq. (3.17), the initial incoming speed is  $v_0 = v_A/\sqrt{S}$ . Therefore, in Sweet–Parker model and for large  $S$ , the inflow velocity is smaller than the outflow velocity. The efficiency of reconnection as a mechanism to exchange energy between fields and particles is quantified by the reconnection rate

$$\Upsilon = \frac{v_0}{v_{out}}. \quad (3.26)$$

Replacing  $v_0$  and  $v_{out}$ , we find

$$\Upsilon_{SP} = \frac{1}{\sqrt{S}} = \frac{\delta_{SP}}{L_{SP}}, \quad (3.27)$$

where we find the last expression follows from the conservation of mass Eq. (3.11). Thus, in the Sweet–Parker model, the reconnection rate is limited by the Lundquist number. For most plasmas, the Lundquist number is much larger than one. For instance,  $S \sim 10^{12} - 10^{14}$  in the solar corona,  $S \sim 10^{15} - 10^{16}$  in the magnetotail, and  $S \sim 10^6 - 10^8$  in fusion plasmas (Loureiro and Uzdensky, 2015). Hence, the reconnection time predicted is big and thus SP reconnection is slow. However, observations in the solar corona show that reconnection is rather a fast and bursty process with a typical reconnection rate  $\Upsilon \sim (0.01 - 0.1)$ . This slowness of the Sweet–Parker reconnection is the fundamental shortcoming of this model. Nonetheless, it is worth quantifying the energy exchange by reconnection based on the divergence of the electromagnetic energy flux

$$\Phi_{EM} = \nabla \cdot \left( \frac{\mathbf{E} \times \mathbf{B}}{\mu_0} \right), \quad (3.28)$$

and the divergence of the kinetic energy flux

$$\Phi_K = \nabla \cdot \left( \frac{1}{2} \rho u^2 \mathbf{u} \right). \quad (3.29)$$

Considering the ratio of the inflowing kinetic energy flux to the inflowing electromagnetic energy flux

$$\frac{\Phi_{K0}}{\Phi_{EM0}} = \frac{\nabla \cdot \left( \frac{1}{2} \rho v_0^2 \mathbf{v}_0 \right)}{\nabla \cdot \left( \frac{\mathbf{E} \times \mathbf{B}_0}{\mu_0} \right)} = \frac{\frac{\rho v_0^3}{2\delta}}{\frac{E_y B_0}{\delta \mu_0}} = \frac{\frac{\rho v_0^3}{2}}{\frac{v_0 B_0^2}{\mu_0}} = \frac{v_0^2}{v_A^2} = \frac{1}{S}, \quad (3.30)$$

where we consider the variation over the distance  $\delta$ . Thus, for  $S \gg 1$ , the inflowing kinetic energy flux is negligible, and most of the incoming energy is of electromagnetic character.

Considering the ratio of the outflowing kinetic energy flux to the outflowing electromagnetic energy flux

$$\frac{\Phi_{Kout}}{\Phi_{EMout}} = \frac{\nabla \cdot \left( \frac{1}{2} \rho v_{out}^2 \mathbf{v}_{out} \right)}{\nabla \cdot \left( \frac{\mathbf{E} \times \mathbf{B}_{out}}{\mu_0} \right)} = \frac{\frac{\rho v_{out}^3}{2L}}{\frac{E_y B_{out}}{L \mu_0}} = \frac{\frac{\rho v_{out}^3}{2}}{\frac{v_0 B_0 B_{out}}{\mu_0}} = \frac{\frac{\rho v_A^3}{2}}{\frac{v_A B_0^2}{S \mu_0}} = \frac{S v_A^3}{2 v_A^3} = \frac{S}{2}, \quad (3.31)$$

where we consider the variation over the distance  $L$ . Therefore, the outflowing magnetic energy flux is negligible. This is related to the fact that  $B_{out} = B_0 \sqrt{S}$  which shows that the reconnected ( $B_{out}$ ) magnetic field is smaller than the reconnecting ( $B_0$ ) magnetic field.

We lastly consider the ratio of the outflowing kinetic energy flux to the inflowing magnetic energy flux

$$\frac{\Phi_{Kout}}{\Phi_{EM0}} = \frac{\nabla \cdot \left( \frac{1}{2} \rho v_{out}^2 \mathbf{v}_{out} \right)}{\nabla \cdot \left( \frac{\mathbf{E} \times \mathbf{B}_0}{\mu_0} \right)} = \frac{\frac{\rho v_{out}^3}{2L}}{\frac{E_y B_0}{\delta \mu_0}} = \frac{\frac{\rho v_A^3}{2L}}{\frac{v_0 B_0^2}{\mu_0 \delta}} = \frac{\sqrt{S} v_A^3 \delta}{2 v_A^3 L} = \frac{\sqrt{S} \delta}{2L} = \frac{1}{2}. \quad (3.32)$$

Therefore, half of the magnetic energy is converted through reconnection into kinetic energy of the outflowing particles. According to the Sweet–Parker model (SP), magnetic reconnection is a process that exchanges energy between the fields and the particles. Although the Sweet–Parker model is a good pedagogical approximation for

reconnection, this model does not address the actual mechanism that breaks down the frozen-in condition. It is based on the existence of an electrical resistivity that is usually associated with collisions. Hence, its extension to collisionless plasmas is not straight-forward because the collisions are too scarce to account for any kind of resistivity. Moreover, even in the resistive case, the predicted reconnection rate is too slow compared with observation (Kliem et al., 2000; Vaivads et al., 2004; Egedal et al., 2007; Yamada et al., 2010). Although anomalous resistivity mechanisms have been proposed to increase the reconnection rate (Ugai, 1984; Che, 2017), the Sweet–Parker model is laminar and it cannot explain the formation of plasmoids (Biskamp, 1986; Loureiro and Uzdensky, 2015) or the bursty nature of the magnetic reconnection that involves a period of energy accumulation (Scholer, 1988; Shay et al., 2003; Birn et al., 2011).

To overcome the slow reconnection problem, the reconnection community have focused their efforts on finding mechanisms able to make  $\delta$  comparable with  $L$ . For instance, Petschek (1964) proposes a model which considers localized regions of resistivity and the presence of standing slow shocks near the diffusion region. In this model, instead of an elongated current sheet, the reconnection region is an X-like structure due to the presence of slow shocks, and a central point where the magnetic field is zero. However, the existence of a mechanism for the self-consistent formation of slow shocks is not clear (Yamada et al., 2010). Nevertheless, artificial variation of the resistivity as a function of the current density produces slow shock formation (Ugai and Tsuda, 1977; Sato and Hayashi, 1979). Although the reconnection rate predicted by the Petschek model is faster than SP, the lack of self-consistency precludes the widespread use of this model.

### 3.2.1 Hall MHD Reconnection

Another attempt to find a better description for 2D reconnection is the *Hall MHD reconnection theory* which is based on the effects related to the electron physics within the diffusion region of the Sweet–Parker model. Following the previous subsection, within the reconnection region, the current is initially carried by both ions and electrons. However, at scales smaller than the ion inertial length, the assumption

of a single neutral fluid is no longer valid. The electron motion is dominant in the rest-frame of the reconnection region, and electrons make the largest contribution to  $\mathbf{J}$ . Thus, ions decouple from the electrons due to the Hall term ( $\sim \mathbf{J} \times \mathbf{B}$ ) in the generalised Ohm's law Eq. (2.37). To see this, we substitute the generalised Ohm's law Eq. (2.37) into Faraday's law Eq. (3.3) to obtain the more general induction equation:

$$\frac{\partial \mathbf{B}}{\partial t} = \nabla \times \left( \mathbf{u} \times \mathbf{B} - \eta \mathbf{J} - \frac{1}{nq} \mathbf{J} \times \mathbf{B} + \frac{1}{nq} \nabla \cdot \bar{\mathbf{P}}_e - \frac{m_e}{nq^2} \frac{\partial \mathbf{J}}{\partial t} \right). \quad (3.33)$$

Considering only the convective and Hall terms,

$$\frac{\partial \mathbf{B}}{\partial t} = \nabla \times \left( \mathbf{u} \times \mathbf{B} - \frac{1}{nq} \mathbf{J} \times \mathbf{B} \right). \quad (3.34)$$

Expressing the electron velocity from Eq. (2.31) as

$$\mathbf{v}_e = \mathbf{v}_i - \mathbf{J}/nq \quad (3.35)$$

and substituting it into Eq. (3.34), we obtain

$$\frac{\partial \mathbf{B}}{\partial t} = \nabla \times \mathbf{v}_e \times \mathbf{B}, \quad (3.36)$$

where  $\mathbf{u} \approx \mathbf{v}_i$  for  $m_e \ll m_i$  according to Eq. (2.34). From Eq. (3.36), it is clear that the effect of the Hall term is the demagnetization of the ions. At these scales, the magnetic field is convected with the electron motion. Moreover, the drift velocity Eq. (3.24), which now only affects electrons, carries them closer to the central region. As the electrons are still magnetised at these scales, they “drag” the magnetic field lines towards the electron diffusion region. Therefore, the diffusion region is divided into an external ion diffusion region and a smaller electron diffusion region inside it (see Figure 3.3). To continue with the discussion, we adopt the definitions of “poloidal field” (in the reconnection plane) and “toroidal field” (out of the reconnection plane) used by [Uzdensky and Kulsrud \(2006\)](#). The incoming magnetic field lines lie in the reconnection plane and their magnetic field is poloidal. The same applies to the

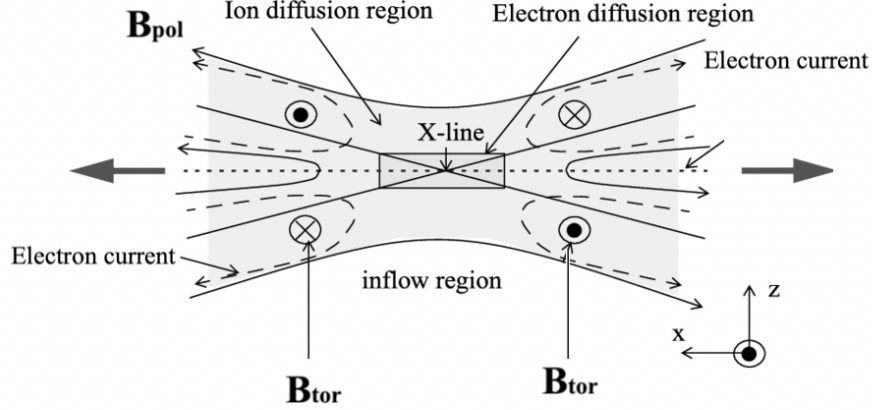


**Figure 3.3:** 2D Hall MHD reconnection model. Unlike in SP, the diffusion region is divided between ion and electron diffusion regions. Poloidal (in plane) electron currents form and generate a characteristic quadrupole-like toroidal (out of the plane) magnetic field. Adapted from [Sonnerup \(1979\)](#).

reconnected magnetic field lines. According to our frame of reference,  $x - z$  is the poloidal plane and  $y$  is the toroidal direction.

We consider the field lines entering (upstream) the ion-diffusion region in a quasi-steady state. As the field lines enter and approach the central part of the current sheet, a portion of the magnetic field of the top is cancelled with the opposite magnetic field of the bottom. Because the magnetic field is reduced, the distance between the field lines increases to keep the magnetic flux constant. As the field expands, the electron gas expands changing its density. Because ions are not affected by this expansion, as they are demagnetised, electrons inflows are required to maintain quasi-neutrality. These electrons flow parallel to the upstream poloidal magnetic field. Likewise, when the reconnected (downstream) fields expand out of the diffusion region, their associated volume is reduced. Thus, electron outflows leave the central region. These electron flows represent currents in the opposite directions. These currents generate a toroidal magnetic field ( $\mathbf{B}_{tor}$ ). In the top-right and bottom-left part of the reconnection region, the toroidal magnetic field points into the plane. In the top-left and bottom-right, the toroidal magnetic field points out of the plane.

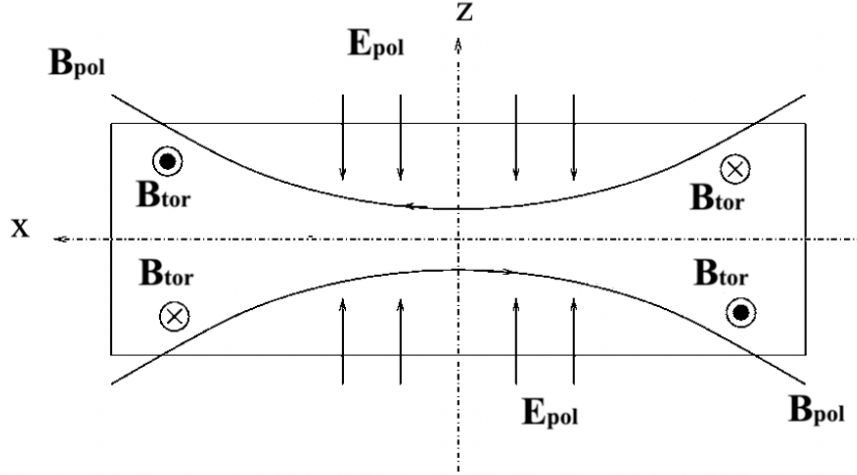


**Figure 3.4:** The charge separation in the ion-diffusion region generates a poloidal electric field  $\mathbf{E}_{pol}$ . Adapted from [Uzdensky and Kulsrud \(2006\)](#).

Another effect of the separation of charges within the reconnection region is the existence of a poloidal electric field ( $\mathbf{E}_{pol}$ ), see Figure 3.4. This electric field is responsible for the acceleration of ions in the ion-diffusion region. Because of the toroidal magnetic field, the entering ions are deflected towards the downstream region where they leave the diffusion region. Outside the electron diffusion region, ions are accelerated out of the reconnection region as in SP. The electron diffusion region length  $L_e$  and width  $\delta_e$  are expected to be of order the electron scales  $\sim d_e$ ; however, observations suggest that the length of the electron diffusion region can reach ion scales ([Deng and Matsumoto, 2001](#); [Wei et al., 2007](#); [Stawarz et al., 2019](#)).

An additional effect of the ion demagnetization is the existence of a toroidal component of the electron velocity within the ion diffusion region. Some authors ([Mandt et al., 1994](#)) argue that these electrons are responsible for dragging the magnetic field out of the reconnection plane, creating the toroidal component of the magnetic field. However, [Uzdensky and Kulsrud \(2006\)](#) state that, in order to have a change in the toroidal field along the electron streamlines, the toroidal velocity of the electrons must be non-uniform. This only happens in a transition region in which the velocity of the ions is not exactly zero. Outside the electron diffusion region, any contribution from electrons to the toroidal field is cancelled by the toroidal contribution of the ions. Deep inside the diffusion region, where the velocity of ions is negligible,



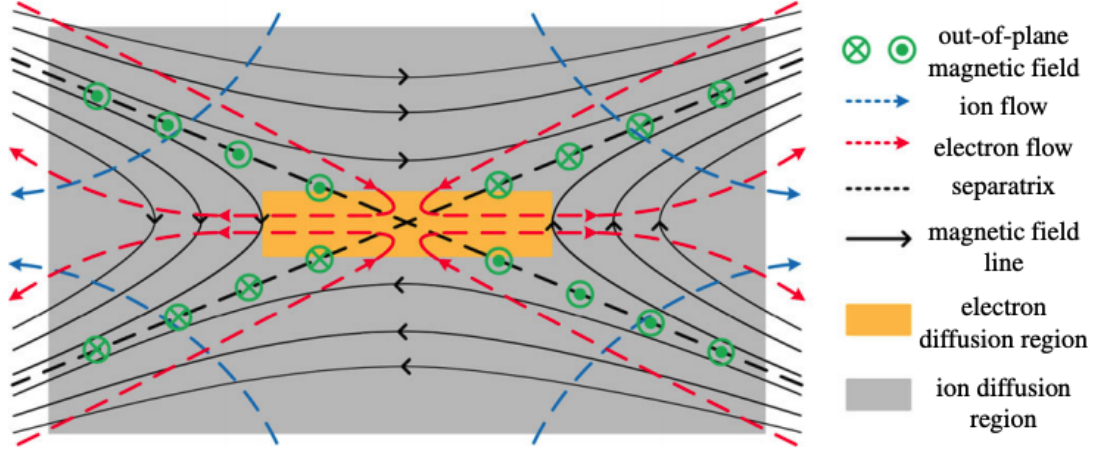


**Figure 3.5:** Reconnection diffusion region. The dashed black lines define the reconnection separatrix. Within the ion diffusion region (gray area) ions are demagnetised and the ion flows (blue dashed lines) accelerate away of the reconnection ion-diffusion region. As magnetic field lines (continuous black lines) are convected to the central region, poloidal electron flows (red dashed lines) form to maintain quasi-neutrality. These flows generates the characteristic toroidal quadrupole-like magnetic field (green crosses and dots). Within the electron diffusion region (yellow area) electrons are demagnetised and accelerated out of the reconnection region. Adapted from [Zweibel and Yamada \(2016\)](#).

the total toroidal component of the electron velocity depends on  $\mathbf{E}_{pol}$  and a drift associated with the gradient of the electron pressure term  $\sim \nabla \cdot \bar{\mathbf{P}}_e$  in Eq. (3.33). This balance maintains uniformity in the toroidal electron velocity. Therefore, the toroidal magnetic fields are generated in this transition region and convected towards the centre by the poloidal electron flow. In addition, as the pressure term does not affect the convection of magnetic field lines, the bend of the field lines out of the reconnection plane in the toroidal direction is due to  $\mathbf{E}_{pol}$ . This shows that, although electrons play a principal role at these scales, the ion contribution must be considered.

Figure 3.5 shows the expected trajectories of particles in the poloidal plane within the reconnection diffusion region according to Hall MHD theory. The dashed black lines define the reconnection separatrix associated with this reconnection model. Within the ion diffusion region (gray area) ions are demagnetised, and the ion flows (blue dashed lines) accelerate away from the reconnection region. As magnetic field lines (continuous black lines) proceed to the central region, poloidal electron flows

(red dashed lines) form to maintain quasi-neutrality. These flows generate the characteristic toroidal, quadrupole-like magnetic field (green crosses and dots). Within the electron diffusion region (yellow area), electrons are demagnetised and accelerated out of the reconnection region. It is worth noting that the quadrupole magnetic field pattern and the poloidal electric fields are independent of the initial direction of the poloidal fields. Although the presence of a quadrupole toroidal field and a poloidal electric field have been supported by two fluid simulations (Mandt et al., 1994; Shay and Drake, 1998; Shay et al., 2001; Le et al., 2014) and observations in the magnetosphere (Mozer et al., 2002; Wygant et al., 2005; Borg et al., 2005), this structure is considerably distorted in the presence of a guide magnetic field (toroidal) or asymmetries in the reconnection region. For instance, when an intense guide magnetic field is present, poloidal electron flows are distorted along the upstream direction (Eastwood et al., 2010). Moreover, shear flows in the reconnection region, asymmetric reconnecting magnetic field and asymmetric density can preclude reconnection by shifting the stagnation point out of the diffusion region (Eastwood et al., 2013).

An important point to highlight from this model is the fact that, at small scales, non-ideal terms such as the gradient of the electron pressure or the electron inertia term ( $\sim \partial \mathbf{J} / \partial t$ ) must be considered where relevant. From Eq. (3.33), even when there is no resistivity term  $\eta \mathbf{J}$ , the additional terms can account for the breaking down of the frozen-in condition. For instance, in collisionless plasmas, the breaking down of the frozen-in condition may be due to the anisotropic electron pressure or the electron inertia terms in Eq. (2.37) (Shay et al., 2001). Therefore, the reconnection diffusion region and the mechanisms that break down the frozen-in condition are governed by sub-proton scale processes. In fact, in Hall MHD reconnection, the reconnection rate is fast and independent of the resistivity.

### 3.2.2 Tearing Reconnection

One important theory of 2D reconnection, which includes turbulence effects and explains a reconnection rate higher than in Sweet–Parker, is the *plasmoid-dominated reconnection model*. In this model, the presence of fluctuations in the initial Sweet–

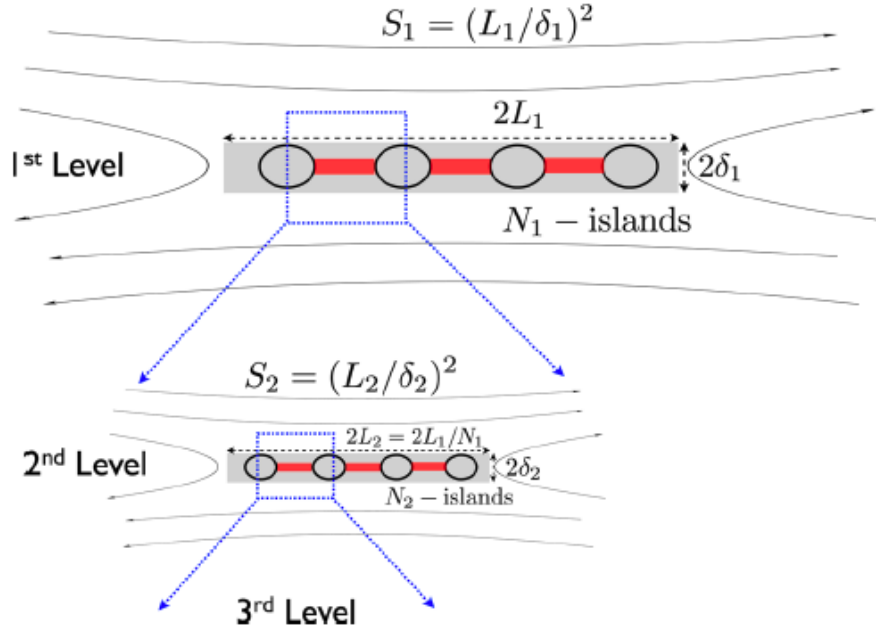


**Figure 3.6:** Plasmoid chain formation. For large plasma size and high Lundquist number  $S$ , the current sheet is unstable to tearing instability. Magnetic islands are formed while the current sheet is disrupted. Adapted from [Ji and Daughton \(2011\)](#).

Parker current sheet induces the production of magnetic islands. As the current sheet is a thin structure, for critical values of non dimensional plasma parameters ([Drake and Lee, 1977](#); [Hosseinpour et al., 2009](#)), the current sheet is highly unstable to the second tearing instability, also known as the plasmoid instability ([Biskamp, 1986](#)). This instability modulates the current sheet and creates magnetic islands (O-points) along with X-like regions between the O-points. As the system evolves, the nonlinear interaction between islands breaks the current sheets even more as long as their size makes them unstable to the plasmoid instability ([Ji and Daughton, 2011](#)), see Figure 3.6. Therefore, during this process, a chain of magnetic islands forms along the current sheet. The x-points between subsequent magnetic islands are potential reconnection sites. Thus the reconnection rate increases ([Samtaney et al., 2009](#); [Loureiro et al., 2009](#)). In this model, the assumption of a steady state is no longer valid, and the process can be bursty as the small-scale interactions become dominant for thin current sheets  $\delta \sim d_i$ .

A natural question regarding this mechanism is whether the plasmoid instability

and the generation of multiple x-like regions can take place at all scales in both the collisional and the collisionless limit. As the Lundquist number is related to the size and aspect ratio of the current sheet, a way to characterise the onset of the plasmoid instability is to use the effective plasma size for the reconnection  $\lambda = L/d_i$ . Figure 3.7 shows a phase diagram relating the critical value of the Lundquist number to the plasma size. In this diagram, there are five sectors. In the sector called *Single x-line collisionless*, if the current sheet length is of order a few  $d_i$ , the current sheet is not unstable to the plasmoid instability and the expected reconnection process is like in Hall MHD. For a current sheet length greater than the critical plasma size  $\lambda_c$ , the current sheet becomes unstable to tearing and a chain of magnetic islands is expected. In the sector called *Single x-line collisional*, the current sheet length is large and the expected reconnection process is the usual Sweet–Parker type. For systems with Lundquist number above the critical value  $S_c$  (the green line), the current sheets become unstable to tearing instability. Finally, in the region defined between  $S = \lambda^2/4$  and  $S = \lambda\sqrt{S_c}/2$ , any collisional reconnection transitions to collisionless reconnection. The diagram also shows ranges in which laboratory plasmas and simulations can proceed (orange square) and the positions of different plasmas in the universe in this phase diagram. The diagram also shows the wide variety of plasmas and broad range of scales where reconnection can take place.

At the end of this section, we highlight the tireless effort that has been done by the reconnection community to understand the 2D process. It is still a matter of ongoing research how effects such as electron inertia or electron pressure are changed by turbulence. Likewise, the effects of a guide field and of asymmetries in the reconnection geometry are important open questions. Although 2D models of magnetic reconnection approximately explain reconnection rates and flow patterns as observed at the Sun, there are 3D structures whose behaviour is very difficult to explain with 2D models. For example, the rising of coronal loops is intimately related with reconnection. Coronal loops reconnect and create solar flares and CMEs. From a 2D model it is not clear how magnetic flux ropes can undergo self-reconnection. This process is associated with open magnetic flux ropes at CMEs ([Gosling et al.](#),

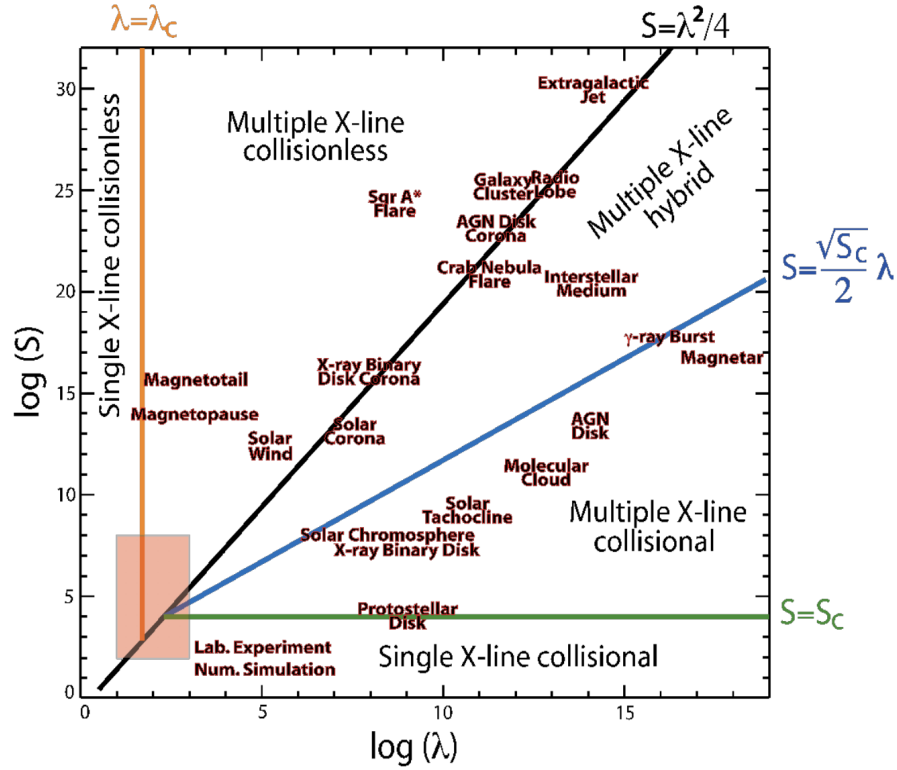


**Figure 3.7:** 2D magnetic reconnection phase diagram as a function of the Lundquist number and the plasma size. The orange vertical line marks the critical plasma size  $\lambda_c$ . The horizontal green line marks the critical Lundquist number  $S_c$ . The diagonal black line marks the transition from multiple X-line collisionless reconnection to the hybrid phase. The blue diagonal line marks the transition from multiple X-line collisional reconnection to the hybrid phase. In the hybrid phase, collisional and collisionless reconnection can proceed with single and multiple X-lines. The orange square shows the range of plasma size and Lundquist number that can be studied by laboratory experiments and numerical simulations. Adapted from [Ji et al. \(2019\)](#).

1995). Moreover, reconnection is a 3D process in nature and there are turbulence effects that only appear in a 3D geometry ([Lazarian and Vishniac, 1999](#); [Kowal et al., 2009, 2017](#); [Lazarian et al., 2020](#)).

### 3.3 3D Magnetic Reconnection

From the previous section, it is clear that, in general and even in the 2D picture, toroidal fields and currents as well as guide fields are present with a third vector component, out of the reconnection plane. Thus there is a need to study reconnection in a 3D geometry. The study of 3D magnetic reconnection, as in 2D, has been divided into a steady, non-turbulent approach which focuses on the study mag-

netic field topology change through the diffusion region (Hesse and Schindler, 1988; Schindler et al., 1988; Priest and Démoulin, 1995; Priest et al., 2003; Pontin, 2011) and a turbulent approach in which the effect of a turbulent field on top of the background magnetic field and in the reconnection current sheet (Lazarian and Vishniac, 1999; Lazarian, 2006; Lazarian et al., 2020). Important mechanisms such as the 3D plasmoid instability are considerably different from the 2D approach. For example, the equivalent to magnetic islands are twisted flux tubes also known as flux ropes in 3D (Daughton et al., 2011). The non-linear interaction of flux ropes is considerably different from the non-linear interaction of magnetic islands. In addition, the extension of the reconnection phase diagram to 3D reconnection is still a topic of active research which requires the use of Peta-scale simulations to test and constrain the models of 3D reconnection.

### 3.3.1 Laminar 3D Reconnection

Null points are regions in which oppositely directed field lines converge, either into the region or out of the region, forming a dense structure, the so-called “spine”, see Figure 3.8 left. The spine spreads in or out of the region, forming a fan-like structure. When these structures are perturbed, they collapse and form current sheets. Magnetic reconnection models in 2D require the presence of region in which  $B = 0$ . Conversely, in 3D steady state reconnection, there is no need of regions with  $B = 0$  inside the diffusion region for reconnection to happen (Priest et al., 2003; Pontin, 2011). For regions without null points, fan surfaces can intersect, generating a separator line, see Figure 3.8 right, which also forms current sheets.

The formation of a current sheet alone is not a sufficient condition for reconnection. In a topological sense, reconnection represents a change in the magnetic field line mapping when crossing diffusion region. Additionally, the magnetic flux through the diffusion region is conserved. Before reconnection, plasma elements are frozen into a particular field line, and after reconnection, the plasma elements are connected to another field line. For the 3D case, Schindler et al. (1988) show that this happens whenever a component of the electric field parallel to the magnetic field,  $E_{\parallel}$ , is non-zero within the diffusion region. In other words, a sufficient condition for magnetic

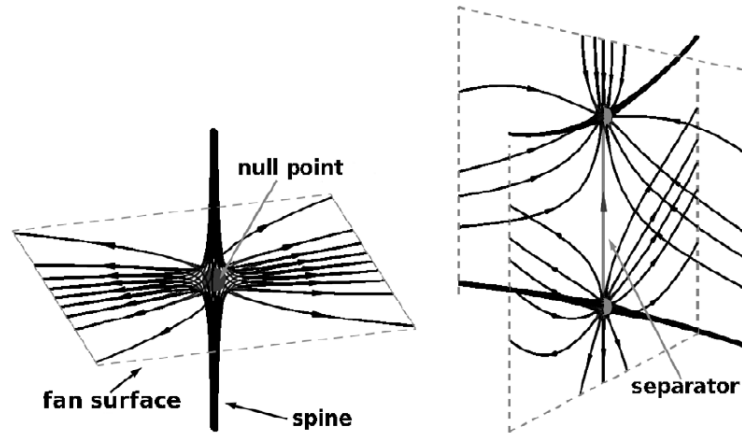


**Figure 3.8:** Left: In the neighbourhood of a null point, hyperbolic magnetic field lines converge to the spine line and spread out, forming a fan-like structure. The spine-fan configuration can collapse and form current sheets. Right: In the absence of magnetic null points, the intersection of spine-fan structures define the so-called separator. Separators can collapse as well. Adapted from [Pontin \(2011\)](#).

reconnection in regions in which the magnetic field is non-zero, is

$$\int_{fl} E_{\parallel} ds \neq 0, \quad (3.37)$$

where  $fl$  refers to the trajectory along the magnetic field line, and  $ds$  is a line element of this trajectory. Thus, unlike in 2D reconnection where  $E_{\parallel}$  in the null region must be zero, in 3D reconnection,  $E_{\parallel} \neq 0$  is a necessary condition for the onset of reconnection. Another fundamental difference between 2D and 3D reconnection is that magnetic reconnection no longer presents a unique mapping between a pair of field lines. In contrast, the plasma elements bond to one magnetic field line connect to different field lines during reconnection ([Priest et al., 2003](#)). On the contrary, the connectivity of plasma elements to reconnected field lines is more complicated. A review of this geometrical approach to magnetic reconnection in 3D is given by [Pontin \(2011\)](#).

In 3D reconnection the interconnection of braided magnetic flux ropes which reconnect multiple times until the system reaches a stationary state ([Parnell et al., 2010](#)). [Haynes and Parnell \(2010\)](#) apply these concepts to solar flux emergence and

magnetospheric MHD models. However, the direct application of these geometrical approaches to turbulent systems in which the magnetic field lines are not tied to a surface or without null-point formation is not clear (Daughton et al., 2014). Since the quantification of the reconnection rate in simulations requires the identification of reconnection events at each time step, the formation of current sheets as places where reconnection *may* happen has been widely used. However, there is evidence for reconnection sites located at places without null points, as well as places shifted to a different location away from the current sheets (Zhdankin et al., 2013). Moreover, the existence of a current sheet is not a guarantee for reconnection in 3D; the parallel component of the electric field is a more reliable parameter to identify reconnection. Moreover, the formation of coherent acceleration of particles (ions and electrons) in and out of the diffusion region must be consistent with reconnection flow patterns. Although the reconnection rate changes in time as the system is driven away from the stationary case (Owen and Cowley, 1987), a reconnection theory is successful if it accounts for a fast reconnection rate, in agreement with, for example, the rate estimated for solar flares (Narukage and Shibata, 2006). In addition, it must describe the exchange of energy between particles and fields as well as the presence of kinetic instabilities which can produce conditions for local resistivity even in collisionless plasmas (Chen et al., 1997; Del Sarto et al., 2003; Divin et al., 2012; Moser and Bellan, 2012).

### 3.4 Observations of Reconnection in the Solar Wind

Although magnetic reconnection was first presented as a process mostly occurring in the low solar atmosphere, there has been considerable evidence of in-situ observations of reconnection in the solar wind across interplanetary space. Ulysses measurements show encounters with magnetic flux ropes and coincident electron heating at the heliospheric current sheet (HCS) which suggests reconnection (Moldwin et al., 1995). Helios and Wind measurements show regions with characteristic Alfvénic outflows, named “exhaust regions” bounded by back-to-back rotational dis-



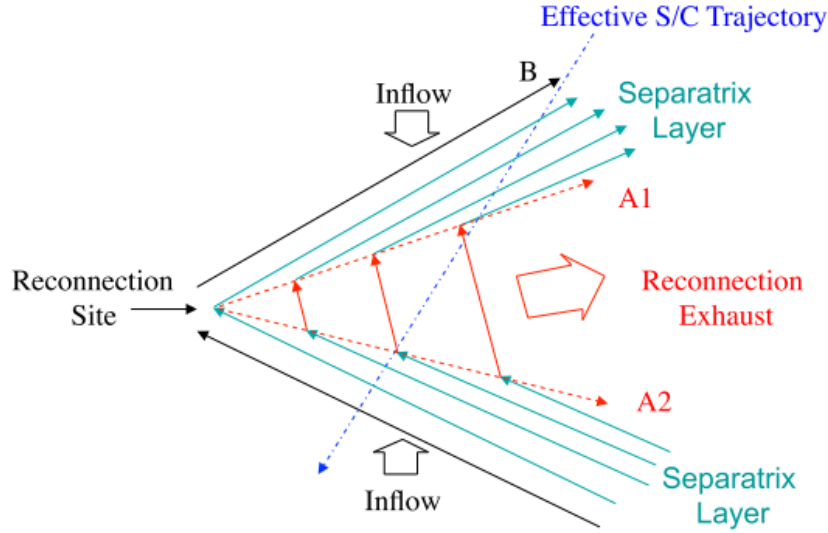


**Figure 3.9:** Idealised 2D projection of an exhaust region. The continuous black (red) lines and arrows represent the reconnecting (reconnected) magnetic field. The dashed red lines and arrows represent the rotational discontinuities associated with the reconnection region and the dash-dotted line illustrate a representative spacecraft trajectory. Adapted from [Gosling \(2012\)](#).

continuities, indicating reconnection events between 0.3 au to 5.4 au ([Gosling et al., 2006](#); [Gosling, 2007](#)). ISEE data show evidence of accelerated Alfvénic plasma flows across rotational discontinuities at Earth’s magnetopause ([Paschmann et al., 1979](#)). Data from Cluster and the Magnetospheric Multiscale (MMS) mission show numerous reconnection events in the Earth’s magnetosheath and magnetotail ([Runov et al., 2003](#); [Borg et al., 2005](#); [Burch and Phan, 2016](#)).

The main feature used to identify spacecraft encounters with reconnection exhausts is the existence of a rotation in the magnetic field (quantified by the shear angle). Figure 3.9 shows an idealized sketch of a reconnection site where two field lines with (at least) one opposite component reconnect (continuous black lines and arrows). The reconnected lines (continuous red lines and arrows) are convected away from the reconnection site driven by Alfvénic disturbances. The separatrix layers are current sheets, and  $A_1$  and  $A_2$  represent the pair of rotational discontinuities that bound the exhaust.

The events studied by [Gosling \(2012\)](#) show exhaust widths within the range  $10 - 400 d_i$ , crossing times of around  $3 - 100$  s, and shear angles in the range  $0 - 180^\circ$  for small  $\Delta\beta$  on the opposite sides, where  $\beta$  is the ratio between the thermal pressure and the magnetic pressure. The exhaust regions identified occur mostly in the slow wind and within ICMEs. They are rarely seen at leading edges of ICMEs or in the Alfvénic fast solar wind. Likewise, [Phan et al. \(2006, 2009\)](#), using multi-spacecraft analysis, identify reconnection X-line lengths in the range of  $1.02 \times 10^2 - 2.47 \times 10^4 d_i$  and estimate the crossing time in the range of 5.5 - 150 minutes. Although it is suggested by the Petscheck model that reconnection is associated with a slow shock, for which increases in proton density and temperature with a decrease in  $|\mathbf{B}|$  are the main signatures, most of the exhaust regions identified by [Gosling \(2012\)](#) do not exhibit these features.

## Chapter 4

# Turbulence in the Solar Wind

In this chapter, I review the concept of plasma turbulence in the context of the solar wind. I start by introducing turbulence and the energy cascade in fluids. I continue by describing the concept of plasma turbulence and the different models of the non-linear energy cascade and related observations in the solar wind. Afterwards, I comment on kinetic turbulence and finish with the effects of turbulence in magnetic reconnection.

### 4.1 Fluid Turbulence

Turbulence is the state of a fluid in which nonlinear interactions between fluid vortices or eddies occur. The equation of motion of a fluid of mass density  $\varrho = nm$  and velocity  $\mathbf{u}$  is the Navier-Stokes equation

$$\frac{\partial \mathbf{u}}{\partial t} + (\mathbf{u} \cdot \nabla) \mathbf{u} = -\frac{\nabla p}{\varrho} + \nu \nabla^2 \mathbf{u}, \quad (4.1)$$

where  $p$  is the scalar pressure of the fluid and  $\nu$  is the kinematic viscosity. The second term on the left-hand side,  $(\mathbf{u} \cdot \nabla) \mathbf{u}$ , is the nonlinear term which represents the interaction between eddies. Considering the characteristic scale of an eddy  $L$  and the characteristic velocity  $U$  at that scale, the nonlinear time  $\tau_{nl} \sim L/U$ . The second term on the right-hand side,  $\nu \nabla^2 \mathbf{u}$ , is the viscous term which represents the effect of viscosity on the fluid evolution. The characteristic time associated with this term is the viscous time  $\tau_\nu \sim L^2/\nu$ . If  $\nabla p \approx 0$  and  $\tau_{nl} \ll \tau_\nu$ , the nonlinear interaction

dominates and the eddies are distorted. Conversely, if  $\tau_{nl} \gg \tau_\nu$ , the viscous term dominates the fluid transport, and turbulence is suppressed. The ratio of  $\tau_\nu$  to  $\tau_{nl}$  is the Reynolds number

$$Re = \frac{LU}{\nu}. \quad (4.2)$$

This non-dimensional number is useful to characterise the fluid. For instance, for low Reynolds numbers  $Re \lesssim 10^{-2}$ , the fluid motion is laminar. In this case, there is no mixing between fluid layers and the fluid remains stable under small perturbations. If  $Re$  increases, the fluid motion becomes sensitive to small perturbations, i.e., the fluid becomes turbulent and chaotic, and mixing between fluid layers takes place (Bohr et al., 1998).

#### 4.1.1 Nonlinear Energy Cascade, K41

The shredding of eddies leads to the formation of smaller eddies and to the energy transport across scales, forming the so-called “energy cascade” (Kolmogorov, 1941; Frisch and Kolmogorov, 1995). The energy is usually injected into the system by large-scale fluctuations, defining the “outer scale” of the energy cascade at lengths  $L_I$ . In closed systems,  $L_I$  is comparable to the size of the system. Conversely, in the solar wind,  $L_I \sim 0.01$  au (Matthaeus et al., 2005; Wicks et al., 2013). The range of scales associated with  $L_I$  is the so-called injection range. As nonlinear interactions occur, the energy is transported without dissipation to smaller eddies with characteristic scales  $l$ . This dissipationless cascade process occurs mostly in the so-called inertial range (Kolmogorov, 1941). Finally, the eddies reach the characteristic lengths scales  $l_D$  at which the energy is dissipated via viscosity. This range of scales is the so-called dissipation or kinetic range.

We can assume that the energy injection rate  $\epsilon_L \sim U^2/\tau_I$  per unit mass is constant, where  $\tau_{L_I} \sim L_I/U$ . In the inertial range, the energy is transported locally, so the local energy rate  $\epsilon_l \sim \epsilon_L/\tau_c$  is fixed. Considering the increments of the fluctuating velocity  $\delta \mathbf{u}(l) = \mathbf{u}(\mathbf{r} + \mathbf{l}) - \mathbf{u}(\mathbf{r})$  with a given set of eddies over a distance  $l = |\mathbf{l}|$ , the kinetic energy of these eddies is  $\epsilon_l \sim \delta u^2$ . Approximating the cascade time as

$\tau_c \sim l/\delta u$ , the kinetic energy scales like  $\varepsilon_l \sim \epsilon_l^{2/3} l^{2/3}$ . Considering the wave number  $k \sim l^{-1}$  associated with the eddy of amplitude  $\delta u$ , the energy transport across scales in k-space is  $E(k) = \varepsilon_l/k$ , i.e., the energy per unit  $k$ , is

$$E(k) \sim \epsilon_l^{2/3} k^{-5/3}. \quad (4.3)$$

This is the so-called Kolmogorov spectrum (K41, [Kolmogorov, 1941](#)) with a spectral slope of  $-5/3$  in the inertial range.

## 4.2 Plasma Turbulence

In plasmas, as in neutral fluids, the nonlinear interactions play a decisive role. In the single-fluid MHD framework and considering the incompressible limit, the momentum equation Eq. (2.36) takes the form

$$\frac{\partial \mathbf{u}}{\partial t} + (\mathbf{u} \cdot \nabla) \mathbf{u} = -\frac{\nabla p}{\varrho} + \nu \nabla^2 \mathbf{u} + (\mathbf{b} \cdot \nabla) \mathbf{b}, \quad (4.4)$$

where the term  $\nu \nabla^2 \mathbf{u}$  is introduced to account for viscous effects and  $\mathbf{b} = \mathbf{B}/\sqrt{\mu_0 \varrho}$  is the magnetic field in Alfvén units. Likewise, the induction equation from Eq. (3.8) can be expressed as

$$\frac{\partial \mathbf{b}}{\partial t} + (\mathbf{u} \cdot \nabla) \mathbf{b} = \eta \nabla^2 \mathbf{b} + (\mathbf{b} \cdot \nabla) \mathbf{u}. \quad (4.5)$$

Eqs. (4.4) and (4.5) are coupled. The four nonlinear terms in Eqs. (4.4) and (4.5) show that the magnetic and velocity fields not only interact with themselves but with each other. The magnetic Reynolds number  $Re_m$  from Eq. (3.9) along with the Reynolds number  $Re$  from Eq. (4.2) characterise the strength of these nonlinear terms.

### 4.2.1 Elsässer Variables

Given the presence of a background magnetic field  $\mathbf{b}_0 = \mathbf{B}_0/\sqrt{\mu_0 \varrho}$ , perturbations in the magnetic field,  $\mathbf{b}' = \mathbf{b} - \mathbf{b}_0$ , travel parallel to  $\mathbf{b}_0$  at the Alfvén speed  $v_A = |\mathbf{b}_0|$ . Considering two wave packages travelling parallel and anti-parallel to  $\mathbf{b}_0$  and using the so-called Elsässer variables  $\mathbf{z}^\pm = \mathbf{u} \pm \mathbf{b}'$  ([Elsässer, 1950](#)), Eqs. (4.4) and (4.5)

can be expressed in a more symmetric form as

$$\frac{\partial \mathbf{z}^\pm}{\partial t} \mp (\mathbf{b}_0 \cdot \nabla) \mathbf{z}^\pm + (\mathbf{z}^\mp \cdot \nabla) \mathbf{z}^\pm = -\frac{\nabla p}{\varrho} + \nu^+ \nabla^2 \mathbf{z}^\pm + \nu^- \nabla^2 \mathbf{z}^\mp, \quad (4.6)$$

where  $\nu^\pm = (\nu \pm \eta)/2$  are the dissipative coefficients (Bruno and Carbone, 2013). Eq. (4.6) describes the evolution of counter-propagating wave packets in an MHD plasma. The solenoidality of the velocity and magnetic fields in the incompressible limit ( $\nabla \cdot \mathbf{u} = 0, \varrho = \text{const}$ ) is presented as  $\nabla \cdot \mathbf{z}^\pm = 0$ . The non-linear term  $(\mathbf{z}^\mp \cdot \nabla) \mathbf{z}^\pm$  shows that if either the parallel ( $z^+$ ) or the anti-parallel ( $z^-$ ) perturbation is zero or aligned with the spatial variation of the opposite perturbation, the non-linear interaction vanishes.

If two counter-propagating Alfvén-wave packets collide, their interaction produces secular non-propagating wave modes with higher  $k_\perp$  while  $k_\parallel$  remains unchanged (Howes et al., 2008b). As the interaction between the different modes proceeds, the anisotropy  $k_\perp > k_\parallel$  increases. This highlights the importance of Alfvén waves as the building blocks of turbulence (Howes et al., 2012; Howes and Nielson, 2013a; Nielson et al., 2013).

In this framework, there are two important interaction times at the scale  $l$ , *i*) the Alfvén time  $\tau_A \sim 1/k_\parallel v_A$  associated with  $(\mathbf{b}_0 \cdot \nabla) \mathbf{z}_l^\pm$  and *ii*) the non-linear time  $\tau_{nl} \sim 1/\delta u_l k_\perp$  associated with  $(\mathbf{z}_l^\mp \cdot \nabla) \mathbf{z}_l^\pm$ , where  $\delta u \sim \delta z^\pm$ . Thus,  $\tau_A$  is the time in which an Alfvénic perturbation travels along  $\mathbf{b}_0$  a distance  $l_\parallel$ , whereas  $\tau_{nl}$  is the time in which the oppositely travelling perturbations interact with each other. Since  $\mathbf{z}^\mp$  and  $\nabla \mathbf{z}^\pm$  lie in the perpendicular plane to  $\mathbf{b}_0$ , the non-linear interaction occurs in the perpendicular plane and the scale of the non-linear interaction is  $l_\perp \sim k_\perp^{-1}$ .

### 4.2.2 Nonlinear Energy Cascade, IK

The first important extension of the non-linear energy cascade in the inertial range to plasma turbulence (Iroshnikov, 1963; Kraichnan, 1965), considered weak non-linear interactions such that  $\tau_{nl} > \tau_A$  and a cascade time of  $\tau_c \sim \tau_{nl}^2/v_A$ . The authors assumed as well an isotropic cascade with  $k_\parallel \sim k_\perp \sim k$ . Thus,  $\epsilon_l = \varepsilon_l/\tau_c$  leads to  $\delta u \sim (\epsilon_l v_A)^{1/4} k_\perp^{-1/4}$  and to the energy transport across the scales in k-space of the

form

$$E(k) \sim (\epsilon_l)^{1/2} k^{-3/2}. \quad (4.7)$$

This is the so-called Iroshnikov–Kraichnan spectrum (IK, [Iroshnikov, 1963](#); [Kraichnan, 1965](#)) with a spectral slope of  $-3/2$ . However, observational evidence ([Horbury et al., 2008](#); [Wicks et al., 2010, 2011](#); [Chen et al., 2011](#)) shows that the energy cascade in the solar wind is indeed highly anisotropic ( $k_{\parallel} \not\sim k_{\perp}$ ), especially at the small-scale end of the inertial range. Unlike in neutral fluid turbulence, the sensitivity of plasma to magnetic field imposes this anisotropy with respect to the local mean magnetic field ([Cho and Vishniac, 2000](#)) in the turbulent evolution of a plasma.

### 4.2.3 Nonlinear Energy Cascade, GS95

In 1994, [Sridhar and Goldreich \(1994\)](#) postulated that the accumulation of weak non-linear interactions will eventually become strong. This leads to the so-called critical balance (CB) condition that  $\tau_{nl} \sim \tau_A$  ([Goldreich and Sridhar, 1995](#)) henceforth GS95. Thus, the non-linear time is comparable to the linear time. If  $\tau_{nl} \gg \tau_A$ , where the non-linear interaction is weak, the non-linear interaction will pile up so  $\tau_{nl} \sim \tau_A$  ([Ng and Bhattacharjee, 1997](#); [Perez and Boldyrev, 2007](#); [Boldyrev and Perez, 2009](#); [Meyrand et al., 2016](#)). Conversely, if  $\tau_{nl} \ll \tau_A$ , the non-linear interactions shred eddies, and the perturbations cease to propagate, which terminates the non-linear interactions and stops the energy cascade ([Boldyrev, 2005](#); [Nazarenko and Schekochihin, 2011](#); [Howes, 2015a](#)).

In the inertial range, the characteristic cascade time in the perpendicular direction is  $\tau_c \sim \tau_{nl}$ . Considering an anisotropy with  $k_{\perp} \not\sim k_{\parallel}$ ,  $\epsilon_{l\perp} = \epsilon_{l\perp}/\tau_c$  leads to  $\delta u \sim (\epsilon_{l\perp})^{1/3} k_{\perp}^{-1/3}$  and to the perpendicular energy transport across the scales  $E(k_{\perp}) = \epsilon_{l\perp}/k_{\perp}$  of the form

$$E(k_{\perp}) \sim (\epsilon_{l\perp})^{2/3} k_{\perp}^{-5/3}, \quad (4.8)$$

which is the same scaling as in K41, but with  $k_{\perp}$  instead of  $k$ . Likewise, considering the characteristic cascade time in the parallel direction  $\tau_c \sim \tau_A$ ,  $\epsilon_{l\parallel} = \epsilon_{l\parallel}/\tau_c$  leads

to  $\delta u \sim (\epsilon_{l_{\parallel}}/v_A)^{1/2}(k_{\parallel})^{-1/2}$  and to the parallel energy transport across the scales  $E(k_{\parallel}) = \epsilon_{l_{\parallel}}/k_{\parallel}$  of the form

$$E(k_{\parallel}) \sim \frac{\epsilon_{l_{\parallel}}}{v_A} k_{\parallel}^{-2}. \quad (4.9)$$

Eqs. (4.8) and (4.9) constitute the scaling laws of the so-called Goldreich–Sridhar spectrum (GS95, [Goldreich and Sridhar, 1995](#)). Additionally, since  $\epsilon_{l_{\perp}} \sim \epsilon_{l_{\parallel}} \sim \epsilon_l$ , the relation between the parallel and perpendicular scales is

$$k_{\parallel} \sim \frac{\epsilon_l^{1/3}}{v_A} k_{\perp}^{2/3}. \quad (4.10)$$

Thus, in GS95, the energy cascade is anisotropic. The spectral slope for the perpendicular fluctuations is  $-5/3$  and the slope for the parallel fluctuations is  $-2$ .

#### 4.2.4 Nonlinear Energy Cascade and Dynamic Alignment

In 2006, [Boldyrev \(2006\)](#) proposed an additional condition for the nonlinear time based on  $\theta_{\lambda}$ , the angle of alignment between  $\delta \mathbf{u}$  and  $\delta \mathbf{b}$ . Since  $\delta \mathbf{z}^{\pm}$  and any gradient of  $\delta \mathbf{z}^{\pm}$  mostly occur in the plane perpendicular to  $\mathbf{b}_0$ , there are three scales involved:  $l_{\parallel}$  (along  $\mathbf{b}_0$ ),  $l_{\perp}$  (along  $\delta \mathbf{z}^{\pm}$ ) and  $\lambda$  (perpendicular to  $l_{\parallel}$  and  $l_{\perp}$ ), where  $\lambda \sim l_{\perp} \sin \theta_{\lambda}$ , and  $l_{\parallel} \gg l_{\perp} \gg \lambda$ . Thus, the non linear time is

$$\tau_{nl}^{\pm} \sim \frac{l_{\perp}}{\delta z^{\pm}} \sim \frac{\lambda}{\delta z^{\pm} \sin \theta_{\lambda}}, \quad (4.11)$$

which leads to the perpendicular energy transport across the scales  $E(k_{\perp}) = \epsilon_{\lambda}/k_{\perp}$  of the form

$$E(k_{\perp}) \sim (\epsilon_{\lambda} v_A)^{1/2} k_{\perp}^{-3/2}, \quad (4.12)$$

where  $k_{\perp} \sim 1/\lambda$ . Additionally, the relation between the parallel and perpendicular scales is

$$k_{\parallel} \sim \frac{\epsilon_{\lambda}^{1/2}}{v_A^{3/2}} k_{\perp}^{1/2}. \quad (4.13)$$



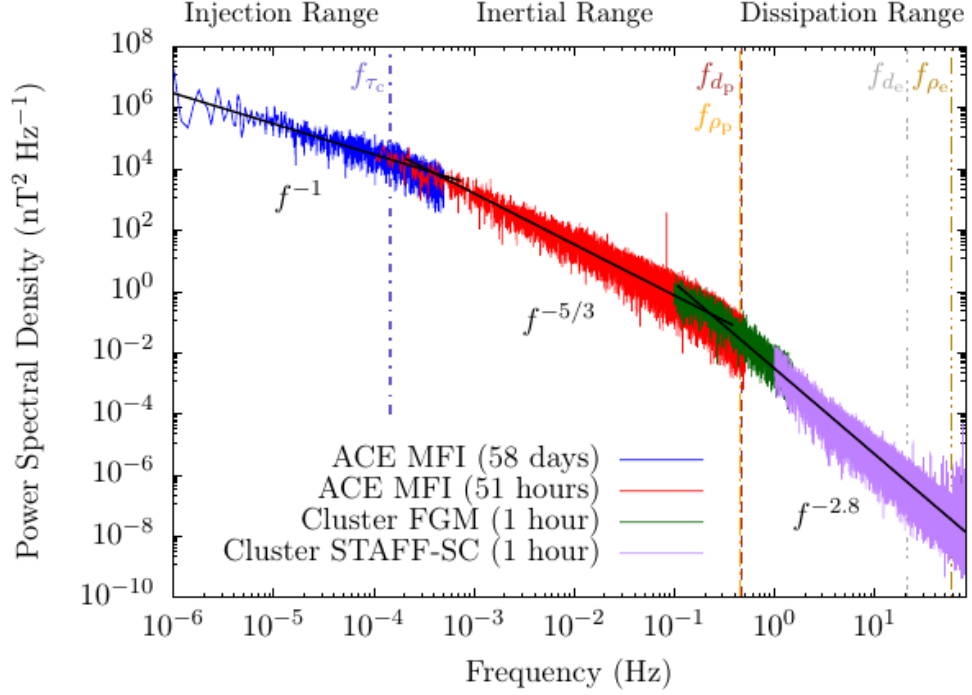


**Figure 4.1:** Power spectral density of magnetic field fluctuations. The vertical dashed lines corresponds to the frequencies associated, through the Taylor hypothesis, with spatial variations at different scales in the spacecraft frame. Adapted from [Verscharen et al. \(2019\)](#).

This model recovers the IK slope in the perpendicular direction while keeping the same parallel-cascade slope of  $-2$ .

#### 4.2.5 Plasma Turbulence in the Solar Wind

Since the solar wind is supersonic and super-Alfvénic, the time required for  $\delta \mathbf{z}^\pm$  to evolve significantly is greater than the travelling time over a fixed point in the Sun-at-rest frame. For low-frequency fluctuations ( $\omega \ll \omega_{pi}$ ), a time series of spacecraft measurements represents convected fluctuations in the plasma. Therefore, the frequencies ( $f$ ), based on temporal variations in a fixed-point measurement ( $\Delta t$ ), correspond to wavenumbers ( $k$ ) associated with spatial fluctuations ( $\Delta l$ ) in the plasma frame. This is known as Taylor’s hypothesis ([Taylor, 1938](#)).

Figure 4.1 shows omnidirectional power spectral density ( $\sim \varepsilon/f$ ) of the magnetic field fluctuations as a function of frequency measured by different spacecraft in the solar wind. In the injection range, the spectral slope is  $-1$  ([Bavassano et al., 1982](#);

Denskat and Neubauer, 1983; Matthaeus and Goldstein, 1986; Kiyani et al., 2015). In the inertial range, the index is often observed as  $-5/3$ . However, the spectral slopes for the perpendicular and parallel cascades are different. Multiple different theories agree on a slope of  $-2$  for the parallel cascade (Goldreich and Sridhar, 1995; Boldyrev, 2006; Beresnyak, 2015). The slope of the perpendicular cascade is under constant debate. Although solar wind observations (Horbury et al., 2008; Podesta, 2009; Wicks et al., 2011; Chen, 2016) support a  $-5/3$  slope, simulations of incompressible MHD (Cho and Vishniac, 2000; Maron and Goldreich, 2001; Müller et al., 2003) present a  $-3/2$  slope. Moreover, recent solar wind observations (Chen et al., 2020) have shown that the spectral slope varies between  $-3/2$  close to the Sun and  $-5/3$  at larger heliocentric distances.

In the dissipation range, the index is about  $-2.8$ , but this value shows an even larger variability than the spectral slopes in the other ranges. At sub-proton scales, below the ion inertial length or the ion gyroradius, wave-particle interactions become stronger. The exchange of energy between fluctuations and particles at these scales generates the acceleration of particles and energy dissipation as well as entropy increase. At these scales, kinetic processes such as Landau damping, ion-cyclotron damping or magnetic reconnection are candidate processes to explain the exchange of energy between waves and particles.

#### 4.2.6 Kinetic Turbulence

In the kinetic range, at sub-proton scales where MHD is no longer valid, the GS95 theory of critical balance has been extended to account for the anisotropy at small scales where kinetic Alfvén waves (KAW) (Leamon et al., 1999; Salem et al., 2012; Boldyrev et al., 2013) and whistler waves (Cho and Lazarian, 2004; Narita, 2016) carry the turbulence at sub-proton scales. These theories predict an anisotropy in the range  $k_{\parallel} \sim k_{\perp}^{1/3}$  to  $k_{\parallel} \sim k_{\perp}^{2/3}$ . However it is still a matter of debate whether the main carriers of turbulence at kinetic scales are KAWs, whistler waves, or even other structures and modes (Roberts et al., 2013; Huang et al., 2014; Roberts et al., 2017; Zhu et al., 2019b; Narita et al., 2020; He et al., 2020). In the kinetic range, the spectral index for the parallel cascade is between  $-5$  and  $-3.5$ , whereas for the

perpendicular cascade, it is observed at values between -2.8, and -1.5 (Chen et al., 2010a; Boldyrev et al., 2011; Chen et al., 2011; Alexandrova et al., 2013).

In the dissipation range, there are several mechanisms that can be involved in the turbulent cascade. The importance of unambiguously determining the spectral slope lies in the fact that it constrains the mechanisms that take place in the energy cascade and in the energy partition. It is not well understood what mechanisms at small scales ( $\sim d_i, d_e$ ) are responsible for the transition from the inertial range to the kinetic range. The phenomena responsible for the change in the slope at proton scales is also matter of ongoing research (Goldstein et al., 2015).

At the end of the energy cascade, ions and electrons are heated by different processes and at different rates. Magnetic reconnection is a candidate to explain how plasma evolves to states in which different acceleration and heating processes appear. For instance, reconnection is attributed to particle acceleration during solar flares (Goldstein et al., 1986) and in the fast solar wind (Gosling, 2007). The parallel component of the electric field during reconnection is a strong channel for electron acceleration and plasma heating (Egedal et al., 2012). Moreover, using 2D MHD simulations of incompressible decaying turbulence, the spontaneous occurrence of thin current sheets and magnetic reconnection has been recognised when the systems reaches a fully developed turbulent state (Servidio et al., 2011). Thus, it is clear that reconnection plays a fundamental role in the particle acceleration at the end of the cascade.

#### 4.2.7 Turbulent 3D Reconnection

A common system used to study reconnection is the Harris current sheet (Harris, 1962), which is a single laminar sheet that divides two regions of uniform magnetic field with opposite directions. The effect of turbulence in 3D reconnection has been approached in two ways. On one hand, there have been simulation studies of the effects of a turbulent field within the Harris current sheet and how it changes the current sheet size Karimabadi et al. (2013); Zweibel and Yamada (2016). Previous studies (Rogers et al., 2000; Eastwood et al., 2009; Daughton et al., 2011; Muñoz and

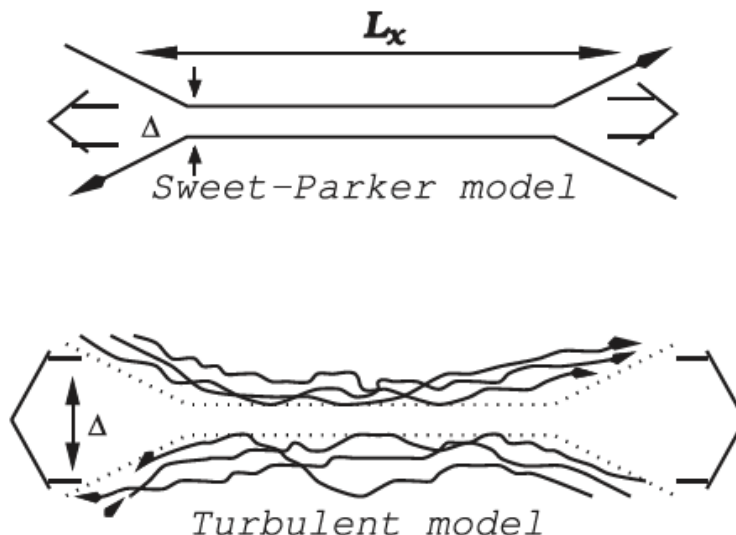


**Figure 4.2:** In the laminar SP model, the aspect ratio ( $\Delta/L$ ) is defined by the size of the current sheet. In the presence of pre-existing turbulence, the magnetic field lines wander and change the effective width  $\Delta$  of the reconnection region. This change increases the aspect ratio and thus the reconnection rate. Adapted from [Lazarian et al. \(2020\)](#).

[Büchner, 2018](#)) have shown the self-consistent onset of turbulent fluctuations in the ion diffusion region and in the exhaust jets. These fluctuations lead to the generation of flux ropes as a consequence of the plasmoid instability and a turbulent cascade as the result of the non-linear interaction of filamentary currents ([Karimabadi et al., 2013](#); [Zweibel and Yamada, 2016](#)). On the other hand, there have been simulation studies of the effects of turbulence that changes the initial reconnection magnetic field from a laminar to a turbulent state ([Lazarian and Vishniac, 1999](#); [Lazarian et al., 2020](#)). This is a more general theory of turbulent reconnection in which the effective width of the current sheet is associated with an initial wandering of the magnetic field lines (see Figure 4.2).

In this theory, the wandering of the magnetic field lines is associated with a time-dependent mechanism called *Richardson dispersion*, which accounts for a stochastic separation of magnetic field lines and for the violation of the flux freezing. An interesting result from this theory is the fact that the reconnection rate becomes independent of the Lundquist number and depends on the level of turbulence present in the system. This is a powerful result since it can be applied to all scales on which

the fluid treatment of plasma is appropriate. It can also account for the different reconnection rates. Thus, a system can have slow reconnection or fast reconnection, depending on its level of turbulence ([Lazarian and Vishniac, 1999](#)). However, it is not clear how this theory can be extended to small scales where the fluid approximation is not longer valid and where the Richardson dispersion ([Richardson, 1926](#); [Eyink et al., 2013](#)) produces a diffusion of magnetic field lines consistent with a Lyapunov growth ([Lazarian, 2006](#)).

Finally, it has been shown that turbulence can affect the magnetic reconnection process ([Matthaeus and Lamkin, 1986](#); [Karimabadi and Lazarian, 2013](#)) through an enhancement of viscous and resistive dissipation as well as the occurrence of reconnection at thin current sheets generated by turbulence in the solar wind.

## Chapter 5

# Simulation method: Particle In Cell Simulations

In this chapter I give an overview of the computational method that I use to simulate plasmas at small-scales. Afterwards, I present the initial conditions to simulate anisotropic turbulence. I finish this chapter by presenting a set of numerical tests and the method that I use to establish the presence of turbulent fluctuations in the simulation.

### 5.1 Overview Particle-In-Cell Method

Simulations are widely used to address the reconnection problem ([Birn et al., 2001](#)). The approaches from MHD theory include resistive MHD (RMHD; [Biskamp, 1986](#); [Shay et al., 1999](#)), Hall MHD (HMHD; [Huba and Rudakov, 2004](#); [Ma and Bhattacharjee, 2001](#); [Shay et al., 2001](#)), lattice-Boltzmann based methods ([Chen et al., 1991](#); [Mendoza and Munoz, 2010](#); [Zhu et al., 2019a](#)) and electron MHD (EMHD; [Drake et al., 1997](#)). However, in order to understand the energy dissipation at the end of the turbulent cascade, it is crucial to resolve the ion and electron scales. At this point, the MHD assumptions are no longer valid, and the use of either hybrid codes (ions as particles – electrons as a fluid; [Mandt et al., 1994](#); [Lottermoser et al., 1998](#); [Karimabadi et al., 2004](#)) or fully kinetic codes ((ions and electrons as particles); [Hesse et al., 2001b](#); [Ricci et al., 2004b](#); [Drake et al., 2006](#); [Fox et al., 2011](#);

[Wang et al., 2015](#); [Daughton et al., 2014](#)) is essential.

The advantage of particle-in-cell (PIC) methods lies mostly in the fact that they are fully kinetic and simultaneously resolve the ion and electron plasma frequencies  $\omega_{pi}$  and  $\omega_{pe}$  as well as the ion and electron inertial lengths  $d_i$  and  $d_e$ . Therefore, these methods reproduce kinetic effects beyond MHD. However, they are computationally expensive, memory intensive and require the use of High-Performance-Computing (HPC) facilities that allow the parallelization of computational calculations to reduce the total simulation time to a few weeks instead of thousands of years. Notwithstanding the use of HPC facilities, the scalability (parallelization) is limited ([Amdahl, 1967](#); [Gustafson, 1988](#)). This limits the resolution and the size of 3D simulation boxes  $L_x \times L_y \times L_z$  to  $\sim 10^2 d_i \times 10^2 d_i \times 10^2 d_i$ . Thus, these methods are suitable for the study of local kinetic phenomena at small scales rather than inertial-range physics where fluid-like models are more appropriate.

In PIC methods, the particle distribution function  $f_s(\mathbf{x}, \mathbf{v}, t)$  is approximated as a superposition of  $M_s$  extended quasi-particles in the phase space:

$$f_s(\mathbf{x}, \mathbf{v}, t) = \sum_{k=1}^{M_s} f_k(\mathbf{x}, \mathbf{v}, t), \quad (5.1)$$

where  $\mathbf{x}$  and  $\mathbf{v}$  are the phase-space coordinates and

$$f_k(\mathbf{x}, \mathbf{v}, t) = N_k^s S_{\mathbf{x}}(\mathbf{x} - \mathbf{x}_k^s(t)) S_{\mathbf{v}}(\mathbf{v} - \mathbf{v}_k^s(t)) \quad (5.2)$$

is the distribution function of the quasi-particle  $k$ . The number of real particles of species  $s$  is  $N_k^s$ . The  $N_k^s$  are represented by a quasi-particle  $k$  who lives in an element of the phase space. The functions  $S_{\mathbf{x}}$  and  $S_{\mathbf{v}}$  are symmetric shape functions with compact support and with the property

$$\int_{-\infty}^{\infty} S_{\mathbf{x}}(\mathbf{x} - \mathbf{x}_k^s(t)) d\mathbf{x} = 1; \quad \int_{-\infty}^{\infty} S_{\mathbf{v}}(\mathbf{v} - \mathbf{v}_k^s(t)) d\mathbf{v} = 1. \quad (5.3)$$

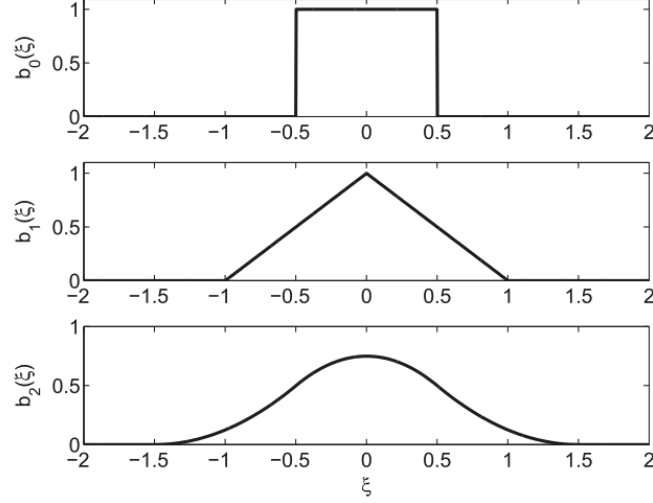


**Figure 5.1:** First three standard b-splines functions. Adapted from [Lapenta \(2012\)](#).

The shape function for the velocity variables  $\mathbf{x}$  is typically a delta function

$$S_{\mathbf{v}}(\mathbf{v} - \mathbf{v}_k^s(t)) = \delta(v_x - v_{xk})\delta(v_y - v_{yk})\delta(v_z - v_{zk}). \quad (5.4)$$

This ensures that all the particles in the phase space element represented by the quasi-particle  $k$  have the same speed ([Lapenta, 2012](#)). The shape function for the spatial variables  $\mathbf{x}$  is typically of the functional form

$$S_{\mathbf{x}}(\mathbf{x} - \mathbf{x}_k^s(t)) = \frac{1}{\Delta x_k \Delta y_k \Delta z_k} b_l\left(\frac{x - x_k}{\Delta x_k}\right) b_l\left(\frac{y - y_k}{\Delta y_k}\right) b_l\left(\frac{z - z_k}{\Delta z_k}\right), \quad (5.5)$$

where  $\Delta x_k, \Delta y_k$  and  $\Delta z_k$  are the lengths of the support of the quasi-particle. The standard b-splines functions  $b_l$  are high order function of compact support. The first three functions (Figure 5.1) are

$$b_0(\zeta) = \begin{cases} 1 & \text{if } |\zeta| \leq 1/2 \\ 0 & \text{otherwise,} \end{cases} \quad (5.6)$$

$$b_1(\zeta) = \begin{cases} 1 + \zeta & \text{if } -1 \leq \zeta \leq 0 \\ 1 - \zeta & \text{if } 0 < \zeta \leq 1 \\ 0 & \text{otherwise,} \end{cases} \quad (5.7)$$



and

$$b_2(\zeta) = \begin{cases} \frac{1}{2} \left( \frac{3}{2} + \zeta \right)^2 & \text{if } -\frac{3}{2} \leq \zeta \leq -\frac{1}{2} \\ \frac{3}{4} - \zeta^2 & \text{if } -\frac{1}{2} < \zeta < \frac{1}{2} \\ \frac{1}{2} \left( \frac{3}{2} - \zeta \right)^2 & \text{if } \frac{1}{2} \leq \zeta \leq \frac{3}{2} \\ 0 & \text{otherwise.} \end{cases} \quad (5.8)$$

### 5.1.1 Equation of Motion of the Quasi-Particles

The use of quasi-particles instead of the real particles not only reduces the computational requirements needed by Vlasov methods (Pukhov, 2005), but also simplifies the equations of motion to be solved. To derive the equation of motion for the quasi-particles, we take the zeroth moment of the Vlasov equation Eq. (2.11) for  $f_k(\mathbf{x}, t)$ ,

$$\frac{\partial \langle f_k \rangle}{\partial t} + \langle \mathbf{v} \cdot \nabla_{\mathbf{x}} f_k \rangle + \left\langle \frac{q_s}{m_s} (\mathbf{E} + \mathbf{v} \times \mathbf{B}) \cdot \nabla_{\mathbf{v}} f_k \right\rangle = 0, \quad (5.9)$$

where we have used the interchangeability of the time partial derivative and the integration in  $d\mathbf{x}d\mathbf{v}$  and

$$\langle (\dots) \rangle = \int_{-\infty}^{\infty} \int_{-\infty}^{\infty} (\dots) d\mathbf{x}d\mathbf{v}. \quad (5.10)$$

Considering Eqs. (5.2) and (5.3), the first term on the left-hand side of Eq. (5.9) is  $\partial N_k^s / \partial t$ . The second term is zero given the compact support of  $S_{\mathbf{x}}$ . Likewise, the factor with the electric field  $\mathbf{E}$  in the third term of vanishes. The factor with  $\mathbf{v} \times \mathbf{B}$  also vanishes due to the coordinates in the phase space are independent and the components in the product  $\mathbf{v} \times \mathbf{B}$  are different from the components in  $\nabla_{\mathbf{v}}$ . Thus, the first equation of motion for the quasi-particles is

$$\frac{dN_k^s}{dt} = 0. \quad (5.11)$$

To derive the second equation of motion, we consider the moment

$$\frac{\partial \langle \mathbf{x} f_k \rangle}{\partial t} + \langle \mathbf{x} \mathbf{v} \cdot \nabla_{\mathbf{x}} f_k \rangle + \left\langle \frac{q}{m} \mathbf{x} (\mathbf{E} + \mathbf{v} \times \mathbf{B}) \cdot \nabla_{\mathbf{v}} f_k \right\rangle = 0. \quad (5.12)$$

Since by definition  $\langle \mathbf{x} f_k \rangle = N_k^s \mathbf{x}_k$  and  $\langle \mathbf{v} f_k \rangle = N_k^s \mathbf{v}_k$ , the first term in Eq. (5.12) is  $\partial(N_k^s \mathbf{x}_k)/\partial t$ . For the second term, we consider a component-wise notation

$$\langle \mathbf{x} \mathbf{v} \cdot \nabla_{\mathbf{x}} f_k \rangle = \left\langle x_i v_j \frac{\partial f_k}{\partial x_j} \hat{\mathbf{e}}^i \hat{\mathbf{e}}^j \right\rangle, \quad (5.13)$$

where  $\hat{\mathbf{e}}^i \hat{\mathbf{e}}^j = \delta(i, j)$ . In virtue of the fact that  $S_{\mathbf{x}}$  has compact support, the off diagonal terms ( $i \neq j$ ) vanish, the diagonal terms are

$$\int \int v_i x_i \frac{\partial f_k}{\partial x_i} dx_i dv_i = - \int \int v_i f_k dx_i dv_i = -N_k^s v_{ik}^s, \quad (5.14)$$

and the second term in Eq.(5.12) is  $-N_k^s \mathbf{v}_k^s$ . The third term is zero due to the integration in  $\mathbf{v}$ . Therefore, the second equation of motion is

$$\frac{d\mathbf{x}_k^s}{dt} = \mathbf{v}_k^s. \quad (5.15)$$

To derive the third equation of motion, we consider the moment

$$\frac{\partial \langle \mathbf{v} f_k \rangle}{\partial t} + \langle \mathbf{v} \mathbf{v} \cdot \nabla_{\mathbf{x}} f_k \rangle + \left\langle \frac{q}{m} \mathbf{v} (\mathbf{E} + \mathbf{v} \times \mathbf{B}) \cdot \nabla_{\mathbf{v}} f_k \right\rangle = 0. \quad (5.16)$$

The first term in Eq. (5.16) is  $\partial(N_k^s \mathbf{v}_k)/\partial t$ . The second term is zero in virtue of integration over  $\mathbf{x}$ . The third term in Eq. (5.16) is analogous to the second term in Eq. (5.12), i.e.,

$$\langle \mathbf{v} (\mathbf{E} + \mathbf{v} \times \mathbf{B}) \cdot \nabla_{\mathbf{v}} f_k \rangle = \frac{q_s}{m_s} \left\langle v_i (E_j + v_\mu B_\nu) \frac{\partial f_k}{\partial v_j} \hat{\mathbf{e}}^i \hat{\mathbf{e}}^j \right\rangle, \quad (5.17)$$

where the indices  $\mu, \nu \neq j$ . The off diagonal terms ( $i \neq j$ ) vanish due to  $S_{\mathbf{v}}$  has compact support. The diagonal terms are

$$\frac{q_s}{m_s} \int \int v_i (E_j + v_\mu B_\nu) \frac{\partial f_k}{\partial v_j} dx_i dv_i = -\frac{q_s}{m_s} \int \int (E_j + v_\mu B_\nu) f_k dx_i dv_i \quad (5.18)$$

and defining the electric and magnetic field acting on each quasi-particle are calculated as

$$\mathbf{E}_k = \int \mathbf{E} S_{\mathbf{x}}(\mathbf{x} - \mathbf{x}_k^s) d^3x \quad (5.19)$$

and

$$\mathbf{B}_k = \int \mathbf{B} S_{\mathbf{x}}(\mathbf{x} - \mathbf{x}_k^s) d^3x, \quad (5.20)$$

the third term in Eq. (5.16) becomes

$$\langle \mathbf{v}(\mathbf{E} + \mathbf{v} \times \mathbf{B}) \cdot \nabla_{\mathbf{v}} f_k \rangle = -N_k^s \frac{q_s}{m_s} \mathbf{E}_k + (\mathbf{v}_k \times \mathbf{B}_k), \quad (5.21)$$

which leads to the third equation of motion

$$\frac{d\mathbf{v}_k^s}{dt} = \frac{q_s}{m_s} (\mathbf{E}_k + \mathbf{v}_k^s \times \mathbf{B}_k). \quad (5.22)$$

Equations (5.11), (5.15) and (5.22) describe the evolution of each quasi-particle. This set of equations resemble Newton's equations of motion for real particles and this system of equations is easier to resolve than Eq. (2.11).

### 5.1.2 Method for Solving the Equations of Motion

The Plasma Simulation Code (PSC; [Germaschewski et al., 2016](#)) is an explicit code that solves the equations (5.11), (5.15) and (5.22) for each species  $s$  and self-consistently evolves the electromagnetic fields using Maxwell's equations (2.3) - Eq. (2.6). The quasi-particle charge density is

$$\rho^s(\mathbf{x}, t) = \sum_k q_s N_k^s S_{\mathbf{x}}(\mathbf{x} - \mathbf{x}_k^s), \quad (5.23)$$

and the quasi-particle current density is

$$\mathbf{J}^s(\mathbf{x}, t) = \sum_k q_s N_k^s \mathbf{v}_i^s S_{\mathbf{x}}(\mathbf{x} - \mathbf{x}_k^s). \quad (5.24)$$

To solve the equations of motion, PSC uses a finite-difference time domain method in which space is discretized as a  $L_x \times L_y \times L_z$  mesh, employing the staggered Yee grid (Yee, 1966) as shown in Figure 5.2). The time steps are discretized using the leap-frog algorithm (Figure 5.3).

On a Yee grid, magnetic fields are represented on the faces of each cell, electric fields and current densities on its edges, and charge densities in its corners. The use of a Yee grid guarantees that, if the initial magnetic field is divergence-free ( $\nabla \cdot \mathbf{B} = 0$ ), this condition is always fulfilled at any later time.

In the leap-frog algorithm, position, electric field and density are calculated at integer times whereas momentum, magnetic field and current density are calculated at half time steps between the integer time steps.

To advance the particles in the electromagnetic fields, the update of the momentum of each particle is made in three steps according to the Boris algorithm (Boris and Shanny, 1972; Birdsall and Langdon, 2018):

1. a half-time-step acceleration due to the electric field;
2. a rotation of the momentum vector due to the magnetic field, and
3. another half-time-step acceleration due to the electric field.

Afterwards, the evaluated charge and current densities, according to Eqs. (5.23) and (5.24), are used to feed back into Maxwell's equations. Hence, when the particles are advanced, the fields are static and, when the electromagnetic fields are advanced, the particles are static (Germaschewski et al., 2016).

The explicit discretization in time requires a small time step  $\Delta t$  to ensure stability in the solution. For a characteristic frequency of the system  $\Omega$ , the condition

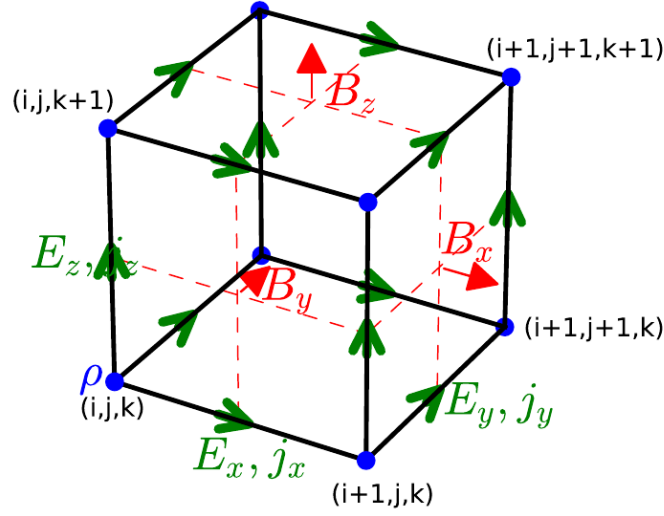


**Figure 5.2:** Yee grid unit cell. The magnetic field components are calculated on the cell faces. The components of the electric field and the electric current density are calculated on the edges of the cell. The charge density is calculate on the corners of the cell. Adapted from [Germaschewski et al. \(2016\)](#).

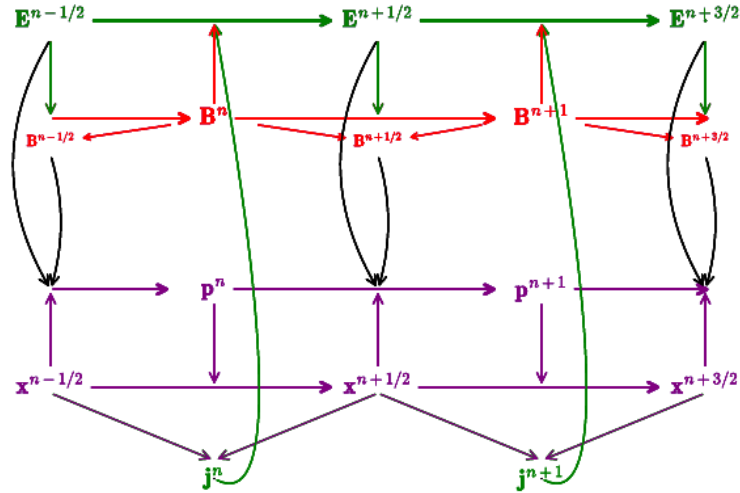


**Figure 5.3:** Leap-frog algorithm. The position, the electric field and the charge density are calculated at integer times. The momentum, the magnetic field and the electric current density are calculated at half time steps between the integer time steps. Adapted from [Germaschewski et al. \(2016\)](#).

$\Omega\Delta t < 2$  needs to be hold. Moreover, to avoid numerical heating the time step needs to fulfil the condition  $\Omega\Delta t < 0.1$  (Birdsall and Langdon, 2018). Likewise, space discretization introduces a spatial constraint as  $\Delta x/\lambda_{De} \lesssim 1$  for the spatial resolution  $\Delta x$  (Lapenta, 2012). Notwithstanding the large amount of steps required by this method to simulate the evolution of plasmas, PSC shows good scalability on supercomputer clusters and uses a load-balancing algorithm which redistributes the computational power onto each core such that the computation time per time step remains roughly constant as the number of time steps increases (Germaschewski et al., 2016).

Finally, along with the fact that, in reality, the fields are not stagnant when the particles move and vice versa, another pitfall of explicit PIC methods is that they use a uniform and finite fixed-shape discretization of phase space. This neglects the possibility of distortion in the phase space elements representing the particles. These distortions due to microscopic electromagnetic field would represent collisions between individual plasma particles (Lapenta, 2012).

There is another family of PIC codes available that use an implicit integration in time to avoid the space and time resolution constraints allowing larger time steps (Brackbill and Forslund, 1982; Lapenta et al., 2003; Markidis et al., 2009). However, their scalability is not straightforward, and due to the fact that this study requires the resolution of length scales near the Debye length, an explicit code as PSC is a more suitable option.

## 5.2 Initial Conditions to Simulate Anisotropic Turbulence

In this section, I introduce the initial conditions for the turbulence simulations that we use to study turbulent reconnection. We initialise the simulation with eight anisotropic low-frequency counter-propagating Alfvén waves within a box of volume  $L_x \times L_y \times L_z$  (see section 2.3). We take the background magnetic field to be along the  $z$ -axis,  $\mathbf{B}_0 = B_0 \hat{z}$ , and set up the fluctuations with wavevectors following the theory

of critical balance by GS95. According to GS95, turbulence is isotropic at the large-scale end of the inertial range and develops an anisotropic cascade of energy with respect to the local magnetic field. The anisotropic cascade of energy is associated with a wavevector anisotropy  $k_{\parallel} \propto (|\mathbf{k}_{\perp}|)^{\gamma}$ , where  $k_{\parallel}$  and  $k_{\perp}$  are the wavevector components in the directions parallel and perpendicular with respect to the local background magnetic field. The index  $\gamma$  is a power index that is approximately constant in each wavevector range of the turbulent power spectrum. For the inertial range,  $\gamma = 2/3$ . The relation between  $k_{\perp}$  and  $k_{\parallel}$  can be expressed as

$$k_{\parallel} d_i = C (k_{\perp} d_i)^{2/3}, \quad (5.25)$$

where  $C$  is a constant which is chosen so that  $k_{\parallel} = k_{\perp}$  at the large-scale end of the inertial range, which we set up as  $k_{\perp} d_i = 10^{-4}$  consistent with observations (Wicks et al., 2010; Chen et al., 2012). Defining  $k_{m,\perp} = \sqrt{k_{m,x}^2 + k_{m,y}^2}$  where the index  $m$  refers to the mode of the wave. We use periodic boundary conditions and adjust the wavelengths of the initial modes  $\lambda_{m,i}$  so that  $L_i$  is an integer multiple of  $\lambda_{m,i}$ . Then, the wavevector components are

$$k_{m,x} = m \frac{2\pi}{L_x}; \quad k_{m,y} = m \frac{2\pi}{L_y}; \quad \text{and} \quad k_{m,z} = m \frac{2\pi}{L_z}. \quad (5.26)$$

Since we only use  $m = 1$ , we drop the index  $m$  for simplicity. Each wave satisfies the Alfvénic polarisation relation

$$\frac{\delta \mathbf{u}_{s,\alpha}}{v_{A,i}} = (-1)^{\alpha} \frac{\delta \mathbf{B}_{\alpha}}{B_0}, \quad (5.27)$$

where  $v_{A,i} = B_0 / \sqrt{\mu_0 n_i m_i}$  is the Alfvén speed,  $n_i$  is the ion density,  $m_i$  is the ion mass, and  $\mathbf{u}_{s,\alpha}$  is the bulk velocity of the species  $s$ . The index  $\alpha = 1, \dots, 8$  refers to each wave. The four waves with odd  $\alpha$  travel along the  $z$ -direction and the other four in the opposite direction. The amplitude  $\mathbf{A}_{\alpha}$  of the perturbation  $\delta \mathbf{B}_{\alpha}$  of each wave is perpendicular to both the background magnetic field  $\mathbf{B}_0$  and to the wave's

wavevector  $\mathbf{k}_\alpha$ . Thus, the components of the wavevector can be written as

$$k_{\alpha,x} = k_{\alpha,\perp} \cos \phi_\alpha \quad (5.28)$$

and

$$k_{\alpha,y} = k_{\alpha,\perp} \sin \phi_\alpha, \quad (5.29)$$

where  $\phi_\alpha$  is the azimuthal angle of  $\mathbf{k}_{\alpha,\perp}$ . The waves propagating in the  $+z$ -direction have  $\phi_\alpha = 0, \pi, \pi/4$  and  $5\pi/4$  whereas the waves propagating in the  $-z$ -direction have  $\phi_\alpha = \pi/2, 3\pi/2, 3\pi/4$  and  $7\pi/4$ . This distribution of azimuthal angles produces a quasi-gyrotropic distribution of fluctuations in the plane perpendicular to the background magnetic field while keeping the initial magnetic field divergence-free. The components of the fluctuating fields for each wave are given by

$$\delta B_{\alpha,x} = -|\mathbf{A}_\alpha| \cos(k_{\alpha,x}x + k_{\alpha,y}y + (-1)^{\alpha+1}k_{\alpha,z}z + \psi_\alpha) \sin \phi_\alpha \quad (5.30)$$

and

$$\delta B_{\alpha,y} = |\mathbf{A}_\alpha| \cos(k_{\alpha,x}x + k_{\alpha,y}y + (-1)^{\alpha+1}k_{\alpha,z}z + \psi_\alpha) \cos \phi_\alpha, \quad (5.31)$$

where  $\psi_\alpha$  represents a random phase for each  $\alpha$ . The amplitude  $|\mathbf{A}_\alpha|$ , according to [Chandran et al. \(2010\)](#), follows

$$|\mathbf{A}_\alpha| = CB_0 \left( |\mathbf{k}_{\alpha,\perp}| d_i \right)^{-1/3}. \quad (5.32)$$

Thus, the components of the total initial magnetic variations are

$$\delta B_{T,x} = D \sum_{\alpha=1}^8 \delta B_{\alpha,x} \quad \text{and} \quad \delta B_{T,y} = D \sum_{\alpha=1}^8 \delta B_{\alpha,y}, \quad (5.33)$$



where  $D$  is a normalization constant defined as

$$D = \frac{B_0}{\sqrt{\sum_{\alpha=1}^8 |\mathbf{A}_\alpha|^2}}, \quad (5.34)$$

which ensures that the total amplitude of all modes  $|\delta \mathbf{B}_T/B_0| \sim 1$  at the beginning of the simulation. Assuming that the nonlinear time is comparable to the linear time at the initial time step, we initialise the simulation with strong turbulence. The nonlinearity parameter  $\chi = (\delta B_T/B_0)/(k_\parallel/k_\perp) \sim L_z/L_x \sim 5.2$  at the initial time which quantitatively states that the initialised turbulence is strong. The components of the velocity fluctuations  $\delta \mathbf{u}_T$  are calculated self-consistently according to Eq. (5.27).

The wavelengths of the initial waves at  $k_\perp d_i = 1$  are  $\lambda_\perp = 2\pi d_i$  and  $\lambda_\parallel = 2\pi/10^{-4/3} d_i$ . Therefore, the size of the box required to simulate the initial ( $m = 1$ ) anisotropic Alfvén waves is  $L_z = \lambda_\parallel$  and  $L_x = L_y = \sqrt{2}\lambda_\perp$ . However, we use  $L_z = 125d_i$ ,  $L_x = L_y = 24d_i$ ,  $\lambda_\parallel = L_z$  and  $\lambda_\perp = \sqrt{2}L_x/4$ . This choice keeps the ratio  $\lambda_\perp/\lambda_\parallel \approx 10^{-4/3}$  while allowing a several wavelengths in the perpendicular direction.

The critical-balance scaling  $k_\parallel \sim k_\perp^{2/3}$  applies to Alfvén waves in the inertial range. The initial fluctuations in the simulation have  $k_\perp d_i \sim 1$ , which is at the transition scale from the inertial to the dissipation range. Natural fluctuations at this scale have an anisotropy consistent with the critical-balance scaling based on the size of the inertial range (Wicks et al., 2010). The scale dependence of the anisotropy in the inertial range also varies when considering dynamic alignment and intermittency (Cho and Lazarian, 2004; Boldyrev et al., 2011; Chandran et al., 2015; Chen, 2016). We assume a critical-balance scaling over an inertial range of four decades to capture the relative amplitude of the anisotropy without including the true evolution of the inertial-range turbulence. Therefore, we initialise with fluctuations at  $k_\perp d_i \sim 1$  that have such an anisotropy. The wavevector anisotropy in the dissipation range is less well understood and, at kinetic scales, it is not clear whether the turbulence is mostly carried by KAWs, whistler waves or a combination of compressive and non-compressive modes (Schekochihin et al., 2009; Chen et al., 2010b; Boldyrev

and Perez, 2012). Moreover, pressured-balanced structures also contribute to the turbulent cascade (Verscharen et al., 2012; Narita and Marsch, 2015; Verscharen et al., 2017). Nevertheless, the anisotropic initialisation is supported by solar-wind measurements (Horbury et al., 2008; Alexandrova et al., 2009; Wicks et al., 2010, 2011) and allows a kinetic cascade to develop self-consistently as the simulation evolves.

## 5.3 Numerical Tests

In this section, I show a series of test simulations with the aim to establish the most appropriate configuration and parameters to study 3D turbulent reconnection using explicit PIC simulations.

In PIC simulations, especially in the PSC code, the normalization parameters are  $c$ ,  $\epsilon_0$ ,  $\mu_0$ ,  $k_B$ ,  $e$ ,  $m_i$ ,  $n_i = n_e$   $d_i$  and  $\omega_{pi}$ . This means that all equations are normalised in such a way that these parameters have a numerical dimensionless value of one.

The main parameters that affect an explicit PIC simulation performance as well as the applicability of the simulation results are: the Alfvén speed ratio  $v_{A,i}/c$ ,  $c$  is the speed of light; the mass ratio  $m_i/m_e$  where  $m_e$  is the electron mass, and the number of quasi-particles per cell (*ppc*). Thus, we run 17 different tests. Table 5.1 shows the list of parameters used in these tests.

For these tests, we simulate eight isotropic, counter-propagating Alfvén waves travelling along the  $\hat{z}$ -direction in an ion-electron plasma. The simulation domain is a cubic box of size  $L_x = L_y = L_z = 10d_i$ . The magnetic field is normalised to the value of the constant background field  $B_0$ . We set  $\beta_{s,\parallel} = 1$  and  $T_{s,\parallel}/T_{s,\perp} = 1$ , where  $\beta_{s,\parallel} = 2n_s\mu_0k_BT_{s,\parallel}/B_0^2$  is the ratio of the parallel thermal pressure to the magnetic pressure,  $\mathbf{B}_0$  is the background magnetic field, and the index  $s$  indicates the plasma species.  $T_{s,\parallel}$  and  $T_{s,\perp}$  are the parallel and perpendicular temperatures respectively.

### 5.3.1 Evidence of Turbulence

To estimate the effects of these simulation parameters on the turbulent evolution in the simulation, we use a spectral analysis of the magnetic field fluctuations following

Test #	$v_{A,i}/c$	$ppc$	$m_i/m_e$	$\tau_A(\omega_{pi}^{-1})$	$t_R(\tau_A)$	$d_e(d_i)$	$\lambda_D(d_i)$
s1	0.06	100	100	32	1.5	0.100	0.042
s2	0.08	100	100	24	3.0	0.100	0.057
s3	0.10	100	100	19	3.0	0.100	0.071
s4	0.10	50	100	19	3.0	0.100	0.071
s5	0.10	150	100	19	3.0	0.100	0.071
s6	0.10	200	100	19	3.0	0.100	0.071
s7	0.10	250	100	19	3.0	0.100	0.071
s8	0.10	300	100	19	3.0	0.100	0.071
s9	0.06	100	1	32	1.5	1.000	0.042
s10	0.06	100	10	32	1.5	0.316	0.042
s11	0.06	100	50	32	1.5	0.141	0.042
s12	0.06	100	150	32	1.5	0.081	0.042
s13	0.06	100	200	32	1.5	0.070	0.042
s14	0.06	100	250	32	1.5	0.063	0.042
s15	0.06	100	300	32	1.5	0.057	0.042
s16	0.06	100	400	32	1.5	0.050	0.042
s17	0.06	100	500	32	1.5	0.044	0.042

**Table 5.1:** Simulation test runs.

[Franci et al. \(2018\)](#). We calculate the energy associated with the 3D Fourier modes  $\psi_{3D}(\mathbf{k})$  of a quantity  $\psi$  as

$$\psi_{3D}(\mathbf{k}) = \tilde{\psi}(\mathbf{k})\tilde{\psi}^*(\mathbf{k}), \quad (5.35)$$

where  $\mathbf{k}$  is the wavevector,  $\tilde{\psi}(\mathbf{k})$  is the 3D spatial Fourier transform of  $\psi$  and  $\tilde{\psi}^*(\mathbf{k})$  represents its complex conjugate. If  $\psi$  is a vector quantity, the 3D Fourier transform is taken over each component and the product is defined as

$$\tilde{\psi}(\mathbf{k})\tilde{\psi}^*(\mathbf{k}) = \sum_i \tilde{\psi}_i(\mathbf{k})\tilde{\psi}_i^*(\mathbf{k}), \quad (5.36)$$

where the index  $i$  represents the components  $x, y$  and  $z$ . Since the system does not include any anisotropy within the plane perpendicular to the background magnetic field on average, we assume that the energy distribution in the turbulent fluctuations remains axially symmetric on average. Thus, the wavevector can be expressed, without loss of generality, as its perpendicular and parallel components  $(k_\perp, k_\parallel)$ . We calculate the perpendicular and parallel components of the wavevector as  $k_\perp =$

$\sqrt{k_x^2 + k_y^2}$  and  $k_{\parallel} = k_z$ , respectively, and assume that the fluctuations are statistically independent of the azimuthal angle. We integrate  $\psi_{3D}$  over concentric rings in  $k_{\perp}$ -space. The energy associated with the  $j$ th-ring is

$$\psi_{2D}^j(k_{\perp}, k_{\parallel}) = \int_{k_{\perp}^j}^{k_{\perp}^j + dk_{\perp}} \psi_{3D}(k'_{\perp}, k_{\parallel}) 2\pi k_{\perp}^{j'} dk'_{\perp}, \quad (5.37)$$

where the thickness  $dk'_{\perp}$  of these rings is taken as the magnitude of the smallest perpendicular wavevector in the system  $dk'_{\perp} = 2\pi/\sqrt{2}L_x$ . To visualise the energy cascade in  $k$ -space as well as the level of anisotropy in the system, we compute the reduced 2D power spectral density  $P_{2D}^{\psi}(k_{\perp}, k_{\parallel})$  as

$$P_{2D}^{\psi}(k_{\perp}, k_{\parallel}) = \sum_j \frac{1}{k_{\perp}} \psi_{2D}^j(k_{\perp}, k_{\parallel}). \quad (5.38)$$

In order to explore the effect of the simulation parameters on the anisotropic energy cascade, we compute the perpendicular one-dimensional reduced power spectral density

$$P_{1D\perp}^{\psi}(k_{\perp}) = \int_0^{\infty} P_{2D}^{\psi}(k_{\perp}, k_{\parallel}) dk_{\parallel}, \quad (5.39)$$

and the parallel one-dimensional reduced power spectral density

$$P_{1D\parallel}^{\psi}(k_{\parallel}) = \int_0^{\infty} P_{2D}^{\psi}(k_{\perp}, k_{\parallel}) dk_{\perp}. \quad (5.40)$$

In plasmas, the properties of wave modes such as kinetic Alfvén waves (KAWs), Alfvén/ion-cyclotron (A/IC) waves and fast-magnetosonic/whistler (FM/W) waves depend on the values of the plasma frequency  $\omega_{pi}$  and the gyro-frequency  $\Omega_i$ . The ratio between the plasma frequency  $\omega_{pi}$  and the gyro-frequency  $\Omega_i$  depends on the ratios  $v_{A,i}/c$  and  $m_i/m_e$  as

$$\frac{\Omega_i}{\omega_{pi}} = \frac{v_{A,i}}{c} \sqrt{\frac{m_i}{m_e}}. \quad (5.41)$$

A realistic value of  $v_{A,i}/c$  and  $m_i/m_e$  leads to an accurate description of the plasma

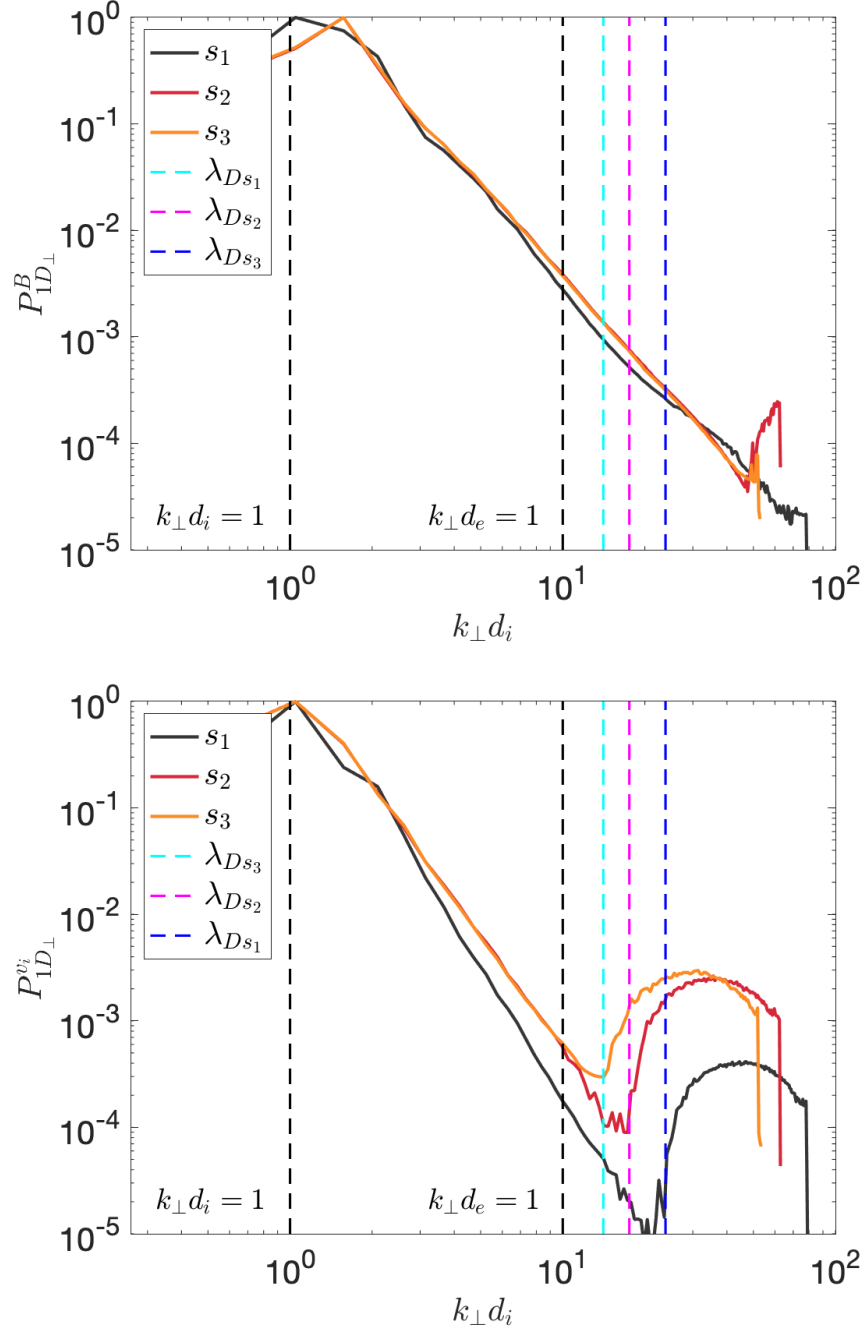


**Figure 5.4:** Perpendicular one-dimensional reduced power spectral density of the magnetic field fluctuations  $P_{1D\perp}^B$  (top) and of the ion velocity fluctuations  $P_{1D\perp}^{v_i}$  (bottom) for the test runs s1 ( $v_{A,i}/c = 0.06$ ; black), s2 ( $v_{A,i}/c = 0.08$ ; red) and s3 ( $v_{A,i}/c = 0.1$ ; orange) at  $t = t_R$ . The vertical dashed lines from left to right indicate  $k_{\perp} d_i = 1$ ,  $k_{\perp} d_e = 1$ ,  $k_{\perp} \lambda_{Ds3} = 1$ ,  $k_{\perp} \lambda_{Ds2} = 1$  and  $k_{\perp} \lambda_{Ds1} = 1$ .

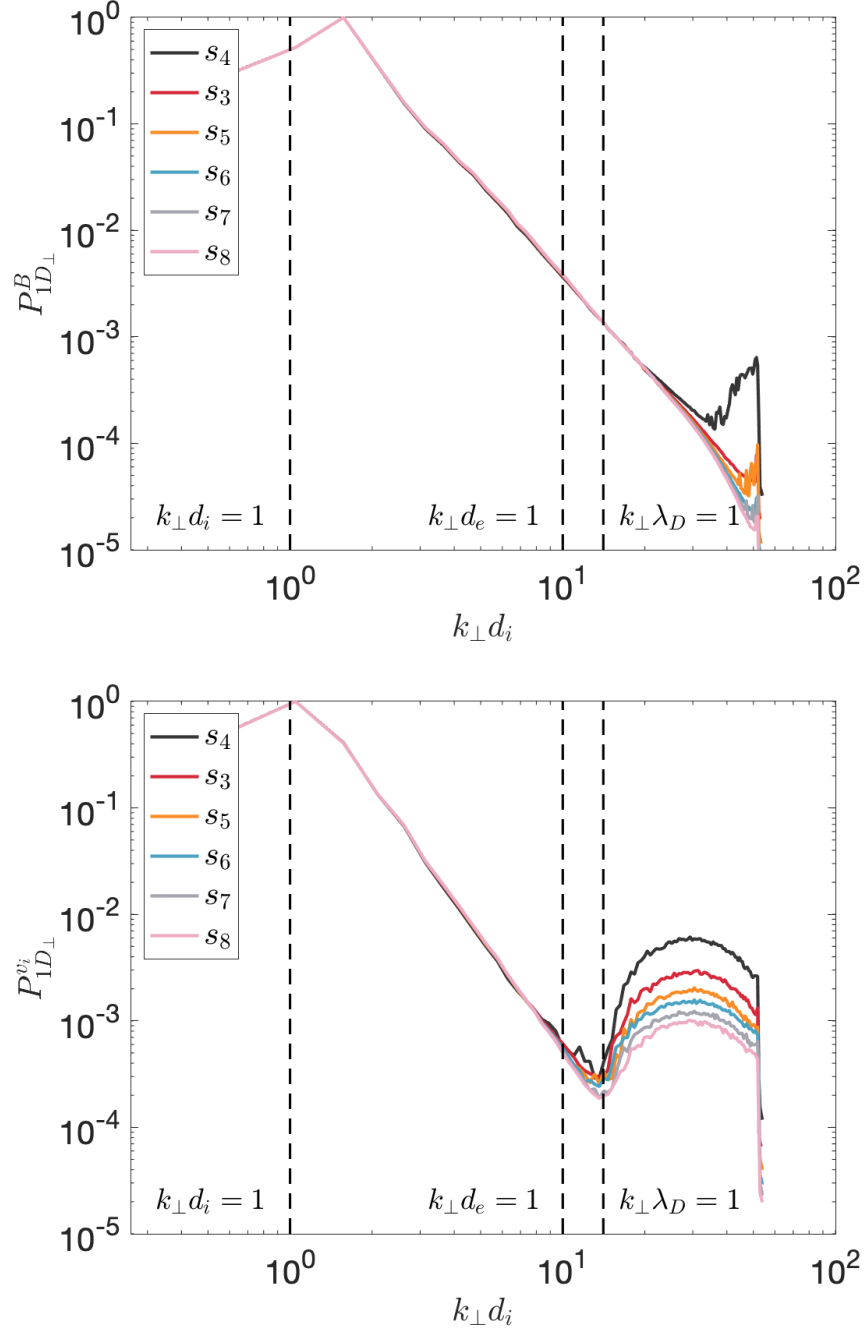


**Figure 5.5:** Perpendicular one-dimensional reduced power spectral density of the magnetic field fluctuations  $P_{1D\perp}^B$  (top) and the ion velocity fluctuations  $P_{1D\perp}^{v_i}$  (bottom) for the test runs s4 ( $ppc = 50$ ; black), s3 ( $ppc = 100$ ; red), s5 ( $ppc = 150$ ; orange), s6 ( $ppc = 200$ ; blue), s7 ( $ppc = 250$ ; gray) and s8 ( $ppc = 300$ ; pink) at  $t = t_R$ . The vertical dashed lines from left to right indicate  $k_{\perp} d_i = 1$ ,  $k_{\perp} d_e = 1$ ,  $k_{\perp} \lambda_D = 1$ .

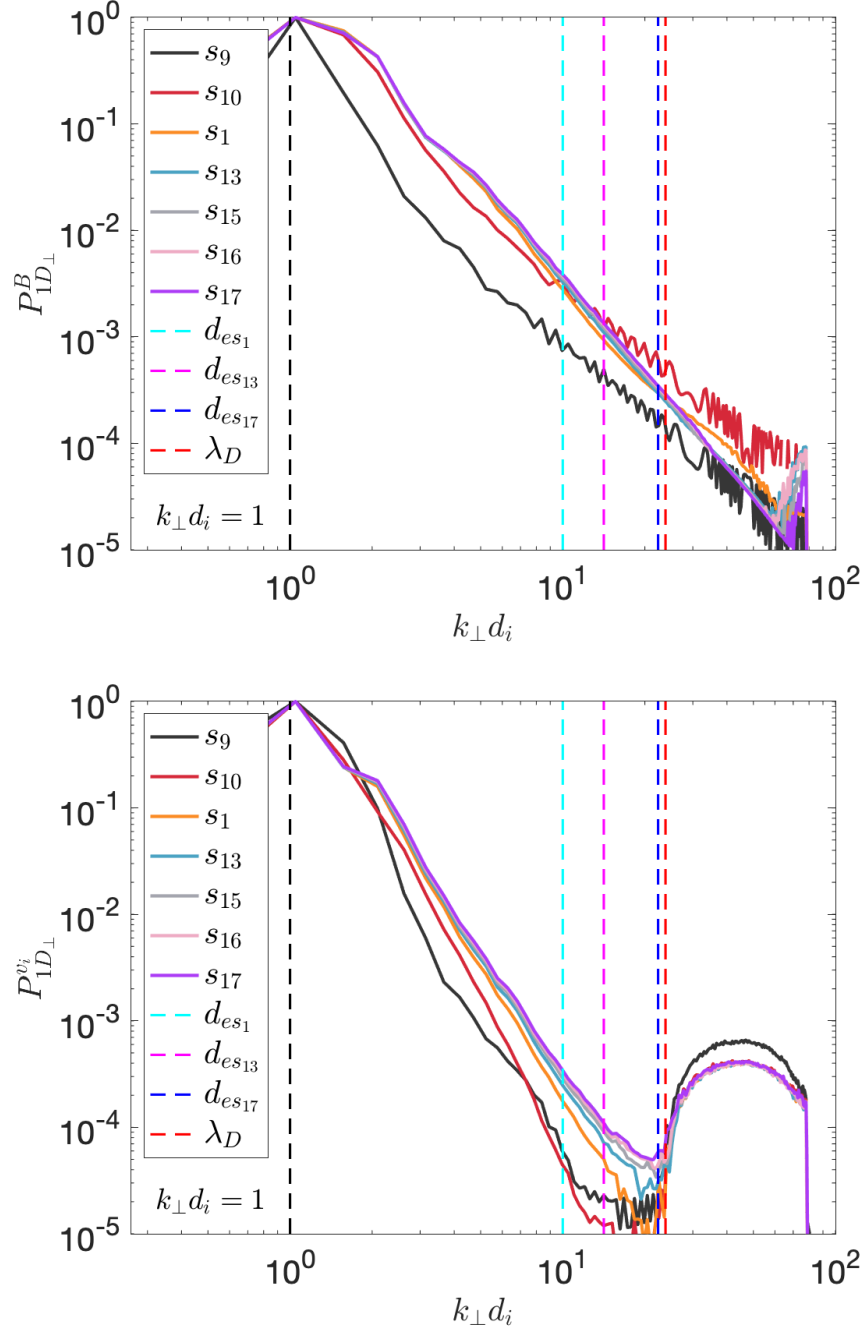


**Figure 5.6:** Perpendicular one-dimensional reduced power spectral density of the magnetic field fluctuations  $P_{1D\perp}^B$  (top) and the ion velocity fluctuations  $P_{1D\perp}^{v_i}$  (bottom) for the test runs  $s_9$  ( $m_i/m_e = 1$ ; black),  $s_{10}$  ( $m_i/m_e = 10$ ; red),  $s_1$  ( $m_i/m_e = 100$ ; orange),  $s_{13}$  ( $m_i/m_e = 200$ ; blue),  $s_{15}$  ( $m_i/m_e = 300$ ; gray),  $s_{16}$  ( $m_i/m_e = 400$ ; pink) and  $s_{17}$  ( $m_i/m_e = 500$ ; purple) at  $t = t_R$ . The vertical dashed lines from left to right indicate  $k_{\perp} d_i = 1$ ,  $k_{\perp} d_{es1} = 1$ ,  $k_{\perp} d_{es13} = 1$ ,  $k_{\perp} d_{es17} = 1$  and  $k_{\perp} \lambda_D = 1$ .

dynamics. However, using a realistic  $v_{A,i}/c$  increases the spatial resolution since the minimum spatial scale that needs to be resolved in an explicit PIC simulation is the Debye length, which depends on  $v_{A,i}/c$  as  $\lambda_D = d_i \sqrt{\beta_i/2}(v_A/c)$ .

In order to establish a reasonable value for  $v_{A,i}/c$  which can be used in a large PIC simulation with the set up described in section 5.2, we explore the effect of  $v_{A,i}/c$  on the perpendicular one-dimensional reduced power spectral density of the magnetic field fluctuations  $P_{1D\perp}^B$  and on the perpendicular one-dimensional reduced power spectral density of the ion velocity fluctuations  $P_{1D\perp}^{v_i}$  according to Eq. (5.39). The top panel of Figure 5.4 shows  $P_{1D\perp}^B$  for the test runs s1 ( $v_{A,i}/c = 0.06$ ; black), s2 ( $v_{A,i}/c = 0.08$ ; red) and s3 ( $v_{A,i}/c = 0.1$ ; orange) at each  $t = t_R$  according to Table 5.1. The quantity  $P_{1D\perp}^B$  is steeper for test s1 compared with tests s2 and s3 in the range between  $k_\perp d_i \sim 1$  and  $k_\perp d_e \sim 1$ , and s2 and s3 show the same trend. At the  $k_\perp \lambda_{Ds1} \sim 1$  (blue dashed line),  $P_{1D\perp}^B$  for s1 becomes slightly shallower. Conversely,  $P_{1D\perp}^B$  for s2 and s3 show no change in the slope at  $k_\perp \lambda_{Ds2} \sim 1$  (magenta dashed line) and  $k_\perp \lambda_{Ds3} \sim 1$  (cyan dashed line) respectively. The bottom panel of Figure 5.4 depicts  $P_{1D\perp}^{v_i}$ . Like for the magnetic case  $P_{1D\perp}^B$ ,  $P_{1D\perp}^{v_i}$  is steeper for s1 than for s2 and s3. The sudden jump in  $P_{1D\perp}^{v_i}$  for each test corresponds to the scale at which the fluctuations reach the scale of the Debye length.

In PIC simulations, the finite number of  $ppc$  directly impacts the resolution of the particle distribution function. The more  $ppc$ , the better is the resolution of the non-thermal effects. A low number of  $ppc$  may preclude the onset of kinetic effects which are triggered by non-thermal features. We explore the effect of the number of  $ppc$  on  $P_{1D\perp}^B$  and  $P_{1D\perp}^{v_i}$  in order to define a number of  $ppc$  that allows the simulation to accurately describe nonlinear interactions while keeping the computational demands reasonable. The top panel of Figure 5.5 shows  $P_{1D\perp}^B$  for the test runs s4 ( $ppc = 50$ ; black), s3 ( $ppc = 100$ ; red), s5 ( $ppc = 150$ ; orange), s6 ( $ppc = 200$ ; blue), s7 ( $ppc = 250$ ; gray) and s8 ( $ppc = 300$ ; pink) at each  $t = t_R$  according to Table 5.1. The quantity  $P_{1D\perp}^B$  presents the same trend in each of the runs. Conversely,  $P_{1D\perp}^{v_i}$  (bottom panel) shows a bump for s4 (black line) between  $k_\perp d_i \sim 1$  and  $k_\perp d_e \sim 1$ . This suggests that  $ppc = 50$  is not sufficient to resolve the turbulent motion of ions at scales below  $d_i$ .



The use of an unrealistic mass ratio  $m_i/m_e$  is often necessary, even though it affects the plasma evolution as the inertial effects of ions and electrons may become artificially comparable. However, using the realistic  $m_i/m_e$  considerably decreases  $d_e$  and  $\lambda_D$  compared to  $d_i$  which utterly increases the spatial resolution needed for the PIC simulations to be stable. We explore the effect of  $m_i/m_e$  on  $P_{1D\perp}^B$  and  $P_{1D\perp}^{v_i}$  to define a value of  $m_i/m_e$  that accurately describes the energy transfer at small scales while keeping a feasible spatial resolution for the simulation of anisotropic turbulence described in section 5.2. The top panel of Figure 5.5 depicts  $P_{1D\perp}^B$  for the test runs s9 ( $m_i/m_e = 1$ ; black), s10 ( $m_i/m_e = 10$ ; red), s1 ( $m_i/m_e = 100$ ; orange), s13 ( $m_i/m_e = 200$ ; blue), s15 ( $m_i/m_e = 300$ ; gray), s16 ( $m_i/m_e = 400$ ; pink) and s17 ( $m_i/m_e = 500$ ; purple) at  $t = t_R$ . The quantity  $P_{1D\perp}^B$  for s9 (black line) and s10 (red line) presents large fluctuations at small scales. This is because, in an electron-positron plasma, there are no de-coupling effects between positive and negative charges, i.e., no Hall effect that contributes to the cascade of magnetic energy towards smaller scales (Blackman and Field, 1993; Bessho and Bhattacharjee, 2005; Mininni et al., 2007). For the rest of the tests presented in this figure,  $P_{1D\perp}^B$  follows the same trend up to  $k_\perp d_e \sim 1$ . For the ion velocity fluctuations, the bottom panel of Figure 5.5 shows that, at small scales,  $P_{1D\perp}^{v_i}$  presents a shallower trend that shifts towards smaller scales as  $m_i/m_e$  increases.

Although more realistic values of  $m_i/m_e$  and  $v_{A,i}/c$  and a greater number of *ppc* yield better results as shown in Figures 5.4, 5.5 and 5.6, PIC codes are computationally extremely expensive, and the use of realistic values for simulations in 3D is not feasible yet, even for the latest outstanding high-performance computing (HPC) facilities. Therefore, to accurately simulate anisotropic turbulence in an elongated box as described in section 5.2, we select the following parameters:  $v_{A,i}/c = 0.1$ ,  $ppc = 100$  (100 ions and 100 electrons), and  $m_i/m_e = 100$ . The use of  $m_i/m_e = 100$  leads to  $d_e = 0.1d_i$  in the simulation which ensures at least one order of magnitude of separation in  $k$ -space. This is important in order for a simulation to account for kinetic effects, such as the quadrupolar magnetic field characteristic of the Hall magnetic reconnection, which emerge due to the de-magnetisation of ions and electrons

at different spatial scales. A value of  $v_{A,i}/c = 0.1$ , which implies  $\lambda_D = 0.07d_i$ , allows a minimum spatial resolution of  $\Delta x = \Delta y = \Delta z = 0.06d_i$ . Finally, for a simulation domain of size  $L_z = 125d_i$  and  $L_x = L_y = 24d_i$ , the spatial resolution of  $0.06d_i$  and  $ppc = 100$  represents a total number of  $6.4512 \times 10^{10}$  particles. This is the number of particles for the largest successful simulation that we managed to perform on the DiRAC Data Intensive service at Leicester, operated by the University of Leicester IT Services, which forms part of the STFC DiRAC HPC Facility ([www.dirac.ac.uk](http://www.dirac.ac.uk)).

## Chapter 6

# Three-dimensional magnetic reconnection in particle-in-cell simulations of anisotropic plasma turbulence

In this chapter, I present the PIC simulations of anisotropic Alfvénic turbulence that we have performed. We conduct a scaling analysis as well as a spectral analysis to characterise the turbulence that develops in the simulation. We find that the initial anisotropic shape of the magnetic structures evolves into smaller structures that tend towards more isotropic shapes. Afterwards, I introduce the general reconnection indicators that we use to find reconnection sites in my simulation and we perform a statistical analysis of the reconnection events that we find using the set of indicators. We select one reconnection event and study its properties. We find that, in a 3D geometry, the magnetic reconnection events that occur from a turbulent cascade present reconnection exhaust with complex geometries that differ from the Harris current-sheet configuration often used to study reconnection. Finally, we use the reconnection event to produce synthetic data to mimic the type of observations that a single spacecraft mission would encounter when crossing near and through the reconnection site. I discuss the variation of the plasma quantities along 1D

trajectories.

This work is published in: Agudelo Rueda, J. A., Verscharen, D., Wicks, R. T., Owen, C. J., Nicolaou, G., Walsh, A. P., Zouganelis, I., Germaschewski, K., and Vargas Domínguez, S. (2021). Three-dimensional magnetic reconnection in particle-in-cell simulations of anisotropic plasma turbulence. *Journal of Plasma Physics*, 87(3):905870228

## 6.1 Introduction

It is unclear how turbulence and reconnection affect each other and how the energy is partitioned between particles and fields through both processes. For instance, although the role of reconnection in the small-scale turbulent cascade has been studied previously (Franci et al., 2017; Boldyrev and Loureiro, 2017; Cerri and Califano, 2017; Papini et al., 2019b), it is still unclear how 3D reconnection proceeds in the turbulent solar wind. It is not well understood whether 3D reconnection disrupts current sheets and coherent magnetic-field structures associated with intermittency at small scales in the same way as it disrupts these structures at large scales (Boldyrev et al., 2013; Mallet et al., 2017). Moreover, it is unclear how reconnection changes the turbulent cascade as the wavevector anisotropy increases with decreasing scale and how turbulence affects the reconnection process itself (Boldyrev and Loureiro, 2017). Therefore, it is necessary to study the energy partition as well as the links between turbulence and reconnection at small scales in order to fully understand the mechanisms of energy dissipation and plasma heating in the solar wind.

Kinetic simulations of magnetic reconnection are often based on idealised conditions, such as the Harris current-sheet configuration (Shay et al., 2001; Scholer et al., 2003; Shay et al., 2004; Ricci et al., 2004b; Daughton et al., 2006, 2011; Liu et al., 2013; Leonardis et al., 2013; Goldman et al., 2016; Beresnyak, 2016). In this work, we study the formation of current structures and the occurrence of 3D magnetic reconnection as a result of turbulent dynamics in PIC simulations of collisionless anisotropic Alfvénic turbulence. We initialise our simulation with counter-propagating Alfvén

waves (see Sections 2.3 and 5.2) that then self-consistently interact and generate turbulence (Howes and Nielson, 2013b; Howes, 2015a) (see Section 4.2.1), current-sheet structures (Howes, 2016), and regions of magnetic reconnection. The overall objective of this work is to discover the properties of reconnection events that terminate the inertial-range cascade of solar-wind turbulence and define criteria that can identify such features in future 3D simulations and in spacecraft data. These results will allow future work to advance the study of linked reconnection and turbulence based on a solid and consistent framework of observable features. In Section 6.2, we describe our initial conditions for the simulation as well as our numerical setup. We present our results in Section 6.3 and our conclusions in Section 6.4.

## 6.2 Simulation Setup

We use the explicit Plasma Simulation Code (PSC, Germaschewski et al., 2016) to simulate eight anisotropic counter-propagating Alfvén waves in an ion-electron plasma. Since the theories of turbulence dissipation through reconnection in the solar wind are intrinsically connected to anisotropy through the generation of thin structures that form the precursors of current sheets, our initial waves are anisotropic. The anisotropy of the initial fluctuations is set up according to the theory of critical balance GS95. A detailed explanation of the initial conditions is presented in Section 5.2.

For this simulation, we set  $\beta_{s,\parallel} = 1$  and  $T_{s,\parallel}/T_{s,\perp} = 1$ . The magnetic field is normalised to the value of the constant background field  $B_0$  and the Alfvén speed ratio is  $v_A/c = 0.1$ . We use 100 particles per cell (100 ions and 100 electrons), a mass ratio of  $m_i/m_e = 100$  so that  $d_e = 0.1d_i$  as discussed in Section 5.3. The simulation box size has a size of  $L_x \times L_y \times L_z = 24d_i \times 24d_i \times 125d_i$ , and the spatial resolution is  $\Delta x = \Delta y = \Delta z = 0.06d_i$ . We use a time step of  $\Delta t = 0.06/\omega_{pi}$ . In our normalisation,  $\lambda_D = 0.07d_i$  defines the minimum spatial distance that needs to be resolved in the simulation. Although our numerical parameters  $V_A/c$  and  $m_i/m_e$  are not identical to the corresponding parameters in the solar wind, they allow us to perform simulations within the computational limitations. With these parameters, the simulated

electrons are mildly relativistic, which they are not in the real solar wind. However, the effect of mildly relativistic electrons on the propagation and damping of kinetic-scale normal modes, including kinetic Alfvén waves (KAWs), Alfvén/ion-cyclotron (A/IC) waves, and fast-magnetosonic/whistler (FM/W) waves, is negligible (Verscharen et al., 2020) and not important for the evolution of the turbulent cascade regardless of the processes that carry the cascade to sub-proton scales.

## 6.3 Results

In this section, we discuss the time evolution (Section 6.3.1) and the spectral properties of the turbulence in our simulation (Section 6.3.2). We then define a new set of indicators of reconnection based on 2D and 3D reconnection models and study a self-consistently formed reconnection region in detail (Section 6.3.3). We then record and discuss the plasma properties that an artificial spacecraft observes in the spacecraft frame as it passes through our simulation box (Section 6.3.4).

### 6.3.1 Time Evolution and Formation of Current Structures

We first identify a representative time  $t_R$  for our subsequent analysis of the turbulence properties. The root mean square (rms) of the current density  $J^{rms}$  is an indicator commonly used to identify the time at which the system reaches a quasi-stationary state. At this time, the generation of current sheets by waves is balanced by their decay so that the growth of  $J^{rms}$  saturates, which marks the time of maximum turbulent activity in the simulation (Franci et al., 2017). The rms of a quantity  $\psi$  is defined as

$$\psi^{rms} = \sqrt{\langle \psi^2 \rangle - \langle \psi \rangle^2}, \quad (6.1)$$

where  $\langle \dots \rangle$  represents the spatial average over the whole simulation domain. Figure 6.1 shows the time evolution of the rms of the current density  $\mathbf{J}$  (blue), the magnetic field  $\mathbf{B}$  (black), and the ion velocity  $\mathbf{v}_i$  (red) in our simulation. Since we start our simulation under the assumption that the linear time  $\tau_l$  is approximately equal to the nonlinear time  $\tau_{nl}$ , we estimate  $\tau_{nl} \sim \tau_l \sim 1/k_{\parallel} v_A \sim L_z/2\pi v_A \approx 200/\omega_{pi}$ . This estimate for the nonlinear time  $\tau_{nl}$  is therefore related to the scale of the initial

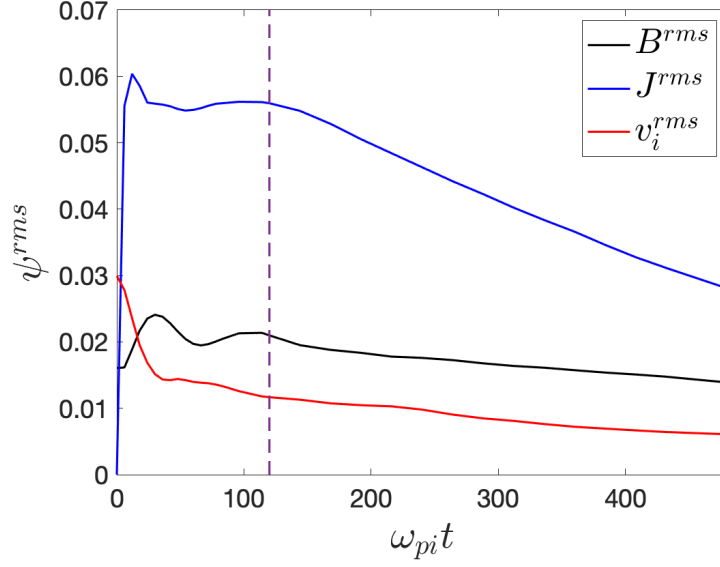
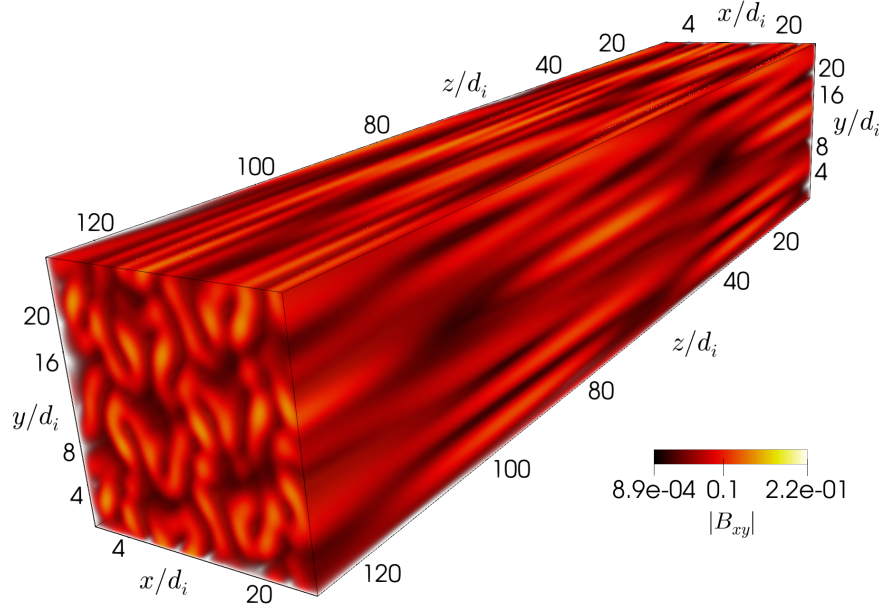


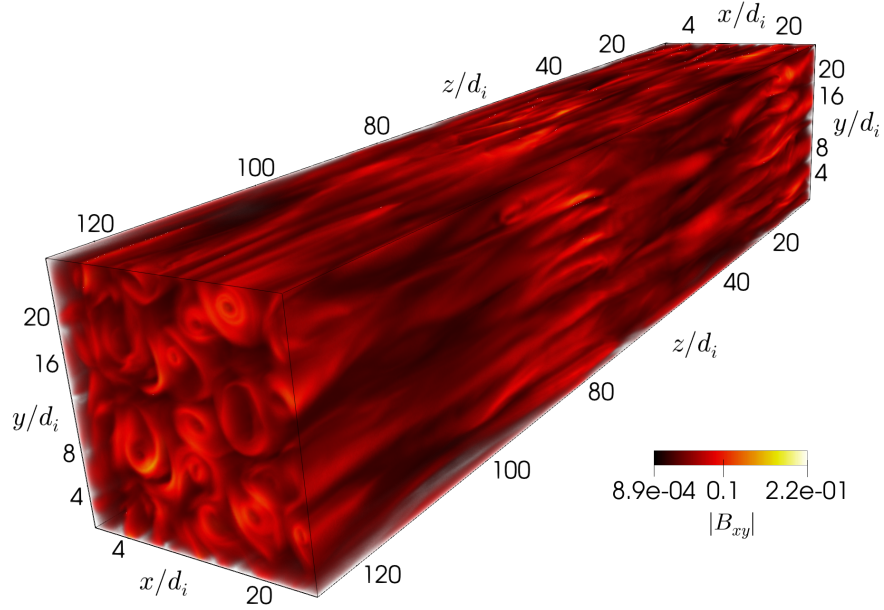
**Figure 6.1:** Time evolution of the rms of the current density  $\mathbf{J}$  (blue), magnetic field  $\mathbf{B}$  (black), and ion velocity  $\mathbf{v}_i$  (red). The vertical dashed line marks the time  $t_R = 120/\omega_{pi}$  at which  $J^{rms}$  begins to decrease.

fluctuations and represents an upper limit. We observe a peak in  $J^{rms}$  at  $t = 12/\omega_{pi}$  which is due to the self-consistent formation of current structures as a response to the initial magnetic-field fluctuations. The variation in  $B^{rms}$  and  $J^{rms}$  during the initial phase, between  $t = 12/\omega_{pi}$  and  $t = 96/\omega_{pi}$ , suggests that the system is still in a phase of self-adjustment. The formation of the plateau in  $J^{rms}$  at  $t \approx \tau_{nl}/2 \approx 100/\omega_{pi}$  indicates that the system has reached a quasi-stationary state. Therefore, we expect the formation of current structures such as current sheets and current filaments by this time. The vertical dashed line marks the time  $t = 120/\omega_{pi}$  at which  $J^{rms}$  begins to decrease monotonously until the simulation ends. In this sense, the time  $t = 120/\omega_{pi}$  represents the beginning of the decaying phase in our system. As the system evolves in time, current and magnetic structures dissipate, and we expect an exchange of the energy stored in the magnetic field with the kinetic energy of the particles. Based on these considerations, we use the time  $t = t_R = 120/\omega_{pi}$  to study the spectral properties of the turbulence in our system.

Figure 6.2 shows a 3D rendering of the magnitude of the transverse magnetic field  $|\mathbf{B}_{xy}| = \sqrt{B_x^2 + B_y^2}$  at two different time steps: panel (a) at  $t = 0$  and panel (b) at  $t = t_R$ . Panel (a) shows the anisotropic interference pattern of the linear superposi-



(a)



(b)

**Figure 6.2:** 3D rendering of the transverse magnetic field magnitude  $|\mathbf{B}_{xy}| = \sqrt{B_x^2 + B_y^2}$  at  $t=0$  (a) and  $t=t_R$  (b). The colour bar ranges from the minimum magnitude (black) to the maximum magnitude (yellow) throughout the simulation domain at  $t=t_R$ . We use the same colour bar in both panels for a direct comparison. The initial background magnetic field is directed along  $z$ -direction. At the initial time, the fluctuations are anisotropic and elongated along the  $z$ -direction. At  $t=t_R$ , small-scale magnetic eddies have formed and interact nonlinearly with each other. The eddies present varying cross section diameters  $L_D$  and lengths  $L_{\parallel}$ .



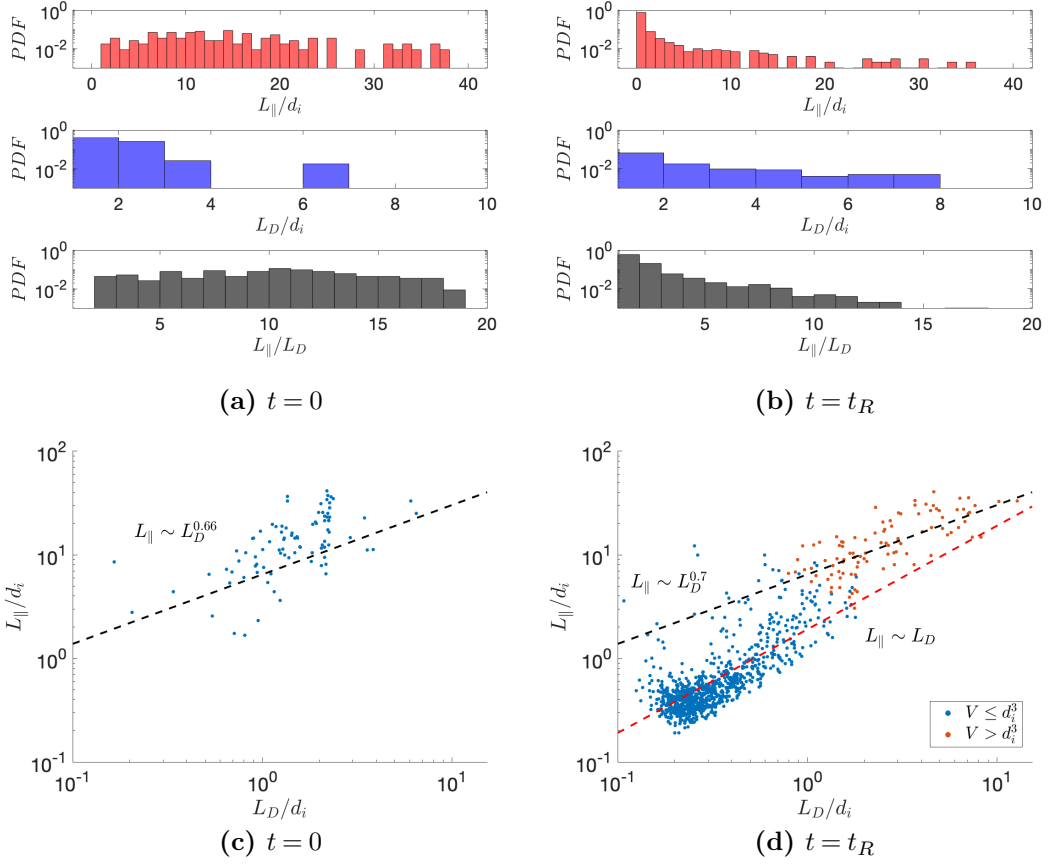
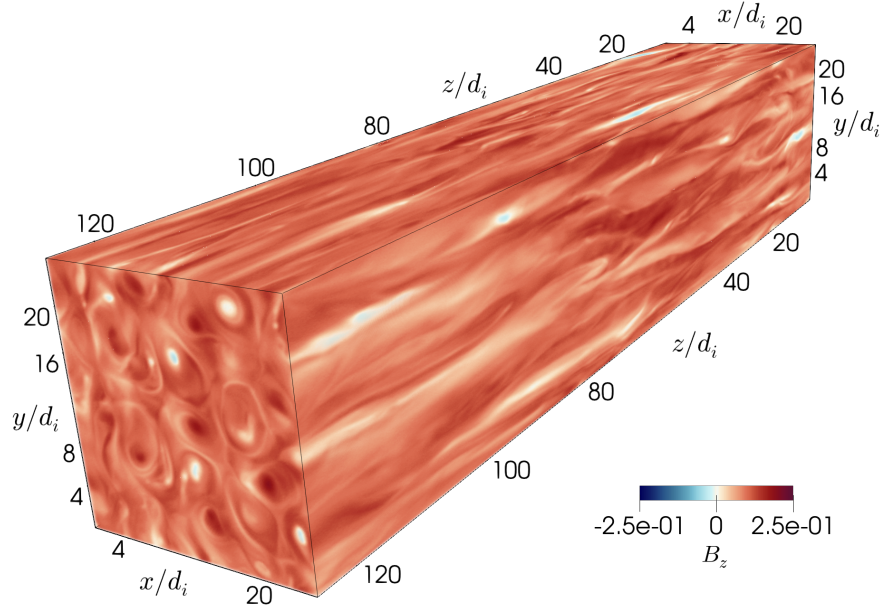
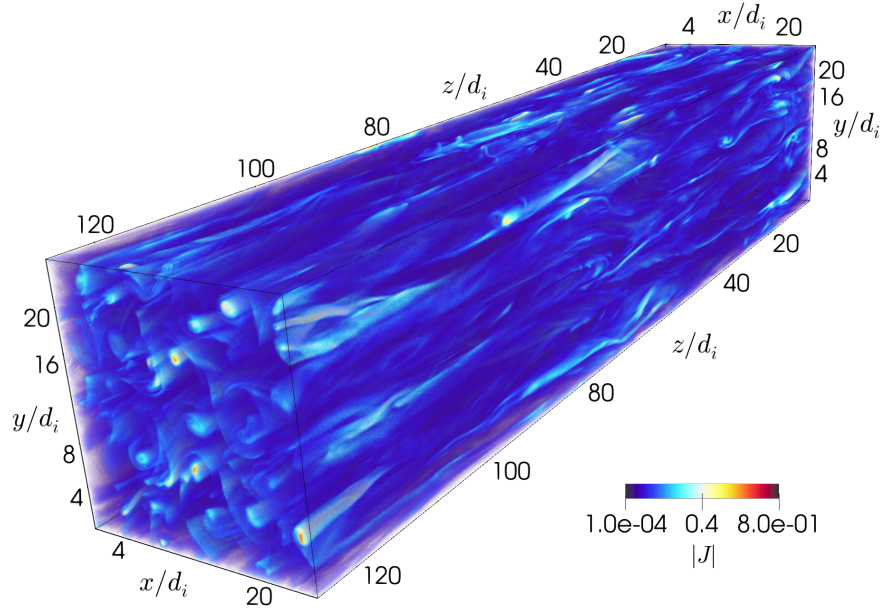


**Figure 6.3:** Panels (a) and (b): Probability distribution functions of elongations  $L_{\parallel}$  (top), cross section diameters  $L_D$  (middle), and aspect ratios  $L_{\parallel}/L_D$  (bottom) of the magnetic structures at  $t = 0$  (a) and  $t = t_R$  (b). Panel (c): Scaling between  $L_{\parallel}$  and  $L_D$  at  $t = 0$ . The black dashed line shows a linear fit. Panel (d): Scaling between  $L_{\parallel}$  and  $L_D$  of the large-scale population (orange) and small-scale population (blue) at  $t = t_R$ . The top black dashed line shows a linear fit to the former while the bottom red dashed line shows a linear fit to the latter.

tion of Alfvén waves at  $t = 0$ . Initially, there are no coherent eddies present because no nonlinear interaction has taken place yet. However, the initial magnetic-field fluctuations are already anisotropic. Panel (b) shows that, at time  $t = t_R$ , there is a clear presence of magnetic eddies with varying cross section diameters  $L_D$  and elongations  $L_{\parallel}$ , where  $L_{\parallel}$  represents the length of these eddies along the local magnetic field. Even though we start with a superposition of only eight waves, nonlinear interactions generate magnetic eddies of different shapes and anisotropies. At this time, the magnetic-field structures consist of a combination of linear fluctuations and magnetic eddies. To estimate the shape of the magnetic structures at  $t = 0$  and



(a)



(b)

**Figure 6.4:** Visualisations of the simulation domain at  $t = t_R$ . (a) 3D rendering of the magnetic-field component  $B_z$ . Blue represents negative, red positive and white zero values of  $B_z$ . The eddies' centres present different values of  $B_z$  with either positive or negative polarity. (b) 3D rendering of the magnitude of the current density  $|\mathbf{J}|$  from the same vantage point as (a). The colour represents in blue (red) the smallest (largest) values of  $|\mathbf{J}|$ . Filaments of intense current density are aligned with the eddies' centres. Current filaments and extended current-sheet-like structures are mainly elongated along the  $z$ -direction.

$t = t_R$ , we calculate

$$\Delta B = \sqrt{B_x^2 + B_y^2 + (B_z - B_0)^2} \quad (6.2)$$

and use an intensity threshold defined as

$$\Delta B > \langle \Delta B \rangle + 2\Delta B^{rms}. \quad (6.3)$$

We define a magnetic structure as the combination of those cells in our simulation that are connected as next neighbours and fulfil Eq. (6.3). The exact value of the threshold is chosen to improve the performance of the algorithm in the identification of these structures. After the identification of the structures, we calculate their principal axes. We define  $L_D = \sqrt{L_{\perp 1}^2 + L_{\perp 2}^2}$ , where  $L_{\perp 1}$  and  $L_{\perp 2}$  are the two orthogonal diameters in the plane perpendicular to the local magnetic field and  $L_{\parallel}$  is the axis along the local magnetic field.

Panel (a) of Figure 6.3 shows the probability distribution function (*PDF*) of  $L_{\parallel}$ ,  $L_D$ , and the aspect ratio  $L_{\parallel}/L_D$  at  $t = 0$  and panel (b) at  $t = t_R$ . The mean value and standard deviation of the distributions of  $L_{\parallel}$ ,  $L_D$ , and  $L_{\parallel}/L_D$  at  $t = 0$  are  $L_{\parallel} = (16.33 \pm 8.32)d_i$ ,  $L_D = (1.55 \pm 0.95)d_i$ , and  $(L_{\parallel}/L_D) = (11.01 \pm 7.06)d_i$ . At  $t = t_R$ , we find  $L_{\parallel} = (2.16 \pm 5.08)d_i$ ,  $L_D = (0.62 \pm 0.72)d_i$ , and  $L_{\parallel}/L_D = (2.55 \pm 1.94)d_i$ . This shows that the nonlinear interaction has formed magnetic structures with smaller elongations and cross section diameters continuously distributed between  $L_D = 1d_i$  and  $8d_i$ . The distribution of aspect ratios is less uniform at  $t = t_R$  than at  $t = 0$ . The number of magnetic structures with nearly isotropic aspect ratios is greater at  $t = t_R$ . To study the distribution of the large-scale structures at  $t = t_R$ , we further apply a filter to remove all regions with an equivalent volume  $V \leq 1d_i^3$ , where  $V$  is defined as the space filled by the sum of all contiguous cells associated with a given magnetic structure. For all structures with  $V > d_i^3$ , we find  $L_{\parallel} = (14.97 \pm 9.01)d_i$ ,  $L_D = (3.14 \pm 2.25)d_i$ , and  $L_{\parallel}/L_D = (5.46 \pm 2.48)d_i$ . The distribution of the large-scale magnetic structures maintains an anisotropy consistent with our initial conditions. Panel (c) of Figure 6.3 shows the scaling between  $L_{\parallel}$  and  $L_D$  for the magnetic

structures at  $t = 0$ . The linear fit to these structures, dashed line, reveals the scaling  $L_{\parallel} \sim L_D^{0.66}$  which is consistent with our initial anisotropy, i.e.,  $L_{\parallel} \sim L_D^{2/3}$ . Panel (d) of Figure 6.3 shows the scaling between  $L_{\parallel}$  and  $L_D$  for the magnetic structures at  $t = t_R$ . The orange dots represent the structures satisfying  $V > d_i^3$  while the blue dots show the structures satisfying  $V \leq d_i^3$ . The linear fit to the former population, top black dashed line, reveals the scaling  $L_{\parallel} \sim L_D^{0.7}$ . In contrast, the linear fit to the latter population, bottom red dashed line, shows the isotropic scaling,  $L_{\parallel} \sim L_D$ . Around  $L_D \sim d_i$ , we find a transition and mixing between structures with both scalings. This suggests that the large-scale structures tend to maintain the initial anisotropy while the small-scale structures become more isotropic. This isotropic scaling at sub-proton scales has also been observed in hybrid simulations (Franci et al., 2018; Arzamasskiy et al., 2019; Landi et al., 2019).

Figure 6.4 shows 3D renderings of  $B_z$  and  $|\mathbf{J}|$  at  $t = t_R$ . Panel (a) shows  $B_z$ , from the same vantage point as panel (b) of Figure 6.2. Although the initial  $\mathbf{B}_0$  is uniform and points into the  $+z$ -direction, nonlinear interactions generate regions in which  $B_z$  is negative. These regions are mostly localised in the centres of the small eddies in panel (b) of Figure 6.2. Panel (b) in Figure 6.4 shows that the locations of the most intense current filaments coincide with the centres of the magnetic eddies. Current filaments are intense quasi-cylindrical current structures. Similar to the case of the magnetic structures, we apply the threshold  $|J| \geq \langle |J| \rangle + 4(|J|)^{rms}$  to determine the shape of the current filaments. The mean cross section diameter of these current filaments is  $\hat{L}_D = (1.94 \pm 0.84)d_i$ . Their mean length is  $\hat{L}_{\parallel} = (12.32 \pm 6.70)d_i$ , and their mean aspect ratio is  $\hat{L}_{\parallel}/\hat{L}_D = (6.84 \pm 3.48)$ . The filaments are mostly elongated along the  $z$ -direction. Some filaments have undergone bending and twisting due to the nonlinear interactions. The elongations of the current filaments are distributed similarly to the elongations of the magnetic eddies (not shown here) and vary in the range of scales from  $\sim 4d_i$  to  $\sim 30d_i$ . Panel (b) shows in addition the formation of thin current-sheet-like structures at the edges of the eddies where the perpendicular component of the magnetic field is nearly zero (see panel (b) in Figure 6.2). We define current sheets as current structures in which  $L_{cs} \gg \delta_{cs}$  and  $\Delta_{cs} \gg \delta_{cs}$ , where

$L_{cs}$  is the current-sheet length along the local magnetic field,  $\Delta_{cs}$  is the current-sheet width tangential to the magnetic eddies, and  $\delta_{cs}$  is the current-sheet thickness normal to the edge of the eddies. The formation of these current sheets is due to the turbulent motions that “squeeze” the eddies together. In the supplementary material to the published paper (Agudelo Rueda et al., 2021), we provide a movie that shows the time evolution of the volume rendering of  $J_z$  in the  $zx$ -plane. We observe the tearing and breaking up of current sheets as well as the onset of instabilities arising from the nonlinear interactions and of jets oblique to the major axes of the current sheets as a result of the turbulent evolution. However, a detailed study of these phenomena is beyond the scope of this thesis.

### 6.3.2 Evidence of Turbulence in Our Simulation

A broad power-law spectrum of the fluctuations indicates the presence of turbulence as the energy cascades from large to small scales (see Chapter 4). Following Franci et al. (2018), we use the formalism introduced in Section 5.3.1 to analyse the spectral properties of the system. We note that the local (rather than the global) average magnetic field defines the cylindrical symmetry axis for the turbulent fluctuations (Cho and Vishniac, 2000). However, we use the global background magnetic field as a proxy for the local field. This simplification is motivated by the strong alignment of the eddies with the background magnetic field at this time in our simulation (see Figures 6.2 and 6.4). Moreover, the definition of the local magnetic field is a matter of ongoing research and debate (Podesta, 2009; Chen et al., 2011; TenBarge et al., 2012; Oughton et al., 2015; Gerick et al., 2017), and the development of an anisotropic energy cascade is sufficient for the determination of reconnection events in the present study.<sup>1</sup> Thus, we compute the reduced 2D power spectral density  $P_{2D}^\psi(k_\perp, k_\parallel)$  using Eq. (5.38).

Figure 6.5 shows the logarithm of the 2D reduced power spectral density of the magnetic-field fluctuations  $P_{2D}^B$  normalised to  $\max P_{2D}^B$  in the  $k_\parallel$ - $k_\perp$  plane at  $t = 0$  (panel (a)),  $t = 12/\omega_{pi}$  (panel (b)),  $t = t_R$  (panel (c)), and  $t = 240/\omega_{pi}$  (panel (d)).

---

<sup>1</sup>An analysis of the fluctuations with respect to the local magnetic field based on second-order structure functions supports this assumption and is provided in Appendix A.

The horizontal dashed line marks  $k_{\perp}d_e = 1$  which corresponds to  $k_{\perp}d_i = 10$  owing to our mass ratio of  $m_i/m_e = 100$ . The vertical dashed line marks  $k_{\parallel}d_i = 1$ . At  $t = 0$ , the energy is entirely stored in the initial modes. At  $t = 12/\omega_{pi}$ , the isocontours show that the energy has already cascaded to  $k_{\perp}d_e > 1$  whereas the parallel cascade has not yet reached the kinetic range. At  $t = t_R$ , the perpendicular cascade has not proceeded any further but the parallel energy transport reached  $k_{\parallel}d_i > 1$ . At  $t = 240/\omega_{pi}$ , the energy distribution has not considerably changed compared to the distribution at  $t = 120/\omega_{pi}$ . For comparison with analytical predictions, we overplot the expected critical-balance scaling of  $k_{\perp} \sim k_{\parallel}^{3/2}$  (see Section 4.2.3) as a dashed line at small  $k_{\perp}$ . We note, however, that  $P_{2D}^B$  exhibits a broad distribution in  $\mathbf{k}$ -space around this prediction.

In order to explore the anisotropy of the cascade in more detail, we compute the perpendicular one-dimensional reduced power spectral density using Eq. (5.39) and the parallel one-dimensional reduced power spectral density using Eq. (5.40) of multiple fluctuating quantities  $\psi$ . Panel (a) in Figure 6.6 shows the perpendicular one-dimensional reduced power spectral density of the magnetic-field fluctuations  $P_{1D_{\perp}}^B$  (black line), of the ion velocity fluctuations  $P_{1D_{\perp}}^{v_i}$  (red line), and of the ion density fluctuations  $P_{1D_{\perp}}^{n_i}$  (blue line) at  $t = t_R$ . The vertical dashed lines mark  $k_{\perp}d_i = 1$ ,  $k_{\perp}d_e = 1$ , and  $k_{\perp}\lambda_D = 1$ . The enhancement in  $P_{1D_{\perp}}^{v_i}$  at  $k_{\perp}d_i = 17$  is an artefact created by Debye-length effects and the finite spatial resolution of the system. The scale of the initial waves in the perpendicular direction coincides with the transition point of the energy cascade from inertial to kinetic scales, i.e.,  $k_{\perp}d_i = 1$ . Therefore, our simulations do not describe the cascade at  $k_{\perp}d_i \leq 1$ . During the first nonlinear time, the system develops a broadband spectrum of perpendicular density fluctuations in the kinetic range.  $P_{1D_{\perp}}^B$  and  $P_{1D_{\perp}}^{v_i}$  exhibit similar spectral indices in part of the kinetic range between  $k_{\perp}d_i \sim 3$  and  $\sim 6$ . Within the same interval,  $P_{1D_{\perp}}^{n_i}$  follows a steeper spectrum. These features suggest the presence of both Alfvénic and compressive fluctuations, consistent with the presence of kinetic Alfvén waves.  $P_{1D_{\perp}}^B$  in the interval  $k_{\perp}d_i \sim 1.8$  to  $\sim 7$ , follows a power-law scaling with a spectral slope of  $-3$ . In the range between  $k_{\perp}d_i \sim 7$  and  $\sim 20$ , the slope is slightly steeper with

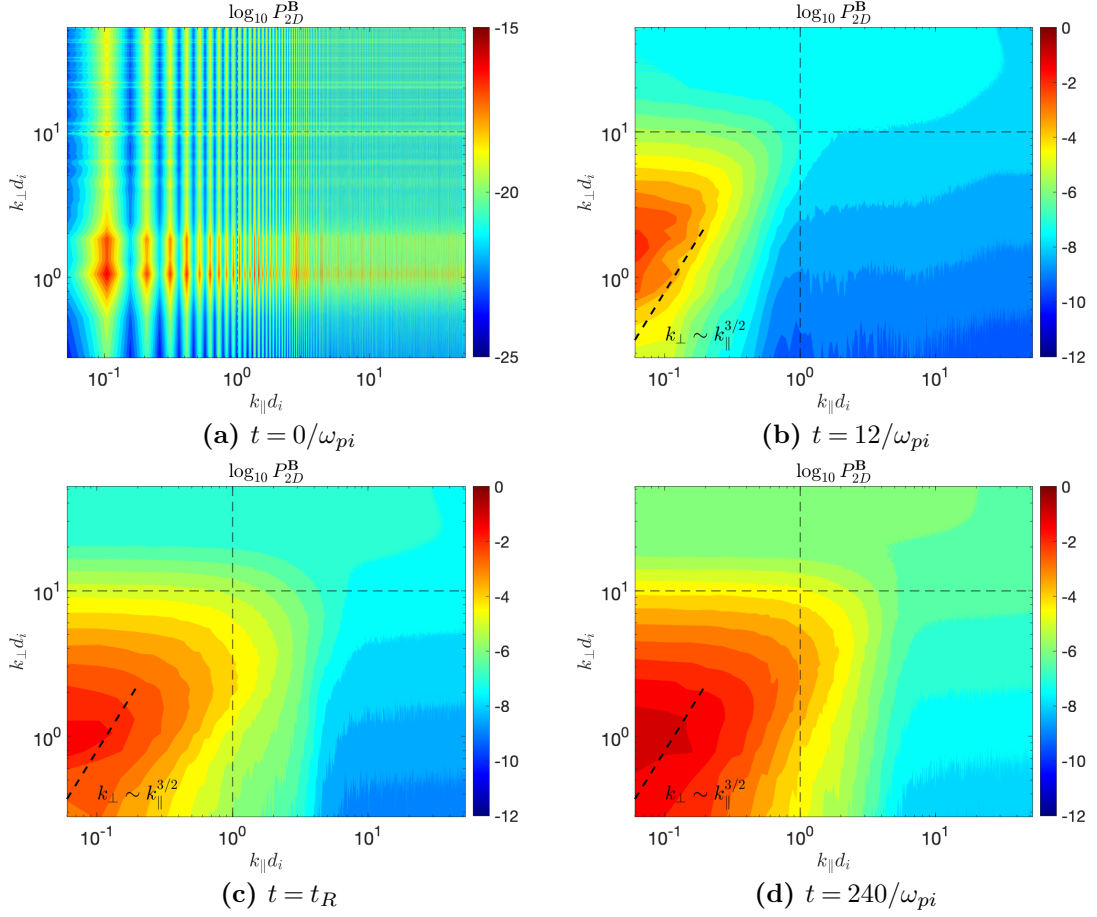


**Figure 6.5:** Isocontours of  $\log_{10} P_{2D}^B$  of the fluctuating magnetic field as a function of  $k_{\parallel}$  and  $k_{\perp}$  at different time-steps. The dashed lines provide a reference for the scaling of  $k_{\perp}$  and  $k_{\parallel}$ . The horizontal (vertical) dashed line marks  $k_{\perp} d_e = 1$  ( $k_{\parallel} d_i = 1$ ). At  $t = 0$ , the spectrum shows the modes of our initialisation and their Fourier harmonics. At  $t = 12/\omega_{pi}$ , the cascade in the perpendicular direction (vertical axis) has proceeded beyond electron scales ( $k_{\perp} d_i \geq 10$ ). At  $t = t_R$ , although the perpendicular cascade has not proceeded significantly further, the cascade in the parallel direction (horizontal axis) has reached the kinetic range ( $k_{\parallel} d_i \approx 1$ ) up to ion scales but not to electron scales. At  $t = 240/\omega_{pi}$  the distribution has not considerably changed compared to  $t = t_R$ .

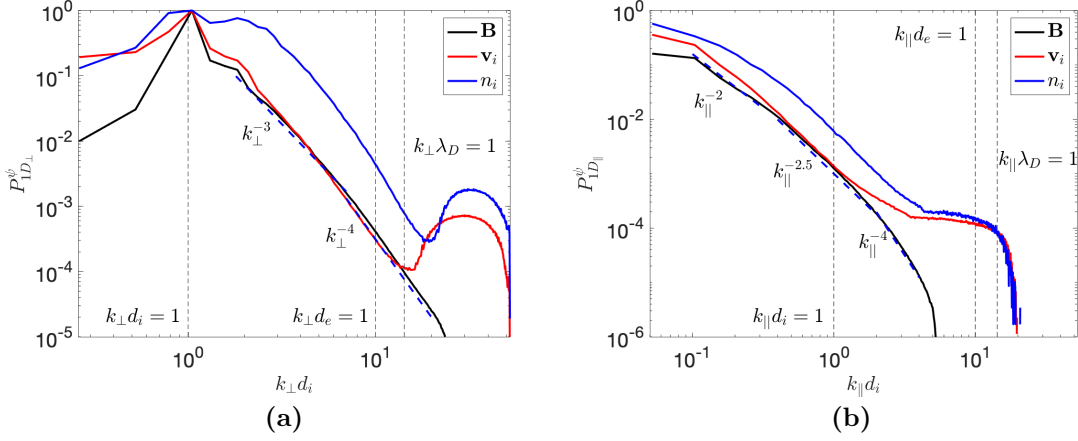


**Figure 6.6:** (a) Perpendicular and (b) parallel reduced one-dimensional power spectral densities  $P_{1D\parallel,\perp}^B$  (black),  $P_{1D\parallel,\perp}^{v_i}$  (red), and  $P_{1D\parallel,\perp}^{n_i}$  (blue) at  $t = t_R$ . The vertical dashed lines indicate  $k_{\parallel,\perp} d_i = 1$ ,  $k_{\parallel,\perp} d_e = 1$ , and  $k_{\parallel,\perp} \lambda_D = 1$ .

a power index of approximately  $-4$ <sup>2</sup>. Although we calculate the energy spectrum of the magnetic-field fluctuations using the global background magnetic field, these values are within the range of slope variability measured in the solar wind (Chen et al., 2010a; Bruno et al., 2014) as well as in hybrid simulations (Franci et al., 2018; González et al., 2019).

Panel (b) in Figure 6.6 shows the parallel one-dimensional reduced power spectral density of the magnetic-field fluctuations  $P_{1D\parallel}^B$  (black line), ion velocity fluctuations  $P_{1D\parallel}^{v_i}$  (red line), and ion density fluctuations  $P_{1D\parallel}^{n_i}$  (blue line) at  $t = t_R$ . The vertical dashed lines mark  $k_\parallel d_i = 1$ ,  $k_\parallel d_e = 1$ , and  $k_\parallel \lambda_D = 1$ . At  $k_\parallel d_i \leq 1$ ,  $P_{1D\parallel}^B$  and  $P_{1D\parallel}^{v_i}$  follow a similar trend as expected for Alfvénic turbulence. The spectral slope for  $P_{1D\parallel}^B$  is close to  $-2$  between  $k_\parallel d_i \sim 0.1$  and  $\sim 0.3$  which is in agreement with the magnetic-field power spectrum  $k_\parallel^{-2}$  observed in the solar wind (Bavassano and Bruno, 1989; Grappin et al., 1991; Wicks et al., 2010, 2011; Chen et al., 2011). At smaller parallel scales, the spectrum steepens to  $-2.5$  between  $k_\parallel d_i \sim 0.4$  and  $\sim 2$ , and further towards  $-4$  between  $k_\parallel d_i \sim 2$  and  $\sim 4$ . Both the perpendicular and parallel spectral indices have values of  $-4$ . The equality of these exponents has been observed

<sup>2</sup>We note that we observe a change in slope within a single decade in  $k_\perp$ . The change in slope over such a small range of scales must be interpreted with caution. Although it indicates a steepening in  $P_{1D\perp}^B$  towards increasing  $k_\perp$ , the scale separation is insufficient to apply Kolmogorov-like scaling arguments to these spectral slopes.



in 3D hybrid PIC simulations and has been suggested to be a consequence of the anisotropy being frozen at sub-proton scales (Franci et al., 2018; Arzamasskiy et al., 2019; Cerri et al., 2019; Landi et al., 2019). Although we initialise the system with non-compressive waves, the simulation swiftly develops a cascade of density fluctuations which suggests that compressive modes form self-consistently in the energy cascade. The development of compressive fluctuations has been suggested to depend on the plasma parameters rather than the initial conditions (Cerri et al., 2017a). The level of compressive fluctuations in our simulation is greater than observed in the solar wind (Chen, 2016), but the reasons for the creation of such strong compressive fluctuations is unknown. At  $k_{\parallel}d_i \approx 1.4$ , the slope of  $P_{1D_{\parallel}}^{v_i}$  separates from the slope of  $P_{1D_{\parallel}}^{\tilde{B}}$  and approaches the slope of  $P_{1D_{\parallel}}^{n_i}$ . The flattening of  $P_{1D_{\parallel}}^{n_i}$  at  $k_{\parallel}d_i \approx 4$  is due to finite particle noise.

### 6.3.3 Reconnection Sites

In this section, we confirm that magnetic reconnection occurs in our simulation domain. Methods to find reconnection sites in 2D simulations are based on the identification of magnetic islands and their closest x-point within a current sheet (Wan et al., 2014; Papini et al., 2019a). However, the interaction of magnetic structures such as flux tubes, which are the 3D equivalent of 2D magnetic islands, is more complex than in the 2D case, and magnetic reconnection does not happen at a single point but in an extended region (Daughton et al., 2011; Liu et al., 2013; Daughton et al., 2014). In 2D and 3D theories of reconnection, strong current sheets are often associated with reconnection events as the key locations of energy dissipation. However, there are events in which the x-points are not placed exactly within the current-sheet (Priest and Démoulin, 1995; Wan et al., 2014). The presence of a strong guide magnetic field and asymmetries of the reconnection event can shift the position of the x-point and even preclude the occurrence of the reconnection event (Eastwood et al., 2010, 2013). Moreover, proton temperature anisotropies in reconnection events can trigger kinetic instabilities, which then have a stabilising effect on the current sheet (Matteini et al., 2013).

In our turbulent simulation setup, we expect that, once the reconnection events oc-

curred, most of them exhibit local asymmetries due to the turbulent nature of the domain. Moreover, the background magnetic field acts as a guide field in reconnecting flux ropes. Therefore, in order to capture all reconnection events in such a complex and asymmetric field geometry, we require a new method to determine reconnection sites in our 3D simulations. Strong gradients in at least one component of the magnetic field as well as magnetic null points are common features of both 2D and 3D reconnection events. Strong gradients are directly related to the presence of current sheets according to Ampère’s law. The presence of magnetic null points is not a requirement for reconnection. In 2D reconnection, for instance, the presence of a guide field removes this requirement (Hesse et al., 2004). 3D reconnection, on the other hand, can take place in collapsing structures that form current sheets related to quasi-separator lines, which do not require magnetic null points (Pritchett and Coroniti, 2004; Pontin, 2011), see Section 3.3.1. Exhaust regions in which particles are accelerated to velocities near the Alfvén speed are another common feature. Magnetic reconnection not only accelerates particles but also increases their thermal energy. Hence, an enhancement in the population of heated particles is a further indicator of reconnection as long as it occurs near a region in which accelerated particles and magnetic field gradients are present.

During magnetic reconnection, the electric field is responsible for the energy exchange between particles and fields in the current sheet. The associated heating is quantified by  $\mathbf{J} \cdot \mathbf{E}$  (Somov and Titov, 1985; Ni et al., 2016). We expect to find coherent regions in the simulation domain in which  $\mathbf{J} \cdot \mathbf{E}$  is non-zero. According to 3D steady-state theories of magnetic reconnection (Hesse and Schindler, 1988; Priest et al., 2003; Pontin, 2011), when a magnetic field line enters a diffusion region, the integral of the parallel electric field ( $E_{\parallel} = \mathbf{E} \cdot \mathbf{B}/|\mathbf{B}|$ ) along the magnetic field line within the diffusion region must be different from zero. Since a non-zero  $E_{\parallel}$  can indicate the presence of non-vanishing diffusive terms in Ohm’s law (see Section 3.1), we use the presence of non-zero  $E_{\parallel}$  as a possible indicator for a diffusion region located within a finite volume. Although  $E_{\parallel}$  is not a good indicator in the absence of a guide magnetic field, we expect to find coherent regions in the simulation domain

with non-zero  $E_{\parallel}$ .

In summary, we identify the following indicators that we consider essential for the presence of reconnection in a region of our simulation domain. We adopt a clustering detection method (Uritsky et al., 2010) based on the mean value of each quantity  $\psi$ , its rms value  $\psi^{rms}$ , and a threshold value  $N_{th}$ . Thus, we search the simulation domain for regions in which  $\psi \geq \langle \psi \rangle + N_{th}(\psi)^{rms}$ . Our indicators for magnetic reconnection are:

- C1 Current-density structures,  $|\mathbf{J}| \geq \langle |\mathbf{J}| \rangle + N_{th}(|\mathbf{J}|)^{rms}$ ; <sup>3</sup>
- C2 Fast ions and electrons,  $|\mathbf{v}_{i,e}| \geq \langle |\mathbf{v}_{i,e}| \rangle + N_{th}(|\mathbf{v}_{i,e}|)^{rms}$ ;
- C3 Heated particles,  $T_{i,e} \geq \langle T_{i,e} \rangle + N_{th}(T_{i,e})^{rms}$ ;
- C4 Energy transfer between fields and particles,  $|\mathbf{J} \cdot \mathbf{E} - \langle \mathbf{J} \cdot \mathbf{E} \rangle| \geq N_{th}(|\mathbf{J} \cdot \mathbf{E}|)^{rms}$ ;
- C5 Non-zero parallel electric fields,  $|E_{\parallel} - \langle E_{\parallel} \rangle| \geq N_{th}(|E_{\parallel}|)^{rms}$ .

To find the number of events satisfying these conditions, we use the first-neighbour volumetric method described in Section 6.3.1. We apply the algorithm to identify clusters of contiguous cells fulfilling each condition separately as well as combinations of them. Afterwards, we apply a filter to remove all regions with an equivalent volume  $V \leq 1d_i^3$ , where  $V$  is defined as the sum of the volumes of all contiguous cells associated with the cluster. This is motivated by the fact that we are mostly interested in events in which both ions and electrons experience reconnection. Therefore, we expect to find coherent regions with a size of at least  $d_i^3$ . We analyse two values for the threshold:  $N_{th} = 3$  and  $N_{th} = 4$ .

We present our results in Table 6.1, where C2<sub>i</sub> and C2<sub>e</sub> refer to the separate application of criterion C2 to ions and to electrons respectively. The same definitions apply

---

<sup>3</sup>We note that given the ambiguity in the definition of current sheets when studying observational data, the indicator C1 can be defined with  $\nabla \times \mathbf{B}$  instead of  $|\mathbf{J}|$ .

$N_{th}$	C1	C2 <sub>e</sub>	C2 <sub>i</sub>	C3 <sub>e</sub>	C3 <sub>i</sub>	C4 <sub>+</sub>	C4 <sub>-</sub>	C5 <sub>+</sub>	C5 <sub>-</sub>
3	149	144	77	92	82	68	77	0	0
4	97	92	29	50	39	23	17	0	0

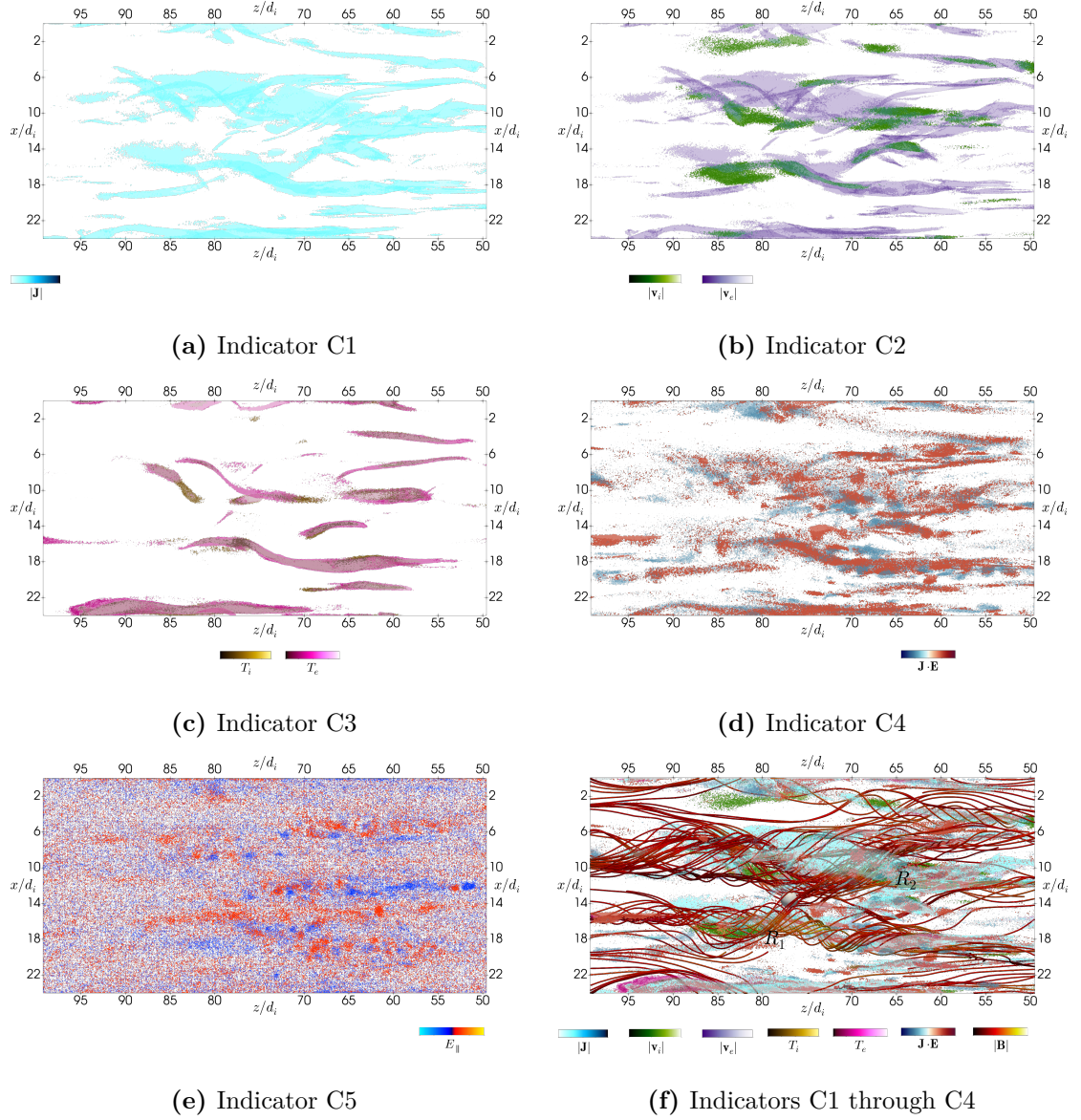
  

$N_{th}$	C1 & C2 <sub>i,e</sub>	C1 & C3 <sub>i,e</sub>	C1 – C3 <sub>i,e</sub>	C1 – C4 <sub>-</sub>	C1 – C4 <sub>+</sub>
3	34	55	24	3	3
4	9	27	6	6*	6*

**Table 6.1:** Number of events in our simulation domain at time  $t = t_R$  fulfilling each of our criteria for reconnection.

to C3. C4<sub>+</sub> and C4<sub>-</sub> refer to the application of condition C4 separated by cases in which  $\mathbf{J} \cdot \mathbf{E} > 0$  (+) and  $\mathbf{J} \cdot \mathbf{E} < 0$  (-). The same definitions apply to C5. As expected, a larger number of locations fulfil these conditions if the threshold is lower. Moreover, all events detected with  $N_{th} = 4$  are also detected when using  $N_{th} = 3$ . There are no events that fulfil our condition C5. The reason for this result is that, although local regions fulfil C5, the size of contiguous volumes of cells fulfilling C5 are never greater than  $1d_i^3$ . We attribute this effect to particle noise, which has a strong effect on parallel electric fields in PIC simulations. If we reduce the threshold to  $N_{th} = 2$ , the algorithm is also unable to define clusters of cells, because our method is based on intensity thresholds which perform well for quantities with heavy-tail distributions. The distribution of  $E_{\parallel}$  in our simulation is spread with  $\langle |E_{\parallel}| \rangle = 2.0 \times 10^{-3} B_0 c$  and standard deviation  $(|E_{\parallel}|)_{std} = 1.5 \times 10^{-3} B_0 c$ . The same argument applies to  $\mathbf{J} \cdot \mathbf{E}$ . Despite detecting at least 17 regions fulfilling C4 with  $N_{th} = 4$ , there are no regions that satisfy all conditions C1 through C4 within a volume greater than  $1d_i^3$ . However, if we reduce the equivalent volume threshold to  $0.3d_i^3$ , we find 6 regions that fulfil conditions C1 through C4. We mark the corresponding numbers with an asterisk in Table 6.1.

In Figure 6.7, we visualise our indicators for magnetic reconnection. We use a 2D projection on the  $zx$ -plane of a part of our simulation domain,  $50d_i < z < 100d_i$ . Panel (a) shows the isosurfaces of  $|\mathbf{J}| = \langle |\mathbf{J}| \rangle + 3(|\mathbf{J}|)^{rms}$  (indicator C1) colour-coded in light blue. The selected structures mainly correspond to current filaments. Panel (b) shows regions in which  $|\mathbf{v}_i| = \langle \mathbf{v}_i \rangle + 3(\mathbf{v}_i)^{rms}$  (green) and  $|\mathbf{v}_e| = \langle \mathbf{v}_e \rangle + 3(\mathbf{v}_e)^{rms}$  (purple), our indicator C2. The locations of fast electrons according to C2 coincide



**Figure 6.7:** Reconnection indicators projected onto a 2D cut in the  $zx$ -plane at  $y = 21d_i$ . (a) Indicator C1: Isosurfaces of  $|\mathbf{J}| = \langle |\mathbf{J}| \rangle + 3(|\mathbf{J}|)^{rms}$  (light blue). (b) Indicator C2: Isosurfaces of  $|\mathbf{v}_{i,e}| = \langle \mathbf{v}_{i,e} \rangle + 3(\mathbf{v}_{i,e})^{rms}$  for ions (green) and for electrons (purple). (c) Indicator C3: Isosurfaces of  $T_{i,e} = \langle T_{i,e} \rangle + 3(T_{i,e})^{rms}$  for ions (gold) and for electrons (pink). (d) Indicator C4: Isosurfaces of  $\mathbf{J} \cdot \mathbf{E} = \langle \mathbf{J} \cdot \mathbf{E} \rangle \pm 3(\mathbf{J} \cdot \mathbf{E})^{rms}$  for positive  $\mathbf{J} \cdot \mathbf{E}$  (red) and negative  $\mathbf{J} \cdot \mathbf{E}$  (blue). (e) Indicator C5: Isosurfaces of  $E_{\parallel} = \langle |E_{\parallel}| \rangle \pm 2(|E_{\parallel}|)^{rms}$  for positive  $E_{\parallel}$  (orange) and negative  $E_{\parallel}$  (blue). Panel (f) shows, on top of the isosurfaces related to indicators C1 through C4, magnetic field lines colour-coded with  $|\mathbf{B}|$ . The magnetic field lines suggest the reconnection of a twisted flux rope with an adjacent flux rope. The white sphere of radius  $1d_i$  at  $(z, x) = (77, 13.5)d_i$  in panel (f) is a reference point that marks the position of a reconnection site. In panel (f), we also indicate the regions  $R_1$  and  $R_2$  defined in the text.

with the locations of large currents according to C1, since the electrons are the main carriers of the electric current. This electron behaviour is consistent with observations in space plasma and reproduced in simulations (Phan et al., 2018). We identify five structures in which accelerated ions coincide with our condition C1. Panel (c) shows isosurfaces of  $T_i = \langle T_i \rangle + 3(T_i)^{rms}$  (gold) and  $T_e = \langle T_e \rangle + 3(T_e)^{rms}$  (pink), according to our indicator C3. Although the electric current is mostly carried by electrons, we find current structures that are not associated with high-temperature electrons and vice-versa. The structures associated with heated electrons have mostly filamentary shapes. Panel (d) shows the application of our indicator C4. The regions in which  $\mathbf{J} \cdot \mathbf{E} = \langle \mathbf{J} \cdot \mathbf{E} \rangle \pm 3(\mathbf{J} \cdot \mathbf{E})^{rms}$  is positive (negative) are colour-coded in red (blue). There are large and diffuse clusters of positive and negative  $\mathbf{J} \cdot \mathbf{E}$  between  $z = 55d_i$  and  $z = 85d_i$ . We also locate filamentary structures of positive  $\mathbf{J} \cdot \mathbf{E}$  which partially coincide with the regions fulfilling C3. Panel (e) shows our indicator C5. The regions in which  $E_{\parallel} = \langle |E_{\parallel}| \rangle \pm 2(|E_{\parallel}|)^{rms}$  is positive (negative) are colour-coded in orange (blue). The effect of particle noise on the electric field leads to difficulties in the determination of the associated clusters. Panel (f) shows the combination of our indicators C1 through C4. We define two regions,  $R_1$  and  $R_2$ , as the regions in which our indicators C1 through C4 are fulfilled. This suggests that magnetic reconnection is taking place in the vicinity of these regions.

To visualise the change of magnetic connectivity, we trace magnetic field lines in our simulation domain. The region of most intense  $|\mathbf{B}|$  is co-located with  $R_1$ . The magnetic field lines suggest the reconnection of a twisted flux rope with an adjacent flux rope. The white sphere of radius  $1d_i$  at  $(z, x) = (77, 13.5)d_i$  is a reference region that marks the position at which the magnetic field lines associated with the flux ropes exchange connectivity. We provide a movie to support this claim in the supplementary material of the paper (Agudelo Rueda et al., 2021). The change of connectivity between the flux ropes lasts for  $\sim 96/\omega_{pi} \sim 0.46\tau_{nl}$ , which is a long time compared to the time the turbulent cascade requires to develop. The long existence of connectivity exchange and of the current structure can be associated with the suppression of nonlinearities in the current sheet. In 2D geometries, the rate of

magnetic-flux change between two magnetic islands, the so-called reconnection rate, is determined by the electric field at the x-point (Smith et al., 2004; Servidio et al., 2011). It can also be computed as the difference in the out-of-plane component of the magnetic vector potential between the x-point and the o-point (Franci et al., 2017; Papini et al., 2019a). In 3D, the reconnection rate can be computed by integrating  $E_{\parallel}$  along the magnetic field lines crossing the diffusion region (Schindler et al., 1988; Pontin, 2011). However, the complex structure of the field lines makes it unclear how to apply this method to our type of simulations (Liu et al., 2013; Daughton et al., 2014). An extension of 2D methods that avoid the use of the electric field (Franci et al., 2017; Papini et al., 2019a) to the 3D case requires the calculation of the vector potential which (a) is elaborate in 3D PIC simulations of the type used in this study and (b) impractical in the comparison with spacecraft data.

As the flux rope twists, it bends towards the region of changing magnetic connectivity, henceforth we refer to this region as the “x-region”. During the flux-rope bending, plasma ions are accelerated towards the x-region. To illustrate this behaviour, we visualise the streamlines of the ion and electron bulk velocities that leave the reconnection region. Panel (a) in Figure 6.8 shows a view over an  $xy$ -plane cut of  $J_z$ . Gray colour represents negative values, red colour represents positive values, and white indicates a value of zero for  $J_z$ . The displayed streamlines of the ion bulk velocity emerge from the centre of the x-region. The streamlines are colour-coded with  $v_{ix}$ . The dark-blue segment near the dark-gray region indicates that the ions primarily move towards the reconnection site in the negative  $x$ -direction. As the ions approach the x-region, their speed decreases, and their trajectories are deflected into the  $y$ -direction. The displayed streamlines maintain a coherent shape of width  $\sim 2d_i$  along the  $z$ -direction. Panel (c) shows the same ion velocity streamlines but over an  $zx$ -plane cut of  $J_z$ . The region where ions have large  $|v_{ix}|$  coincides with the core of the twisted flux rope in panel (f) of Figure 6.7 (black region) which suggests that they are accelerated by the bending of the flux rope.

Considering the ion velocity streamlines as indicative of the shape of the exhaust region associated with the x-region, the branch of the stream lines on the right-hand



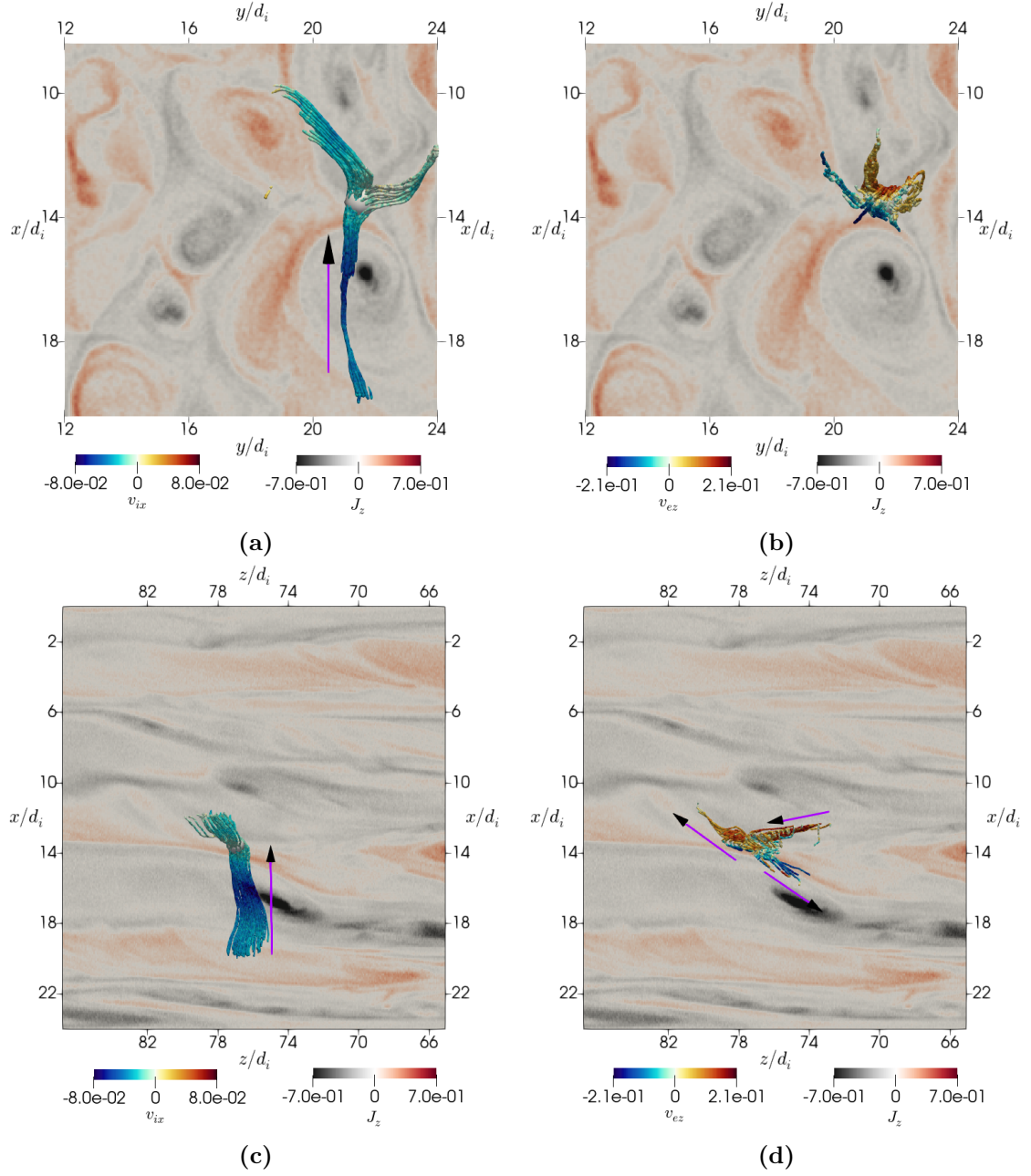


**Figure 6.8:** Streamlines of the ion and electron bulk velocities over 2D cuts of the simulation plane showing  $J_z$ . (a) and (b) view over the  $xy$ -plane in which the  $x$ -direction points downward and the  $y$ -direction points towards the right-hand side. (c) and (d) view over the  $xz$ -plane in which the  $x$ -direction points downward and the  $z$ -direction points towards the left-hand side. (a) and (c) show ion bulk velocity streamlines colour-coded with  $v_{ix}$ . (b) and (d) show electron velocity streamlines colour-coded with  $v_{ez}$ . The arrows indicates the direction of the ion bulk motion and of the electron bulk motion.



side in panel (a) represents the reconnection exhaust of the event. It is three-dimensional and asymmetric. Likewise, the electron motion associated with the x-region is asymmetric. However, it differs considerably from the ion motion. Panel (b) shows the electron velocity streamlines colour-coded with  $v_{ez}$  in the same view as in panel (a). These streamlines remain contained within a smaller region compared to the ion streamlines. They are mainly aligned with the  $z$ -direction. On the left-hand side of the reconnection site in panel (d), the electron streamlines are directed along the  $J_z$  structure as expected since the current is mostly (but not entirely) carried by electrons. In contrast, on the right-hand side of the reconnection site, the electrons move in directions towards and away from the reconnection site as is shown by the arrows. Considering the electron velocity streamlines, the electron exhaust is also asymmetric and three-dimensional but smaller than the ion exhaust. The diffusion region associated with the x-region of the reconnection event is likely to be the large structure of positive  $J_z$  crossing the x-region in the  $z$ -direction in panel (c). The shape of the electron streamlines suggests a diffusion region that resembles the distorted diffusion region observed in 3D Hall magnetic reconnection (Drake et al., 2008; Yamada et al., 2014).

In summary, our set of criteria suggests the presence of multiple reconnection sites in our simulation domain. Our automated identification based on our criteria allows for a detailed inspection of the magnetic-field connectivity of each event. Our method searches for clusters of cells fulfilling all conditions. This approach misses events in which ions and electrons are accelerated and heated in different locations near the reconnection site. If the event is large enough to affect both ions and electrons, we expect streams of accelerated particles for both species related to the reconnection event. Given the variability in the shape and size of these particle outflows, the volume threshold must be adjusted depending on the problem at hand in different simulation setups.

### 6.3.4 1D Trajectories Across the Reconnection Region

In-situ measurements of spacecraft typically record the plasma and magnetic-field fluctuations along the spacecraft trajectory. In order to compare such measurements

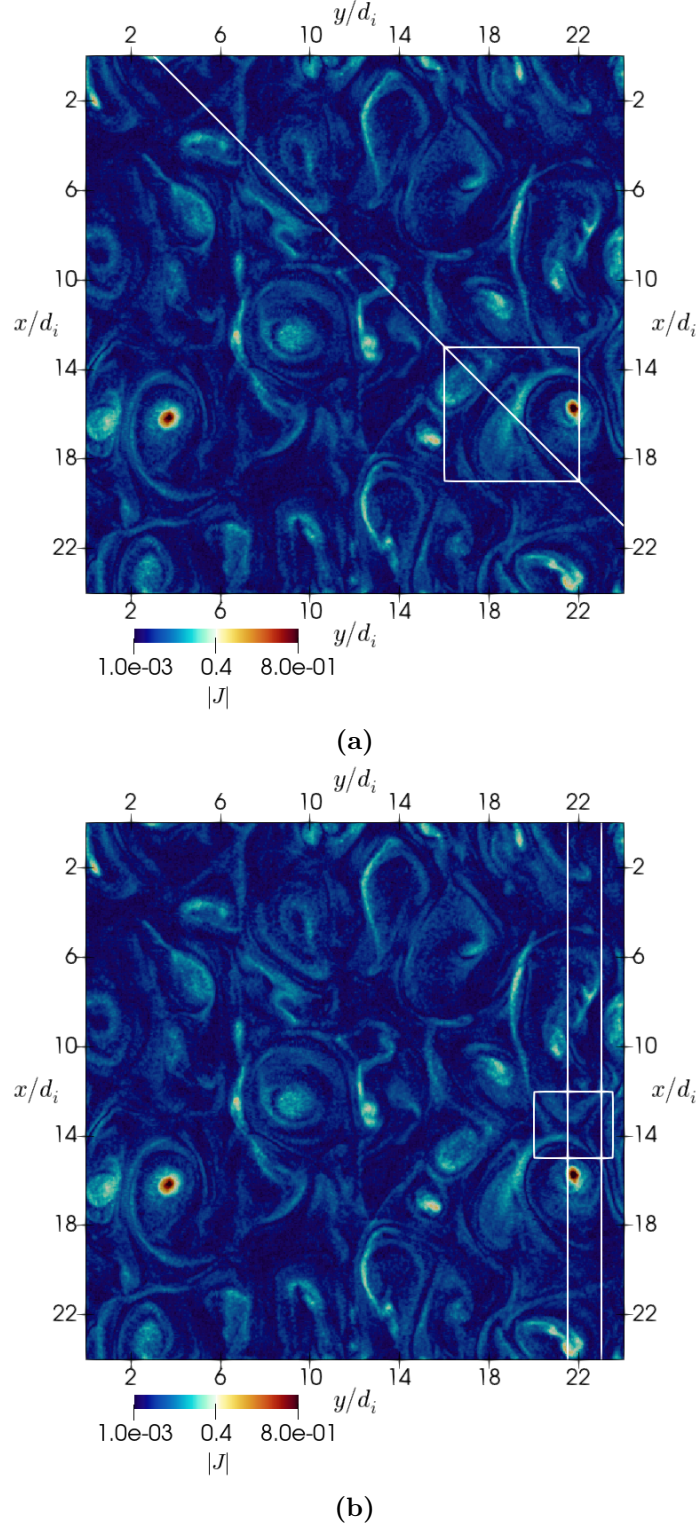
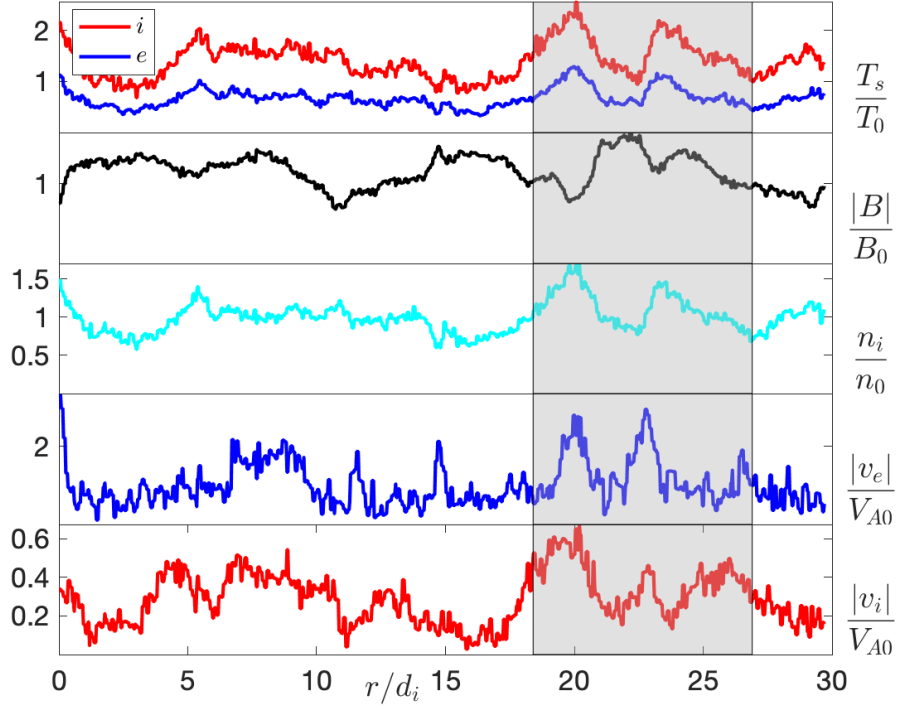
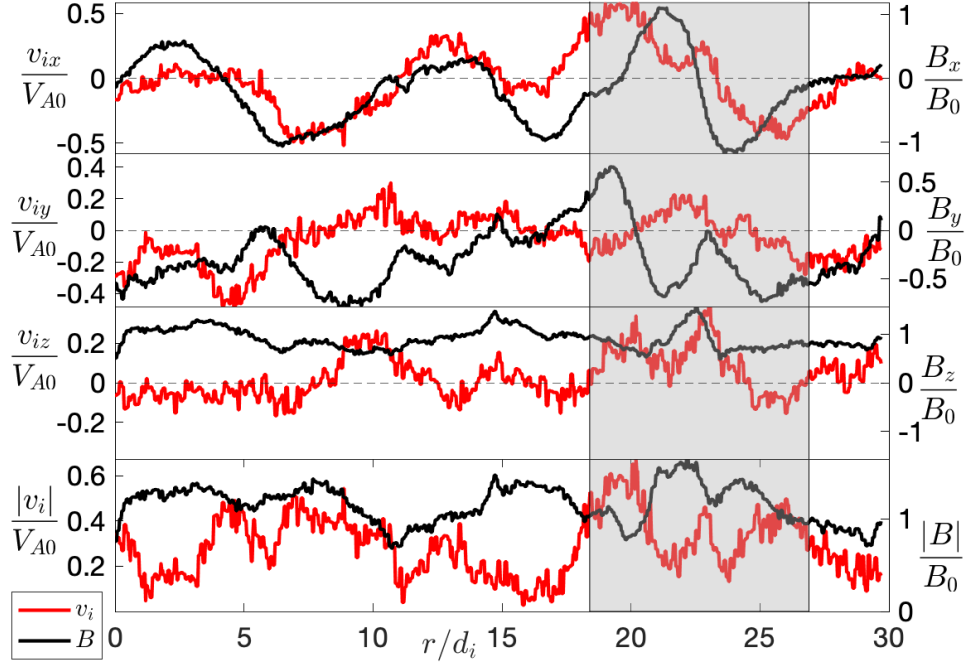


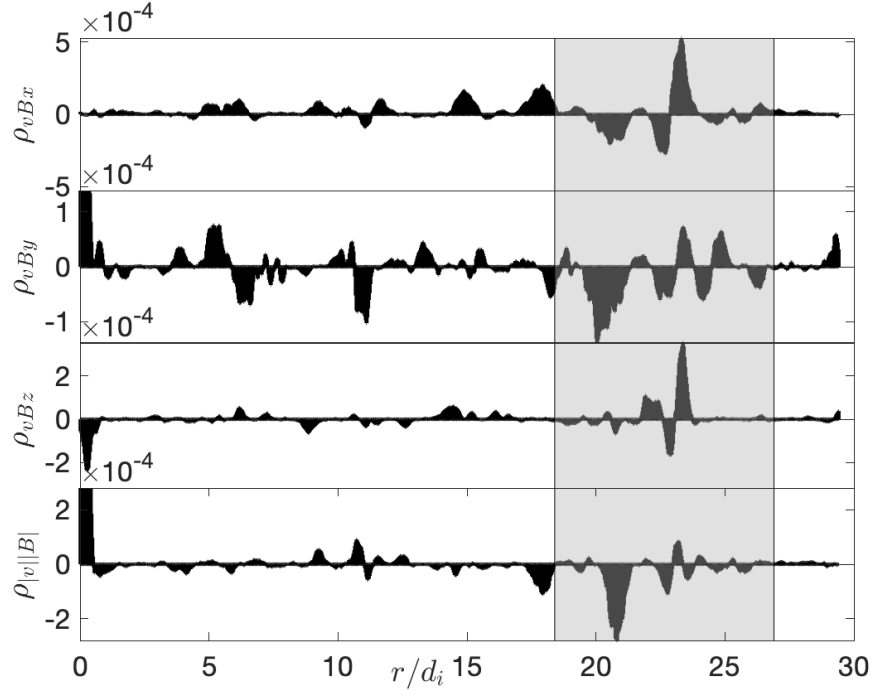
**Figure 6.9:** Trajectories of an artificial spacecraft crossing our simulation domain. (a) Trajectory  $T1$ . The spacecraft moves from the top-left corner to the bottom-right corner. This trajectory crosses a region that we identify as a reconnection exhaust. (b) Trajectories  $T2$  and  $T3$  are parallel to each other. The former crosses through the reconnection site while the latter passes right outside of the reconnection site.



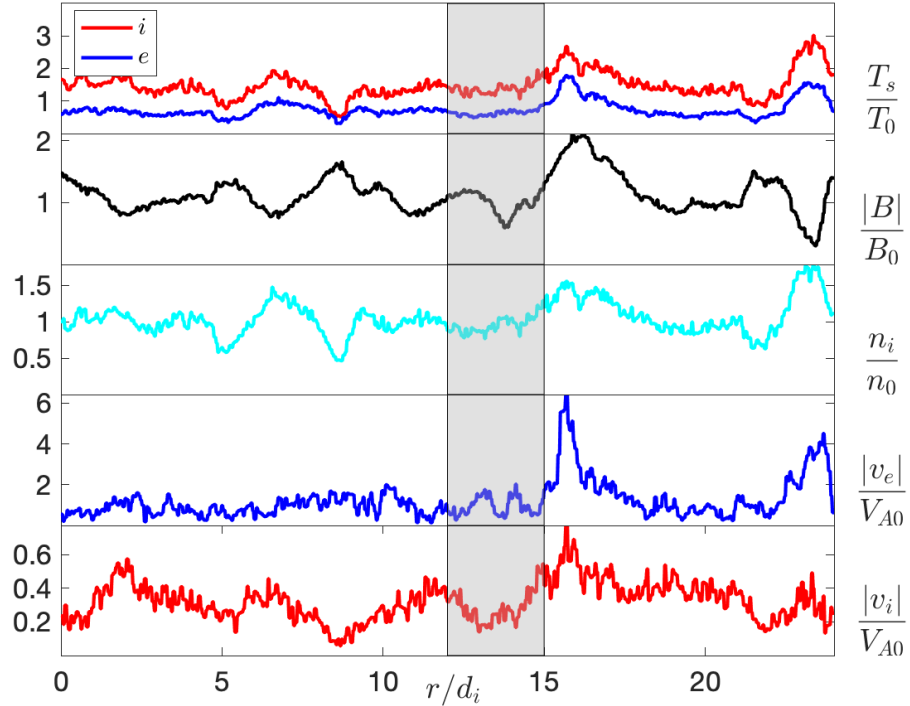
(a) Particle temperature  $T_{i,e}$ , magnetic field  $B$ , ion density  $n_i$ , and particle speed  $v_{i,e}$  normalised as described in the text. The shaded areas mark the data recorded within the white squares in panel (a) of Figure 6.9.



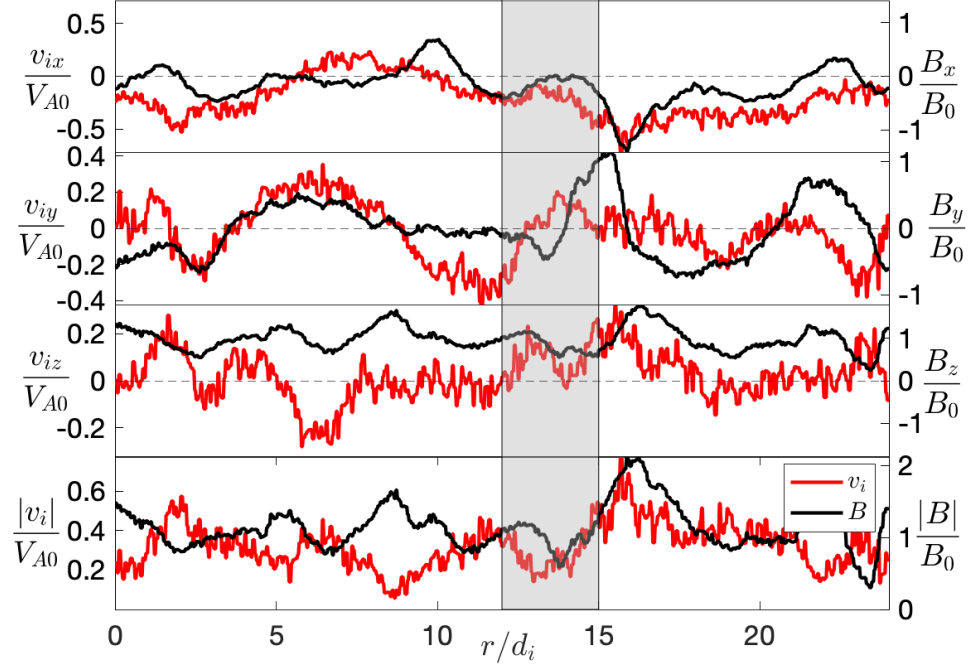
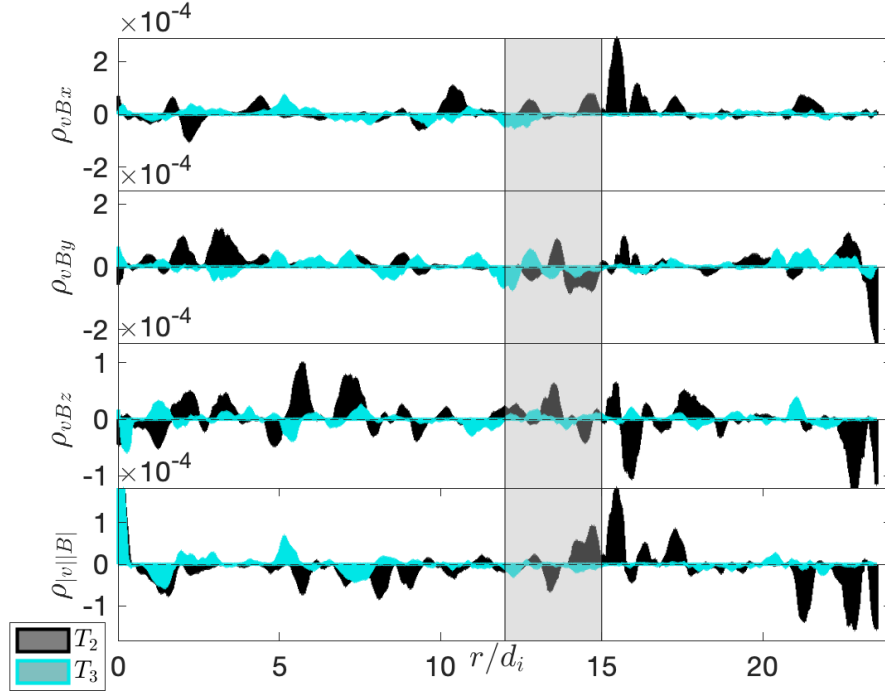
(b) Components of the magnetic field (black) and ion velocity (red) for  $T1$ .



(c) Derivative correlations  $\rho_{v_i B}$  and  $\rho_{|v||B|}$  for trajectory  $T1$ .



(d) Particle temperature  $T_{i,e}$ , magnetic field  $B$ , ion density  $n_i$ , and particle speed  $v_{i,e}$  normalised as described in the text. The shaded areas mark the data recorded within the white squares in panel (b) of Figure 6.9.

(e) Components of the magnetic field (black) and ion velocity (red) for  $T2$ .(f) Derivative correlations  $\rho_{v_i B}$  and  $\rho_{|v||B|}$  for trajectories  $T2$  and  $T3$ .**Figure 6.10:** Plasma and magnetic-field fluctuations associated with our trajectories  $T1$  and  $T2$ .

with our 3D simulations, we “fly” an artificial spacecraft through our simulation box along three trajectories,  $T1$ ,  $T2$ , and  $T3$ , and record the plasma and magnetic-field fluctuations along these trajectories. According to Taylor’s hypothesis, we assume that the plasma structures are static as they are convected over the spacecraft with the average solar-wind bulk speed. The trajectories are taken within the  $xy$ -plane and are shown as the white lines in Figure 6.9.

The trajectory  $T1$ , shown in panel (a) of Figure 6.9, passes close to the reconnection site when it crosses the white square, although it does not carry the spacecraft right through the centre of the x-region. Panel (a) of Figure 6.10 shows the plasma and magnetic-field fluctuations for our trajectory  $T1$ . We normalise these quantities to their initial values at the beginning of the simulation. Thus, the ion and electron temperatures are normalised to  $T_0$ . The magnetic field and its components are normalised to the initial background magnetic field  $B_0$ . The ion density is normalised to the initial density  $n_0$ . The ion and electron velocities are normalised to the initial Alfvén speed  $v_{A0}$ . The shaded area in panel (a) of Figure 6.10 represents the region delimited by the white square in panel (a) of Figure 6.9. The ion and electron temperatures are positively correlated with each other as well as with the density across this trajectory. The magnetic-field and ion-density fluctuations exhibit mainly anti-correlation with each other across the trajectory. This correlation directly reflects the presence of slow-mode-like compressive fluctuations. The electron speed shows local peaks at  $r \sim 11d_i$  and  $r \sim 15d_i$  with no associated peaks in ion speed. This behaviour suggests the presence of local mechanisms that accelerate electrons only. This behaviour resembles “electron-only reconnection events” (Phan et al., 2018; Stawarz et al., 2019; Sharma Pyakurel et al., 2019; Mallet, 2020). However, our indicators show that both ions and electrons interact with this reconnection region.

When the artificial spacecraft trajectory  $T1$  enters the region marked with the white square in panel (a) of Figure 6.9, it encounters a coherent structure which exhibits an enhancement in the ion and electron temperatures by a factor of about 1.5 to 2 compared to the background level at  $r \sim 20d_i$ . At this position, the spacecraft observes a decrease in the magnetic field associated with an increase in the particle

speed as well as an increase in the particle density. These are characteristic features associated with slow-mode-like fluctuations and shocks. Since in the trajectories shown in this section the particle bulk speed is always less than the local magnetosonic speed, these events are not slow-mode shocks but rather fluctuations with a slow-mode-like polarisation. At  $r \sim 22d_i$ , there is a slight enhancement in the electron speed which corresponds to the spike within the two large eddies seen in the white square in panel (a) of Figure 6.10. At  $r \sim 23d_i$ , the spacecraft observes another slow-mode-polarised region which corresponds to the large structure in the middle of the square. According to the [Petschek \(1964\)](#) model of magnetic reconnection, the exhaust of particles is limited by a pair of slow-mode shocks. However, in recent studies of reconnection in the solar wind ([Phan et al., 2006, 2009](#); [Gosling, 2012](#)), the boundaries of reconnection exhausts often lack these features. Instead, exhausts are typically characterised through a rotation in the magnetic field along with a change in the sign of the correlation between the particle speed and the magnetic field ([Gosling, 2012](#); [Phan et al., 2020](#)), consistent with our simulation results.

Panel (b) of Figure 6.10 shows from top to bottom  $B_x$ ,  $B_y$ ,  $B_z$ , and  $|B|$  in black as well as  $v_{ix}$ ,  $v_{iy}$ ,  $v_{iz}$ , and  $|v_i|$  in red for trajectory *T1*. In the shaded area (i.e., near the reconnection site), the velocity component  $v_{ix}$  changes its sign between  $r \sim 19d_i$  and  $r \sim 25d_i$ , while  $\mathbf{B}$  undergoes a partial rotation. During the same interval,  $v_{iy}$  shows little variation and  $B_{iy}$  reverses its sign. Since the background magnetic field dominates  $B_z$ , the variations in the magnetic components  $B_x$  and  $B_y$  are more pronounced than the variations in  $B_z$ . As seen in the profile of  $v_{iz}$ , although ions are mostly stationary in the direction parallel to the background magnetic field, they are accelerated in the parallel direction near the slow-mode-like fluctuations. We note that the velocity spikes and magnetic-field drop-offs seen in the  $z$ -component of  $\mathbf{B}$  to a certain degree resemble the properties of the magnetic-field switchbacks observed in the solar wind ([Kasper et al., 2019](#); [McManus et al., 2020](#)). Moreover, the blue regions in panel (a) of Figure 6.4 suggest the possibility of magnetic reversals within the simulation domain. A comparison and further study is required to establish a potential correspondence between our simulation and observational data.



To visualise the correlation between the magnetic-field and velocity components, we define the derivative correlation between the two variables  $v_j$  and  $B_j$  as

$$\rho_{vBj} = \frac{\Delta v_j}{\Delta r} \frac{\Delta B_j}{\Delta r}, \quad (6.4)$$

where  $\Delta r$  is a distance increment,  $\Delta v_j = v_j(r + \Delta r) - v_j(r)$ , and  $\Delta B_j = B_j(r + \Delta r) - B_j(r)$ . We use  $\Delta r = 0.6d_i$  to reduce the effect of noise when calculating the derivative while keeping the spatial step small to cover small-scale fluctuations. Panel (c) of Figure 6.10 shows from top to bottom  $\rho_{vBx}$ ,  $\rho_{vBy}$ ,  $\rho_{vBz}$ , and  $\rho_{|v||B|}$  for trajectory *T1*, where  $\rho_{|v||B|}$  is defined accordingly with the magnitudes of  $\mathbf{v}$  and  $\mathbf{B}$ . The  $v_{ix}$  and  $B_x$  components exhibit mostly positive correlation along the trajectory. However, there are two strong peaks of anti-correlation within the shaded area. Likewise, the  $v_{iy}$  and  $B_y$  components show more variability in the correlations from positive and negative derivative correlations within the shaded area than outside the area. This is due to the transit of the artificial spacecraft through the slow-mode-like fluctuations. In particular, around  $r = 23d_i$ , all three components present a change from anti-correlation to positive correlation. The presence of a pair of slow-mode-like fluctuations along with a magnetic-field rotation suggests that this region is indeed an exhaust region similar to those reported in previous observational studies in the solar wind (Gosling, 2012).

Trajectory *T2* (the white line on the left in panel (b) of Figure 6.9) carries the spacecraft right through the centre of the x-region. In panel (d) of Figure 6.10, at  $r \sim 5d_i$  and  $r \sim 9d_i$ , the artificial spacecraft records particle temperature minima associated with density cavities as well as local peaks in the magnetic field. As the spacecraft moves towards the x-region, within the shaded region, the particle temperature remains approximately constant. There is a local minimum in the magnetic field which corresponds to the centre of the x-region at  $r = 14d_i$ . On either side of the x-region, we find small enhancements in the electron speed. These peaks, in addition to the electron streams in panel (d) of Figure 6.8, suggest the presence of electron-only streams in the vicinity of the x-region. The ion speed decreases as the spacecraft enters the x-region and increases as the spacecraft leaves the x-



region. After leaving this region, the spacecraft encounters the highly twisted flux rope at  $r = 16d_i$ , where it records an enhancement in all bulk quantities as well as in the magnetic field. The pair formed by the x-region and the closest twisted flux rope resembles the pairs of x-points and magnetic islands known from 2D models of reconnection. At the end of the trajectory, at  $r \sim 23d_i$ , the spacecraft encounters a slow-mode-polarised structure which corresponds to the bright structure in the right-bottom-corner in panel (b) of Figure 6.9. Panel (e) of Figure 6.10 shows the components of the magnetic field and ion bulk velocity for trajectory *T2*. From  $r = 10d_i$  to  $r = 16d_i$ ,  $B_x$  changes polarity, and from  $r = 8d_i$  to  $r = 15d_i$ ,  $B_y$  undergoes a partial rotation. The change in the sign of  $v_{iy}$  at the point where the spacecraft enters the shaded area and its value of approximately zero at the point where it leaves the shaded area in *T2* shows a local stream of particles leaving the region along the  $y$ -direction. This corresponds to the right-hand side branch of the ion streamline velocity in panel (a) of Figure 6.8. At  $r = 13d_i$ ,  $v_{iz}$  presents a mild peak corresponding to a weak current sheet. Entering the shaded area and up to  $r \sim 19d_i$ ,  $v_{ix}$  is negative along *T2* consistent with the stream of ions described in Figure 6.8.

Trajectory *T3* is parallel to trajectory *T2*, and the separation of these trajectories is  $1.5d_i$ . Along trajectory *T3*,  $B_z$  and  $B_y$  as well as  $v_{iz}$  and  $v_{iy}$  follow approximately similar behaviours (not shown here). However, the local variations along *T2* are more pronounced as this trajectory crosses through the centres of multiple structures. Panel (f) shows the derivative correlation of the magnetic field and velocity components for trajectories *T2* (black) and *T3* (cyan). Trajectory *T2* shows stronger positive and negative correlations in all components due to the transit through the structures. For the  $x$ -component, the peak of positive correlation corresponds to the transit through the flux rope which is associated with particle acceleration.

## 6.4 Discussion and Conclusions

The nonlinear interaction of the anisotropic waves self-consistently creates Alfvénic turbulence and generates magnetic-field and current-density structures such as current filaments and current sheets as part of the turbulent cascade ([Howes and Niel-](#)

son, 2013b; Howes, 2015a, 2016). The initial scaling between  $L_{\parallel}$  and  $L_D$ , for the magnetic structures, is  $L_{\parallel} \sim L_D^{2/3}$ . At  $t = t_R$ , the magnetic structures satisfying  $V > d_i^3$  maintain an anisotropy consistent with the initial conditions and follow a  $L_{\parallel} \sim L_D^{0.7}$  scaling. Although theoretical predictions including those based on intermittency (Boldyrev and Perez, 2012; Boldyrev and Loureiro, 2019), kinetic simulations (Cerri et al., 2017b, 2019), and observations in the solar wind (Wang et al., 2020) suggest the scaling  $L_{\parallel} \sim L_D^{2/3}$  at sub-proton scales, our analysis of structures with  $V \leq d_i^3$  is more consistent with an isotropic scaling  $L_{\parallel} \sim L_D$  which has been observed in hybrid simulations as well (Franci et al., 2018; Arzamasskiy et al., 2019; Landi et al., 2019). The change of anisotropy over time (Figure 6.3) is also observed in the evolution of the 2D reduced power spectral density (Figure 6.5). The anisotropy initially decreases due to the change in the mean value of the distribution of cross-section diameters and of the elongation of the magnetic structures.

The spectral index of the corresponding perpendicular 1D power spectrum of the magnetic-field fluctuations in the kinetic range varies between  $-3$  and  $-4$ . Meanwhile, the spectral index of the parallel power spectrum of the magnetic-field fluctuations varies from  $-2$  in the interval  $0.1 \lesssim k_{\parallel} d_i \lesssim 0.3$  to  $-4$  at sub-proton scales. These results show that the simulation develops an anisotropic turbulent cascade and the associated 3D structures predicted to contribute to reconnection as a dissipation mechanism for turbulence.

The critical-balance theory of Alfvénic turbulence has been tested using gyrokinetic simulations (Howes et al., 2008a; TenBarge and Howes, 2012) and 3D PIC simulations (Grošelj et al., 2018). The evolution and morphology of 3D reconnection events, starting from a Harris current-sheet configuration, have been studied at kinetic scales (Hesse et al., 2001b; Pritchett and Coroniti, 2001; Wiegmann and Büchner, 2001; Lapenta et al., 2006; Vapirev et al., 2013; Liu et al., 2013; Muñoz and Büchner, 2018; Lapenta et al., 2020), as has been the effect of turbulence on the development of reconnection events (Daughton et al., 2014; Lapenta et al., 2015; Pucci et al., 2017; Papini et al., 2019b). However, little attention has been given to the occurrence of small-scale reconnection as a product of the turbulent cascade

in a fully 3D geometry. Our study contributes to the understanding, identification, and to the knowledge of the geometry of these reconnection events.

We identify three regions that fulfil our set of indicators C1 through C4 for  $N_{th} = 3$  and have an equivalent volume greater than  $1d_i^3$ . We also illustrate the working of our method in a subset of our simulation domain. We inspect the time evolution of the magnetic field lines and observe the change of connectivity between a highly twisted flux rope and a less twisted flux rope. We find a good agreement between the geometry of the flux ropes formed by turbulence in our simulation with the flux ropes formed by the turbulent disruption of a Harris current sheet (Daughton et al., 2011). We observe the occurrence of a complex reconnection event in which the region of changing connectivity (x-region) has a volume of  $\sim 12.5d_i^3$ . This event dissipates turbulent fluctuations in current structures of order a few  $d_i$  which are smaller than the smallest events recently observed in the solar wind (Phan et al., 2020) and different from the events observed in space which are mostly very large interface regions between plasmas (Phan et al., 2006; Gosling, 2007).

Recent studies show the presence of reconnection events in the turbulent magnetosheath (Phan et al., 2018; Stawarz et al., 2019). Most of these events are reconnection-only events in which there are no associated ion flows. Numerical studies support the occurrence of predominantly electron-only events from a turbulent cascade (Franci et al., 2022). Kinetic-scale current sheets whose thickness is  $\sim 0.1 - 10d_i$  have been recently identified in the solar wind (Lotekar et al., 2022). The occurrence of electron-only reconnection (Phan et al., 2018; Stawarz et al., 2019), electron-scale turbulent fluctuations and kinetic scale current sheets suggests that events as the one we describe take place in the solar wind as well as in the magnetosheath.

Although there is good agreement between studies using the Harris configuration and solar-wind observations (Mistry et al., 2016), our event is considerably more complex than the idealised steady and non-turbulent Harris current-sheet configuration often invoked to study magnetic reconnection. The shape of our reconnection region is

asymmetric, and the regions in which particle heating and acceleration occur are mostly associated with current filaments rather than current sheets. This suggests that the twist of the flux ropes plays a crucial role for the particle heating in our simulation. In addition, this finding supports the notion that reconnection events occur in the solar wind through small-scale flux ropes (Crooker et al., 1996; Moldwin et al., 2000).

We trace 1D artificial-spacecraft trajectories across the simulation domain to study the fluctuations in the bulk quantities  $n_i$ ,  $\mathbf{v}_{i,e}$ ,  $T_{i,e}$ , and  $\mathbf{B}$ . These samplings may facilitate direct comparisons between our simulations and spacecraft observations in the solar wind. Our trajectories  $T1$  and  $T3$  pass near the identified reconnection region, and our trajectory  $T2$  crosses through the centre of the x-region. We observe the presence of slow-mode-polarised fluctuations as anti-correlated fluctuations in  $n_i$  and  $|B|$ , rotations in the magnetic field, and changes in the sign of the correlation between the magnetic field and the ion velocity consistent with reconnection exhausts observed in the solar wind (Gosling, 2012). Our artificial-spacecraft trajectory  $T2$  (panel (d) in Figure 6.10) shows an enhancement in all bulk quantities, which may be associated with a reconnecting flux rope. Moreover, this trajectory suggests that the encounter of a magnetic minimum followed by an enhancement in all bulk quantities may be associated with the encounter of an x-region and a flux rope. Such a pair x-region/flux-rope corresponds to the traditional pair x-point/o-point in 2D models of reconnection. It would be worthwhile to compare our simulated spacecraft trajectories with spacecraft observations of small-scale reconnection events and reconnection exhausts in the solar wind. The instrumentation onboard Solar Orbiter and Parker Solar Probe has the appropriate time resolution for such a comparison.

In our reconnection event, ions and electrons behave differently as shown in Figure 6.8. Both ions and electrons move towards and away from the x-region but in different directions. Our trajectories in the vicinity of the reconnection event suggest that the slow-mode-like features associated with the partial rotation in the magnetic field and the change in the  $\mathbf{v}_i$ - $\mathbf{B}$  correlation are also present in these spontaneously created small-scale events.

The finite number of particles per cell has an important effect on the determination of coherent regions of strong  $E_{\parallel}$ , our indicator C5. Therefore, C5 is not a good indicator when the number of particles per cell is  $\lesssim 100$ . Although 2D studies of turbulence, magnetic reconnection ([Franci et al., 2020](#)), and plasma instabilities ([Hellinger and Štverák, 2018](#)) are able to use considerably larger numbers of particles per cell ( $\sim 1000$ ), our work requires the third dimension in order to model the turbulence and the complex reconnection geometry more appropriately ([Howes, 2015b](#); [Lazarian et al., 2020](#)). Nonetheless, the increasing computational power of high-performance-computing facilities will allow us to perform increasingly more accurate 3D PIC simulations and to test all of our indicators over a wider range of parameters. Before these methods become computationally viable, divergence-cleaning of the electric field ([Jacobs and Hesthaven, 2009](#)) is a possible route to reduce the effect of particle noise.

## Chapter 7

# Energy transport during 3D small-scale reconnection driven by anisotropic turbulence using PIC simulations

In this chapter, I present the framework that we derive from a two-fluid approach based on the Boltzmann equation to study the spatial energy transfer associated with 3D magnetic reconnection events that occur self-consistently in plasma turbulence. In particular, I present the results for the reconnection event that involves two reconnecting flux ropes presented in Chapter 6. We discuss the agyrotropy patterns in the reconnection event and compare them with previous 2D studies. We compare the power density terms in the two-fluid energy equations with standard energy-based damping, heating, and dissipation proxies. Our findings suggest that the electron bulk flow transports thermal energy density more efficiently than kinetic energy density. Moreover, in our turbulent reconnection event, the energy density transfer is dominated by plasma compression. This is consistent with turbulent current sheets and turbulent reconnection events, but not with laminar reconnection.

This work is currently under revision at The Astrophysical Journal under the title

*Energy transport during 3D small-scale reconnection driven by anisotropic turbulence using PIC simulations.*

## 7.1 Introduction

Energy dissipation in collisionless plasmas is a longstanding fundamental physics problem. Although it is well known that magnetic reconnection and turbulence are coupled and transport energy from system-size scales to sub-proton scales, the details of the energy distribution and energy dissipation channels remain poorly understood. Especially, the energy transfer and transport associated with 3D small-scale reconnection that occurs as a consequence of a turbulent cascade is unknown.

Important progress has been made to understand heating and energy dissipation (e.g., [Gary, 1999](#); [Howes et al., 2017](#); [Klein et al., 2017](#); [Matthaeus et al., 2020](#)). Landau damping, ion-cyclotron damping, and stochastic heating are considered collisionless dissipation mechanisms that transfer energy from the electromagnetic field to the plasma particles ([Marsch et al., 2003](#); [Kasper et al., 2008](#); [Chandran et al., 2010, 2013](#)). The dissipation occurs predominantly in intermittent structures which form in plasma turbulence ([Matthaeus et al., 1999](#); [Kiyani et al., 2015](#)).

The energy transfer and transport associated with magnetic reconnection has been addressed by previous studies that focus on idealized 2D Harris current-sheet reconnection ([Yin et al., 2001](#); [Schmitz and Grauer, 2006](#); [Wang et al., 2015](#); [Pezzi et al., 2021](#)), 3D laminar collisionless reconnection in the context of magnetospheres ([Wang et al., 2018](#)), and 2D reconnection in turbulent plasmas ([Fadanelli et al., 2021](#)). In this work, we use particle-in-cell (PIC) simulations to study the energy transfer associated with 3D small-scale magnetic reconnection that self-consistently occurs as a consequence of an anisotropic turbulent cascade. In Section 7.2, we present our theoretical framework to study the energy transfer and transport in our plasma simulations. In Section 6.2, we present our simulation results emphasizing the presence of agyrotropy in Section 7.3.1 and the energy distribution in Section 7.3.2. In Section 7.4, we discuss the implications of our results and in Section 6.4 we provide conclusions for this chapter.

## 7.2 Energy Transfer and Transport

The total energy in a closed volume of plasma is partitioned amongst the particles and the electromagnetic fields. The bulk kinetic energy density of the particle species  $s$  is associated with the first velocity moment of the particle velocity distribution function  $f_s = f_s(\mathbf{x}, \mathbf{v}, t)$  and therefore with the bulk flux of the particles. The thermal energy density is associated with the second velocity moment and thus the pressure of the particles. The evolution of  $f_s$  follows the Boltzmann equation

$$\frac{\partial f_s}{\partial t} + \mathbf{v} \cdot \nabla f_s + \frac{q_s}{m_s} (\mathbf{E} + \mathbf{v} \times \mathbf{B}) \cdot \nabla_{\mathbf{v}} f_s = \left( \frac{\partial f_s}{\partial t} \right)_c, \quad (7.1)$$

where  $\mathbf{v}$  is the velocity,  $\mathbf{E}$  is the electric field,  $\mathbf{B}$  is the magnetic field,  $q_s$  is the charge and  $m_s$  is the mass of the particle of species  $s$  (see Chapter 2). The term  $(\partial f_s / \partial t)_c$  on the right-hand side represents the change in the distribution function due to collisions. This term includes individual correlations between fields and particles, based on the particles' individual Coulomb potentials (Klimontovich, 1997). To study the energy transport, we derive a set of energy equations based on the Boltzmann equation (7.1). Considering the macroscopic quantities  $n_s$  (Eq. 2.12),  $\mathbf{u}_s$  (Eq. 2.13),  $\bar{\mathbf{P}}_s$  (Eq. 2.14) and defining the heat flux vector

$$\mathbf{h}_s \equiv \frac{1}{2} m_s \int f_s (\mathbf{v} - \mathbf{u}_s) \cdot (\mathbf{v} - \mathbf{u}_s) (\mathbf{v} - \mathbf{u}_s) d^3 v. \quad (7.2)$$

We define the first moment of the collision term in Eq. (7.1) as

$$\Xi^1 = \int \mathbf{v} \left( \frac{\partial f_s}{\partial t} \right)_c d^3 v, \quad (7.3)$$

and the second moment as

$$\Xi^2 = \int \mathbf{v} \mathbf{v} \left( \frac{\partial f_s}{\partial t} \right)_c d^3 v. \quad (7.4)$$

With these definitions, we compute the first and second moments of Eq. (7.1); see Appendix B for details. The first moment of Eq. (7.1) yields the kinetic energy



equation

$$\frac{d\varepsilon_s^k}{dt} + \mathbf{u}_s \cdot \nabla \cdot \bar{\mathbf{P}}_s + \varepsilon_s^k \nabla \cdot \mathbf{u}_s - q_s n_s (\mathbf{u}_s \cdot \mathbf{E}) = \Xi_s^k, \quad (7.5)$$

where  $d/dt = \partial/\partial t + (\mathbf{u}_s \cdot \nabla)$  is the total time derivative,

$$\varepsilon_s^k = \frac{1}{2} n_s m_s (\mathbf{u}_s \cdot \mathbf{u}_s) \quad (7.6)$$

is the kinetic energy density, and

$$\Xi_s^k = m_s \mathbf{u}_s \cdot \Xi_s^1 \quad (7.7)$$

represents the irreversible kinetic energy transfer. The terms  $\mathbf{u}_s \cdot \nabla \cdot \bar{\mathbf{P}}_s$ ,  $\varepsilon_s^k \nabla \cdot \mathbf{u}_s$ , and the advective term  $(\mathbf{u}_s \cdot \nabla) \varepsilon_s^k$  are associated with the term  $\mathbf{v} \cdot \nabla f_s$  in Eq. (7.1). Therefore, these terms represent kinetic energy density transport due to the free streaming of particles. Conversely, the term  $-q_s n_s (\mathbf{u}_s \cdot \mathbf{E})$ , associated with the electric field, represents the energy density transfer between particle bulk flows and fields. The second moment of Eq. (7.1) yields the thermal energy equation

$$\frac{d\varepsilon_s^{th}}{dt} + \nabla \cdot \mathbf{h}_s + \nabla \mathbf{u}_s : \bar{\mathbf{P}}_s + \varepsilon_s^{th} \nabla \cdot \mathbf{u}_s = \Xi_s^{th}, \quad (7.8)$$

where

$$\varepsilon_s^{th} = \frac{1}{2} Tr(\bar{\mathbf{P}}_s) \quad (7.9)$$

is the thermal energy density, and

$$\Xi_s^{th} = -m_s \mathbf{u}_s \cdot \Xi_s^1 + \frac{m_s}{2} Tr(\bar{\Xi}^2) \quad (7.10)$$

represents the irreversible thermal energy transfer. The term  $Tr$  stands for the trace of the tensor, and  $\nabla \mathbf{u}_s : \bar{\mathbf{P}}_s$  is the double contraction of the strain tensor  $\nabla \mathbf{u}_s$  with  $\bar{\mathbf{P}}_s$ . The terms  $\nabla \cdot \mathbf{h}_s$ ,  $\nabla \mathbf{u}_s : \bar{\mathbf{P}}_s$ , and  $\varepsilon_s^{th} \nabla \cdot \mathbf{u}_s$ , associated with  $\mathbf{v} \cdot \nabla f_s$  in Eq. (7.1), represent thermal energy density transport due to the free streaming

of particles. The terms on the left-hand sides of Eqs. (7.5) and (7.8) describe collisionless processes, whereas the terms on the right-hand sides describe collisional processes in the plasma which generate an increase in the plasma entropy.

Equations (7.5) and (7.8) alone do not completely capture the energy conservation because they do not account for the rate of change in the electromagnetic energy density  $\partial\varepsilon^{em}/\partial t$ , nor the electromagnetic energy flux  $\nabla \cdot \mathbf{S}$ , where

$$\varepsilon^{em} = \frac{1}{2} \left( \frac{1}{\mu_0} \mathbf{B} \cdot \mathbf{B} + \epsilon_0 \mathbf{E} \cdot \mathbf{E} \right) \quad (7.11)$$

is the electromagnetic energy density and  $\mathbf{S} = \mathbf{E} \times \mathbf{B}/\mu_0$  is the Poynting vector. The expression that account for these changes is the Poynting theorem

$$\frac{\partial \varepsilon^{em}}{\partial t} + \nabla \cdot \mathbf{S} + \mathbf{J} \cdot \mathbf{E} = 0 \quad (7.12)$$

Nevertheless, equations (7.5) and (7.8) are exact and describe the energy density transfer and transport as well as the energy density transfer between fields and particles. Before tackling the energy transfer problem, we explicitly define the following three terms, which are often used interchangeably in the literature:

- *Heating* is any increase in  $\varepsilon_s^{th}$ , and *cooling* is any decrease in  $\varepsilon_s^{th}$ . Heating can be either reversible or irreversible.
- *Damping* is any decrease in  $\varepsilon^{em}$ , and *growth* is any increase in  $\varepsilon^{em}$ . Damping/growth can be either reversible or irreversible.
- *Dissipation* is any irreversible energy transfer leading to an increase in  $\varepsilon_s^{th}$ .

Dissipation is challenging to quantify directly both in space measurements and in simulations. Nonetheless, recent studies (Pezzi et al., 2019; Matthaeus et al., 2020; Pezzi et al., 2021) show that in collisionless plasmas *energy-based dissipation proxies*, such as the Zenitani parameter (Zenitani et al., 2011)

$$D_{z,s} = \mathbf{J} \cdot (\mathbf{E} + \mathbf{u}_s \times \mathbf{B}) - n_s q_s (\mathbf{u}_s \cdot \mathbf{E}) \quad (7.13)$$

and the strain-pressure interaction  $\nabla \mathbf{u}_s : \bar{\mathbf{P}}_s$  (Yang et al., 2017) are spatially correlated with non-dimensional measures of non-thermal distribution function (Kaufmann and Paterson, 2009; Greco et al., 2012; Liang et al., 2019) and plasma agyrotropy (Scudder and Daughton, 2008). In Eq. (7.13),  $\mathbf{J} = \sum_{s=i,e} q_s n_s \mathbf{u}_s$  is the electric current density.

These energy-based dissipation proxies are effectively *power density* terms, derived from the left-hand sides of our Eqs. (7.5) and (7.8). According to our definitions,  $D_{z,s}$  is a damping measure, since it quantifies the energy transfer from the electromagnetic fields into bulk kinetic energy and vice versa.

The strain-tensor interaction has gyrotropic and agyrotropic contributions. We decompose the pressure tensor as  $P_{ij,s} = p_s \delta_{ij} + \Pi_{ij,s}$ , where

$$p_s = \sum_{i=1}^3 P_{ii,s}/3 \quad (7.14)$$

is the isotropic scalar pressure and

$$\Pi_{ij,s} = (P_{ij,s} + P_{ji,s})/2 - p_s \delta_{ij} \quad (7.15)$$

is the deviatoric pressure. Likewise, the strain-rate tensor  $\nabla \mathbf{u}_s$  can be expressed as  $\nabla u_{ij,s} = \theta_s \delta_{ij}/3 + D_{ij,s}$ , where  $\theta_s = \nabla \cdot \mathbf{u}_s$  represents the dilatation term and

$$D_{ij,s} = \frac{1}{2} \left( \frac{\partial u_{i,s}}{\partial x_j} + \frac{\partial u_{j,s}}{\partial x_i} \right) - \frac{1}{3} \theta_s \delta_{ij} \quad (7.16)$$

represents the symmetric traceless strain-rate tensor (Yang et al., 2017). Thus, the strain-tensor interaction, which is a heating/cooling proxy according to our definitions, is

$$\nabla \mathbf{u}_s : \bar{\mathbf{P}}_s = p_s \theta_s + \Pi_{ij,s} D_{ij,s}, \quad (7.17)$$

where the first term on the right-hand side is known as  $p\text{-}\theta_s$ , and the second term on the right-hand side is known as  $Pi\text{-}D_s$  (Yang et al., 2017). For comparison with

previous studies (Pezzi et al., 2021; Bandyopadhyay et al., 2020), in Section 7.3.3, we compute  $D_{ij,s}$ ,  $p_s\theta_s$ , and  $\Pi_{ij,s}D_{ij,s}$  and compare them with the energy transfer and transport terms,  $-n_s q_s(\mathbf{u}_s \cdot \mathbf{E})$  and  $\nabla \mathbf{u}_s : \bar{\mathbf{P}}_s$ , in Eqs. (7.5) and (7.8). This framework can be used to quantify the energy transfer from in-situ observations. In appendix C, we present an extension of Eqs. (7.5) and (7.8) in terms of distribution functions for each species  $s$ .

### 7.2.1 Reconnection Event Overview

For the current analysis, we use the same simulations as described in Chapter 6 the energy analysis. Panel a) in Figure 7.1 shows the volume rendering of the current density in our simulation domain at the simulated time  $t = 120\omega_{pi}^{-1}$ . Current filaments that form in the turbulent cascade are mostly elongated along the direction of the background magnetic field. At this time in the simulation, we apply the set of indicators presented in Section 6.3.3 to identify and locate reconnection sites. We select the reconnection event that we studied in Section 6.3.3, which involves two reconnecting flux-rope as shown in panel b) of Figure 7.1. The magnetic-field lines are colour-coded with  $|\mathbf{B}|$ . The magnetic flux-rope contain an intense magnetic field, especially the lower flux-rope which is more twisted and has a smaller radius than the upper flux-rope. Conversely, the magnetic field between the flux-rope is weak. The cuts in panel b) show  $J_z$  in the  $xy$  simulation plane. For our analysis of this event, we apply a 2D cut in the  $xy$ -plane at  $z = 77d_i$ . Panel c) of Figure 7.1 shows the magnetic-field lines of the field components in the  $xy$ -plane, i.e.,  $(B_x, B_y)$  as black contours. Panel c) illustrates the complexity of the magnetic topology in the region of interest. For our energy analysis, we select a volumetric sub-region of size  $10 d_i^3$  around the identified reconnecting region. The green square in panel c) highlights the intersection of the selected sub-region with the central 2D cut from panel b). Even though the background field is in the  $z$ -direction, the current structures are not exactly aligned with the  $z$ -direction. Instead, the geometric features of the reconnection event are aligned with the plane perpendicular to the current sheet that sustains the magnetic gradient. Therefore, we determine a reference frame that is aligned with the main axis of the current sheet. We determine the direction of

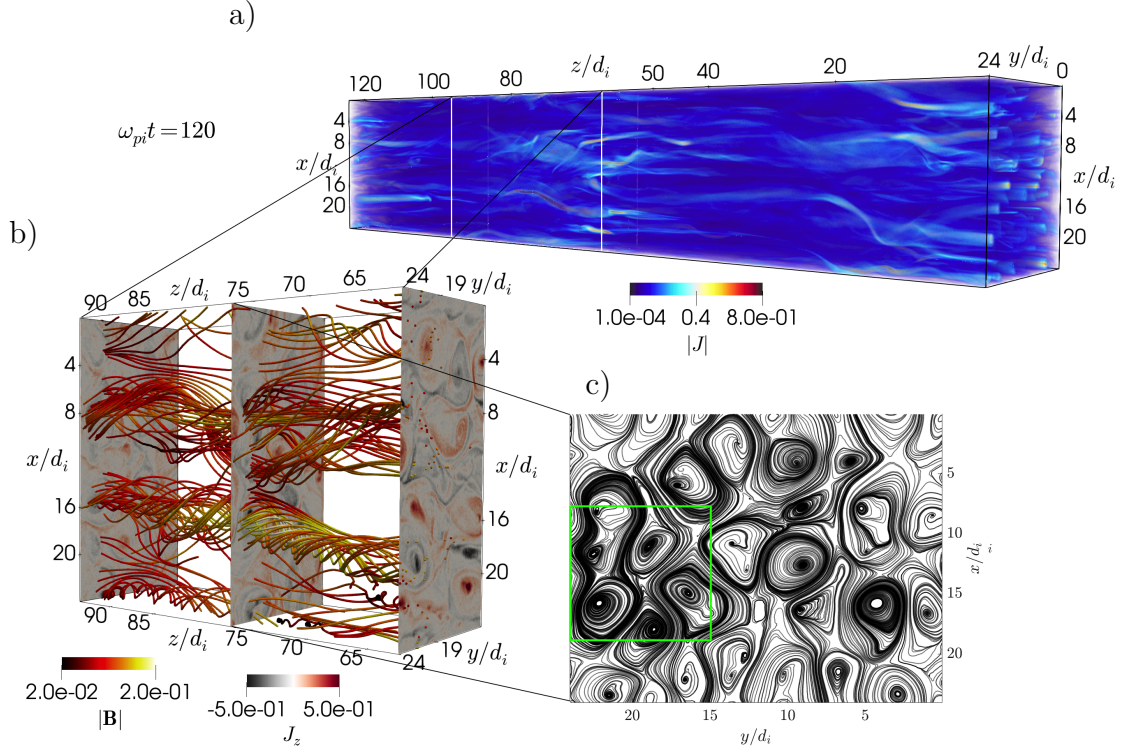


**Figure 7.1:** Spatial context of the reconnection event within the simulation domain. Panel a) shows a volume rendering of  $|\mathbf{J}|$ . Panel b) shows the 3D magnetic field lines colour-coded with  $|\mathbf{B}|$ . On the vertical cuts in panel b), we show  $J_z$ . Panel c) shows the magnetic field lines in the  $xy$ -plane. The black contours show in-plane magnetic-field lines. The green square highlights the size and position of the region for the energy analysis.

the main axis of the current sheet by 3D rendering  $J_z$  and measuring the inclination of the coherent structure that crosses the point  $x = 13.5d_i$  and  $y = 21.5d_i$  in the  $xy$ -plane. We then apply a coordinate transformation from the reference frame (RF)  $(x, y, z)$  to a new RF  $(r, p, a)$  aligned with the main axis of the current sheet. The unit vectors of this RF are  $(\hat{\mathbf{r}}, \hat{\mathbf{p}}, \hat{\mathbf{a}})$ . In this RF,  $\hat{\mathbf{a}}$  is anti-parallel to the main axis of the current sheet,  $\hat{\mathbf{p}}$  is an arbitrary vector in the plane perpendicular to  $\hat{\mathbf{a}}$ , and  $\hat{\mathbf{r}}$  is the vector that completes the right-handed coordinate system. Since the components  $r$  and  $p$  are in the plane perpendicular to the current structure, we denote them as the in-plane components.

In the following analysis, we use the RF  $(r, p, a)$  and select a squared-shape region

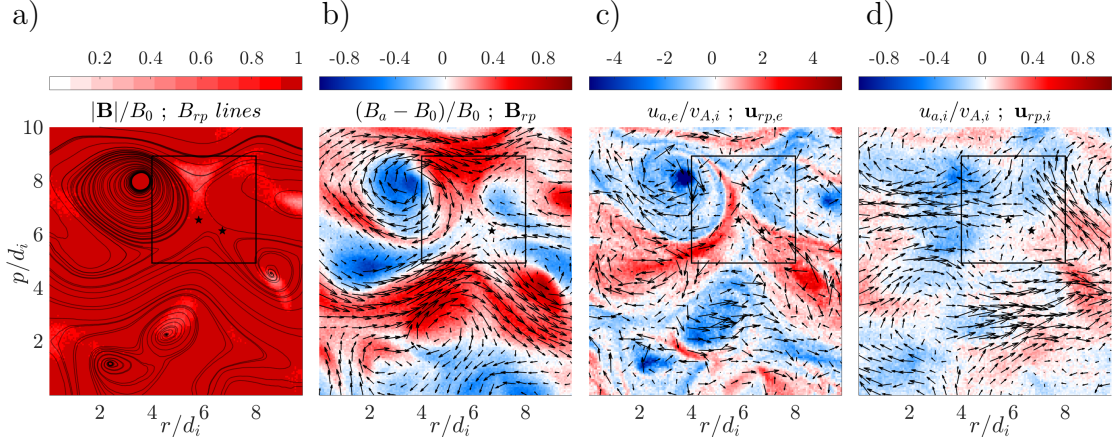


**Figure 7.2:** 2D cuts in the  $rp$ -plane at simulation time  $t = 120\omega_{pi}^{-1}$ . a) Magnetic field magnitude  $|\mathbf{B}|/B_0$ . The black contours represent the in-plane magnetic-field lines, and the black stars represent two x-points. b) Out-of-plane component of the magnetic field,  $(B_a - B_0)/B_0$ . The black arrows in this panel represent the in-plane magnetic vectors ( $\mathbf{B}_{rp}$ ). c) Out-of-plane electron speed  $u_{a,e}/V_{A,i}$ . The black arrows in this panel represent the in-plane electron velocity vectors ( $\mathbf{v}_{rp,e}/V_{A,i}$ ). d) Out-of-plane ion speed  $u_{a,i}/V_{A,i}$ . The black arrows in this panel represent the in-plane ion velocity vectors ( $\mathbf{v}_{rp,i}$ ). In all panels, the black square outlines the diffusion region.

of edge length  $10 d_i$  in the  $rp$ -plane similar to the green square in panel c) of Figure 7.1. Panel a) in Figure 7.2, shows the magnetic field magnitude in the region of interest normalised to  $B_0$ . The black contours are the in-plane magnetic-field lines. Panel b) in Figure 7.2 shows  $(B_a - B_0)/B_0$  where  $B_a$  is the out-of-plane component in the magnetic field. We subtract the background magnetic field to improve the visibility of the multipolar configuration of this component. The black arrows in this panel represent the in-plane magnetic-field vectors  $\mathbf{B}_{rp} = B_r \hat{\mathbf{r}} + B_p \hat{\mathbf{p}}$ . In order for reconnection to occur, the in-plane components of the magnetic fields of reconnecting structures must have different directions. The thin structures of  $(B_a - B_0) \approx 0$  that separate regions of opposite in-plane magnetic field vectors are effectively magnetic separatrices. The in-plane magnetic field lines in panel a) along with the direction of the in-plane magnetic-field vectors suggest the presence of two x-points which we mark with two black stars, one located at  $r = 5.8d_i$  and  $p = 6.6d_i$ , and the other at  $r = 6.7d_i$  and  $p = 6.2d_i$ . The magnetic configuration is complex, and the black square outlines the central region in which reconnection occurs. Within this region, we do not identify a magnetic null region nor a region of sustained uniform magnetic

field. From now on, we refer to the region enclosing the x-points as the diffusion region. Since transverse 2D cuts to 3D magnetic flux-ropes resemble the geometry of magnetic islands, we now refer to the quasi-circular magnetic-field lines in panel a) as magnetic islands.

Panel c) shows the out-of-plane component of the electron velocity  $u_{a,e}$ , normalised to the ion Alfvén speed  $v_{A,i}$ . The red colour indicates electrons moving out of the plane, whereas the blue colour indicates electrons moving into the plane. The black arrows of this panel represent the in-plane electron velocity vectors  $\mathbf{u}_{rp,e} = u_{r,e}\hat{\mathbf{r}} + u_{p,e}\hat{\mathbf{p}}$ . Within the region of interest, there are counter-streaming electrons following the separatrices. Likewise, we locate electrons streaming out of the plane through the diffusion region. Within the magnetic islands, the electrons stream into the plane. In most of the magnetic islands, the electrons follow quasi-circular orbits due to their magnetization. However, in the magnetic island centered at  $r = 4.5d_i$  and  $p = 2.2d_i$ , the electrons demagnetise and traverse into the magnetic island connecting with the stream of electrons at the edge of the magnetic island.

Panel d) shows the out-of-plane component of the ion velocity  $u_{a,i}$ , normalised to  $v_{A,i}$ . The black arrows in this panel represent the in-plane ion velocity vectors  $\mathbf{u}_{rp,i} = u_{r,i}\hat{\mathbf{r}} + u_{p,i}\hat{\mathbf{p}}$ . Within the diffusion region, the out-of-plane ion velocity is small, which suggests that the ion motion is mostly constrained to the plane. The in-plane motion, however, is considerable, and the ions move across the separatrices since they are demagnetised.

## 7.3 Results

### 7.3.1 Particle Agyrotropy in the Diffusion Region

During the reconnection of magnetic flux-ropes, the plasma expansion/contraction is not isotropic. Therefore, at kinetic scales, the plasma pressure of each species can develop anisotropy and agyrotropy. Figure 7.3 shows our pressure terms according to Eqs. (7.14) and (7.15) for electrons and ions, normalised to  $p_0 = n_0 m_i v_{A,i}^2$ . Panels a) and e) show the isotropic scalar pressure for electrons  $p_e$  and ions  $p_i$ . For both species, the scalar pressure is greater inside the magnetic islands than outside due to

the large density of particles (not shown here). Likewise,  $p_e$  and  $p_i$  display gradients along and across the separatrices. We find that  $p_e$  is lower in the region between the magnetic islands as well as between the x-points compared to inside the magnetic islands.

Panels b), c), and d) of Figure 7.3 show the off-diagonal components of the electron pressure tensor according to Eq. (7.15):  $\Pi_{ra,e}$ ,  $\Pi_{pa,e}$ , and  $\Pi_{pr,e}$ . The average absolute values of the off-diagonal terms  $\langle |\Pi_{ra,e}| \rangle$  and  $\langle |\Pi_{pa,e}| \rangle$  are about 10% of  $\langle p_e \rangle$ .  $\Pi_{ra,e}$  and  $\Pi_{pa,e}$  present a strong dipole-like configuration centered on the magnetic islands. There is a shallower, yet visible, gradient in  $\Pi_{ra,e}$ ,  $\Pi_{pa,e}$ , and  $\Pi_{pr,e}$  in the region between the islands as well as in the diffusion region. Conversely,  $\Pi_{pr,e}$  exhibits a quadrupolar configuration within the magnetic islands. The non-zero values of  $\Pi_{ra,e}$ ,  $\Pi_{pa,e}$ , and  $\Pi_{pr,e}$  show that the plasma is agyrotropic, suggesting that small-scale kinetic processes occur. Similar patterns are reported along the separatrices of 2D collisionless reconnection (Yin et al., 2001; Schmitz and Grauer, 2006; Wang et al., 2015) and laminar 3D collisionless reconnection (Wang et al., 2018). However, unlike previous studies, we observe the same patterns within the magnetic islands of turbulent 3D magnetic reconnection. This is a fundamental difference between the reconnection that occurs in turbulence and steady-state reconnection that occurs in Harris current-sheet configurations.

Panels f), g), and h) of Figure 7.3 show the off-diagonal components of the ion pressure tensor according to Eq. (7.15):  $\Pi_{ra,i}$ ,  $\Pi_{pa,i}$ , and  $\Pi_{pr,i}$ . The off-diagonal terms for ions, unlike electrons, have a less coherent pattern attached to the in-plane magnetic field topology. The reason for this detachment lies in the de-magnetization of the ions at these scales. Nevertheless, there is a gradient of these terms suggesting agyrotropy effects in the ion dynamics as well.

Figure 7.4 shows a magnification of the region enclosed by the black square in Figure 7.2. Panels a) to d) show a magnification of the electron pressure terms from panels a) to d) of Figure 7.3. To make a direct comparison with previous 2D studies, panels e) to h) show sketches summarizing known patterns associated with the electron



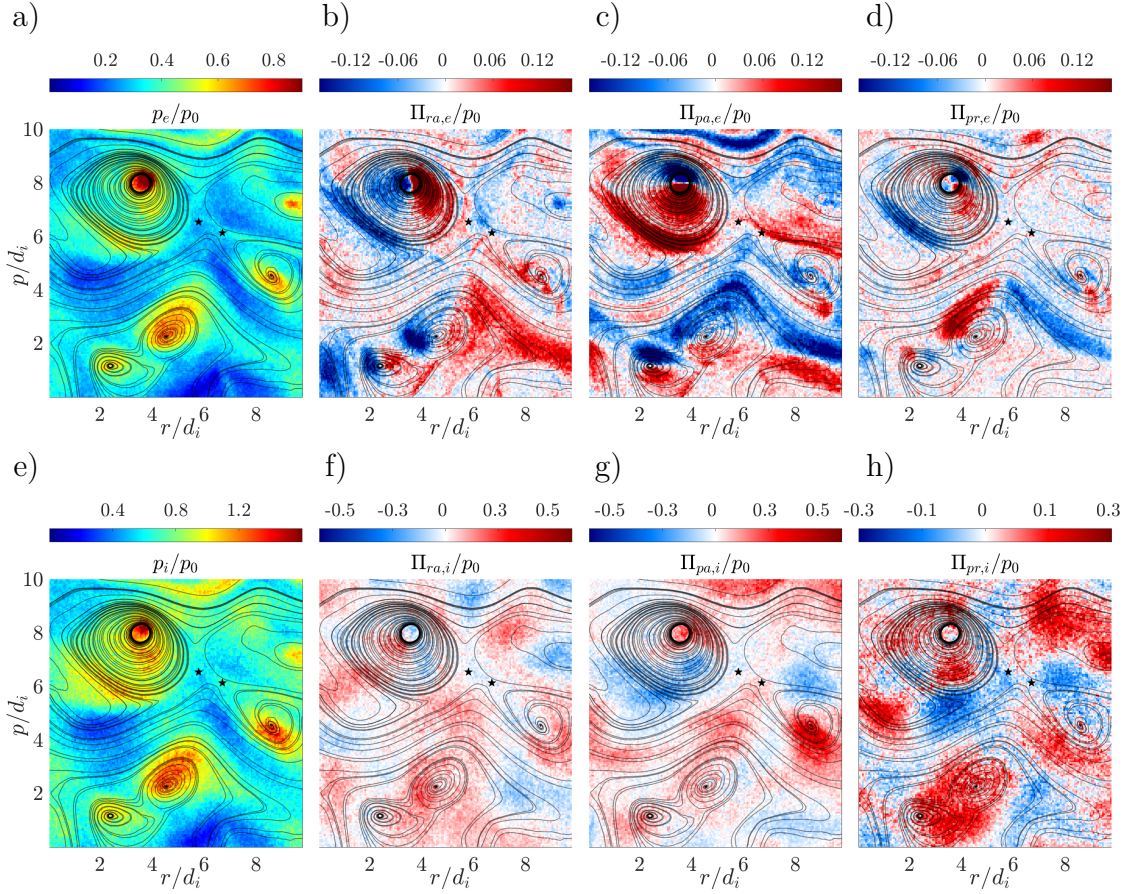


**Figure 7.3:** 2D cuts of the pressure tensor components in the  $rp$ -plane at the simulation time  $t = 120\omega_{pi}^{-1}$ . a) Electron scalar pressure  $p_e/p_0$ . Off-diagonal components of the electron pressure tensor: b)  $\Pi_{ra,e}/p_0$ , c)  $\Pi_{pa,e}/p_0$ , and d)  $\Pi_{pr,e}/p_0$ . e) Ion scalar pressure  $p_i/p_0$ . Off-diagonal components of the ion pressure tensor: f)  $\Pi_{ra,i}/p_0$ , g)  $\Pi_{pa,i}/p_0$ , and h)  $\Pi_{pr,i}/p_0$ .

pressure components that emerge from 2D collisionless reconnection in the absence of a guide field (Yin et al., 2001; Schmitz and Grauer, 2006; Wang et al., 2015). In this region, unlike within the magnetic islands of Figure 7.3, our simulation results of the electron pressure patterns match those patterns shown in the sketches in panels e) to h) in the region where the magnetic field has a local minimum according to panel a) in Figure 7.1. However, below the x-point located at  $r = 5.8d_i$  and  $p = 6.6d_i$ , the pattern no longer corresponds to the sketched expectations. Moreover,  $\Pi_{pr,e}$  is less coherent, and we do not recognise a clear quadrupolar configuration as in the sketches for the 2D case.

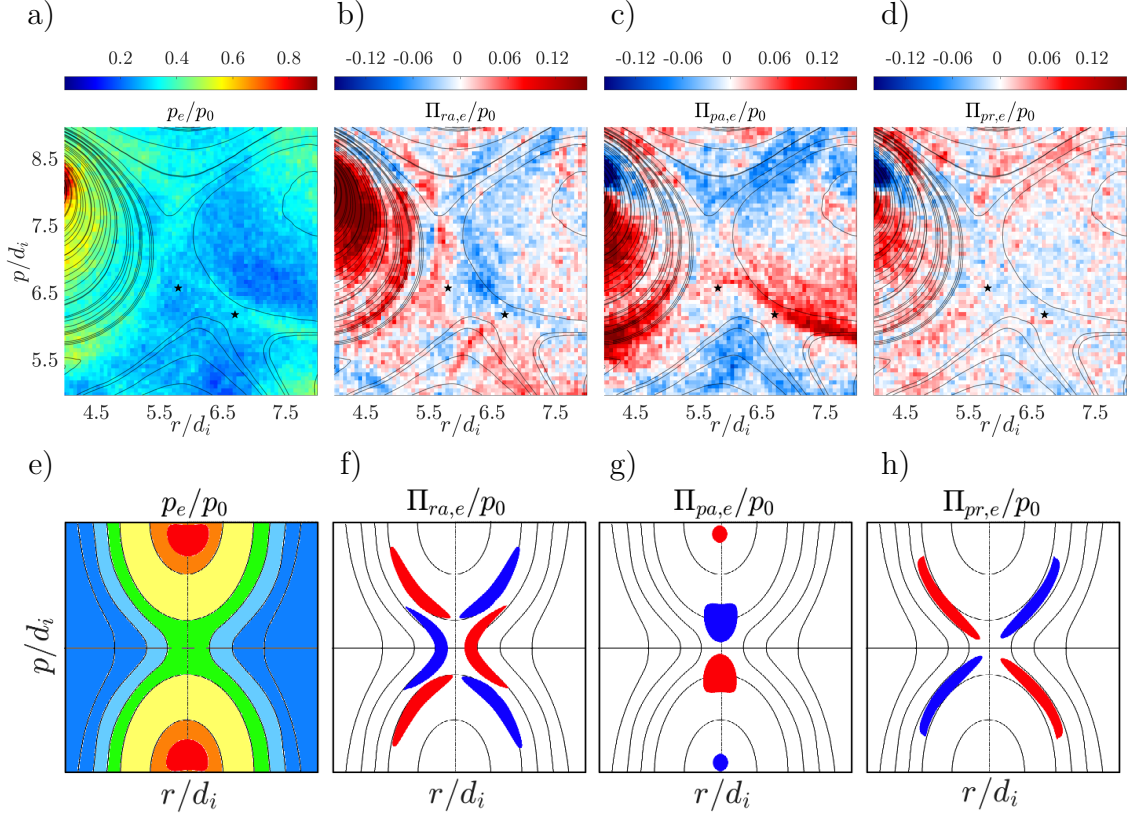


**Figure 7.4:** Magnification of the region delimited by the black square in Figure 7.2 in the  $rp$ -plane at the simulation time  $t = 120\omega_{pi}^{-1}$ . a) Electron scalar pressure  $p_e$ . Off-diagonal components of the electron pressure tensor: b)  $\Pi_{ra,e}$ , c)  $\Pi_{pa,e}$ , and d)  $\Pi_{pr,e}$ . Panel e) shows a sketch of the patterns of the scalar pressure emerging in 2D simulations of reconnection, and f) to h) show sketches of the off-diagonal terms of the electron pressure based on 2D Harris current sheet reconnection without guide field (Yin et al., 2001).

### 7.3.2 Energy Transfer and Transport

We use the power density expressions for the kinetic energy in Eq. (7.5) and thermal energy in Eq. (7.8) to describe the energy transfer and transport associated with our reconnection event. To compute the partial time derivatives of a quantity, we use a central-difference approach. Since the Alfvén transient time is  $\sim 100 \omega_{pi}^{-1}$ , a time resolution of  $6 \omega_{pi}^{-1}$  is sufficient to capture the relevant dynamics of interest. To estimate the spatial derivatives, we use a standard cell-centred first-neighbours approach. We calculate all scalar products cell-wise in the simulation domain. Panels a) to e) of Figure 7.5 show 2D cuts of each term in Eq. (7.5) for electrons, normalised to  $\Delta\varepsilon_0 = \omega_{pi} m_i v_{A,i}^2$ .

Panel a) shows, at the simulation time  $t = 120\omega_{pi}^{-1}$ , the total time derivative of the kinetic energy density  $d\varepsilon_e^k/dt$ . The domain exhibits considerable temporal changes of the kinetic energy density at the centers of the magnetic islands. We also detect negative  $d\varepsilon_e^k/dt$  at the edge of the top-left magnetic island and positive  $d\varepsilon_e^k/dt$  in the diffusion region. Conversely, there is almost no change in  $\varepsilon_e^{th}$  in the region between the x-points.

Panel b) shows the scalar product  $\mathbf{u}_e \cdot \nabla \cdot \bar{\mathbf{P}}_e$  which quantifies the change of kinetic energy due to the advection of the pressure tensor. This energy change is transported by the electron flow. The quantity  $\mathbf{u}_e \cdot \nabla \cdot \bar{\mathbf{P}}_e$  is also known as the pressure work (Fadanelli et al., 2021). There is a strong conversion of energy associated with the pressure work at the center of the magnetic islands. However, the energy change associated with this term is around 10 times greater than the local  $d\varepsilon_e^k/dt$ . Unlike  $d\varepsilon_e^k/dt$ , at the edge of the top-left magnetic island, there is a strong gradient of  $\mathbf{u}_e \cdot \nabla \cdot \bar{\mathbf{P}}_e$  from the left-hand side of the magnetic island to the right-hand side. In addition,  $\mathbf{u}_e \cdot \nabla \cdot \bar{\mathbf{P}}_e$  has a local minimum in the region between the x-points.

Panel c) shows  $\varepsilon_e^k \nabla \cdot \mathbf{u}_e$  which represents the kinetic energy change due to divergent or convergent flow patterns in the electron bulk velocity. Like for the previous terms,  $\varepsilon_e^k \nabla \cdot \mathbf{u}_e$  is greater at the center of the magnetic islands than in the region between them. There is no noticeable gradient of this terms between the x-points. Although panels a), b), and c) show similar patterns in their signs, there are local differences, especially in the diffusion region.

Panel d) shows  $-q_e n_e (\mathbf{u}_e \cdot \mathbf{E})$  which represents the energy exchange between the electrons and the electric field. We find a considerable energy conversion, not only within the magnetic islands but also in the region between the islands as well as in the region between the x-points. In the region between the x-points, the electrons gain kinetic energy from the electric field. Along the separatrix next to the top-left island, the electron bulk motion is decelerated by the electric field. Comparing panels b) and d),  $\mathbf{u}_e \cdot \nabla \cdot \bar{\mathbf{P}}_e$  and  $-q_e n_e (\mathbf{u}_e \cdot \mathbf{E})$  balance with each other in the diffusion region.

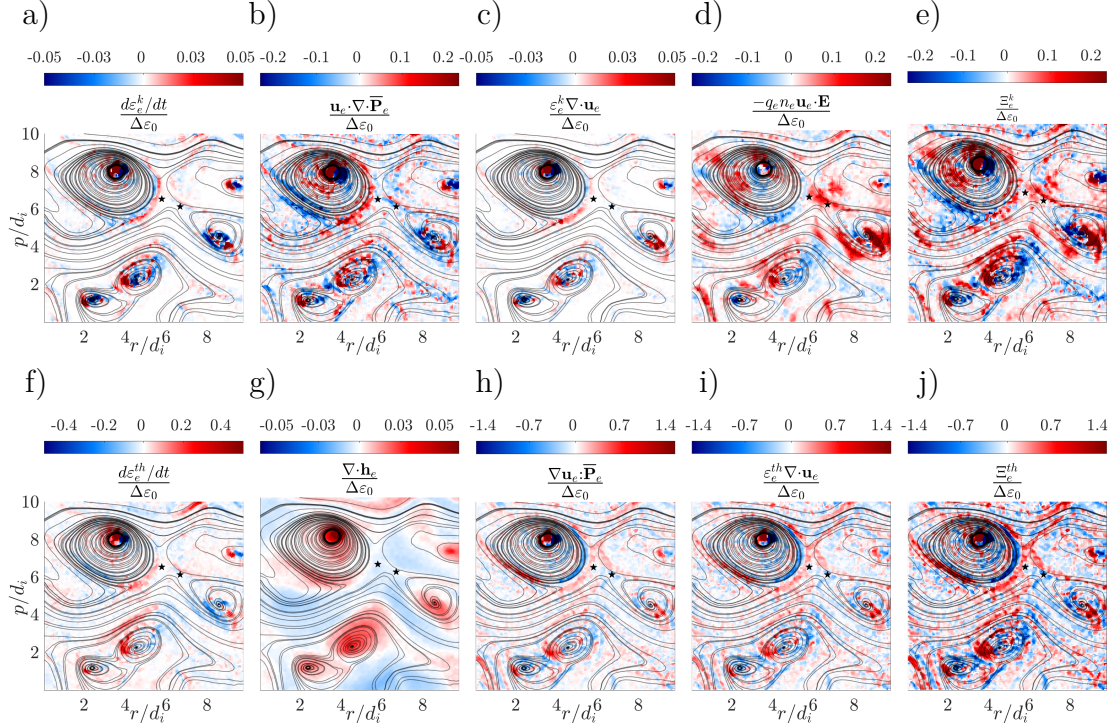


**Figure 7.5:** 2D cuts in the  $rp$ -plane at the simulation time  $t = 120\omega_{pi}^{-1}$ . Panels a) to e): kinetic power density terms for electrons. Panels f) to j): thermal power density terms for electrons. All quantities are normalised to  $\Delta\varepsilon_0 = \omega_{pi}m_i v_{A,i}^2$ .

Panel e), shows  $\Xi_s^k$  which we compute as the sum of all terms at the left-hand side of Eq. (7.5). There are regions with positive and negative  $\Xi_e^k$  within the magnetic islands. On the contrary,  $\Xi_e^k$  is predominately positive within the diffusion region and along the separatrices. Although we do not include binary collisions in our code explicitly, we acknowledge that the finite number of macro-particles affects the system in a way similar to collisions and leads to an undersampling of non-thermal fine structure in the velocity distribution function, which generates a loss of information and thus increase in entropy. We note, however, that this effect occurs earlier in PIC simulations with a finite number of particles than in the real solar wind. We conjecture that the impact is ultimately comparable.

Panels f) to j) of Figure 7.5 show 2D cuts of each term in Eq. (7.8), normalised to  $\Delta\varepsilon_0$ . Panel f) depicts  $d\varepsilon_e^{th}/dt$ . As in the kinetic-energy case,  $d\varepsilon_e^{th}/dt$  has local extrema associated with the magnetic islands. The main change in  $d\varepsilon_e^{th}/dt$  is due to the advective term  $(\mathbf{u}_e \cdot \nabla)\varepsilon_e^{th}$ . By direct comparison with panel b), we note similar



power density patterns between  $d\varepsilon_e^{th}/dt$  and  $\mathbf{u}_e \cdot \nabla \cdot \bar{\mathbf{P}}_e$ .

For the heat-flux term  $\nabla \cdot \mathbf{h}_e$ , we do not directly compute  $\nabla \cdot \mathbf{h}_e$  as a particle moment, but use a Hammett–Perkins approach (Hammett and Perkins, 1990) to estimate its contribution. This approach has been successfully applied in previous collisionless reconnection studies (Wang et al., 2015; Ng et al., 2015, 2017). In this framework, we estimate

$$\nabla \cdot \mathbf{h}_e \approx v_e^{th} \frac{1}{2} |k_0| \text{Tr} [P_{ij,e} - \langle P_{ij,e} \rangle - \delta_{ij} (n_e - \langle n_e \rangle) \langle T_e \rangle], \quad (7.18)$$

where  $v_e^{th} = \sqrt{2k_B T_e / m_e}$  is the thermal speed of the electrons and  $\langle \dots \rangle$  represents the spatial average over the sub-domain. The wave number  $k_0 = \sqrt{3}/|L_s|$  is a representative wave number associated with a sub-domain of volume  $V_s = L_s^3$  where  $L_s = 10.08 d_i$ , which we select as the region where we study the energy conversion during the reconnection event. Panel g) shows our estimation of  $\nabla \cdot \mathbf{h}_e$ . There is a positive power density contribution from particle heat flux inside the magnetic islands. Conversely, there is a negative contribution in the regions between the magnetic islands.

Panel h) depicts the energy transfer  $\nabla \mathbf{u}_e : \bar{\mathbf{P}}_e$  between kinetic and thermal energies. This term has contributions from the diagonal elements of the tensors associated with the isotropic energy transport and from the off-diagonal elements that quantify the agyrotropy in the plasma. There is positive  $\nabla \mathbf{u}_e : \nabla \bar{\mathbf{P}}_e$  in the region between the magnetic islands which is associated with counter-streaming electrons. We locate an x-like structure centered in the region where the magnetic field strength exhibits a local minimum. In the region between the x-points as well as to the left of the diffusion region,  $\nabla \mathbf{u}_e : \bar{\mathbf{P}}_e < 0$ .

Panel i) shows the thermal energy transport  $\varepsilon_e^{th} \nabla \cdot \mathbf{u}_e$  associated with the compression/expansion of the electron flow. At first glance, the positive/negative patterns in  $\varepsilon_e^{th} \nabla \cdot \mathbf{u}_e$  seem very similar to the patterns in  $\nabla \mathbf{u}_e : \bar{\mathbf{P}}_e$ . The reason for this similarity is that the main energy transport in  $\nabla \mathbf{u}_e : \bar{\mathbf{P}}_e$  is associated with the contribution of diagonal elements as we show in Section 7.3.3. However, we find local differences

due to the agyrotropic contributions. From all terms on the left-hand sides of Eqs. (7.5) and (7.8), only the terms associated with the strain tensor present an extended asymmetric x-point-like structure in the diffusion region. Comparing panels c) and i),  $\varepsilon_e^{th} \nabla \cdot \mathbf{u}_e$  is on average greater and forms broader structures than  $\varepsilon_e^k \nabla \cdot \mathbf{u}_e$ .

Panel j), shows  $\Xi_s^{th}$ , which we compute as the sum of all terms on the left-hand side of Eq. (7.8). This energy transfer is significant as the different terms on the left-hand side of Eq. (7.8) do not sum to zero.

In Figure 7.6, we show vertical 1D cuts of the power density terms along the  $p$ -direction at  $r = 5.58 d_i$  to visualise the relation between the different terms for plasma electrons. We further show a magnification of the region delimited by the black square from Figure 7.2. Panel a) shows the kinetic power density terms in Eq. (7.5). We observe that the fluctuations in  $d\varepsilon_e^k/dt$  (green line) and  $\varepsilon_e^k \nabla \cdot \mathbf{u}_e$  (black line) are negligible compared with  $\mathbf{u}_e \cdot \nabla \cdot \bar{\mathbf{P}}_e$  (red line) and  $-q_e n_e \mathbf{E} \cdot \mathbf{u}_e$  (yellow line). However, there is a noticeable disturbance in all quantities in the range  $p = 6.96 d_i$  to  $p = 7.84 d_i$  which is located in the region of the diffusion region where the magnetic field is nearly zero. Along the 1D cut,  $\mathbf{u}_e \cdot \nabla \cdot \bar{\mathbf{P}}_e$  and  $-q_e n_e \mathbf{E} \cdot \mathbf{u}_e$  are anti-correlated. This anti-correlation breaks down when the disturbances in  $d\varepsilon_e^k/dt$  and  $\varepsilon_e^k \nabla \cdot \mathbf{u}_e$  occur. For this panel, the curve of  $\Xi_s^k$  (blue line) changes sign when crossing the x-point.

Panel b) shows the thermal power density terms in Eq. (7.8). Comparing panels a) and b), we observe that the fluctuations in the thermal power density terms are more pronounced than those in the kinetic power density. In panel b), the fluctuations in  $d\varepsilon_e^{th}/dt$  (green line) and  $\nabla \cdot \mathbf{h}_e$  (red line) are negligible compared with  $\nabla \mathbf{u}_s : \bar{\mathbf{P}}_e$  (black line) and  $\varepsilon_e^{th} \nabla \cdot \mathbf{u}_e$  (yellow line). Unlike in the kinetic power density case, the contributions from all terms in Eq. (7.8) are either positive or negative at the same location, showing no anti-correlation between the dominant terms. We note that  $\Xi_e^{th}$  (blue line), unlike  $\Xi_e^k$ , is positive on both sides of the x-point.

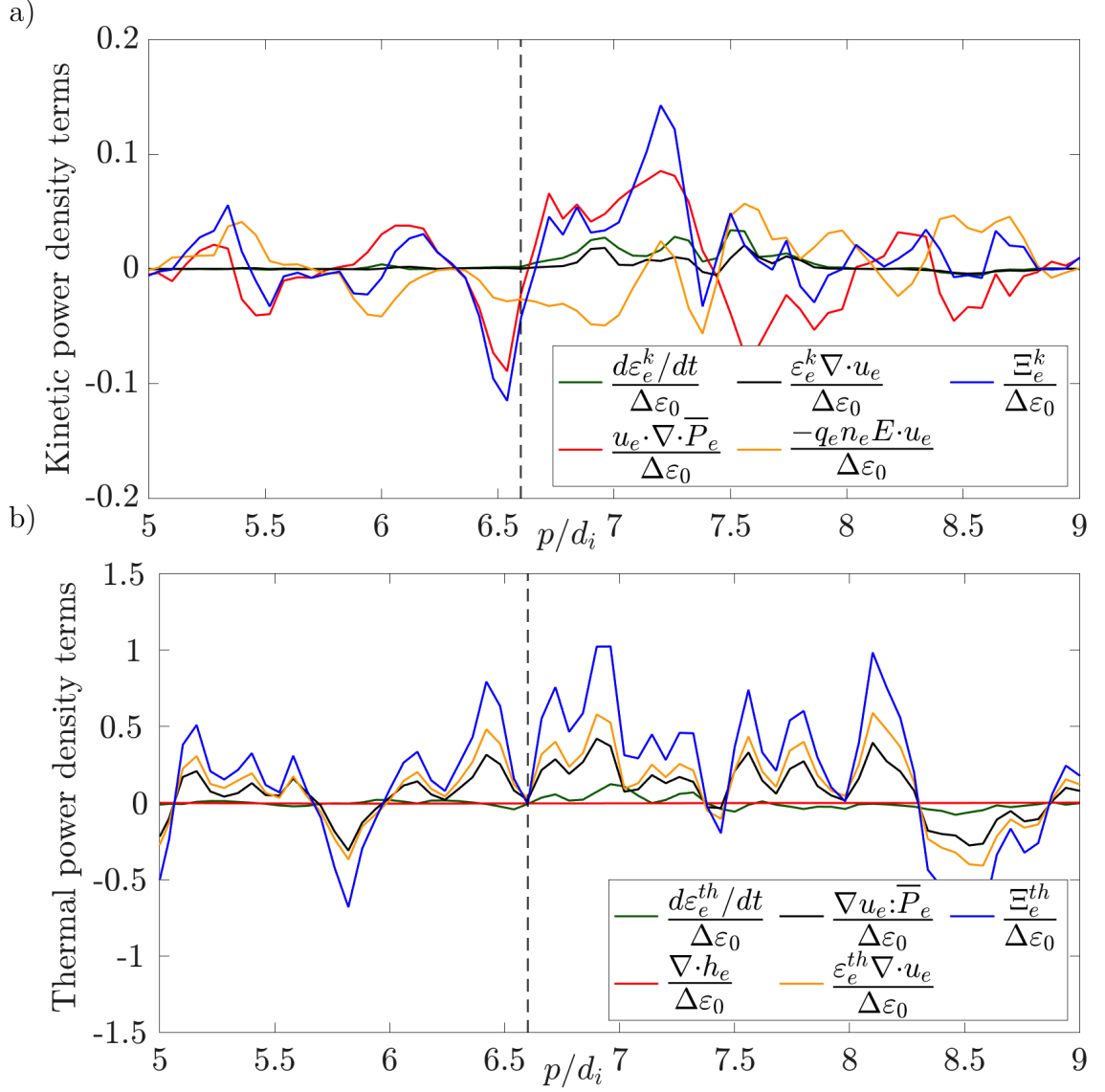


**Figure 7.6:** 1D cuts of the power density terms along the  $\hat{p}$ -direction at  $r = 5.58 d_i$  and at the simulation time  $t = 120\omega_{pi}^{-1}$ . a) Kinetic power density terms in Eq. (7.5). b) Thermal power density terms in Eq. (7.8). The vertical dashed line represents the crossing of the x-point  $r = 5.8d_i$  and  $p = 6.6d_i$ .

### 7.3.3 Comparison with Damping and Heating Proxies

In recent studies (Yang et al., 2017; Pezzi et al., 2019; Matthaeus et al., 2020; Pezzi et al., 2021), the collisionless energy dissipation problem is tackled by studying quantities such as the Zenitani parameter defined in Eq. (7.13) and the strain-pressure interaction defined in Eq. (7.17). We also explore these damping and heating proxies for comparison with our methods. Figure 7.7 depicts 2D cuts in the  $rp$ -plane and 1D cuts of these damping and heating proxies. Panel a) shows  $D_{ze}$ . Similar to our kinetic and thermal power density terms, the magnetic islands present strong variations of  $D_{ze}$ . On the contrary, in the diffusion region, we see a coherent positive  $D_{ze}$  signature.

Panel b) shows  $p\theta_e$ . The positive/negative patterns of this quantity are almost identical to our patterns of  $\nabla \mathbf{u}_e : \bar{\mathbf{P}}_s$  (panel h) in Figure 7.5. This similarity illustrates that the main contribution to the strain-tensor interaction comes from the diagonal elements of the strain tensor.

Panel c) shows  $Pi-D_e$ . Although the positive/negative patterns in  $Pi-D_e$  are similar to those in  $p\theta_e$ ,  $Pi-D_e$  presents clear differences, especially near the null region where  $Pi-D_e$  has the opposite sign of  $p\theta_e$  along the separatrices. Moreover, along the separatrices,  $|Pi-D_e| > D_{ze}$  and they share the same sign, whereas in the region between the x-points,  $Pi-D_e < 0$  and  $D_{ze} > 0$ .

Panel d) shows 1D cuts of  $D_{ze}$  (blue line),  $p\theta_e$  (red line), and  $Pi-D_e$  (black line). We find that  $p\theta_e$  is highly variable and, on average, greater than  $D_{ze}$  and  $Pi-D_e$ . This is considerably different compared with the Harris current-sheet case (Pezzi et al., 2021) in which  $D_{ze}$  is the dominant energy-transfer proxy. However, this behaviour is consistent with turbulent simulations (Pezzi et al., 2021) and with observations of turbulent reconnection (Bandyopadhyay et al., 2021).

## 7.4 Discussion and Conclusions

The type of magnetic reconnection that occurs from a turbulent cascade (Servidio et al., 2010a; Loureiro and Boldyrev, 2020; Fadanelli et al., 2021; Agudelo Rueda



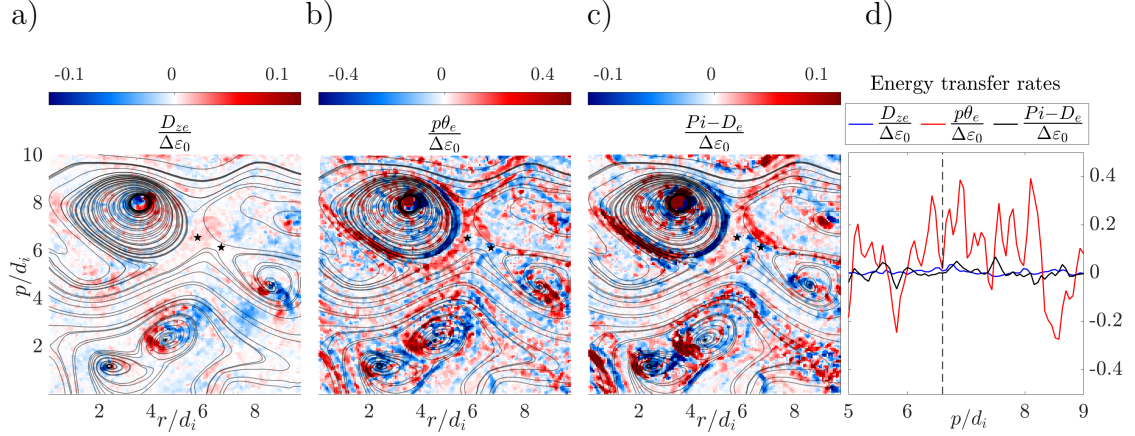


**Figure 7.7:** Damping and heating proxies at the simulation time  $t = 120\omega_{pi}^{-1}$ . 2D cuts in the  $rp$ -plane of a) The Zenitani parameter for electrons  $D_{ze}$ . b) Diagonal part of the strain-pressure interaction  $p\theta_e$ . c) Off-diagonal part of the strain-pressure interaction  $Pi-D_e$ . d) 1D cut of these terms like in Figure 7.6.

et al., 2021) presents a more complex geometry of the diffusion region compared to its laminar counterpart. Likewise, the geometry of the regions with enhanced energy transport and transfer is more complex. Moreover, in a 3D geometry, the particle motion along the out-of-plane direction allows energy transfer that 2D geometry precludes. For instance, the agyrotropic patterns in magnetic islands of 2D reconnection (Scudder and Daughton, 2008) are located in the diffusion region outside the magnetic islands. Conversely, in our 3D case, we observe agyrotropic patterns in the cross-section of the flux-ropes, which we call magnetic islands.

Since the plasma density is greater in the centers of the magnetic islands, these regions exhibit a greater plasma pressure compared to outside the islands. Patterns of agyrotropic plasma pressure are present, not only within the magnetic islands but also in the regions between them (Figure 7.3).

The non-uniform guide magnetic field present in this reconnection event affects its geometry. Despite the 3D nature of this event, for the diffusion region in which  $|\mathbf{B}|$  is negligible (no guide field), we observe gyrotropic/agyrotropic patterns (Section 7.3.1) similar to those observed in 2D laminar reconnection without guide field (Yin et al., 2001). However, given the complex geometry of our event, we do not observe gyrotropic/agyrotropic patterns matching 2D reconnection in the part of the diffu-

sion region below the x-points. Moreover, we do not observe a quadrupolar pattern of the in-plane component  $\Pi_{pr,e}$  (Figure 7.4d) within the diffusion region which is characteristic of agyrotropy in 2D reconnection without guide field (Yin et al., 2001).

In the reconnection event that we analyze, although of turbulent nature, the out-of-plane electron motion is consistent with the 3D shape of electron diffusion regions observed in laboratory plasmas (Furno et al., 2005; Yoo et al., 2013; Yamada et al., 2014).

In our event,  $d\varepsilon_e^k/dt > 0$  along the separatrices, and  $d\varepsilon_e^k/dt < 0$  in the outer part of the reconnecting magnetic island (Figure 7.5a). This corresponds to the acceleration of electrons along the separatrices (Figure 7.5c) and the presence of a stagnation region. The shear between the flux ropes increases the electron thermal energy and pressure, and the bulk kinetic energy reduces at the stagnation point.

At the locations of the separatrices,  $\mathbf{u}_e \cdot \nabla \cdot \bar{\mathbf{P}}_e > 0$  (Figure 7.5b). This suggests electron streams that increase the electron pressure. Conversely,  $\mathbf{u}_e \cdot \nabla \cdot \bar{\mathbf{P}}_e < 0$  in the region between the x-points. This suggests electron streams that reduce the electron pressure and drive the plasma within the diffusion region to a local thermal equilibrium. While reconnection is occurring, the high-pressure electrons are allowed to fill the diffusion region.

Within the diffusion region, the electric field increases the electron kinetic energy density, and the work done by the electric field on the electrons  $-q_e n_e (\mathbf{u}_e \cdot \mathbf{E})$  partially balances with the advection of the electron pressure. This is consistent with previous studies (Fadanelli et al., 2021).

The irreversible electron energy density change  $\Xi_e^k$  (Figure 7.5e) is non-zero everywhere in the vicinity of the reconnecting structures. The quantity  $\Xi_e^k$  displays structures with positive and negative values within the magnetic islands, suggesting that collisional processes accelerate and decelerate electron bulk flows within the magnetic islands. Conversely, in the diffusion region, the positive value of  $\Xi_e^k$  indicates that electrons are irreversibly accelerated.

Unlike previous studies of turbulent reconnection (Fadanelli et al., 2021), we estimate the electron thermal energy transfer associated with each term of Eq. (7.8). Compared to the case of the kinetic power density, the thermal power density terms present stronger fluctuations. This is evident when comparing  $d\varepsilon_e^k/dt$  (Figure 7.5a) and  $d\varepsilon_e^{th}/dt$  (Figure 7.5f) as well as comparing  $\varepsilon_e^k \nabla \cdot \mathbf{u}_e$  (Figure 7.5c) and  $\varepsilon_e^{th} \nabla \cdot \mathbf{u}_e$  (Figure 7.5i). This difference suggests that the electron bulk flows more efficiently transport thermal energy density than bulk kinetic energy density.

The power density terms associated with the compression/expansion of the flow,  $\nabla \mathbf{u}_e : \bar{\mathbf{P}}_s$  and  $\varepsilon_e^{th} \nabla \cdot \mathbf{u}_e$ , exhibit a strong coherence with the electron motion along the reconnection separatrices. The electron streams gain thermal energy (i.e., heating) associated with the reconnection. This is consistent with simulations of fast collisionless reconnection at low  $\beta$  (Loureiro et al., 2013) and observations of magnetospheric reconnection (Chasapis et al., 2017; Holmes et al., 2019). The most important contribution to  $\nabla \mathbf{u}_e : \bar{\mathbf{P}}_s$  comes from the isotropic part of the strain-pressure term. Correspondingly,  $\varepsilon_e^{th} \nabla \cdot \mathbf{u}_e$  presents patterns similar to  $\nabla \mathbf{u}_e : \bar{\mathbf{P}}_s$ . Moreover, the contribution of the off-diagonal elements in  $\nabla \mathbf{u}_e$  and  $\bar{\mathbf{P}}_e$  to the thermal energy transport is less than the isotropic contribution, which is consistent with previous studies of turbulent reconnection (Fadanelli et al., 2021; Bandyopadhyay et al., 2021). The terms associated with electron compressibility  $\varepsilon_e^{th} \nabla \cdot \mathbf{u}_e$  and  $\nabla \mathbf{u}_e : \bar{\mathbf{P}}_s$  are typically greater than the heat-flux contribution  $\nabla \cdot \mathbf{h}_s$ , suggesting that compressible thermal energy density transport is important for electrons in collisionless reconnection.

Similar to the irreversible kinetic energy density transfer  $\Xi_e^k$ , the irreversible thermal energy transfer  $\Xi_e^{th}$  is non-zero within the reconnecting structures as well as within the diffusion region. Moreover, electrons irreversibly gain thermal energy density at the location of the separatrices and within the diffusion region.

Comparing our results with damping ( $D_{z,e}$ ) and heating ( $p\theta_e$  and  $Pi-D_e$ ) proxies (Pezzi et al., 2021), we observe that fluctuations of  $p\theta_e$  inside the diffusion region (Figure 7.7d) are typically greater than fluctuations of  $D_{z,e}$  and  $Pi-D_e$ . This is consistent with results from turbulent simulations (Pezzi et al., 2021) and observa-

tions of turbulent reconnection (Bandyopadhyay et al., 2021), but not with results from simulations of laminar reconnection (Scudder and Daughton, 2008; Pezzi et al., 2021). The proxies  $p\theta_e$  and  $Pi-D_e$  share the same signs at most locations in our simulation domain. However, in the diffusion region near the null region, the opposite signs of  $Pi-D_e$  and  $p\theta_e$  suggest that agyrotropic heating mechanisms can emerge to compensate for any reduction or increase in the thermal energy density due to isotropic heating mechanisms.

The positive values of  $D_{z,e}$  and the negative value of  $p\theta_e$  and  $Pi-D_e$  in the region between the x-points suggest that electrons gain kinetic energy density from the fields while losing thermal energy density.

## Chapter 8

# A method to reconstruct magnetic field from multi-spacecraft measurements in preparation of MagneToRE

In this chapter, I present my contribution to the mission concept “Magnetic Topology Reconstruction Explorer” (MagneToRE, [Maruca et al., 2021](#)). MagneToRE is a mission concept that will use a multi-spacecraft set-up consisting of one main spacecraft (hub) and a large number ( $\sim 24$ ) of 6U Cubesats (probes) that will carry magnetometers. The aim of MagneToRE is to study and characterise the interplanetary magnetic field at scales corresponding to the inertial range of turbulence. With this configuration, the mission budget fits into a SMEX or MIDEX envelope within NASA’s Explorer Program.

In section 8.2, I present the simulations and synthetic data that I use to develop a magnetic-field topology reconstruction method for a mission like MagneToRE. In Section 8.2.1, I describe the method itself, and in Section 8.3, I present our results. Finally, in Section 8.4, I present the discussion and conclusions from this study.

## 8.1 The Need of Multi-spacecraft Missions

The evolution of collisional and collisionless plasmas is largely determined by the topology of the magnetic field. The prediction of the energy cascade quantified by the spectral slope in the existing plasma turbulence models (see Chapter 4) depends on the geometric properties of the magnetic structures (Narita, 2018; Zhou et al., 2020). The geometry of the magnetic structures (e.g., their aspect ratio) is associated with the turbulence anisotropy. The anisotropy of the turbulent fluctuations that results from the turbulent cascade determines the energy dissipation channels. For instance, if  $k_{\perp} \gg k_{\parallel}$ , KAW modes can continue the cascade, and the energy is ultimately dissipated by resonant electrons (Leamon et al., 1999). Conversely, if  $k_{\perp} \ll k_{\parallel}$ , whistler waves or ion-cyclotron waves can continue the energy cascade (Stawicki et al., 2001), and resonant ions dissipate the energy. Moreover, the role of magnetic reconnection in the turbulent cascade is a matter of ongoing research (Franci et al., 2017; Loureiro and Boldyrev, 2017; Vech et al., 2018; Bhat et al., 2021, see also Chapter 6). To resolve this open question, multi-spacecraft measurements are required (Büchner, 2007; Viall and Borovsky, 2020).

For over 50 years, single-spacecraft missions have been our best tool to study space plasma with in-situ measurements. Although single-spacecraft missions have proven to be crucial for our understanding of plasma phenomena that occur in the solar wind and the Earth's magnetosphere, the use of 1D trajectories precludes the correct representation of the 3D characteristics of the plasma and, crucially, of the magnetic field.

Single-spacecraft missions have been wisely combined, whenever possible, to study events from multiple observation points. For instance, Phan et al. (2006) use measurements from ACE, Wind, Geotail, Stereo A, and Stereo B to study large-scale reconnection events in the solar wind. More recently, Parker Solar Probe and Solar Orbiter have been used jointly to study the radial evolution of the solar wind properties (Jannet et al., 2021; Telloni et al., 2021). However, the use of combined single spacecraft is very limited to certain observation windows defined by the spacecraft orbits. Therefore, a longitudinal study in which the plasma properties are mea-

sured over long periods of time spanning multiple days is very challenging with this approach. To overcome this limitation, multi-point measurement missions such as THEMIS (Angelopoulos, 2009), Cluster (Escoubet et al., 1997) and Magnetospheric Multi Scale (MMS, Burch et al., 2016) were designed to study plasma properties using four spacecraft. Moreover, multi-spacecraft mission concepts (DeForest et al., 2019; Klein et al., 2019; Maruca et al., 2021) have flourished in recent years as the need for multi-point measurements has become evident to understand the 3D character of the mechanisms involved in the energy evolution in collisionless plasmas.

MagneToRE is designed to study the mesoscales, i.e. the inertial range in the turbulent jargon, see Figure 8.1. Although mesoscales are routinely covered but single space craft, there is no multi-spacecraft mission that has ever catalogued 3D magnetic structures and their properties, namely morphology (shape), topology (inter-linking), and interactions. MagneToRE has three main objectives: *i*) “Determine the 3-D morphology and topology of mesoscale IMF structures.”, *ii*) “Determine how time variations affect the mesoscale IMF” and *iii*) “Determine how the mesoscale IMF varies with solar-wind conditions”. To achieve these objectives, MagneToRE would carry observation windows of at least one hour on the solar wind for multiple periods over at least one year. Under these time-window conditions, there are several orbits that can be used. e.g., lunar orbit or L1 orbit to name a few.

## 8.2 Case Study: Magnetic Field Reconstruction

For the MagneToRE mission, the required reconstruction method must resolve the geometry and topology of the magnetic field in the solar wind, which is a turbulent environment (see Chapter 4). In addition to the background turbulence, there is a broad range of magnetic structures present in the solar wind, e.g., magnetic flux-ropes (Moldwin et al., 2000; Janvier et al., 2014) and magnetic clouds (Burlaga, 1991; Bothmer and Schwenn, 1997; Hu and Sonnerup, 2002). The topology of the magnetic field is highly complex. Therefore, the reconstruction method must be designed, calibrated, and tested against different magnetic configurations. For this purpose, we produce a set of synthetic data in a simulation box with dimensions

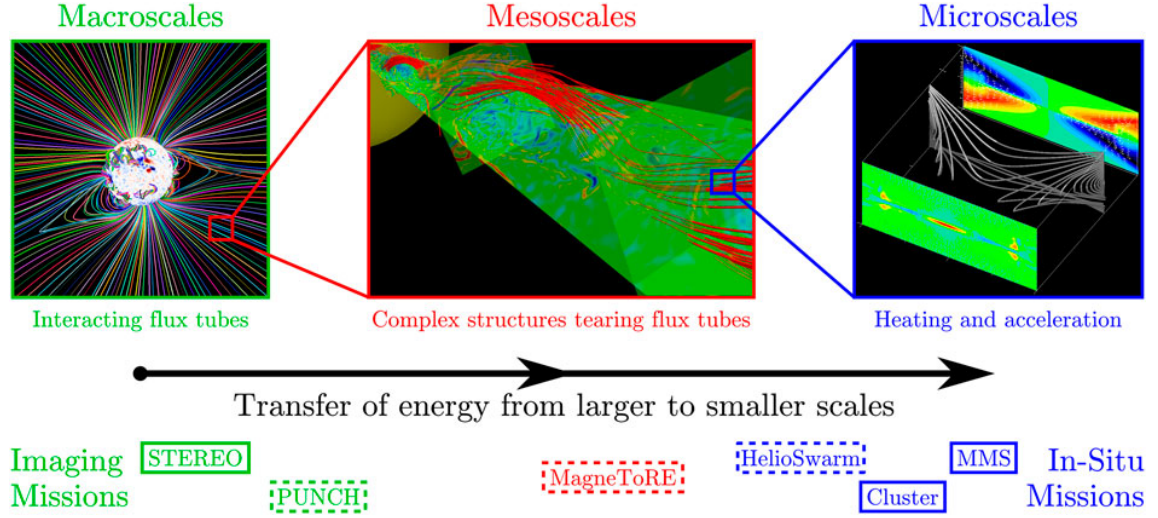


**Figure 8.1:** Representation of the macroscales (left), mesoscales (middle) and microscales (right) in the interplanetary magnetic field (IMF) and of the scales covered by multi-spacecraft missions past/present (solid) and future (dashed). Adapted from [Maruca et al. \(2021\)](#)

$L_x = L_y = L_z = 40d_i$ . The set consists of:

- A magnetic dipole oriented along the  $\hat{z}$ -direction (Figure 8.2a). The Cartesian components of the magnetic dipole are

$$B_x = \frac{\mu_0}{4\pi} \frac{3M(x-x_0)(z-z_0)}{r^5}, \quad (8.1)$$

$$B_y = \frac{\mu_0}{4\pi} \frac{3M(y-y_0)(z-z_0)}{r^5}, \quad (8.2)$$

$$B_z = \frac{\mu_0}{4\pi} \frac{M(3(z-z_0)^2 - r^2)}{r^5}, \quad (8.3)$$

where  $x_0 = L_x/2, y_0 = L_y/2, z_0 = L_z/2$  are the coordinates of the dipole's centre,  $M$  is a constant that represents the dipole magnetic moment and,  $r = \sqrt{(x-x_0)^2 + (y-y_0)^2 + (z-z_0)^2}$ . For simplicity, we set  $M = 4\pi/\mu_0$  and we use non-dimensional units for the magnetic field.

- Multiple dipoles oriented along the  $\hat{z}$ -direction (Figure 8.2b). The centres of eight dipoles described by Eqs. (8.1) through (8.1) are randomly selected in the simulation box.
- A flux-rope oriented along the  $\hat{x}$ -direction (Figure 8.2c). Following [Inoue and](#)



Kusano (2006), we model the magnetic field  $\mathbf{B}$  of a flux-rope centred at  $L_0 = L_y/8$  and  $h = L_z/16$  as the superposition of an external (if  $r_c > r_0$ ) magnetic field  $\mathbf{B}^{out}$  and an internal (if  $0 < r_c < r_0$ ) magnetic field  $\mathbf{B}^{in}$ , so that  $\mathbf{B} = \mathbf{B}^{out} + \mathbf{B}^{in}$ . The external field is a uniform dipole elongated along the  $\hat{x}$ -direction, and the internal field is a co-axial force-free magnetic field. The distance from the centre of the flux rope is  $r_c = \sqrt{(y - L_0)^2 + (z - h)^2}$ , and  $r_0 = 10d_i$  is the boundary between the inner and external fields. The internal field is produced by an internal current

$$I_0 = 2r_0\pi B_c J_1(x_1), \quad (8.4)$$

where  $B_c = 0.01$  is the non-dimensional strength of the axial field,  $J_1(x_1)$  is the Bessel function of first kind and order 1, and  $x_1 = 2.4045$  is the first zero of the Bessel function  $J_0(x_1)$ . The Cartesian components of  $\mathbf{B}^{in}$  are

$$B_x^{in} = B_c J_0(\alpha r_c), \quad (8.5)$$

$$B_y^{in} = -B_c J_1(\alpha r_c) \frac{z - h}{\sqrt{(y - L_0)^2 + (z - h)^2}} + \frac{I_0}{2\pi} \frac{z + h}{\sqrt{(y - L_0)^2 + (z + h)^2}}, \quad (8.6)$$

$$B_z^{in} = B_c J_1(\alpha r_c) \frac{y - L_0}{\sqrt{(y - L_0)^2 + (z - h)^2}} - \frac{I_0}{2\pi} \frac{y - L_0}{\sqrt{(y - L_0)^2 + (z + h)^2}}, \quad (8.7)$$

where  $\alpha = x_1/r_0$ . The Cartesian components of  $\mathbf{B}^{out}$  are

$$B_x^{out} = 0, \quad (8.8)$$

$$B_y^{out} = -\frac{I_0}{2\pi} \frac{z - h}{\sqrt{(y - L_0)^2 + (z - h)^2}} + \frac{I_0}{2\pi} \frac{z + h}{\sqrt{(y - L_0)^2 + (z + h)^2}}, \quad (8.9)$$

$$B_z^{out} = \frac{I_0}{2\pi} \frac{y - L_0}{\sqrt{(y - L_0)^2 + (z - h)^2}} - \frac{I_0}{2\pi} \frac{y - L_0}{\sqrt{(y - L_0)^2 + (z + h)^2}}. \quad (8.10)$$

- Three flux-rope oriented along the  $\hat{x}$ -direction (Figure 8.2d). The centres of the three flux-rope, where each one is described by Eqs. (8.5) through (8.10), are shifted by  $20d_i$  with respect to  $L_0$  and  $h$  to the positions  $(y - 20d_i, z + 20d_i)$ ,  $(y - 20d_i, z + 20d_i)$ , and  $(y - 20d_i, z - 20d_i)$ .

Additionally, I use a simulation of anisotropic Alfvénic turbulence based on the same configuration of 8 counter-propagating anisotropic Alfvén waves as in Section 5.2. The dimension of the simulation domain in this latter case is  $L_x = L_y = 18d_i$  and  $L_z = 63d_i$  (Figure 8.3).

### 8.2.1 Reconstruction Method

To produce synthetic measurements of the magnetic field components  $B_x, B_y$ , and  $B_z$  that emulate the transit of spacecraft through the solar wind plasma, we trace 1D trajectories along the  $\hat{z}$ -direction and throughout the simulation domain. We consider a magnetometer data acquisition rate of  $10Hz$  and a typical value for the solar-wind speed of  $v_{sw} = 400km/s$ . These values and Taylor’s hypothesis (see Section 4.2.5) yield a spatial resolution of  $\Delta r = 0.3d_i$ .

The number of simultaneous 1D trajectories depends on the spacecraft configuration (SC) which will be discussed in Section 8.2.1.1. The combination of the different 1D trajectories in each SC constitutes a data set. The length of the arrays in each data set corresponds to  $L_z$  multiplied by  $\Delta r$ .

Our method for the reconstruction of the magnetic field is based on the interpolation algorithm *ParaView point volume interpolator*. This interpolation method generates a set of equally distributed points  $\mathbf{q}_N$  in a volumetric Cartesian domain of size  $M_x \times M_y \times M_z$ . The resolution of this domain is  $\Delta r$ .

This interpolation algorithm uses an interpolation kernel (IK) to estimate the value of a given function (Schoenberg, 1973), for instance the magnetic field  $\mathbf{B}_q$ , at each point  $\mathbf{q}$  of the set  $\mathbf{q}_N$ . The value  $\mathbf{B}_q$  is computed as the weighted average of the neighbouring measurements  $\mathbf{B}_p$  at the  $N$ -closest probe points  $\mathbf{p}$ .

The probe points  $\mathbf{p}$  for the interpolation correspond to positions of the measurements in the data set. Thus, the estimated value for the magnetic field at a given point  $\mathbf{q}$  is

$$\mathbf{B}_q = \frac{1}{N} \sum_{p=1}^N w_p \mathbf{B}_p, \quad (8.11)$$

where  $w_p$  is the normalised weight ( $\sum_{p=1}^N w_p = 1$ ) assigned by the IK to the measure-

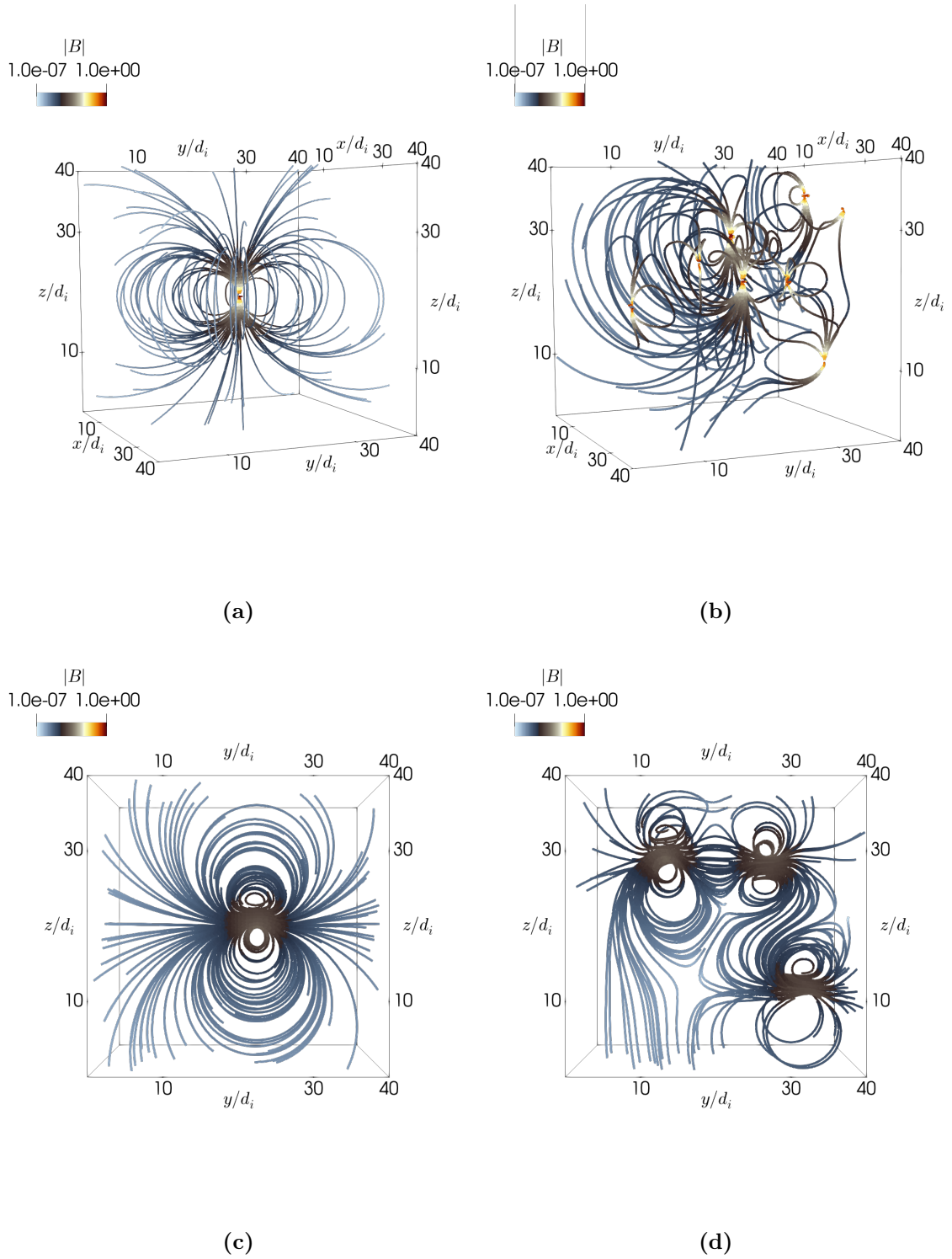


**Figure 8.2:** Synthetic data set designed to test the reconstruction method. Magnetic field lines for a) a dipole, b) multiple dipoles, c) a flux-rope, and d) multiple flux-rope. The magnetic-field lines are colour-coded with  $|\mathbf{B}|$  in logarithmic scale.

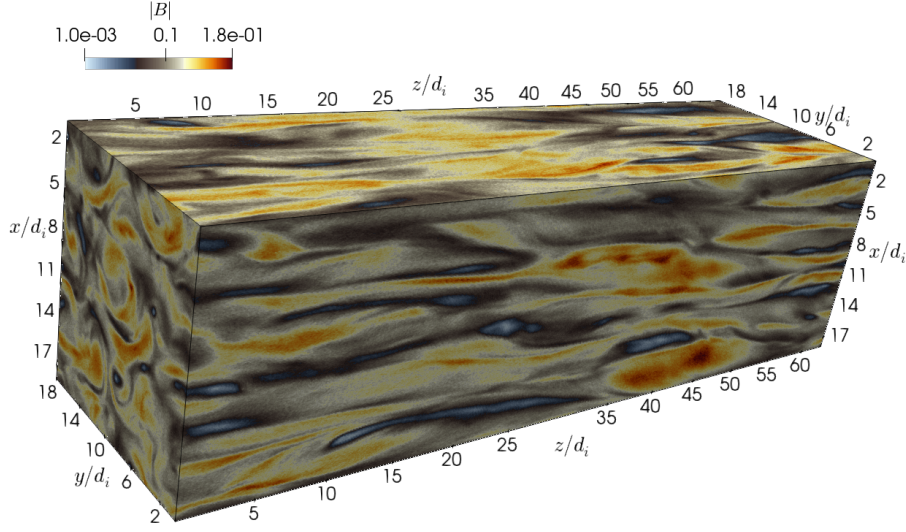


**Figure 8.3:** Magnetic field magnitude  $|\mathbf{B}|$  on the surface of the simulation domain in the turbulence case. The magnetic field shows elongated structures such as null regions (dark patches) and intense magnetic field regions (orange patches).

ment  $\mathbf{B}_p$ . Although several IKs can be employed to estimate  $w_p$  (Schoenberg, 1973; Maz'ya and Schmidt, 1996; Rasche et al., 1999; Romano-Díaz and Van De Weygaert, 2007; Hockney and Eastwood, 2021), the interpolation algorithm is sensitive to the IK. Therefore, the geometry of the reconstructed magnetic field is also sensitive to the selection of the IK.

The Voronoi interpolation kernel (Fortune, 1995; Rasche et al., 1999)<sup>1</sup> estimates  $w_p = 1$  for the  $B_p$  at the closest point  $\mathbf{p}$  to the point  $\mathbf{q}$ . The Euclidean distance between  $\mathbf{p}$  and  $\mathbf{q}$  is  $r_{pq} = \sqrt{(x_p - x_q)^2 + (y_p - y_q)^2 + (z_p - z_q)^2}$ . Using the Voronoi kernel, the estimated value for the magnetic field is

$$\mathbf{B}_q = B_p|_{\min(r_{pq})}, \quad (8.12)$$

where  $B_p|_{\min(r_{pq})}$  represents the magnetic field at the point  $p$  with the minimum distance to the point  $q$ , i.e., the closest neighbour point. Although this kernel is simple, the geometry of the reconstructed magnetic field is biased by the geometry of the Voronoi cells (Fortune, 1995), and the reconstructed magnetic field presents

<sup>1</sup><https://fossies.org/dox/ParaView-v5.9.1/classvtkVoronoiKernel.html>

sharp discontinuities at the boundaries of the cells.

The Gaussian IK (Rasche et al., 1999; Platte and Driscoll, 2005)<sup>2</sup> returns a reconstructed magnetic field with less sharp discontinuities at the boundaries. The weight is computed with the Gaussian IK as

$$w_p = c_p e^{-\left(\frac{sr_{pq}}{R}\right)^2}, \quad (8.13)$$

where  $R$  is the radius of the sphere containing the  $N$  closest points, and  $c_p$  is a normalisation coefficient. The parameter  $s$  is the sharpness which represents the rate of fall-off of the Gaussian. The estimated value for the magnetic field  $\mathbf{B}_q$  is then given by Eq. (8.11).

Although the Gaussian IK overcomes the limitations of the Voronoi IK, the performance of the reconstruction method for a given  $R$  depends on the SC. Thus, the parameter  $R$  must be adjusted based on the specific SC.

Alternatively, the selection of the  $N$  closest points  $p$  and computing the weights according to Eq. (8.13), where  $R$  is the distance from  $\mathbf{q}$  to the most distant  $\mathbf{p}$ , allows the use of the same set of parameters for different SCs.

### 8.2.1.1 Spacecraft Configurations (SC)

For a multi-spacecraft mission like MagneToRE, the SC depends on the mission orbital trajectory. The most simple SC is a planar distribution of the spacecraft in a plane perpendicular to the plasma flow. As long as Taylor's hypothesis is valid, a planar configuration has the advantage of capturing the 3D nature of the magnetic field.

To determine the number of spacecraft required to obtain an appropriate 3D picture of the magnetic field, we test four planar SC, namely C1 (4 spacecraft), C2 (8 spacecraft), C3 (16 spacecraft) and C4 (24 spacecraft) as shown in Figure 8.4. In C1, the four spacecraft are equally distributed on a circle centred at  $x_0, y_0$  with

---

<sup>2</sup><https://fossies.org/dox/ParaView-v5.9.1/classvtkGaussianKernel.html>

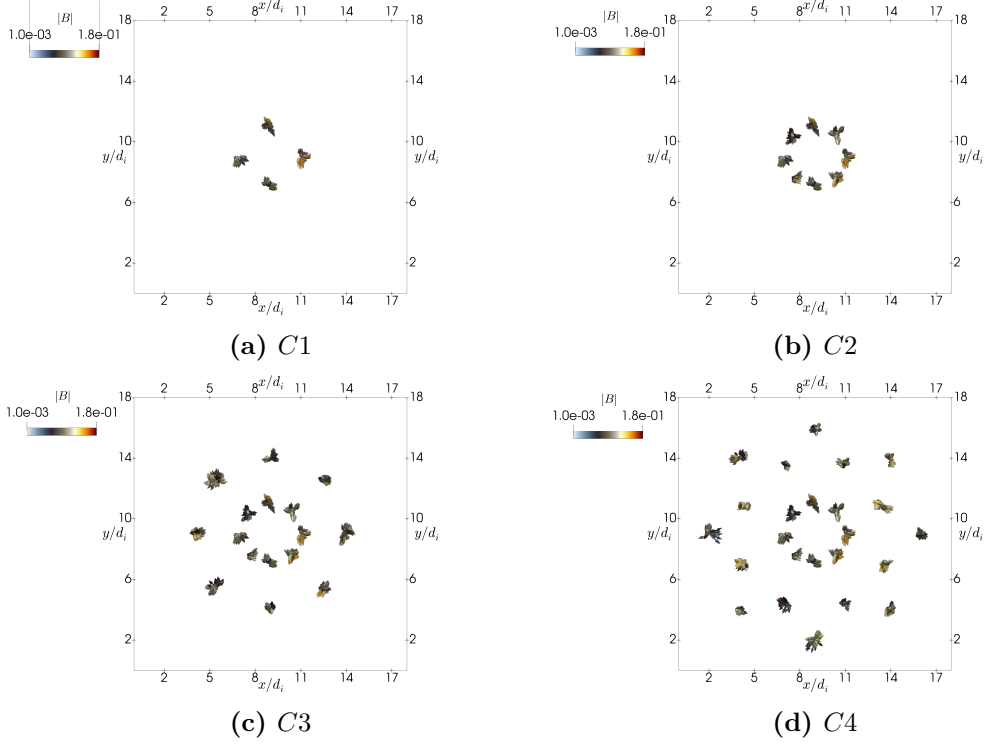


**Figure 8.4:** Spacecraft configurations a) C1: 4 spacecraft, b) C2: 8 spacecraft, c) C3: 16 spacecraft, and d) C4: 24 spacecraft in the  $xy$ -plane. Each bundle of arrows represents a point in the plane perpendicular to the direction of the spacecraft motion in the  $\hat{z}$ -direction. The arrows show the direction of the magnetic field at each point along the trajectory.

diameter  $d_1$  (Figure 8.4a). In C2, four spacecraft are added to C1 on the same circle for a total of eight spacecraft (Figure 8.4b). In C3, eight spacecraft are added to C2 in a concentric circle with diameter  $d_2$  for a total of 16 spacecraft. The spacecraft in the two concentric circles are aligned (Figure 8.4c). In C4, eight more spacecraft are added to C3 in a concentric circle with diameter  $d_3$  for a total of 24 spacecraft. The spacecraft in the outer-most circle are out of phase by  $\pi/6$  with respect to the spacecraft in the inner circles. The diameters of the circles fulfil  $d_1 < d_3 < d_2$  (Figure 8.4d). The diameters  $d_1$ ,  $d_2$ , and  $d_3$  required to accurately capture the geometry of the local magnetic field is practically defined based on the scale of interest  $\ell$ .

## 8.3 Results

We use a visual comparison between the original magnetic field  $\mathbf{B}_{org}$  and the reconstructed magnetic field  $\mathbf{B}_{rec}$  to select the kernel and parameters  $N$  and  $s$  (not shown here). We test the kernels and parameters across the set of synthetic data and the turbulent simulation. To apply the reconstruction method, we use a Gaussian kernel with  $N = 16$  points and  $s = 2$ . For the synthetic data set, the SCs are centred at  $x_0 = 20d_i$  and  $y_0 = 20d_i$ . For C1 and C2, we use  $d_1 = 20d_i$ . For C3,  $d_1 = 6d_i$  and  $d_2 = 20d_i$ . Additionally, for C4  $d_1 = 6d_i$ ,  $d_2 = 20d_i$ , and  $d_3 = 10d_i$ .

### 8.3.1 Magnetic Dipole

Panel a) in Figure 8.5 shows the 3D magnetic field lines of the synthetic magnetic field colour-coded with  $|\mathbf{B}|$  in a logarithmic colour scale. Panel b) shows the magnetic field lines of the reconstructed magnetic field for C1. The magnetic field lines of the reconstructed magnetic field exhibit a similar curvature like the magnetic dipole near the equatorial plane ( $10d_i < z < 30d_i$ ). However, in the polar regions ( $z < 10d_i$  and  $z > 30d_i$ ), the curvature of the reconstructed field lines is opposite to the input dipole.

Panel c) shows the magnetic field lines of the reconstructed magnetic field for C2. There is no improvement between C1 and C2 because the additional 4 measurement points in C2 add no significant extra information given the symmetry of the magnetic dipole. Panel d) shows the magnetic field lines of the reconstructed magnetic field for C3. The reconstructed magnetic field exhibits internal structure that is not captured by C2. There is a discontinuity in the curvature at the outer circle of C3 ( $d_2$ ) because the interpolation does not capture the rapid change in the magnetic field direction. The magnetic field lines of the reconstructed magnetic field for C4 (not shown here) are similar to the magnetic field lines in panel c), but with a less sharp discontinuity. Comparing panels a) to d), the spacecraft configuration C1 already captures the external dipolar nature of the magnetic field well. This is expected given the smoothness and uniformity of a magnetic dipole. However, a SC of concentric rings of spacecraft as C3 or C4 is necessary for capturing details and substructures.

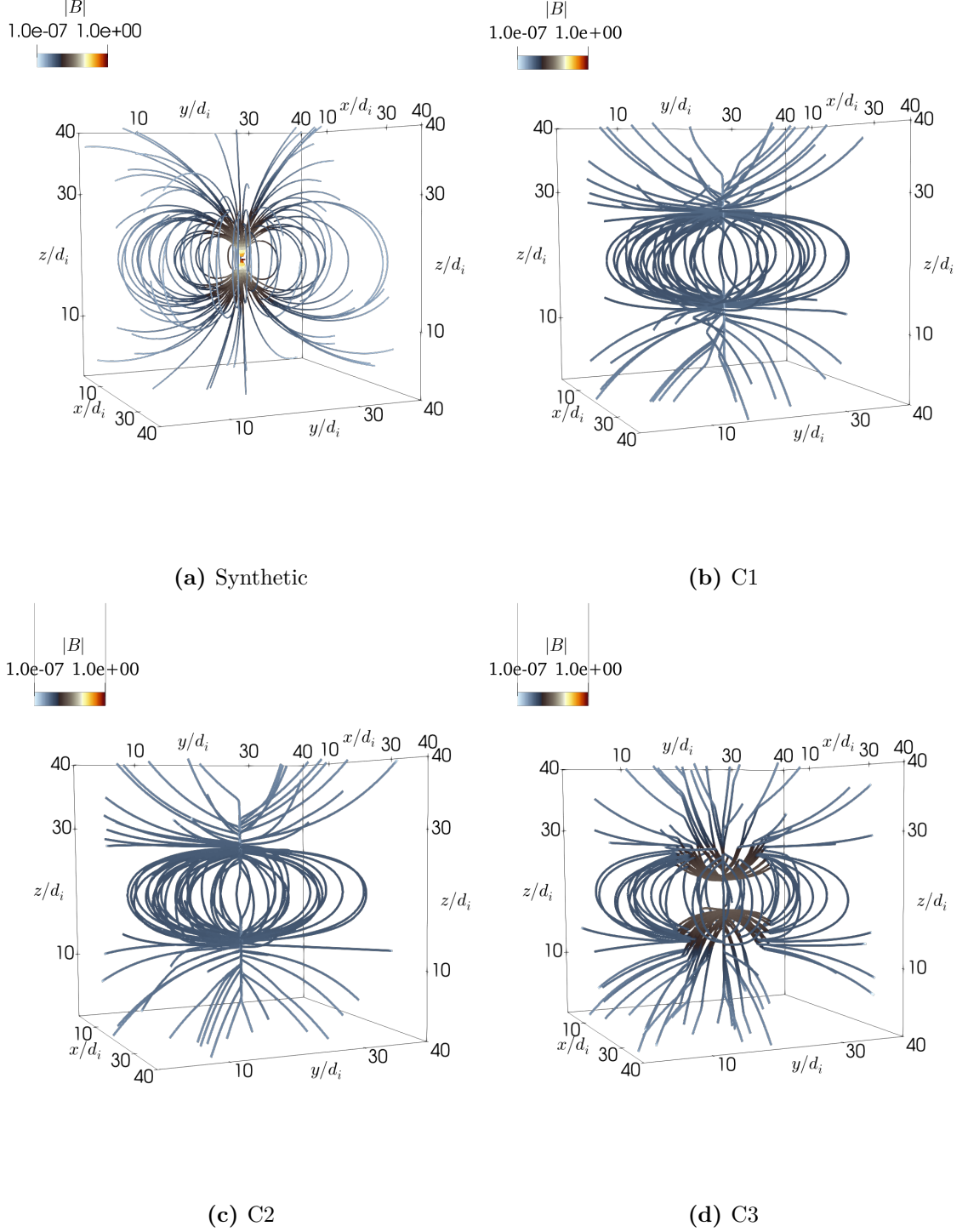


**Figure 8.5:** a) Magnetic field lines of the synthetic magnetic dipole. b) Reconstructed magnetic field for C1. c) Reconstructed magnetic field for C2. d) Reconstructed magnetic field for C3. The magnetic field lines are colour-coded with  $|\mathbf{B}|$  on a logarithmic scale.



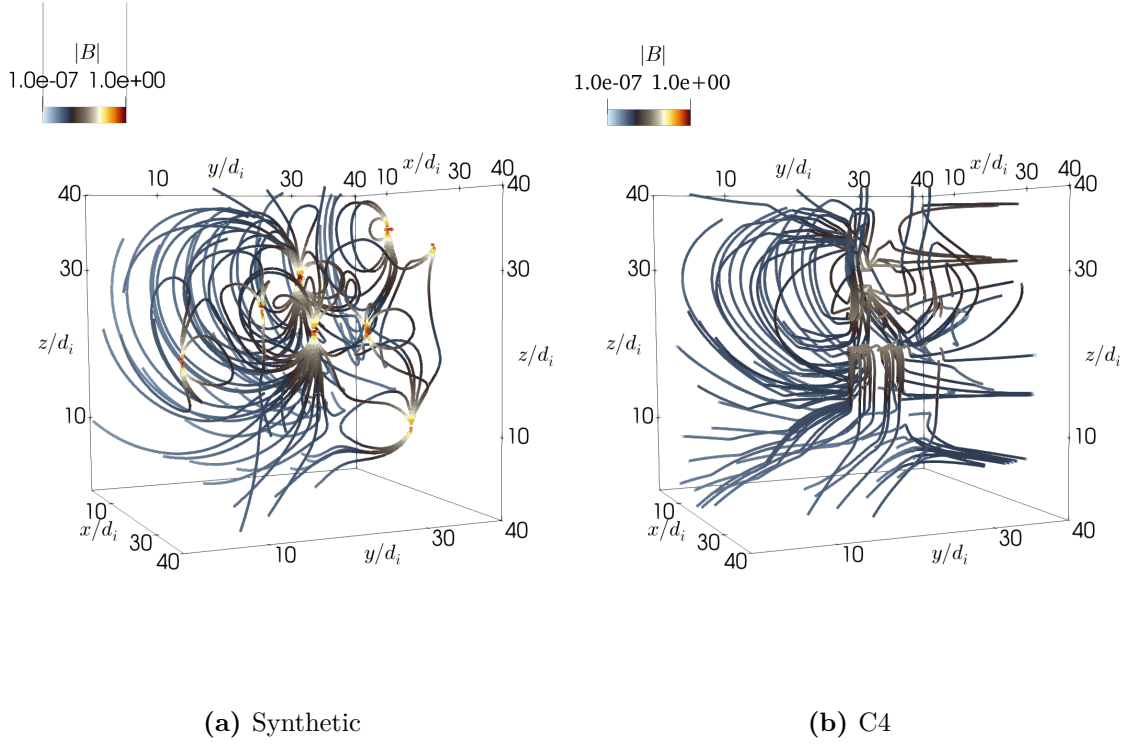


**Figure 8.6:** Magnetic field lines. a) Synthetic multiple magnetic dipoles. b) Reconstructed magnetic field of the multiple dipoles for C4. The magnetic field lines are colour-coded with  $|B|$  on a logarithmic scale.

### 8.3.2 Multiple Magnetic Dipoles

Panel a) in Figure 8.6 shows the magnetic field lines of the synthetic multiple magnetic dipoles. The magnetic field topology of multiple randomly located magnetic dipoles is clearly more complex than a single dipole. The reconstruction method for C1 (not shown here) captures the large-scale features of the magnetic field but not the details between the dipoles. Given the complexity of this magnetic field topology, it is worth showing the results for the best spacecraft configuration. Panel b) shows the magnetic field lines of the reconstructed magnetic field for C4. The reconstruction method captures some of the original complexity of the input data. However, it is unable to resolve individual magnetic structures near the centres of the magnetic dipoles.

### 8.3.3 Magnetic Flux-Rope

Panel a) in Figure 8.7 shows the magnetic field lines of the synthetic magnetic flux-rope oriented along the  $\hat{x}$ -direction. Panel b) shows the magnetic field lines of the

reconstructed magnetic field for C4. By comparison between panels a) and b), it is clear that the reconstruction method resolves the external shape of the magnetic topology, and two lobes are visible in panel b). However, the details of the inner part of lobes are lost.

#### 8.3.4 Multiple Magnetic Flux-Ropes

Panel a) in Figure 8.8 shows the magnetic field lines of the synthetic multiple magnetic flux-rope oriented along the  $\hat{x}$ -direction. Panel b) shows the magnetic field lines of the reconstructed magnetic field for C4. Like in the previous cases, the reconstructed magnetic field is similar to the input data at large scales. Unlike for the multiple magnetic dipole case (Figure 8.6), the reconstruction method correctly identifies sub-structure of the field: three different structures (dark lines) corresponding to the three flux ropes can be identified in the reconstructed field. The region where the magnetic-field lines separate at  $y \approx 17d_i$  and  $z \approx 12d_i$  is partially resolved by the method. This suggests that our method performs better for extended magnetic structures that have a smooth spatial variation (i.e., flux ropes) than for structures with sharp spatial variation (such as a combination of dipoles).

#### 8.3.5 Turbulent Magnetic Field

For the turbulent simulation, the SCs are centred at  $x_0 = 9d_i$  and  $y_0 = 9d_i$ . For C1 and C2, we use  $d_1 = 14d_i$ . For C3,  $d_1 = 4d_i$  and  $d_2 = 14d_i$ . Additionally for C4,  $d_3 = 10d_i$ . Panel a) in Figure 8.9 shows the 3D magnetic field lines of the synthetic magnetic field colour-coded with  $|\mathbf{B}|$  on a linear colour scale. The magnetic field lines are mainly oriented along the  $\hat{z}$ -direction. There are distinct regions with high/low  $|\mathbf{B}|$ . The magnetic field lines present local variations in direction and regions of high magnetic helicity, i.e., regions where the magnetic field lines are highly twisted.

Panel b) shows the magnetic field lines of the reconstructed magnetic field in the turbulence case for C2. The reconstructed magnetic field lines are less twisted than in the synthetic input data. Although C2 captures some of the regions with high  $|\mathbf{B}|$ , the position of these reconstructed regions is shifted with respect to their actual location in the input data.

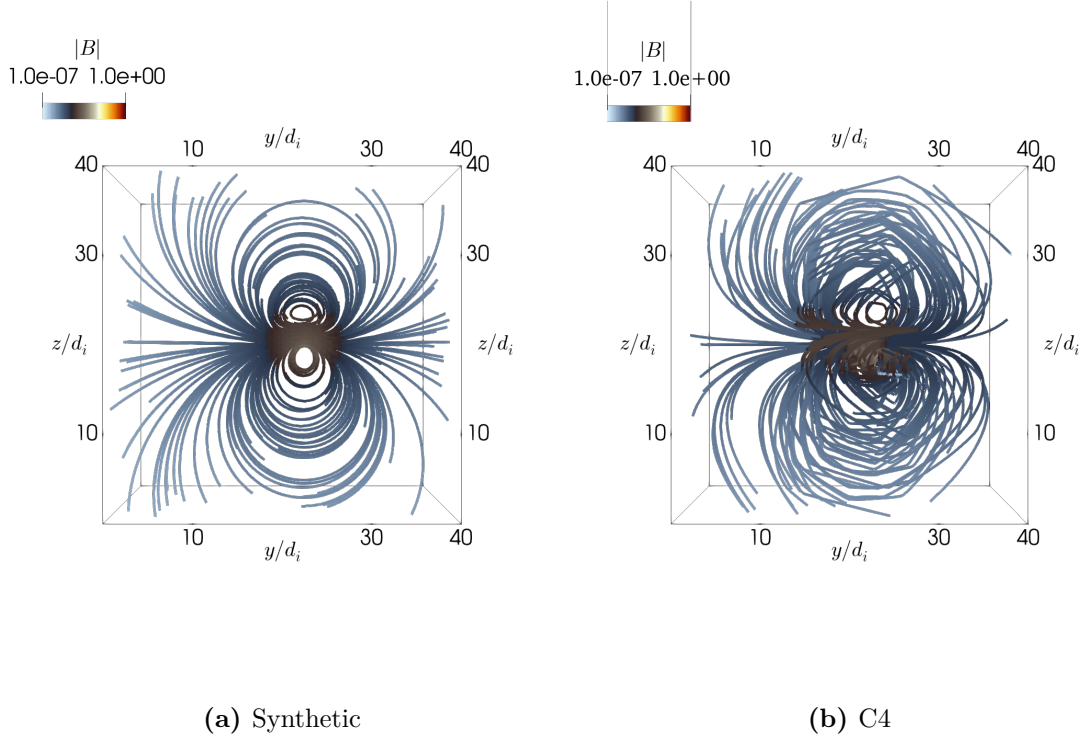


**Figure 8.7:** Magnetic field lines. a) Synthetic magnetic flux-rope. b) Reconstructed magnetic field of the flux-rope for C4. The magnetic field lines are colour-coded with  $|\mathbf{B}|$  on a logarithmic scale.

Panel c) shows the magnetic field lines of the reconstructed magnetic field for C3. As expected, the reconstructed magnetic field lines for a SC with multiple spacecraft rings capture more details. The position of the regions with high  $|\mathbf{B}|$  for C3 is closer to the synthetic data than for C2. However, the magnetic helicity is not recovered.

Panel d) shows the magnetic field lines of the reconstructed magnetic field for C4. The reconstructed magnetic field lines for these SC are more similar to the magnetic field lines of the synthetic input data than for the other configurations, as it clearly captures local details of the magnetic field, for instance, the intense magnetic field at  $x \approx 12d_i$  and  $z \approx 10d_i$ . Visually, the magnetic helicity is still not properly recovered though. This suggests that our method does not accurately capture the magnetic helicity of highly twisted structures with any of the chosen SCs.

### 8.3.6 Goodness of the Reconstruction Method

According to our qualitative analysis in Sections 8.3.1 through 8.3.5, the reconstruction method does not accurately capture structures below the spacecraft separation.

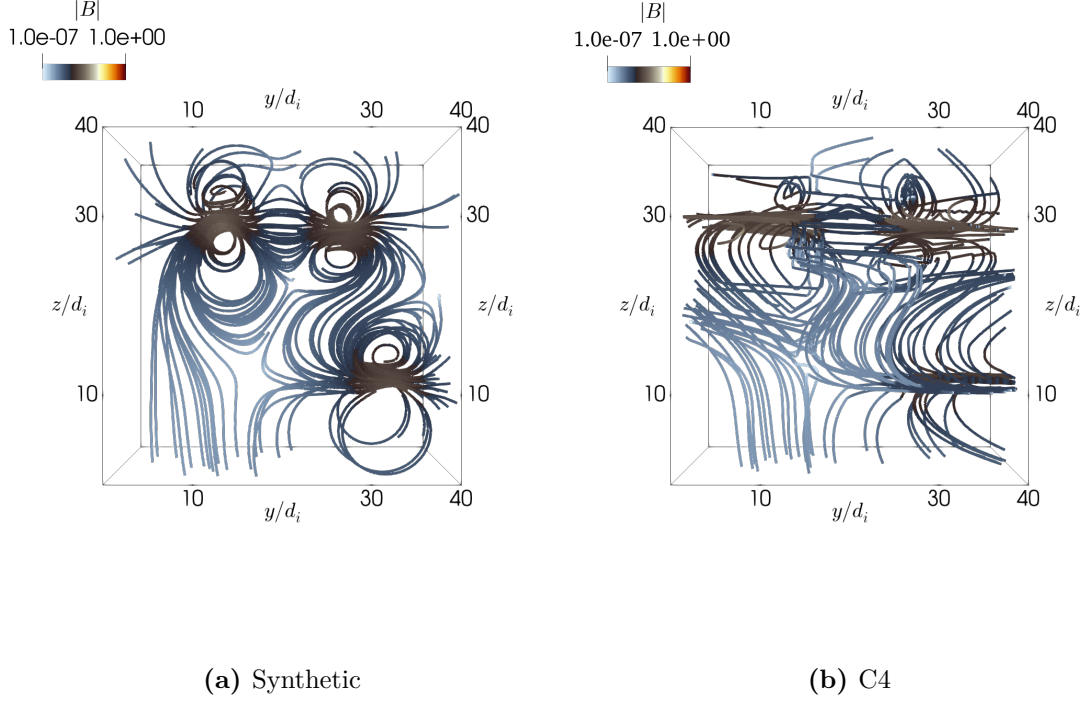


**Figure 8.8:** Magnetic field lines. a) Synthetic multiple magnetic flux-ropes. b) Reconstructed magnetic field of the multiple magnetic flux-ropes for C4. The magnetic field lines are colour-coded with  $|\mathbf{B}|$  on a logarithmic scale.

Nevertheless, the aim of the MagneToRE mission is to resolve magnetic structures at scales greater than  $d_i$  (Maruca et al., 2021). Therefore, we consider a  $3d_i$  coarse-grained down-sampling for  $\mathbf{B}_{org}$  and  $\mathbf{B}_{rec}$ . In this section, we only consider the reconstruction method using the spacecraft configuration C4 as it returns the best qualitative results.

To estimate the goodness of our reconstruction method, we define the point-wise error of the magnetic field strength

$$\epsilon_B = \frac{|\mathbf{B}_{org}| - |\mathbf{B}_{rec}|}{\langle |\mathbf{B}_{org}| \rangle}, \quad (8.14)$$

where

$$\langle |\mathbf{B}_{org}| \rangle = \frac{1}{V} \sum |\mathbf{B}_{org}|, \quad (8.15)$$

and  $V$  is the total number of cells. According to our definition in Eq. (8.14),  $\epsilon_B < 0$  in

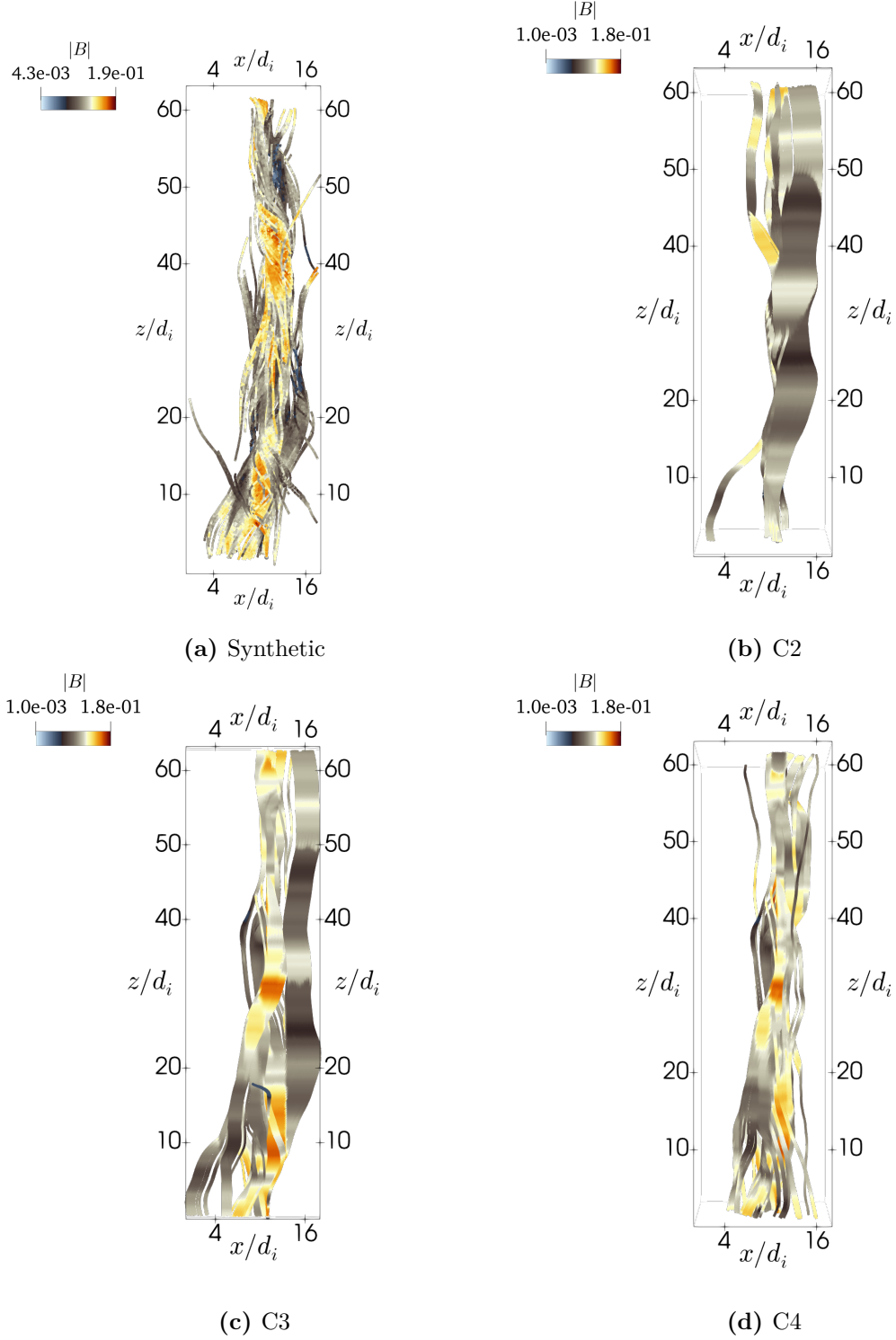


**Figure 8.9:** Magnetic field lines of the turbulence simulation data set designed to test the reconstruction method. a) Magnetic field lines of the synthetic input data. b) Reconstructed magnetic field lines for C2. c) Reconstructed magnetic field lines for C3. d) Reconstructed magnetic field lines for C4. The magnetic field lines are colour-coded with  $|\mathbf{B}|$  on a linear scale.

a given point represents  $|\mathbf{B}_{org}| < |\mathbf{B}_{rec}|$ , i.e., the reconstruction method overestimates the magnetic field strength  $|\mathbf{B}|$ . Conversely, if  $\epsilon_B > 0$  the reconstruction method underestimates  $|\mathbf{B}|$  in that point.

To quantify the goodness of the reconstruction method for obtaining the correct  $|\mathbf{B}|$ , we compute the average absolute error

$$\langle |\epsilon_B| \rangle = \frac{1}{V} \sum |\epsilon_B|, \quad (8.16)$$

and the conditioned number of counts with  $|\epsilon_B|$  less than 30%:

$$CN_{\epsilon 0.3}(|\epsilon_B| < 0.3) = \frac{\text{Counts}(|\epsilon_B| < 0.3)}{N}, \quad (8.17)$$

where  $N_c$  is the total number of counts. Figure 8.10 depicts the point-wise error (Eq. 8.14) distribution for the synthetic data set. For the magnetic dipole case, panel (a),  $\langle |\epsilon_B| \rangle = 0.8$ , and the error distribution is asymmetric, showing that the reconstruction method overestimates  $|\mathbf{B}|$  more than underestimating it. According to Eq. (8.17),  $CN_{\epsilon 0.3} = 0.42$ . Thus, the reconstructed magnetic field strength differs by less than 30% of the  $\langle |\mathbf{B}_{org}| \rangle$  for 42% of the counts.

For the case of multiple magnetic dipoles, panel (b),  $\langle |\epsilon_B| \rangle = 0.78$ ,  $CN_{\epsilon 0.3} = 0.77$ , and the error distribution is slightly asymmetric towards positive  $\epsilon_B$  suggesting that the method underestimates  $|\mathbf{B}|$  on average.

For the case of the magnetic flux-rope, panel (c),  $\langle |\epsilon_B| \rangle = 0.95$ ,  $CN_{\epsilon 0.3} = 0.47$ , and the error distribution is slightly asymmetric towards negative  $\epsilon_B$ , showing that the method overestimates  $|\mathbf{B}|$  on average.

For the case of multiple magnetic flux-ropes, panel (d),  $\langle |\epsilon_B| \rangle = 1.13$ ,  $CN_{\epsilon 0.3} = 0.32$ , and the error distribution presents small peaks for  $|\epsilon_B| > 1$ , slightly skewed towards positive  $\epsilon_B$ . Thus, the method underestimates  $|\mathbf{B}|$  on average for this configuration.

To estimate the goodness of the reconstruction method in terms of obtaining the direction of  $\mathbf{B}$  correctly, we define the point-wise relative direction between  $\mathbf{B}_{org}$

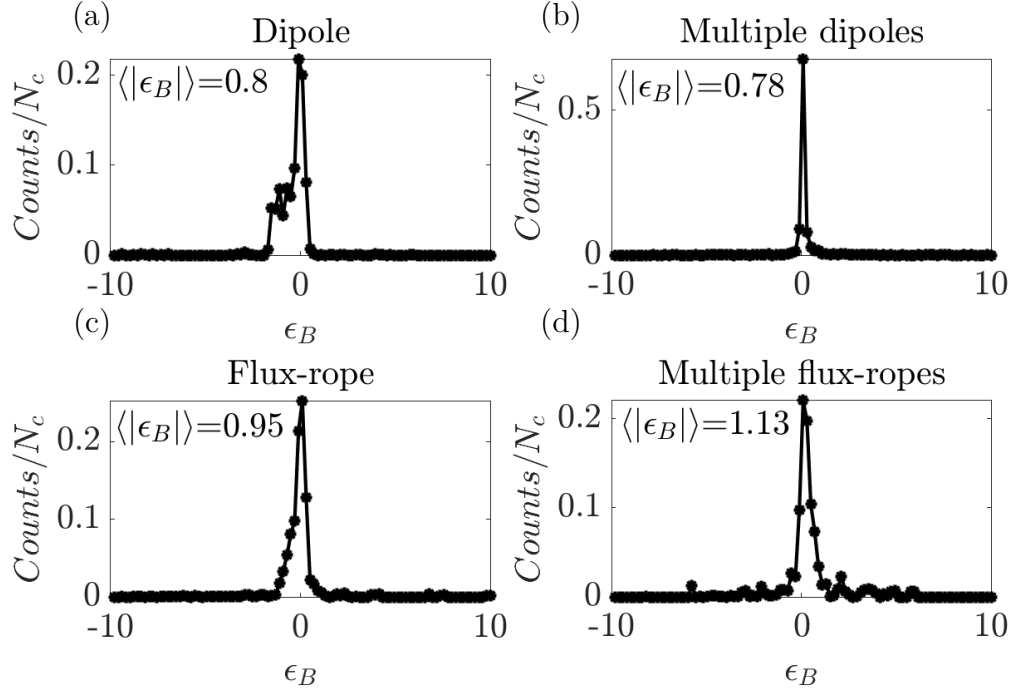


**Figure 8.10:** Point-wise error distribution for (a) the magnetic dipole, (b) multiple magnetic dipoles, (c) the magnetic flux-rope, and (d) multiple magnetic flux-ropes. The counts are normalised to the total number of counts  $N_c$ .

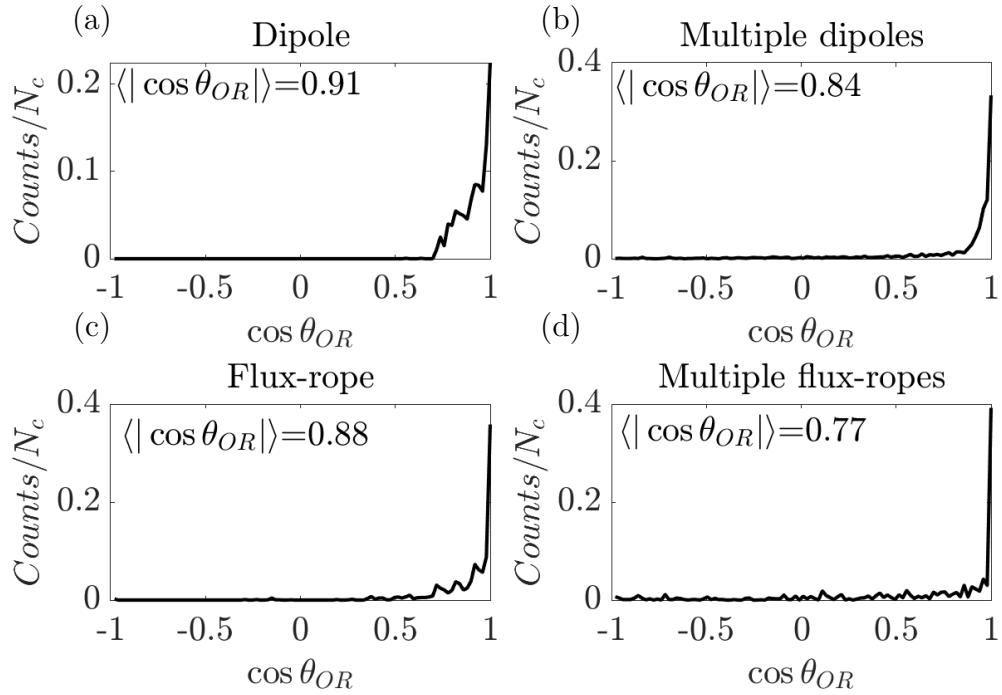


**Figure 8.11:** Point-wise relative direction distribution for (a) the magnetic dipole, (b) multiple magnetic dipoles, (c) the magnetic flux-rope, and (d) multiple magnetic flux-ropes.

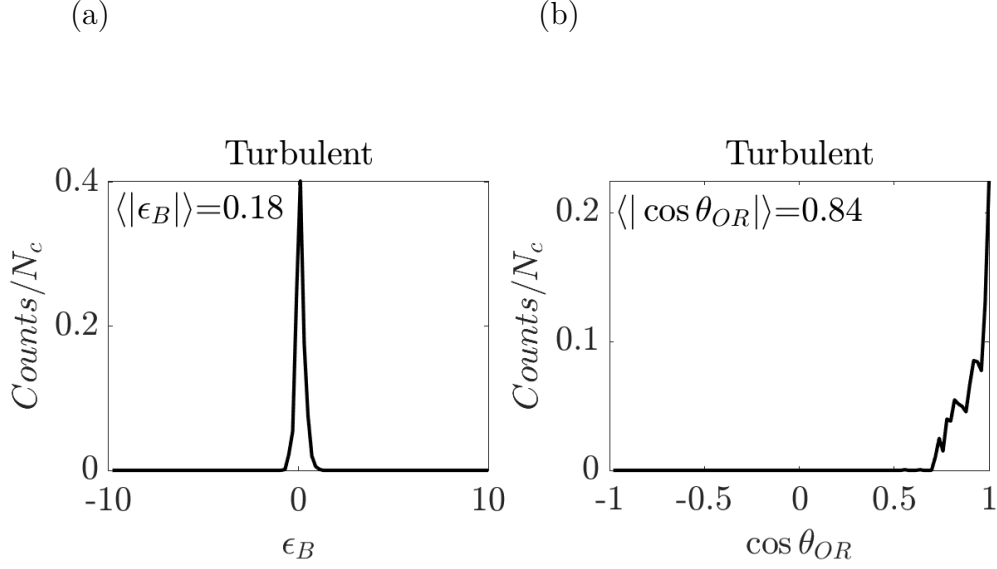


**Figure 8.12:** (a) Point-wise error distribution for the turbulence simulation. (b) Point-wise relative direction distribution for the turbulence simulation.

and  $\mathbf{B}_{rec}$  as

$$\cos \theta_{OR} = \frac{\mathbf{B}_{org} \cdot \mathbf{B}_{rec}}{|\mathbf{B}_{org}| |\mathbf{B}_{rec}|}. \quad (8.18)$$

If  $\cos \theta_{OR} \approx 1$ , the reconstruction method accurately estimates the direction of  $\mathbf{B}$  in that point. For comparison of the different configurations, we define the average absolute relative direction

$$\langle |\cos \theta_{OR}| \rangle = \frac{1}{V} \sum |\cos \theta_{OR}|. \quad (8.19)$$

Figure 8.10 depicts the point-wise relative direction (Eq. 8.18) distribution for the synthetic data set. For the magnetic dipole, panel (a), the direction of  $\mathbf{B}_{rec}$  deviates from the direction of  $\mathbf{B}_{org}$  up to  $45^\circ$  ( $\cos \theta_{OR} = 0.707$ ). Since  $\langle |\cos \theta_{OR}| \rangle = 0.91$ , the average deviation is  $\theta_{OR} = 24.49^\circ$ . For the multiple magnetic dipoles, panel (b),  $\langle |\cos \theta_{OR}| \rangle = 0.84$ . The average deviation in the relative direction is  $\theta_{OR} = 32.86^\circ$  which is greater than in the single dipole case. For the magnetic flux-rope, panel (c),  $\langle |\cos \theta_{OR}| \rangle = 0.88$ , and the average deviation in the relative direction is  $\theta_{OR} = 28.35^\circ$ . In the case of multiple magnetic flux-ropes, panel (d),  $\langle |\cos \theta_{OR}| \rangle = 0.77$ , and the average deviation in the relative direction is  $\theta_{OR} = 39.64^\circ$ .



Magnetic structure	$\langle  \epsilon_B  \rangle$	$CN_{\epsilon 0.3}$	$\langle  \cos \theta_{OR}  \rangle$
Dipole	0.80	0.42	0.91
Multiple dipoles	0.78	0.77	0.84
Flux-rope	0.95	0.47	0.88
Multiple flux-ropes	1.13	0.32	0.77
Turbulent	0.18	0.64	0.84

**Table 8.1:** Parameters to estimate the goodness of the reconstruction method.

For the turbulent scenario, panel (a) in Figure 8.12 depicts the point-wise distribution of errors  $\epsilon_B$ . Compared to the previous cases, the average absolute error is small,  $\langle |\epsilon_B| \rangle = 0.18$ . Moreover, since  $CN_\epsilon = 0.64$ , the reconstructed magnetic field differs less than 30% in 64% of the points. Panel (b) in Figure 8.12 shows the point-wise distribution of relative directions  $\cos \theta_{RO}$ . Since  $\langle |\cos \theta_{OR}| \rangle = 0.84$ , the average deviation in the magnetic field direction is  $\theta_{OR} = 32.86^\circ$ . This value is comparable with the average deviation of the multiple magnetic dipoles case. We summarise the values of the aforementioned parameters for each magnetic configuration in table 8.1.

## 8.4 Discussion and Conclusions

We study the three-dimensional geometric properties of magnetic structures in space plasmas using multi-point measurement methods. To estimate spatial gradients and volumetric tensors requires the use of at least four spacecraft (Harvey, 1998; Shen et al., 2003, 2007). Linear approximation methods, such as trilinear methods (Haynes and Parnell, 2007) and first-order Taylor expansion methods (Fu et al., 2016; Chen et al., 2019; Broeren et al., 2021), are widely used due to their simplicity. In this chapter, we present an alternative magnetic reconstruction method designed for the mission concept MagneToRE (Maruca et al., 2021). The method is based on an interpolation algorithm that uses a Gaussian interpolation kernel. The method is tested against a set of synthetic data representing different characteristic magnetic topologies. Moreover, four planar spacecraft configurations are tested to assess the impact of the number of spacecraft and their relative orientation on the reconstruction method.

The magnetic reconstruction method accurately captures the magnetic topology for simple magnetic structures, such as a single magnetic dipole. For more complex configurations, our method captures the large-scale geometry of the magnetic field even with simple spacecraft configurations such as C1 and C2, as long as the spatial variation of the magnetic field is smooth. Conversely, the method does not recover complex magnetic topologies that involve sharp spatial variations at scales smaller than the spacecraft separation. This caveat is generally shared among multi-spacecraft methods (Robert et al., 1998; Forsyth et al., 2011).

The use of spacecraft configurations with multiple spacecraft rings, e.g., C3 and C4, allows the method to capture more complex structures. This is especially important for turbulent environments like the solar wind in which the local magnetic field is highly twisted.

In Section 8.3.6, we estimate the goodness of our reconstruction method. Although our qualitative analysis for the magnetic dipole (Section 8.3.1) suggests an accurate representation, the average absolute error  $\langle |\epsilon_B| \rangle = 0.8$  is greater than in the turbulent case where  $\langle |\epsilon_B| \rangle = 0.91$ . This is because our method does not capture the region of most intense magnetic field (the centre of the dipole). Nevertheless, our method accurately estimates the direction of the magnetic field for this case with a deviation of about  $24.49^\circ$ . The least accurate reconstructed magnetic field, both in terms of the  $\langle |\epsilon_B| \rangle = 1.13$  and  $\langle |\cos \theta_{OR}| \rangle = 0.77$ , is the multiple magnetic flux-rope configuration. Our method underestimates the magnetic field strength and poorly estimates the direction of  $\mathbf{B}$  for this configuration. This is due to the orientation of the magnetic structures relative to the direction of travel of the spacecraft configuration. This geometric effect also explains that, for this study, the reconstructed turbulent magnetic field is more accurate with  $\langle |\epsilon_B| \rangle = 0.18$  and  $\langle |\cos \theta_{OR}| \rangle = 0.84$ . Thus, our reconstruction method strongly depends on the relative orientation between the direction of propagation of the spacecraft formation and the magnetic structures. However, over a longer time interval, the solar wind will naturally provide the constellation with different alignments and geometries.

Although the work presented in this chapter is still in progress as the mission concept MagneToRE is under development, it is an important contribution since it permits to identify the limitations of reconstruction methods. For instance, the spacecraft separation must be chosen according to the scales of interest. Moreover, magnetic field reconstruction methods based on interpolation algorithms must be calibrated to account for any underestimation of the magnetic field direction and of the magnetic helicity.

## Chapter 9

# Conclusions and Future Work

In this thesis, I explore the links between turbulence and magnetic reconnection in plasma conditions similar to the solar wind. Particularly, I develop an understanding of the geometric and energy transfer properties associated with the type of reconnection events that occur self-consistently as part of an anisotropic turbulent cascade.

In my first study, Chapter 6, we simulate plasma turbulence created by the collision of counter-propagating Alfvén waves with a wavevector anisotropy consistent with the GS95 theory of critical balance at the small-scale end of the inertial range. Our initial waves have wavenumbers near the spectral breakpoint from the inertial to the kinetic range of turbulence. This choice allows us to set up the system with Alfvén waves and let the system develop kinetic and compressive fluctuations in the kinetic range self-consistently and with an anisotropy reminiscent of the solar wind, with the aim of developing reconnection features consistent with solar-wind turbulence. The use of such a consistent anisotropy in the initial waves allows the system to undergo nonlinear interactions and to create flux ropes during the first nonlinear time, which is in agreement with earlier simulation work ([Grošelj et al., 2018](#)). Our initial anisotropic setup reduces the simulation time that a full 3D PIC simulation of turbulence without this imposed anisotropy would require in order to develop reconnection as a product of anisotropic turbulence.

We establish a set of indicators to find regions in which magnetic reconnection takes place in 3D PIC simulations consistent with existing reconnection theories. These indicators are based on the presence of current-sheet structures (C1), fast particles (C2), heated particles (C3), diffusion regions marked by energy transfer between fields and particles (C4), and non-zero parallel electric fields (C5). Since our method is based on thresholds for the bulk quantities, the selected regions correspond to high-intensity structures. Our method uses fast ions as an indicator (C2). Thus, this method does not identify all reconnection events, especially not those related to electron-only reconnection (Phan et al., 2018; Sharma Pyakurel et al., 2019; Mallet, 2020). In a follow-up study, it is worthwhile to investigate the role of the threshold level for the identification of reconnection sites and the relaxation of ion-based conditions to enable the identification of electron-only reconnection events. Our method is a first approach in the exploration of reconnection events in large 3D PIC simulations in which the handling of the kinetic particle information is computationally expensive due to the large number of particles. In a future work it is important to compare with novel methods (Scudder and Daughton, 2008; Liu and Hesse, 2016; Li et al., 2021) that are possibly applicable to 3D geometries without dimensional constraints.

Our data set possibly includes further reconnection sites that can be studied in more detail in the future. In future work, it would be interesting to study the changes in the particle distribution functions as a result of the identified small-scale reconnection events. Such a more detailed study of the associated particle kinetics will allow us to understand the energy exchange between fields and particles, and the details of the energy dissipation through small-scale reconnection events in the solar wind.

In my second study, Chapter 7, we derive a framework to quantify the collision-like effects that lead to irreversible energy transfer and thus dissipation in PIC plasmas. We identify and locate magnetic reconnection as a key mechanism for heating, damping, and dissipation in plasma turbulence in low-collisionality systems like the solar wind. In previous studies, the transfer and transport of energy in plasmas

with low collisionality has been investigated separately in simulations of reconnection (Hesse and Winske, 1998; Hesse et al., 2001a; Zenitani et al., 2011; Muñoz et al., 2017; Pucci et al., 2018; Pezzi et al., 2019, 2021) and turbulence (Wan et al., 2012; Yang et al., 2017; Li et al., 2019; Pezzi et al., 2021). The transfer and transport in magnetic reconnection that forms from a turbulent cascade have been limited to 2D geometries (Parashar et al., 2009; Fadanelli et al., 2021) and observations (Chasapis et al., 2018; Bandyopadhyay et al., 2020), while the 3D case has received little attention. We study, for the first time, the energy transport associated with 3D magnetic reconnection that occurs as a consequence of a turbulent cascade to a high level of detail and including all power density terms resulting from the full Boltzmann equation. We extend the analysis of similar studies (e.g., Fadanelli et al., 2021) by exploring the transfer and transport of kinetic and thermal electron energy.

The energy transfer and transport in collisionless plasmas is believed to be governed by non-thermal and kinetic mechanisms such as resonant (Marsch et al., 2003; Kasper et al., 2008) and non-resonant heating processes (Chandran et al., 2010, 2013). However, the irreversible energy transport must ultimately be associated with collisional effects (Schekochihin et al., 2009).

The agyrotropy signatures present in the reconnection diffusion region allow for agyrotropic energy transfer mechanisms such as agyrotropic-driven instabilities to take place in the diffusion region (Ricci et al., 2004a; Roytershteyn et al., 2012; Graham et al., 2017). Since similar signatures are also present in the reconnecting magnetic structures, it is expected that agyrotropic energy transfer occurs within the magnetic structures. A study of the instabilities that occur during a 3D turbulent reconnection event would be worthwhile to enhance our understanding of the collisionless energy dissipation mechanisms.

We show that the contribution to the energy density transfer from collisions is not negligible. To determine the exact source of this contribution, future work must use larger numbers of particles while keeping the 3D geometry. In addition, the inclusion of a controllable collision operator would allow for a detailed study of collisions in

3D reconnection ([Pezzi, 2017](#); [Donnel et al., 2019](#); [Boesl et al., 2020](#); [Pezzi et al., 2021](#)).

The general framework that we introduce is suitable for estimating the reversible and irreversible energy density transfer of the particle species in the solar wind. For instance, Eqs. (7.5) and (7.8) can be applied to spacecraft data to study the radial evolution of energy density as a function of heliospheric distance in the solar wind (see Appendix C). This work would be of interest both for the energetics of the solar-wind electrons ([Scime et al., 1994](#); [Innocenti et al., 2020](#)) and the solar-wind protons ([Matteini et al., 2007](#); [Hellinger et al., 2011](#); [Adhikari et al., 2020a](#))

Regarding the solar wind, the literature on magnetic reconnection is biased to the use of two-dimensional models due to their simplicity and their accurate description of reconnection events especially at the heliospheric current sheet ([Gosling et al., 2007](#); [Gosling, 2007](#); [Phan et al., 2009, 2020, 2021](#)). From the research that I present in Chapters 6 and 7, three-dimensional reconnection between turbulent magnetic structures presents more complex configurations of the diffusion region as well as of the exhausts than in the 2D case. Therefore, my research clearly emphasises the importance of 3D treatments to capture the physics of reconnection in turbulence accurately.

In spite of the unprecedented high-cadence measurements in the solar wind from Parker Solar Probe and Solar Orbiter, multi-spacecraft missions such as MMS and Cluster are required to explore the solar wind plasma at close distance from the Sun. The lack of simultaneous multi-scale measurements based on a large number of measurements points in the solar wind precludes the scientific community from forming a clear picture of three-dimensional reconnection. For this reason, new multi-spacecraft missions are required.

In my third study, Chapter 8, I present part of my contributions to the multi-spacecraft mission concept MagneToRE ([Maruca et al., 2021](#)). We propose a method to reconstruct the magnetic field using simultaneous multi-spacecraft measurements. The method uses a Gaussian interpolation kernel with a finite number of closest

neighbours. We test four different planar configurations of spacecraft using a set of synthetic magnetic field configurations with different degrees of topological complexity. We also test our method against turbulent simulations. In qualitative terms, our reconstruction method captures the magnetic field geometry at scales greater than the separation between spacecraft. However, the performance of our method depends on the relative direction between the direction of propagation of the spacecraft configuration and the orientation of the magnetic structures. Nevertheless, our method accurately reconstructs the magnetic field strength and direction in turbulent conditions which makes it suitable to be applied in the solar wind.

Future work requires the exploration of new multi-spacecraft methods to reconstruct the magnetic field topology. Additionally, the effect of spacecraft drifting on the performance of the different methods must be quantified to better assess the limitations of these methods. Finally, it is important to define a benchmark set of magnetic field configurations to evaluate all the available methods. My work sets a starting point for these important studies to underpin our understanding of turbulence and reconnection in the solar wind.



## Appendix A

# Second-order structure functions

Following [Cho and Vishniac \(2000\)](#), we define the local magnetic field between two points  $\mathbf{r}_1$  and  $\mathbf{r}_2$  as

$$\mathbf{B}_l = \frac{\mathbf{B}(\mathbf{r}_2) + \mathbf{B}(\mathbf{r}_1)}{2}. \quad (\text{A.1})$$

We define the coordinate parallel to  $\mathbf{B}_l$  as  $r_{\parallel} = \hat{z} \cdot (\mathbf{r}_2 - \mathbf{r}_1)$  and the coordinate perpendicular as  $r_{\perp} = |\hat{z} \times (\mathbf{r}_2 - \mathbf{r}_1)|$ , where  $\hat{z} = \mathbf{B}_l / |\mathbf{B}_l|$ . With these definitions, we calculate the second-order structure function of the magnetic fluctuations  $\mathbf{b}(\mathbf{r}_1) = \mathbf{B}_l - \mathbf{B}(\mathbf{r}_1)$  as

$$Fb2(r_{\perp}, r_{\parallel}) = \langle |\mathbf{b}(\mathbf{r}_2) - \mathbf{b}(\mathbf{r}_1)|^2 \rangle, \quad (\text{A.2})$$

where  $\langle \rangle$  represents the average over the spatial domain. In order to discretize the  $r_{\perp} r_{\parallel}$ -plane, we calculate the values of  $r_{\perp}$ ,  $r_{\parallel}$ , and  $Fb2$  for each pair of points  $\mathbf{r}_1, \mathbf{r}_2$ . Then, for each pixel, we calculate the mean value as the sum of all  $Fb2$  divided by the number of combinations  $(\mathbf{r}_1, \mathbf{r}_2)$  in each pixel. We apply a filter to remove the pixels with less than  $\sqrt{N}$  combinations, where  $N$  is the total number of combinations in the  $r_{\perp}, r_{\parallel}$  space.

Figure A.1 shows  $\log(Fb2)$  in the  $r_{\perp}, r_{\parallel}$ -plane for the time steps  $t = 0, t = 12/\omega_{pi}, t = 120/\omega_{pi}$ , and  $t = 240/\omega_{pi}$ . At  $t = 12/\omega_{pi}$ , the structure function indicates a perpen-

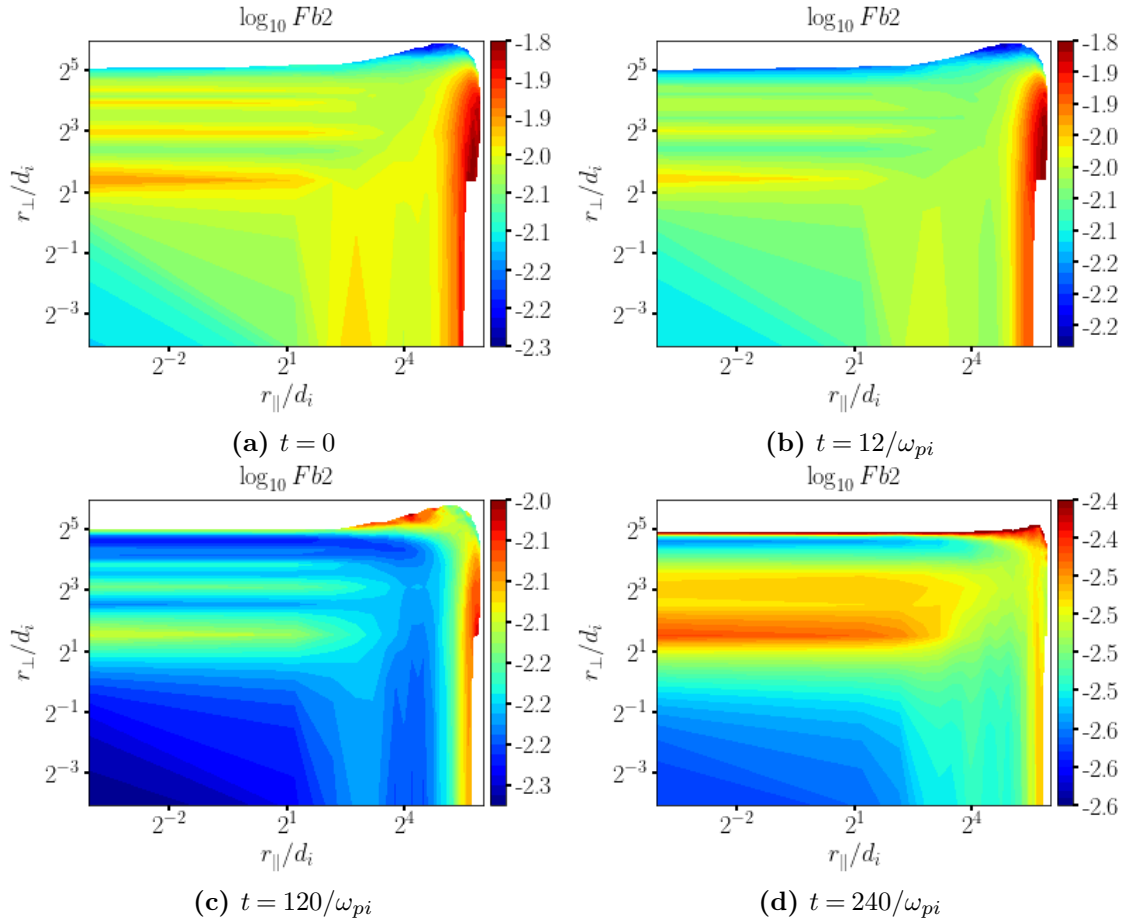


**Figure A.1:** Second-order structure functions of the magnetic fluctuation  $\mathbf{b}$  in the  $r_{\perp}, r_{\parallel}$ -plane as  $\log_2 Fb2$  at  $t = 0/\omega_{pi}$  (a),  $t = 12/\omega_{pi}$  (b),  $t = t_R$  (c), and  $t = 240/\omega_{pi}$  (d). At  $t = 0$ , while the magnetic energy is distributed across multiple perpendicular scales, it is mainly stored at large parallel scales. At  $t = t_R$ , the magnetic energy is distributed across multiple parallel scales.

dicular cascade of the magnetic energy. On the other hand, the structure function does not give evidence of a strong parallel cascade and is, instead, still consistent with our initial conditions in terms of the parallel extent of the magnetic-field fluctuations. At  $t = 120/\omega_{pi}$ , the green horizontal structure suggests that the magnetic energy has been redistributed and cascaded to smaller parallel scales. The analysis of the structure functions is consistent with our analysis of the Fourier spectra in Figure 6.5 in Section 6.3.2.

## Appendix B

# Detailed Derivation of the Energy Equations

### B.1 Derivation of the Equations for the Energy Densities

To derive the  $n$ th moment of the Boltzmann equation (7.1), we take the dyadic product of Eq. (7.1) with  $\mathbf{v}^n$  on the left and integrate over the entire velocity space.

The zeroth moment

$$\int \left[ \frac{\partial f_s}{\partial t} + \mathbf{v} \cdot \nabla f_s + \frac{q}{m} (\mathbf{E} + \mathbf{v} \times \mathbf{B}) \cdot \nabla_v f_s \right] d^3v = \int \left( \frac{\partial f_s}{\partial t} \right)_c d^3v, \quad (\text{B.1})$$

leads to

$$\frac{\partial n_s}{\partial t} + \nabla \cdot (n_s \mathbf{u}_s) = \Xi_s^0. \quad (\text{B.2})$$

If we assume the number of particles in velocity space to remain constant as collisions proceed,  $\Xi_s^0 = 0$ , and we recover the continuity equation. For the first-moment,

$$\int \mathbf{v} \left( \frac{\partial f_s}{\partial t} + \mathbf{v} \cdot \nabla f_s + \frac{q}{m} (\mathbf{E} + \mathbf{v} \times \mathbf{B}) \cdot \nabla_v f_s \right) d^3v = \int \mathbf{v} \left( \frac{\partial f_s}{\partial t} \right)_c d^3v, \quad (\text{B.3})$$

we obtain

$$\frac{\partial n_s \mathbf{u}_s}{\partial t} + \frac{1}{m_s} \nabla \cdot \bar{\mathbf{P}}_s - \frac{q_s}{m_s} n_s (\mathbf{E} + \mathbf{u}_s \times \mathbf{B}) = \bar{\Xi}_s^1. \quad (\text{B.4})$$

where

$$\bar{\mathbf{P}}_s \equiv m_s \int f_s \mathbf{v} \mathbf{v} d^3 v. \quad (\text{B.5})$$

Considering  $\nabla \cdot \bar{\mathbf{P}}_s = \nabla \cdot \bar{\mathbf{P}}_s + \nabla \cdot (n_s m_s \mathbf{u}_s \mathbf{u}_s)$ , where  $\bar{\mathbf{P}}_s$  has been defined in Eq. (2.14) and using

$$\begin{aligned} \nabla \cdot (n_s m_s \mathbf{u}_s \mathbf{u}_s) &= (\nabla \cdot (n_s m_s \mathbf{u}_s)) \mathbf{u}_s + n_s m_s \mathbf{u}_s \cdot \nabla \mathbf{u}_s \\ &= (\nabla \cdot \mathbf{u}_s) n_s m_s \mathbf{u}_s + \mathbf{u}_s \cdot \nabla (n_s m_s \mathbf{u}_s), \end{aligned} \quad (\text{B.6})$$

Eq. (B.4) takes the form

$$\begin{aligned} \frac{\partial n_s m_s \mathbf{u}_s}{\partial t} + \mathbf{u}_s \nabla \cdot (n_s m_s \mathbf{u}_s) &= \\ - \nabla \cdot \bar{\mathbf{P}}_s - (\nabla \cdot \mathbf{u}_s) n_s m_s \mathbf{u}_s + q_s n_s (\mathbf{E} + \mathbf{u}_s \times \mathbf{B}) + m_s \bar{\Xi}_s^1, \end{aligned} \quad (\text{B.7})$$

which can be further reduced to the standard fluid momentum equation

$$\frac{d n_s m_s \mathbf{u}_s}{dt} = - \nabla \cdot \bar{\mathbf{P}}_s - (\nabla \cdot \mathbf{u}_s) n_s m_s \mathbf{u}_s + q_s n_s (\mathbf{E} + \mathbf{u}_s \times \mathbf{B}) + m_s \bar{\Xi}_s^1, \quad (\text{B.8})$$

This equation describes the total change in time of the bulk momentum density for species  $s$ . Since we are interested in the energy distribution, it is useful to derive similar expressions for the kinetic and thermal energies. To do this, we derive the second moment:

$$\int \mathbf{v} \mathbf{v} \left( \frac{\partial f_s}{\partial t} + \mathbf{v} \cdot \nabla f_s + \frac{q_s}{m_s} (\mathbf{E} + \mathbf{v} \times \mathbf{B}) \cdot \nabla_v f_s \right) d^3 v = \int \mathbf{v} \mathbf{v} \left( \frac{\partial f_s}{\partial t} \right)_c d^3 v, \quad (\text{B.9})$$

which leads to the general energy equation

$$\frac{1}{m_s} \frac{\partial \bar{\mathbf{P}}_s}{\partial t} + \frac{1}{m_s} \nabla \cdot \bar{\mathbf{Q}}_s - \frac{q_s}{m_s} n_s (\mathbf{E} \mathbf{u}_s + \mathbf{u}_s \mathbf{E}) - \frac{q_s}{m_s^2} (\bar{\mathbf{P}}_s \times \mathbf{B} - \mathbf{B} \times \bar{\mathbf{P}}_s) = \bar{\Xi}_s^2. \quad (\text{B.10})$$

where

$$\overline{\mathbb{Q}}_s \equiv m_s \int f_s \mathbf{v} \mathbf{v} \mathbf{v} d^3v \quad (\text{B.11})$$

We further consider

$$\begin{aligned} (\mathbf{v} - \mathbf{u}_s)(\mathbf{v} - \mathbf{u}_s)(\mathbf{v} - \mathbf{u}_s) = \\ \mathbf{v} \mathbf{v} \mathbf{v} - \mathbf{v} \mathbf{v} \mathbf{u}_s - \mathbf{v} \mathbf{u}_s \mathbf{v} + \mathbf{v} \mathbf{u}_s \mathbf{u}_s - \mathbf{u}_s \mathbf{v} \mathbf{v} + \mathbf{u}_s \mathbf{v} \mathbf{u}_s - \mathbf{u}_s \mathbf{u}_s \mathbf{v} - \mathbf{u}_s \mathbf{u}_s \mathbf{u}_s, \end{aligned} \quad (\text{B.12})$$

and

$$\overline{\mathbf{Q}}_s = \overline{\mathbb{Q}}_s + 2n_s m_s \mathbf{u}_s \mathbf{u}_s \mathbf{u}_s - (\overline{\mathbb{P}}_s \mathbf{u}_s + \mathbf{u}_s \overline{\mathbb{P}}_s) - \int f_s \mathbf{v} \mathbf{u}_s \mathbf{v} d^3v. \quad (\text{B.13})$$

to express Eq. (B.10) in terms of  $\overline{\mathbf{Q}}_s$  instead of  $\overline{\mathbb{Q}}_s$ . The last term in Eq. (B.13) does not present a simple form in terms of a dyadic product, we use an element-wise notation for this term and for every term that corresponds to third-rank tensors. Thus, recalling that  $\overline{\mathbb{P}}_s = \overline{\mathbf{P}}_s + n_s m_s \mathbf{u}_s \mathbf{u}_s$ , Eq. (B.13) becomes

$$Q_{ijk,s} = Q_{ijk,s} + u_{i,s} P_{ij,s} + P_{ij,s} u_{k,s} + u_{j,s} P_{ik,s} + n_s m_s u_{i,s} u_{j,s} u_{k,s}, \quad (\text{B.14})$$

and Eq. (B.10) takes the form

$$\begin{aligned} & \frac{1}{m_s} \frac{\partial (\overline{\mathbf{P}}_s + n_s m_s \mathbf{u}_s \mathbf{u}_s)}{\partial t} + \\ & \frac{1}{m_s} \nabla \cdot \left( (Q_{ijk,s} + u_{i,s} P_{ij,s} + P_{ij,s} u_{k,s} + u_{j,s} P_{ik,s} + n_s m_s u_{i,s} u_{j,s} u_{k,s}) \hat{\mathbf{e}}^i \otimes \hat{\mathbf{e}}^j \otimes \hat{\mathbf{e}}^k \right) \\ & - \frac{q_s}{m_s} n_s (\mathbf{E} \mathbf{u}_s + \mathbf{u}_s \mathbf{E}) \\ & - \frac{q_s}{m_s^2} \left( (\overline{\mathbf{P}}_s + n_s m_s \mathbf{u}_s \mathbf{u}_s) \times \mathbf{B} - \mathbf{B} \times (\overline{\mathbf{P}}_s + n_s m_s \mathbf{u}_s \mathbf{u}_s) \right) I = \overline{\Xi}_s^2, \end{aligned} \quad (\text{B.15})$$

which can be expressed as

$$\begin{aligned}
 & \frac{\partial \bar{\mathbf{P}}_s}{\partial t} + \nabla \cdot \left( (Q_{ijk,s} + u_{i,s}P_{ij,s} + P_{ij,s}u_{k,s} + u_{j,s}P_{ik,s}) \hat{\mathbf{e}}^i \otimes \hat{\mathbf{e}}^j \otimes \hat{\mathbf{e}}^k \right) - \\
 & \frac{q_s}{m_s} (\bar{\mathbf{P}}_s \times \mathbf{B} - \mathbf{B} \times \bar{\mathbf{P}}_s) \\
 & = -\nabla \cdot (n_s m_s \mathbf{u}_s \mathbf{u}_s \mathbf{u}_s) - \frac{\partial n_s m_s \mathbf{u}_s \mathbf{u}_s}{\partial t} \\
 & + q_s n_s \left( \mathbf{E} \mathbf{u}_s + \mathbf{u}_s \mathbf{E} + \frac{1}{m_s} (\mathbf{u}_s \mathbf{u}_s \times \mathbf{B} - \mathbf{B} \times \mathbf{u}_s \mathbf{u}_s) \right) + m_s \bar{\Xi}_s^2. \tag{B.16}
 \end{aligned}$$

Although Eq. (B.8) and Eq. (B.16) are the exact first and second moments of the Boltzmann equation, they are not very useful for our energy analysis (see Section 7.2). Instead, we proceed by deriving direct expressions for the scalar energy terms  $\varepsilon_s^k$  and  $\varepsilon_s^{th}$ . Thus, we take the scalar product of Eq. (B.8) with  $\mathbf{u}_s$ , which leads to the equation for the kinetic energy  $\varepsilon_s^k$ :

$$\frac{d\varepsilon_s^k}{dt} + \mathbf{u}_s \cdot (\nabla \cdot \bar{\mathbf{P}}_s) + (\nabla \cdot \mathbf{u}_s) \varepsilon_s^k - q_s n_s \mathbf{u}_s \cdot \mathbf{E} = \Xi_s^k, \tag{B.17}$$

where  $\Xi_s^k = m_s \mathbf{u}_s \cdot \bar{\Xi}_s^1$ . On the other hand, to obtain an expression for the thermal energy  $\varepsilon_s^{th}$ , we take half the trace of Eq. (B.16). The terms involving partial time derivatives of the form

$$\frac{1}{2} \text{Tr} \left( \frac{\partial \bar{\mathbf{P}}_s}{\partial t} \right) = \frac{\partial \varepsilon_s^{th}}{\partial t} \tag{B.18}$$

and

$$\frac{1}{2} \text{Tr} \left( \frac{\partial n_s m_s \mathbf{u}_s \mathbf{u}_s}{\partial t} \right) = \frac{\partial \varepsilon_s^k}{\partial t}. \tag{B.19}$$

Half the trace of the term  $\nabla \cdot ((Q_{ijk,s} + u_{i,s}P_{ij,s} + P_{ij,s}u_{k,s} + u_{j,s}P_{ik,s})\hat{\mathbf{e}}^i \otimes \hat{\mathbf{e}}^j \otimes \hat{\mathbf{e}}^k)$  can be expressed as

$$\begin{aligned} & \frac{1}{2}Tr(\nabla \cdot \bar{\mathbf{Q}}_s) + \frac{1}{2}Tr(\nabla \cdot (u_{i,s}P_{ij,s} + P_{ij,s}u_{k,s} + u_{j,s}P_{ik,s})\hat{\mathbf{e}}^i \otimes \hat{\mathbf{e}}^j \otimes \hat{\mathbf{e}}^k) = \\ & \frac{1}{2}Tr(\nabla \cdot \bar{\mathbf{Q}}_s) + \frac{1}{2}[2(\nabla \mathbf{u}_s : \bar{\mathbf{P}}_s) + (\nabla \cdot \mathbf{u}_s)Tr(\bar{\mathbf{P}}_s) + \mathbf{u}_s \cdot \nabla(Tr(\bar{\mathbf{P}}_s)) + 2\mathbf{u}_s \cdot (\nabla \cdot \bar{\mathbf{P}}_s)] = \\ & \frac{1}{2}Tr(\nabla \cdot \bar{\mathbf{Q}}_s) + \nabla \mathbf{u}_s : \bar{\mathbf{P}}_s + (\nabla \cdot \mathbf{u}_s)\varepsilon_s^{th} + \mathbf{u}_s \cdot \nabla \varepsilon_s^{th} + \mathbf{u}_s \cdot (\nabla \cdot \bar{\mathbf{P}}_s). \end{aligned} \quad (\text{B.20})$$

Similarly,

$$\begin{aligned} & \frac{1}{2}Tr(\nabla \cdot (n_s m_s \mathbf{u}_s \mathbf{u}_s \mathbf{u}_s)) = \frac{1}{2}(\mathbf{u}_s \cdot \nabla(m_s n_s \mathbf{u}_s \cdot \mathbf{u}_s) + (\nabla \cdot \mathbf{u}_s)(n_s m_s \mathbf{u}_s \cdot \mathbf{u}_s)), \\ & = \mathbf{u}_s \cdot \nabla(\varepsilon_s^k) + (\nabla \cdot \mathbf{u}_s)\varepsilon_s^k, \end{aligned} \quad (\text{B.21})$$

and the electric-field terms become

$$\frac{1}{2}Tr(\mathbf{E} \mathbf{u}_s + \mathbf{u}_s \mathbf{E}) = \mathbf{E} \cdot \mathbf{u}_s. \quad (\text{B.22})$$

To calculate the trace of the cross-product terms in Eq. (B.16), we use an element-wise approach. If  $\mathbf{A}$  is a vector and  $\bar{\mathbb{M}}$  is a second-rank tensor, the cross product is  $\mathbf{A} \times \bar{\mathbb{M}} = \epsilon_{lip} A_i M_{pq} \hat{\mathbf{e}}^l \otimes \hat{\mathbf{e}}^q$ . It can be shown that  $\bar{\mathbb{M}} \times \mathbf{A} = -\left(\mathbf{A} \times \bar{\mathbb{M}}^T\right)^T$ , where  $\bar{\mathbb{M}}^T$  represents the transposed of  $\bar{\mathbb{M}}$ , and  $Tr(\mathbf{A} \times \bar{\mathbb{M}}) = \epsilon_{ijk} A_i M_{jk}$ . Moreover, if  $\bar{\mathbb{M}}$  is a symmetric tensor, then  $Tr(\mathbf{A} \times \bar{\mathbb{M}}) = 0$ . In addition, the trace of  $\nabla \cdot \bar{\mathbf{Q}}_s$  corresponds to  $2\nabla \cdot \mathbf{h}_s$ , as defined in Eq. (7.2). Therefore the expression for the thermal energy rate is

$$\begin{aligned} & \frac{\partial \varepsilon_s^{th}}{\partial t} + \frac{\partial \varepsilon_s^k}{\partial t} + \nabla \cdot \mathbf{h}_s + \nabla \mathbf{u}_s : \bar{\mathbf{P}}_s + (\nabla \cdot \mathbf{u}_s)\varepsilon_s^{th} + \mathbf{u}_s \cdot \nabla \varepsilon_s^{th} + \mathbf{u}_s \cdot (\nabla \cdot \bar{\mathbf{P}}_s) = \\ & -\mathbf{u}_s \cdot \nabla \varepsilon_s^k - (\nabla \cdot \mathbf{u}_s)\varepsilon_s^k + q_s n_s \mathbf{E} \cdot \mathbf{u}_s + \frac{1}{2}Tr(m_s \bar{\Xi}_s^2), \end{aligned} \quad (\text{B.23})$$

which can be expressed as

$$\begin{aligned} & \frac{d\varepsilon_s^{th}}{dt} + \frac{d\varepsilon_s^k}{dt} + \nabla \cdot \mathbf{h}_s + \nabla \mathbf{u}_s : \bar{\mathbf{P}}_s + (\nabla \cdot \mathbf{u}_s)\varepsilon_s^{th} + \mathbf{u}_s \cdot (\nabla \cdot \bar{\mathbf{P}}_s) = \\ & -(\nabla \cdot \mathbf{u}_s)\varepsilon_s^k + q_s n_s \mathbf{E} \cdot \mathbf{u}_s + \frac{1}{2}Tr(m_s \bar{\Xi}_s^2). \end{aligned} \quad (\text{B.24})$$

Substituting Eq. (B.17), this last expression can be further simplified to

$$\frac{d\varepsilon_s^{th}}{dt} + \nabla \cdot \mathbf{h}_s + \nabla \mathbf{u}_s : \overline{\mathbf{P}}_s + (\nabla \cdot \mathbf{u}_s) \varepsilon_s^{th} = \Xi_s^{th}, \quad (\text{B.25})$$

where  $\Xi_s^{th} = -m\mathbf{u} \cdot \Xi^1 + \frac{1}{2}Tr(m\Xi^2)$ . The terms on the left-hand side of Eq. (B.17) and Eq. (B.25) describe collisionless processes, whereas the terms on the right-hand side describe collisional/dissipative processes in the plasma.



## Appendix C

# A Framework to Study the Energy-density Transfer Using Fitted Moments from In-situ Data.

In-situ observations show that plasma species  $s$  can be composed of more than one population  $l$ , each of them presenting different thermodynamic properties. For instance, solar-wind electrons often present three populations: core, halo and strahl electrons ([Feldman et al., 1975](#); [Pilipp et al., 1987](#); [Marsch, 2006](#); [Štverák et al., 2009](#)), and solar-wind protons often present two main populations: core and beam protons ([Gazis and Lazarus, 1982](#); [Marsch et al., 1982](#)). Additionally, the plasma properties are understood in terms of the particle distribution function. Therefore, the study of the radial evolution of the plasma populations is often approached by fitting their distributions ([Maksimovic et al., 2005](#); [Štverák et al., 2009](#); [Perrone et al., 2019](#)). The fitted distributions provide a way to compute moments of the overall particle distribution and to analyse its macroscopic properties. In this section, I extend the analysis presented in Section B and derive expressions for Eqs. (B.17) and (B.25) in terms of the different populations. This framework will build upon the results from Section 7.3.2 and motivates the study of heat flux evolution and irreversible energy transfer dependence with heliospheric distance. Therefore, I derive a framework to study the energy density transfer of the different species which can be

applied to in-situ measurements as a way to evaluate these energy density transfer terms. Let us consider that the distribution function  $f_s$  of the plasma species  $s$ , consisting of several populations  $l$ , can be expressed as

$$f_s = \sum_l f_l \quad (\text{C.1})$$

where each  $f_l$  represent the distribution function of the population  $l$ . For instance, in the case of electrons  $l = \text{core}, \text{halo}, \text{strahl}$ . For each population, we define the density

$$n_l = \int f_l d^3v \quad (\text{C.2})$$

and bulk velocity

$$\mathbf{u}_l = \frac{1}{n_l} \int f_l \mathbf{v} d^3v. \quad (\text{C.3})$$

The second moment of  $f_s$ , (pressure tensor, Eq. (2.14)) is

$$\begin{aligned} \overline{\mathbf{P}}_s &= m_s \int f_s (\mathbf{v} - \mathbf{u}_s)(\mathbf{v} - \mathbf{u}_s) d^3v \\ &= m_s \int (\sum_l f_l) (\mathbf{v} - \mathbf{u}_s)(\mathbf{v} - \mathbf{u}_s) d^3v. \end{aligned} \quad (\text{C.4})$$

Since

$$n_s \mathbf{u}_s = \sum_l n_l \mathbf{u}_l, \quad (\text{C.5})$$

The second moment for each population around the species bulk velocity ( $\mathbf{u}_s$ ) is

$$\frac{\overline{\mathbf{P}}_l^{u_s}}{m_s} = \int f_l (\mathbf{v} - \mathbf{u}_s)(\mathbf{v} - \mathbf{u}_s) d^3v, \quad (\text{C.6})$$

and the total pressure tensor of the species  $s$  is the sum over all  $\overline{\mathbf{P}}_l^{u_s}$ , i.e.,

$$\overline{\mathbf{P}}_s = \sum_l \overline{\mathbf{P}}_l^{u_s}. \quad (\text{C.7})$$

The quantity  $\overline{\mathbf{P}}_l^{u_s}$  measures the contribution of the population  $l$  to the overall pressure. On the other hand, considering the second moment around the population bulk speed ( $\mathbf{u}_l$ ) as

$$\frac{\overline{\mathbf{P}}_l}{m_s} = \int f_l(\mathbf{v} - \mathbf{u}_l)(\mathbf{v} - \mathbf{u}_l) d^3v, \quad (\text{C.8})$$

the pressure tensor of the total species  $\overline{\mathbf{P}}_s$  can be expressed as

$$\frac{\overline{\mathbf{P}}_s}{m_s} = \sum_l \int f_l[(\mathbf{v} - \mathbf{u}_l) - (\mathbf{u}_s - \mathbf{u}_l)][(\mathbf{v} - \mathbf{u}_l) - (\mathbf{u}_s - \mathbf{u}_l)] d^3v, \quad (\text{C.9})$$

which after some operations becomes

$$\overline{\mathbf{P}}_s = \sum_l \left( \overline{\mathbf{P}}_l + n_l m_s (\mathbf{u}_s - \mathbf{u}_l)(\mathbf{u}_s - \mathbf{u}_l) \right). \quad (\text{C.10})$$

For simplicity, we define the offset velocity

$$\mathbf{u}_l^s = \mathbf{u}_l - \mathbf{u}_s, \quad (\text{C.11})$$

so that  $\overline{\mathbf{P}}_s$  can be expressed as

$$\overline{\mathbf{P}}_s = \sum_l \left( \overline{\mathbf{P}}_l + n_l m_s \mathbf{u}_l^s \mathbf{u}_l^s \right). \quad (\text{C.12})$$

Accordingly, the third moment of the full species  $s$  ( $\overline{\overline{\mathbf{Q}}}_s$ ) can be expressed in terms of the third moments around the bulk speed of the population ( $\overline{\overline{\mathbf{Q}}}_l$ ) as

$$\frac{\overline{\overline{\mathbf{Q}}}_s}{m_s} = \sum_l \int f_l[(\mathbf{v} - \mathbf{u}_l) - (\mathbf{u}_s - \mathbf{u}_l)]^3 d^3v, \quad (\text{C.13})$$

where,  $[(\mathbf{v} - \mathbf{u}_l) - (\mathbf{u}_s - \mathbf{u}_l)]^3$  represents a triple dyadic product. After some operations, Eq. (C.13) becomes

$$\begin{aligned} \overline{\overline{\mathbf{Q}}}_s = & \sum_l (\overline{\overline{\mathbf{Q}}}_l) - \sum_l (n_l m_s (\mathbf{u}_s - \mathbf{u}_l)^3) \\ & - \sum_l \left( \overline{\mathbf{P}}_l (\mathbf{u}_s - \mathbf{u}_l) + \int f_l (\mathbf{v} - \mathbf{u}_l) (\mathbf{u}_s - \mathbf{u}_l) (\mathbf{v} - \mathbf{u}_l) d^3 v + (\mathbf{u}_s - \mathbf{u}_l) \overline{\mathbf{P}}_l \right). \end{aligned} \quad (\text{C.14})$$

If the distribution function of each population  $l$  is symmetric (even function) with respect to  $\mathbf{u}_l$ , the terms  $\overline{\overline{\mathbf{Q}}}_l$  are zero. Therefore, in our particular case, Eq. (C.14) becomes

$$\overline{\overline{\mathbf{Q}}}_s = \sum_l \left( n_l m_s \mathbf{u}_l^s \mathbf{u}_l^s \mathbf{u}_l^s + \overline{\mathbf{P}}_l \mathbf{u}_l^s + m_s \int f_l (\mathbf{v} - \mathbf{u}_l) \mathbf{u}_l^s (\mathbf{v} - \mathbf{u}_l) d^3 v + \mathbf{u}_l^s \overline{\mathbf{P}}_l \right). \quad (\text{C.15})$$

The heat tensor is not required in the calculation of Eq. (7.8). Instead, the divergence of the electron heat flux vector  $\nabla \cdot \mathbf{h}_s = \text{Tr}(\nabla \cdot \overline{\overline{\mathbf{Q}}}_s)/2$  directly enters the thermal-energy equation. We find

$$\begin{aligned} \frac{\text{Tr}(\nabla \cdot \overline{\overline{\mathbf{Q}}}_s)}{2} = & \sum_l \frac{1}{2} \text{Tr}(\nabla \cdot [n_l m_s \mathbf{u}_l^s \mathbf{u}_l^s \mathbf{u}_l^s]) \\ & + \sum_l \frac{1}{2} \text{Tr} \left( \nabla \cdot \left[ \overline{\mathbf{P}}_l \mathbf{u}_l^s + m_s \int f_l (\mathbf{v} - \mathbf{u}_l) \mathbf{u}_l^s (\mathbf{v} - \mathbf{u}_l) d^3 v + \mathbf{u}_l^s \overline{\mathbf{P}}_l \right] \right). \end{aligned} \quad (\text{C.16})$$

For the first term, we find

$$\frac{1}{2} \text{Tr}(\nabla \cdot [n_l m_s \mathbf{u}_l^s \mathbf{u}_l^s \mathbf{u}_l^s]) = \mathbf{u}_l^s \cdot \nabla \left( \frac{1}{2} m_s n_l \mathbf{u}_l^s \cdot \mathbf{u}_l^s \right) + (\nabla \cdot \mathbf{u}_l^s) \frac{1}{2} n_l m_s \mathbf{u}_l^s \cdot \mathbf{u}_l^s. \quad (\text{C.17})$$

We now define the offset kinetic energy density as

$$\varepsilon_l^{k,s} = \frac{1}{2} n_l m_s \mathbf{u}_l^s \cdot \mathbf{u}_l^s. \quad (\text{C.18})$$

Thus, the first term in Eq.(C.16) can be expressed as

$$\sum_l \frac{1}{2} Tr(\nabla \cdot [n_l m_s \mathbf{u}_l^s \mathbf{u}_l^s]) = \sum_l \left( \mathbf{u}_l^s \cdot \nabla \varepsilon_l^{k,s} + (\nabla \cdot \mathbf{u}_l^s) \varepsilon_l^{k,s} \right). \quad (\text{C.19})$$

The second term in Eq.(C.16) becomes

$$\begin{aligned} \sum_l \frac{1}{2} Tr \left( \nabla \cdot \left[ \bar{\mathbf{P}}_l \mathbf{u}_l^s + m_s \int f_l(\mathbf{v} - \mathbf{u}_l) \mathbf{u}_l^s (\mathbf{v} - \mathbf{u}_l) d^3v + \mathbf{u}_l^s \bar{\mathbf{P}}_l \right] \right) = \\ \sum_l \left( \nabla \mathbf{u}_l^s : \bar{\mathbf{P}}_l + (\nabla \cdot \mathbf{u}_l^s) \varepsilon_l^{th} + \mathbf{u}_l^s \cdot \nabla \varepsilon_l^{th} + \mathbf{u}_l^s \cdot (\nabla \cdot \bar{\mathbf{P}}_l) \right), \end{aligned} \quad (\text{C.20})$$

where we have defined the thermal energy density of each population as

$$\varepsilon_l^{th} = \frac{1}{2} Tr(\bar{\mathbf{P}}_l). \quad (\text{C.21})$$

To obtain  $\nabla \cdot \mathbf{h}_s$  in terms that correspond to each population, we substitute Eq. (C.19) and Eq. (C.20) in Eq. (C.16) and obtain

$$\nabla \cdot \mathbf{h}_s = \sum_l \left( \mathbf{u}_l^s \cdot [\nabla(\varepsilon_l^{k,s} + \varepsilon_l^{th}) + \nabla \cdot \bar{\mathbf{P}}_l] + (\nabla \cdot \mathbf{u}_l^s)(\varepsilon_l^{k,s} + \varepsilon_l^{th}) + \nabla \mathbf{u}_l^s : \bar{\mathbf{P}}_l \right). \quad (\text{C.22})$$

The thermal energy of the entire species  $s$  Eq. (7.9) is

$$\varepsilon_s^{th} = \sum_l \left( \varepsilon_l^{th} + n_l m_s \frac{1}{2} \|\mathbf{u}_s - \mathbf{u}_l\|^2 \right) = \sum_l \left( \varepsilon_l^{th} + \varepsilon_l^{k,s} \right). \quad (\text{C.23})$$

Let us consider the term  $\nabla \mathbf{u}_s : \bar{\mathbf{P}}_s$ . Using Eq. (C.12), we find

$$\nabla \mathbf{u}_s : \bar{\mathbf{P}}_s = \sum_l \left( \nabla \mathbf{u}_s : \bar{\mathbf{P}}_l + n_l m_s \nabla \mathbf{u}_s : (\mathbf{u}_l^s \mathbf{u}_l^s) \right). \quad (\text{C.24})$$

To simplify the comparison of the different terms, we use different colours that represent each term in the thermal power density equation:

$$\frac{d\varepsilon_s^{th}}{dt} + \nabla \cdot \mathbf{h}_s + \nabla \mathbf{u}_s : \bar{\mathbf{P}}_s + (\nabla \cdot \mathbf{u}_s) \varepsilon_s^{th} = \Xi_s^{th}. \quad (\text{C.25})$$

The thermal-energy equation Eq. (C.25) for the species  $s$  in terms of the populations is given by

$$\begin{aligned} \frac{d}{dt}(\varepsilon_s^{th}) + \sum_l \left( \mathbf{u}_l^s \cdot \nabla (\varepsilon_l^{k,s} + \varepsilon_l^{th}) + \mathbf{u}_l^s \cdot \nabla \cdot \bar{\mathbf{P}}_l + (\nabla \cdot \mathbf{u}_l^s)(\varepsilon_l^{k,s} + \varepsilon_l^{th}) + \nabla \mathbf{u}_l^s : \bar{\mathbf{P}}_l \right) \\ + \nabla \mathbf{u}_s : \bar{\mathbf{P}}_s + (\nabla \cdot \mathbf{u}_s) \varepsilon_s^{th} = \Xi_s^{th}. \end{aligned} \quad (\text{C.26})$$

Eqs. (C.12,C.23,C.18) and (C.26) allow for the study of the irreversible thermal energy density transfer using the distribution function of the populations. This can be applied to electrons (Feldman et al., 1975; Pilipp et al., 1987; Marsch, 2006; Štverák et al., 2009; Abraham et al., 2022) and positive ions (Gazis and Lazarus, 1982; Marsch et al., 1982; Perrone et al., 2019) in the solar wind. A similar approach have been presented (Goldman et al., 2020) and applied to MMS observations (Goldman et al., 2021). As Goldman et al. (2020) point out, a multi-beam approach to calculate the moments of the distribution function overcomes the limitations and misleading interpretation of single-fluid moments. Moreover, the thermal energy density  $\varepsilon_s^{th}$  of the entire species  $s$  may lack of meaning for multi-beam distributions. On the contrary, the thermal energy density  $\varepsilon_l^{th}$  of each population  $l$  is clearly defined.

# Bibliography

- Abraham, J. B., Owen, C. J., Verscharen, D., Bakrania, M., Stansby, D., Wicks, R. T., Nicolaou, G., Whittlesey, P. L., Rueda, J. A. A., Jeong, S.-Y., et al. (2022). Radial evolution of thermal and suprathermal electron populations in the slow solar wind from 0.13 to 0.5 au: Parker solar probe observations. *The Astrophysical Journal*, 931(2):118.
- Adhikari, L., Zank, G. P., Zhao, L.-L., Kasper, J. C., Korreck, K. E., Stevens, M., Case, A. W., Whittlesey, P., Larson, D., Livi, R., et al. (2020a). Turbulence transport modeling and first orbit parker solar probe (psp) observations. *The Astrophysical Journal Supplement Series*, 246(2):38.
- Adhikari, S., Shay, M., Parashar, T., Pyakurel, P. S., Matthaeus, W., Godzieba, D., Stawarz, J., Eastwood, J., and Dahlin, J. (2020b). Reconnection from a turbulence perspective. *Physics of Plasmas*, 27(4):042305.
- Agudelo Rueda, J. A., Verscharen, D., Wicks, R. T., Owen, C. J., Nicolaou, G., Walsh, A. P., Zouganelis, I., Germaschewski, K., and Domínguez, S. V. (2021). Three-dimensional magnetic reconnection in particle-in-cell simulations of anisotropic plasma turbulence. *Journal of Plasma Physics*, 87(3).
- Alexandrova, O., Chen, C. H. K., Sorriso-Valvo, L., Horbury, T. S., and Bale, S. D. (2013). Solar wind turbulence and the role of ion instabilities. *Space Science Reviews*, 178(2-4):101–139.
- Alexandrova, O., Saur, J., Lacombe, C., Mangeney, A., Mitchell, J., Schwartz, S. J.,

- and Robert, P. (2009). Universality of solar-wind turbulent spectrum from mhd to electron scales. *Physical review letters*, 103(16):165003.
- Alfvén, H. (1942). Existence of electromagnetic-hydrodynamic waves. *Nature*, 150(3805):405–406.
- Amdahl, G. M. (1967). Validity of the single processor approach to achieving large scale computing capabilities. In *Proceedings of the April 18-20, 1967, spring joint computer conference*, pages 483–485.
- Angelopoulos, V. (2009). The themis mission. *The THEMIS mission*, pages 5–34.
- Arzamasskiy, L., Kunz, M. W., Chandran, B. D., and Quataert, E. (2019). Hybrid-kinetic simulations of ion heating in alfvénic turbulence. *The Astrophysical Journal*, 879(1):53.
- Axford, W. (1984). Magnetic field reconnection. *Magnetic Reconnection in Space and Laboratory Plasmas*, 30:1–8.
- Bandyopadhyay, R., Chasapis, A., Matthaeus, W., Parashar, T., Haggerty, C., Shay, M., Gershman, D., Giles, B., and Burch, J. (2021). Energy dissipation in turbulent reconnection. *arXiv preprint arXiv:2111.03118*.
- Bandyopadhyay, R., Matthaeus, W. H., Parashar, T. N., Yang, Y., Chasapis, A., Giles, B. L., Gershman, D. J., Pollock, C. J., Russell, C. T., Strangeway, R. J., et al. (2020). Statistics of kinetic dissipation in the earth’s magnetosheath: Mms observations. *Physical Review Letters*, 124(25):255101.
- Baumann, G., Galsgaard, K., and Nordlund, Å. (2013). 3d solar null point reconnection mhd simulations. *Solar Physics*, 284(2):467–487.
- Baumjohann, W. and Treumann, R. A. (1997). *Basic space plasma physics*. World Scientific.
- Bavassano, B. and Bruno, R. (1989). Evidence of local generation of alfvénic turbulence in the solar wind. *Journal of Geophysical Research: Space Physics*, 94(A9):11977–11982.



- Bavassano, B., Dobrowolny, M., Mariani, F., and Ness, N. (1982). Radial evolution of power spectra of interplanetary alfvénic turbulence. *Journal of Geophysical Research: Space Physics*, 87(A5):3617–3622.
- Belcher, J., Davis Jr, L., and Smith, E. (1969). Large-amplitude alfvén waves in the interplanetary medium: Mariner 5. *Journal of Geophysical Research*, 74(9):2302–2308.
- Beresnyak, A. (2015). On the parallel spectrum in magnetohydrodynamic turbulence. *The Astrophysical Journal Letters*, 801(1):L9.
- Beresnyak, A. (2016). Three-dimensional spontaneous magnetic reconnection. *The Astrophysical Journal*, 834(1):47.
- Bessho, N. and Bhattacharjee, A. (2005). Collisionless reconnection in an electron-positron plasma. *Physical review letters*, 95(24):245001.
- Bessho, N., Chen, L.-J., Hesse, M., and Wang, S. (2017). The effect of reconnection electric field on crescent and u-shaped distribution functions in asymmetric reconnection with no guide field. *Physics of Plasmas*, 24(7):072903.
- Bhat, P., Zhou, M., and Loureiro, N. F. (2021). Inverse energy transfer in decaying, three-dimensional, non-helical magnetic turbulence due to magnetic reconnection. *Monthly Notices of the Royal Astronomical Society*, 501(2):3074–3087.
- Biermann, L. and Schlüter, A. (1951). Cosmic radiation and cosmic magnetic fields. ii. origin of cosmic magnetic fields. *Physical Review*, 82(6):863.
- Birdsall, C. K. and Langdon, A. B. (2018). *Plasma physics via computer simulation*. CRC press.
- Birn, J., Drake, J., Shay, M., Rogers, B., Denton, R., Hesse, M., Kuznetsova, M., Ma, Z., Bhattacharjee, A., Otto, A., et al. (2001). Geospace environmental modeling (gem) magnetic reconnection challenge. *Journal of Geophysical Research: Space Physics*, 106(A3):3715–3719.

- Birn, J., Nakamura, R., Panov, E., and Hesse, M. (2011). Bursty bulk flows and dipolarization in mhd simulations of magnetotail reconnection. *Journal of Geophysical Research: Space Physics*, 116(A1).
- Biskamp, D. (1986). Magnetic reconnection via current sheets. *The Physics of fluids*, 29(5):1520–1531.
- Blackman, E. G. and Field, G. B. (1993). Ohm’s law for a relativistic pair plasma. *Physical review letters*, 71(21):3481.
- Boesl, M., Bergmann, A., Bottino, A., Brunner, S., Coster, D., and Jenko, F. (2020). Collisional gyrokinetic full-f particle-in-cell simulations on open field lines with picls. *Contributions to Plasma Physics*, 60(5-6):e201900117.
- Bohr, T., Jensen, M. H., Paladin, G., and Vulpiani, A. (1998). *Dynamical Systems Approach to Turbulence*. Cambridge Nonlinear Science Series. Cambridge University Press.
- Boldyrev, S. (2005). On the spectrum of magnetohydrodynamic turbulence. *The Astrophysical Journal Letters*, 626(1):L37.
- Boldyrev, S. (2006). Spectrum of magnetohydrodynamic turbulence. *Phys. Rev. Lett.*, 96:115002.
- Boldyrev, S., Horaites, K., Xia, Q., and Perez, J. C. (2013). Toward a theory of astrophysical plasma turbulence at subproton scales. *The Astrophysical Journal*, 777(1):41.
- Boldyrev, S. and Loureiro, N. F. (2017). Magnetohydrodynamic turbulence mediated by reconnection. *The Astrophysical Journal*, 844(2):125.
- Boldyrev, S. and Loureiro, N. F. (2019). Role of reconnection in inertial kinetic-alfvén turbulence. *Physical review research*, 1(1):012006.
- Boldyrev, S. and Perez, J. C. (2009). Spectrum of weak magnetohydrodynamic turbulence. *Physical review letters*, 103(22):225001.

- Boldyrev, S. and Perez, J. C. (2012). Spectrum of kinetic-alfvén turbulence. *The Astrophysical Journal Letters*, 758(2):L44.
- Boldyrev, S., Perez, J. C., Borovsky, J. E., and Podesta, J. J. (2011). Spectral scaling laws in magnetohydrodynamic turbulence simulations and in the solar wind. *The Astrophysical Journal Letters*, 741(1):L19.
- Borg, A., Øieroset, M., Phan, T., Mozer, F., Pedersen, A., Mouikis, C., McFadden, J., Twitty, C., Balogh, A., and Rème, H. (2005). Cluster encounter of a magnetic reconnection diffusion region in the near-earth magnetotail on september 19, 2003. *Geophysical research letters*, 32(19).
- Boris, J. P. and Shanny, R. A. (1972). *Proceedings: Fourth Conference on Numerical Simulation of Plasmas, November 2, 3, 1970*. Naval Research Laboratory.
- Bothmer, V. and Schwenn, R. (1997). The structure and origin of magnetic clouds in the solar wind. In *Annales Geophysicae*, volume 16, pages 1–24. Springer.
- Brackbill, J. and Forslund, D. (1982). An implicit method for electromagnetic plasma simulation in two dimensions. *Journal of Computational Physics*, 46(2):271–308.
- Brambilla, M. (1998). *Kinetic theory of plasma waves: homogeneous plasmas*. Number 96 in International Series of Monographs on Physics. Oxford University Press.
- Broeren, T., Klein, K., TenBarge, J., Dors, I., Roberts, O., and Verscharen, D. (2021). Magnetic field reconstruction for a realistic multi-point, multi-scale space-craft observatory. *arXiv preprint arXiv:2106.13362*.
- Bruno, R. and Carbone, V. (2013). The solar wind as a turbulence laboratory. *Living Reviews in Solar Physics*, 10(1):2.
- Bruno, R., Trenchi, L., and Telloni, D. (2014). Spectral slope variation at proton scales from fast to slow solar wind. *The Astrophysical Journal Letters*, 793(1):L15.
- Büchner, J. (2007). Astrophysical reconnection and collisionless dissipation. *Plasma Physics and Controlled Fusion*, 49(12B):B325.

- Burch, J., Moore, T., Torbert, R., and Giles, B. (2016). Magnetospheric multiscale overview and science objectives. *Space Science Reviews*, 199(1):5–21.
- Burch, J. and Phan, T. (2016). Magnetic reconnection at the dayside magnetopause: Advances with mms. *Geophysical Research Letters*, 43(16):8327–8338.
- Burlaga, L. F. (1991). Magnetic clouds. In *Physics of the Inner Heliosphere II*, pages 1–22. Springer.
- Cerri, S., Franci, L., Califano, F., Landi, S., and Hellinger, P. (2017a). Plasma turbulence at ion scales: a comparison between particle in cell and eulerian hybrid-kinetic approaches. *Journal of Plasma Physics*, 83(2):705830202.
- Cerri, S. S. and Califano, F. (2017). Reconnection and small-scale fields in 2d-3v hybrid-kinetic driven turbulence simulations. *New Journal of Physics*, 19(2):025007.
- Cerri, S. S., Groselj, D., and Franci, L. (2019). Kinetic plasma turbulence: recent insights and open questions from 3d3v simulations. *Frontiers in Astronomy and Space Sciences*, 6:64.
- Cerri, S. S., Servidio, S., and Califano, F. (2017b). Kinetic cascade in solar-wind turbulence: 3d3v hybrid-kinetic simulations with electron inertia. *The Astrophysical Journal Letters*, 846(2):L18.
- Chandran, B., Verscharen, D., Quataert, E., Kasper, J., Isenberg, P., and Bourouaine, S. (2013). Stochastic heating, differential flow, and the alpha-to-proton temperature ratio in the solar wind. *The Astrophysical Journal*, 776(1):45.
- Chandran, B. D., Li, B., Rogers, B. N., Quataert, E., and Germaschewski, K. (2010). Perpendicular ion heating by low-frequency alfvén-wave turbulence in the solar wind. *The Astrophysical Journal*, 720(1):503.
- Chandran, B. D., Schekochihin, A. A., and Mallet, A. (2015). Intermittency and alignment in strong rmhd turbulence. *The Astrophysical Journal*, 807(1):39.

- Chasapis, A., Matthaeus, W., Parashar, T., LeContel, O., Retinò, A., Breuillard, H., Khotyaintsev, Y., Vaivads, A., Lavraud, B., Eriksson, E., et al. (2017). Electron heating at kinetic scales in magnetosheath turbulence. *The Astrophysical Journal*, 836(2):247.
- Chasapis, A., Yang, Y., Matthaeus, W., Parashar, T., Haggerty, C., Burch, J., Moore, T., Pollock, C., Dorelli, J., Gershman, D., et al. (2018). Energy conversion and collisionless plasma dissipation channels in the turbulent magnetosheath observed by the magnetospheric multiscale mission. *The Astrophysical Journal*, 862(1):32.
- Che, H. (2017). How anomalous resistivity accelerates magnetic reconnection. *Physics of Plasmas*, 24(8):082115.
- Chen, C. (2016). Recent progress in astrophysical plasma turbulence from solar wind observations. *Journal of Plasma Physics*, 82(6):535820602.
- Chen, C., Bale, S., Bonnell, J., Borovikov, D., Bowen, T., Burgess, D., Case, A., Chandran, B., De Wit, T. D., Goetz, K., et al. (2020). The evolution and role of solar wind turbulence in the inner heliosphere. *The Astrophysical Journal Supplement Series*, 246(2):53.
- Chen, C., Horbury, T., Schekochihin, A., Wicks, R., Alexandrova, O., and Mitchell, J. (2010a). Anisotropy of solar wind turbulence between ion and electron scales. *Physical review letters*, 104(25):255002.
- Chen, C., Mallet, A., Schekochihin, A., Horbury, T., Wicks, R., and Bale, S. (2012). Three-dimensional structure of solar wind turbulence. *The Astrophysical Journal*, 758(2):120.
- Chen, C., Mallet, A., Yousef, T., Schekochihin, A., and Horbury, T. (2011). Anisotropy of alfvénic turbulence in the solar wind and numerical simulations. *Monthly Notices of the Royal Astronomical Society*, 415(4):3219–3226.
- Chen, C., Wicks, R., Horbury, T., and Schekochihin, A. (2010b). Interpreting power

- anisotropy measurements in plasma turbulence. *The Astrophysical Journal Letters*, 711(2):L79.
- Chen, Q., Otto, A., and Lee, L. (1997). Tearing instability, kelvin-helmholtz instability, and magnetic reconnection. *Journal of Geophysical Research: Space Physics*, 102(A1):151–161.
- Chen, S., Chen, H., Martnez, D., and Matthaeus, W. (1991). Lattice boltzmann model for simulation of magnetohydrodynamics. *Physical Review Letters*, 67(27):3776.
- Chen, Z., Fu, H., Wang, T., Cao, D., Peng, F., Yang, J., and Xu, Y. (2019). Reconstructing the flux-rope topology using the fote method. *Science China Technological Sciences*, 62(1):144–150.
- Chew, G., Goldberger, M., and Low, F. (1956). The boltzmann equation and the one-fluid hydromagnetic equations in the absence of particle collisions. *Proceedings of the Royal Society of London. Series A. Mathematical and Physical Sciences*, 236(1204):112–118.
- Cho, J. and Lazarian, A. (2004). The anisotropy of electron magnetohydrodynamic turbulence. *The Astrophysical Journal Letters*, 615(1):L41.
- Cho, J. and Vishniac, E. T. (2000). The anisotropy of magnetohydrodynamic alfvénic turbulence. *The Astrophysical Journal*, 539(1):273.
- Chust, T. and Belmont, G. (2006). Closure of fluid equations in collisionless magnetoplasmas. *Physics of plasmas*, 13(1):012506.
- Coleman Jr, P. J. (1968). Turbulence, viscosity, and dissipation in the solar-wind plasma. *The Astrophysical Journal*, 153:371.
- Cranmer, S. R. (2009). Coronal holes. *Living Reviews in Solar Physics*, 6(1):1–66.
- Cranmer, S. R. (2012). Self-consistent models of the solar wind. *Space science reviews*, 172(1):145–156.

- Crooker, N., Burton, M., Phillips, J., Smith, E., and Balogh, A. (1996). Heliospheric plasma sheets as small-scale transients. *Journal of Geophysical Research: Space Physics*, 101(A2):2467–2474.
- Daughton, W., Nakamura, T., Karimabadi, H., Roytershteyn, V., and Loring, B. (2014). Computing the reconnection rate in turbulent kinetic layers by using electron mixing to identify topology. *Physics of Plasmas*, 21(5):052307.
- Daughton, W., Roytershteyn, V., Karimabadi, H., Yin, L., Albright, B., Bergen, B., and Bowers, K. (2011). Role of electron physics in the development of turbulent magnetic reconnection in collisionless plasmas. *Nature Physics*, 7(7):539–542.
- Daughton, W., Scudder, J., and Karimabadi, H. (2006). Fully kinetic simulations of undriven magnetic reconnection with open boundary conditions. *Physics of Plasmas*, 13(7):072101.
- Davis, M., Phan, T., Gosling, J., and Skoug, R. (2006). Detection of oppositely directed reconnection jets in a solar wind current sheet. *Geophysical research letters*, 33(19):L19102.
- DeForest, C. E., Gibson, S. E., Beasley, M., Colaninno, R. C., Killough, R., Kosmann, W., Laurent, G. T., and McMullin, D. R. (2019). Polarimeter to unify the corona and heliosphere (punch): Imaging the corona and solar wind as a single system. In *AGU Fall Meeting Abstracts*, volume 2019, pages SH43B–06.
- Del Sarto, D., Califano, F., and Pegoraro, F. (2003). Secondary instabilities and vortex formation in collisionless-fluid magnetic reconnection. *Physical review letters*, 91(23):235001.
- Deng, X. and Matsumoto, H. (2001). Rapid magnetic reconnection in the earth’s magnetosphere mediated by whistler waves. *Nature*, 410(6828):557.
- Denskat, K. and Neubauer, F. (1983). Observations of hydromagnetic turbulence in the solar wind. *Solar Wind Five*, 2280:81–92.

- Dessler, A. J. (1967). Solar wind and interplanetary magnetic field. *Reviews of Geophysics*, 5(1):1–41.
- Divin, A., Lapenta, G., Markidis, S., Newman, D., and Goldman, M. (2012). Numerical simulations of separatrix instabilities in collisionless magnetic reconnection. *Physics of Plasmas*, 19(4):042110.
- Donnel, P., Garbet, X., Sarazin, Y., Grandgirard, V., Asahi, Y., Bouzat, N., Caschera, E., Dif-Pradalier, G., Ehrlacher, C., Ghendrih, P., et al. (2019). A multi-species collisional operator for full-f global gyrokinetics codes: Numerical aspects and verification with the gysela code. *Computer Physics Communications*, 234:1–13.
- Drake, J., Biskamp, D., and Zeiler, A. (1997). Breakup of the electron current layer during 3-d collisionless magnetic reconnection. *Geophysical research letters*, 24(22):2921–2924.
- Drake, J. and Lee, Y. (1977). Kinetic theory of tearing instabilities. *The Physics of Fluids*, 20(8):1341–1353.
- Drake, J., Shay, M., and Swisdak, M. (2008). The hall fields and fast magnetic reconnection. *Physics of Plasmas*, 15(4):042306.
- Drake, J., Swisdak, M., Che, H., and Shay, M. (2006). Electron acceleration from contracting magnetic islands during reconnection. *Nature*, 443(7111):553.
- Dungey, J. W. (1961). Interplanetary magnetic field and the auroral zones. *Physical Review Letters*, 6(2):47.
- Eastwood, J., Phan, T., Bale, S., and Tjulin, A. (2009). Observations of turbulence generated by magnetic reconnection. *Physical review letters*, 102(3):035001.
- Eastwood, J., Phan, T., Øieroset, M., Shay, M., Malakit, K., Swisdak, M., Drake, J., and Masters, A. (2013). Influence of asymmetries and guide fields on the magnetic reconnection diffusion region in collisionless space plasmas. *Plasma Physics and Controlled Fusion*, 55(12):124001.



- Eastwood, J., Shay, M., Phan, T., and Øieroset, M. (2010). Asymmetry of the ion diffusion region hall electric and magnetic fields during guide field reconnection: Observations and comparison with simulations. *Physical review letters*, 104(20):205001.
- Egedal, J., Daughton, W., and Le, A. (2012). Large-scale electron acceleration by parallel electric fields during magnetic reconnection. *Nature Physics*, 8(4):321.
- Egedal, J., Fox, W., Katz, N., Porkolab, M., Reim, K., and Zhang, E. (2007). Laboratory observations of spontaneous magnetic reconnection. *Physical review letters*, 98(1):015003.
- Elsasser, W. M. (1950). The hydromagnetic equations. *Physical Review*, 79(1):183.
- Escoubet, C., Schmidt, R., and Goldstein, M. (1997). Cluster-science and mission overview. *The Cluster and Phoenix Missions*, pages 11–32.
- Eyink, G., Vishniac, E., Lalescu, C., Aluie, H., Kanov, K., Bürger, K., Burns, R., Meneveau, C., and Szalay, A. (2013). Flux-freezing breakdown in high-conductivity magnetohydrodynamic turbulence. *Nature*, 497(7450):466–469.
- Eyink, G. L. (2015). Turbulent general magnetic reconnection. *The Astrophysical Journal*, 807(2):137.
- Eyink, G. L. (2018). Cascades and dissipative anomalies in nearly collisionless plasma turbulence. *Physical Review X*, 8(4):041020.
- Fadanelli, S., Lavraud, B., Califano, F., Cozzani, G., Finelli, F., and Sisti, M. (2021). Energy conversions associated with magnetic reconnection. *Journal of Geophysical Research: Space Physics*, 126(1):e2020JA028333.
- Feldman, U., Landi, E., and Schwadron, N. (2005). On the sources of fast and slow solar wind. *Journal of Geophysical Research: Space Physics*, 110(A7).
- Feldman, W., Asbridge, J., Bame, S., Gosling, J., and Lemons, D. (1978). Characteristic electron variations across simple high-speed solar wind streams. *Journal of Geophysical Research: Space Physics*, 83(A11):5285–5295.

- Feldman, W., Asbridge, J., Bame, S., Montgomery, M., and Gary, S. (1975). Solar wind electrons. *Journal of Geophysical Research*, 80(31):4181–4196.
- Forsyth, C., Lester, M., Fazakerley, A., Owen, C., and Walsh, A. (2011). On the effect of line current width and relative position on the multi-spacecraft curlometer technique. *Planetary and Space Science*, 59(7):598–605.
- Fortune, S. (1995). Voronoi diagrams and delaunay triangulations. *Computing in Euclidean geometry*, pages 225–265.
- Fox, W., Bhattacharjee, A., and Germaschewski, K. (2011). Fast magnetic reconnection in laser-produced plasma bubbles. *Physical review letters*, 106(21):215003.
- Franci, L., Cerri, S. S., Califano, F., Landi, S., Papini, E., Verdini, A., Matteini, L., Jenko, F., and Hellinger, P. (2017). Magnetic reconnection as a driver for a sub-ion-scale cascade in plasma turbulence. *The Astrophysical Journal Letters*, 850(L16):6pp.
- Franci, L., Landi, S., Verdini, A., Matteini, L., and Hellinger, P. (2018). Solar wind turbulent cascade from mhd to sub-ion scales: Large-size 3d hybrid particle-in-cell simulations. *The Astrophysical Journal*, 853(1):26.
- Franci, L., Papini, E., Micera, A., Lapenta, G., Hellinger, P., Del Sarto, D., Burgess, D., and Landi, S. (2022). Anisotropic electron heating in turbulence-driven magnetic reconnection in the near-sun solar wind. *arXiv preprint arXiv:2205.08670*.
- Franci, L., Stawarz, J. E., Papini, E., Hellinger, P., Nakamura, T., Burgess, D., Landi, S., Verdini, A., Matteini, L., Ergun, R., et al. (2020). Modeling mms observations at the earth’s magnetopause with hybrid simulations of alfvénic turbulence. *The Astrophysical Journal*, 898(2):175.
- Frisch, U. and Kolmogorov, A. N. (1995). *Turbulence: the legacy of AN Kolmogorov*. Cambridge university press.
- Fu, H., Cao, J., Vaivads, A., Khotyaintsev, Y. V., Andre, M., Dunlop, M., Liu, W., Lu, H., Huang, S., Ma, Y., et al. (2016). Identifying magnetic reconnection

- events using the fote method. *Journal of Geophysical Research: Space Physics*, 121(2):1263–1272.
- Furno, I., Intrator, T. P., Hemsing, E. W., Hsu, S. C., Abbate, S., Ricci, P., and Lapenta, G. (2005). Coalescence of two magnetic flux ropes via collisional magnetic reconnection. *Physics of plasmas*, 12(5):055702.
- Gary, S. P. (1999). Collisionless dissipation wavenumber: Linear theory. *Journal of Geophysical Research: Space Physics*, 104(A4):6759–6762.
- Gary, S. P. and Gary, S. P. (1993). *Theory of space plasma microinstabilities*. Number 7 in Cambridge Atmospheric and Space Science Series. Cambridge university press.
- Gazis, P. R. and Lazarus, A. J. (1982). Voyager observations of solar wind proton temperature: 1-10au. *Geophysical Research Letters*, 9(4):431–434.
- Gerick, F., Saur, J., and von Papen, M. (2017). The uncertainty of local background magnetic field orientation in anisotropic plasma turbulence. *The Astrophysical Journal*, 843(1):5.
- Germaschewski, K., Fox, W., Abbott, S., Ahmadi, N., Maynard, K., Wang, L., Ruhl, H., and Bhattacharjee, A. (2016). The plasma simulation code: A modern particle-in-cell code with patch-based load-balancing. *Journal of Computational Physics*, 318:305–326.
- Goldman, M., Newman, D., Eastwood, J., and Lapenta, G. (2020). Multibeam energy moments of multibeam particle velocity distributions. *Journal of Geophysical Research: Space Physics*, 125(12):e2020JA028340.
- Goldman, M., Newman, D., Eastwood, J., Lapenta, G., Burch, J., and Giles, B. (2021). Multi-beam energy moments of measured compound ion velocity distributions. *Physics of Plasmas*, 28(10):102305.
- Goldman, M., Newman, D., and Lapenta, G. (2016). What can we learn about magnetotail reconnection from 2d pic harris-sheet simulations? *Space Science Reviews*, 199(1-4):651–688.

- Goldreich, P. and Sridhar, S. (1995). Toward a theory of interstellar turbulence. 2: Strong alfvénic turbulence. *The Astrophysical Journal*, 438:763–775.
- Goldstein, M., Matthaeus, W., and Ambrosiano, J. (1986). Acceleration of charged particles in magnetic reconnection: Solar flares, the magnetosphere, and solar wind. *Geophysical research letters*, 13(3):205–208.
- Goldstein, M., Wicks, R., Perri, S., and Sahraoui, F. (2015). Kinetic scale turbulence and dissipation in the solar wind: key observational results and future outlook. *Philosophical Transactions of the Royal Society A: Mathematical, Physical and Engineering Sciences*, 373(2041):20140147.
- González, C., Parashar, T., Gomez, D., Matthaeus, W., and Dmitruk, P. (2019). Turbulent electromagnetic fields at sub-proton scales: Two-fluid and full-kinetic plasma simulations. *Physics of Plasmas*, 26(1):012306.
- Gosling, J. (2007). Observations of magnetic reconnection in the turbulent high-speed solar wind. *The Astrophysical Journal Letters*, 671(1):L73.
- Gosling, J. (2012). Magnetic reconnection in the solar wind. *Space science reviews*, 172(1-4):187–200.
- Gosling, J., Birn, J., and Hesse, M. (1995). Three-dimensional magnetic reconnection and the magnetic topology of coronal mass ejection events. *Geophysical research letters*, 22(8):869–872.
- Gosling, J., Eriksson, S., and Schwenn, R. (2006). Petschek-type magnetic reconnection exhausts in the solar wind well inside 1 au: Helios. *Journal of Geophysical Research: Space Physics*, 111(A10):A10102.
- Gosling, J., Skoug, R., McComas, D., and Smith, C. (2005). Direct evidence for magnetic reconnection in the solar wind near 1 au. *Journal of Geophysical Research: Space Physics*, 110(A1):A01107.
- Gosling, J. T., Eriksson, S., Phan, T., Larson, D., Skoug, R., and McComas, D. (2007). Direct evidence for prolonged magnetic reconnection at a continuous x-line within the heliospheric current sheet. *Geophysical research letters*, 34(6).

- Graham, D. B., Khotyaintsev, Y. V., Vaivads, A., Norgren, C., André, M., Webster, J., Burch, J., Lindqvist, P.-A., Ergun, R., Torbert, R., et al. (2017). Instability of agyrotropic electron beams near the electron diffusion region. *Physical Review Letters*, 119(2):025101.
- Grappin, R., Velli, M., and Mangeney, A. (1991). "alfvénic" versus "standard" turbulence in the solar wind. In *Annales Geophysicae*, volume 9, pages 416–426.
- Greco, A., Valentini, F., Servidio, S., and Matthaeus, W. (2012). Inhomogeneous kinetic effects related to intermittent magnetic discontinuities. *Physical Review E*, 86(6):066405.
- Grošelj, D., Mallet, A., Loureiro, N. F., and Jenko, F. (2018). Fully kinetic simulation of 3d kinetic alfvén turbulence. *Physical review letters*, 120(10):105101.
- Gustafson, J. L. (1988). Reevaluating amdahl’s law. *Communications of the ACM*, 31(5):532–533.
- Hammett, G. W. and Perkins, F. W. (1990). Fluid moment models for landau damping with application to the ion-temperature-gradient instability. *Physical review letters*, 64(25):3019.
- Harris, E. G. (1962). On a plasma sheath separating regions of oppositely directed magnetic field. *Il Nuovo Cimento (1955-1965)*, 23(1):115–121.
- Harvey, C. C. (1998). Spatial gradients and the volumetric tensor. *ISSI scientific reports series*, 1:307–322.
- Haynes, A. and Parnell, C. (2010). A method for finding three-dimensional magnetic skeletons. *Physics of Plasmas*, 17(9):092903.
- Haynes, A. L. and Parnell, C. E. (2007). A trilinear method for finding null points in a three-dimensional vector space. *Physics of Plasmas*, 14(8):082107.
- He, J., Zhu, X., Verscharen, D., Duan, D., Zhao, J., and Wang, T. (2020). Spectra of diffusion, dispersion, and dissipation for kinetic alfvénic and compressive tur-

- bulence: comparison between kinetic theory and measurements from mms. *The Astrophysical Journal*, 898(1):43.
- Hellinger, P., Matteini, L., Štverák, Š., Trávníček, P. M., and Marsch, E. (2011). Heating and cooling of protons in the fast solar wind between 0.3 and 1 au: Helios revisited. *Journal of Geophysical Research: Space Physics*, 116(A9).
- Hellinger, P. and Štverák, Š. (2018). Electron mirror instability: particle-in-cell simulations. *Journal of Plasma Physics*, 84(4):905840402.
- Hesse, M., Birn, J., and Kuznetsova, M. (2001a). Collisionless magnetic reconnection: Electron processes and transport modeling. *Journal of Geophysical Research: Space Physics*, 106(A3):3721–3735.
- Hesse, M., Kuznetsova, M., and Birn, J. (2001b). Particle-in-cell simulations of three-dimensional collisionless magnetic reconnection. *Journal of Geophysical Research: Space Physics*, 106(A12):29831–29841.
- Hesse, M., Kuznetsova, M., and Birn, J. (2004). The role of electron heat flux in guide-field magnetic reconnection. *Physics of Plasmas*, 11(12):5387–5397.
- Hesse, M. and Schindler, K. (1988). A theoretical foundation of general magnetic reconnection. *Journal of Geophysical Research: Space Physics*, 93(A6):5559–5567.
- Hesse, M. and Winske, D. (1998). Electron dissipation in collisionless magnetic reconnection. *Journal of Geophysical Research: Space Physics*, 103(A11):26479–26486.
- Hockney, R. W. and Eastwood, J. W. (2021). *Computer simulation using particles*. crc Press.
- Hollweg, J. V. (1999). Kinetic alfvén wave revisited. *Journal of Geophysical Research: Space Physics*, 104(A7):14811–14819.
- Holmes, J., Ergun, R., Nakamura, R., Roberts, O., Wilder, F., and Newman, D. (2019). Structure of electron-scale plasma mixing along the dayside reconnection separatrix. *Journal of Geophysical Research: Space Physics*, 124(11):8788–8803.

- Horbury, T. S., Forman, M., and Oughton, S. (2008). Anisotropic scaling of magnetohydrodynamic turbulence. *Physical Review Letters*, 101(17):175005.
- Hosseinpour, M., Bian, N., and Vekstein, G. (2009). Two-fluid regimes of the resistive and collisionless tearing instability. *Physics of Plasmas*, 16(1):012104.
- Howes, G. (2015a). A dynamical model of plasma turbulence in the solar wind. *Philosophical Transactions of the Royal Society A: Mathematical, Physical and Engineering Sciences*, 373(2041):20140145.
- Howes, G., Dorland, W., Cowley, S., Hammett, G., Quataert, E., Schekochihin, A., and Tatsuno, T. (2008a). Kinetic simulations of magnetized turbulence in astrophysical plasmas. *Physical Review Letters*, 100(6):065004.
- Howes, G., Drake, D., Nielson, K., Carter, T., Kletzing, C., and Skiff, F. (2012). Toward astrophysical turbulence in the laboratory. *Physical review letters*, 109(25):255001.
- Howes, G. G. (2015b). The inherently three-dimensional nature of magnetized plasma turbulence. *Journal of Plasma Physics*, 81(2):325810203.
- Howes, G. G. (2016). The dynamical generation of current sheets in astrophysical plasma turbulence. *The Astrophysical Journal Letters*, 827(2):L28.
- Howes, G. G., Cowley, S. C., Dorland, W., Hammett, G. W., Quataert, E., and Schekochihin, A. A. (2006). Astrophysical gyrokinetics: basic equations and linear theory. *The Astrophysical Journal*, 651(1):590.
- Howes, G. G., Cowley, S. C., Dorland, W., Hammett, G. W., Quataert, E., and Schekochihin, A. A. (2008b). A model of turbulence in magnetized plasmas: Implications for the dissipation range in the solar wind. *Journal of Geophysical Research: Space Physics*, 113(A5):A05103.
- Howes, G. G., Klein, K. G., and Li, T. C. (2017). Diagnosing collisionless energy transfer using field-particle correlations: Vlasov-poisson plasmas. *Journal of Plasma Physics*, 83(1).

- Howes, G. G. and Nielson, K. D. (2013a). Alfvén wave collisions, the fundamental building block of plasma turbulence. i. asymptotic solution. *Physics of Plasmas*, 20(7):072302.
- Howes, G. G. and Nielson, K. D. (2013b). Alfvén wave collisions, the fundamental building block of plasma turbulence. i. asymptotic solution. *Physics of Plasmas*, 20(7):072302.
- Hu, Q. and Sonnerup, B. U. (2002). Reconstruction of magnetic clouds in the solar wind: Orientations and configurations. *Journal of Geophysical Research: Space Physics*, 107(A7):SSH-10.
- Huang, S., Sahraoui, F., Deng, X., He, J., Yuan, Z., Zhou, M., Pang, Y., and Fu, H. (2014). Kinetic turbulence in the terrestrial magnetosheath: Cluster observations. *The Astrophysical Journal Letters*, 789(2):L28.
- Huang, Y.-M. and Bhattacharjee, A. (2016). Turbulent magnetohydrodynamic reconnection mediated by the plasmoid instability. *The Astrophysical Journal*, 818(1):20.
- Huba, J. and Rudakov, L. (2004). Hall magnetic reconnection rate. *Physical review letters*, 93(17):175003.
- Innocenti, M. E., Boella, E., Tenerani, A., and Velli, M. (2020). Collisionless heat flux regulation via the electron firehose instability in the presence of a core and suprathermal population in the expanding solar wind. *The Astrophysical Journal Letters*, 898(2):L41.
- Inoue, S. and Kusano, K. (2006). Three-dimensional simulation study of flux rope dynamics in the solar corona. *The Astrophysical Journal*, 645(1):742.
- Iroshnikov, P. (1963). Turbulence of a conducting fluid in a strong magnetic field. *Astronomicheskii Zhurnal*, 40:742.
- Jacobs, G. and Hesthaven, J. S. (2009). Implicit–explicit time integration of a high-order particle-in-cell method with hyperbolic divergence cleaning. *Computer Physics Communications*, 180(10):1760–1767.



- Jannet, G., Dudok de Wit, T., Krasnoselskikh, V., Kretschmar, M., Ferreau, P., Bergerard-Timofeeva, M., Agrapart, C., Brochet, J.-Y., Chalumeau, G., Martin, P., et al. (2021). Measurement of magnetic field fluctuations in the parker solar probe and solar orbiter missions. *Journal of Geophysical Research: Space Physics*, 126(2):e2020JA028543.
- Janvier, M., Démoulin, P., and Dasso, S. (2014). In situ properties of small and large flux ropes in the solar wind. *Journal of Geophysical Research: Space Physics*, 119(9):7088–7107.
- Ji, H., Alt, A., Antiochos, S., Baalrud, S., Bale, S., Bellan, P., Begelman, M., Beresnyak, A., Blackman, E., Chen, Y., et al. (2019). Major scientific challenges and opportunities in understanding magnetic reconnection and related explosive phenomena throughout the universe. *Astro2020: Decadal Survey on Astronomy and Astrophysics, Bulletin of the AAS, Bd*, 51(5).
- Ji, H. and Daughton, W. (2011). Phase diagram for magnetic reconnection in heliophysical, astrophysical, and laboratory plasmas. *Physics of Plasmas*, 18(11):111207.
- Jokipii, J. and Thomas, B. (1981). Effects of drift on the transport of cosmic rays. iv-modulation by a wavy interplanetary current sheet. *The Astrophysical Journal*, 243:1115–1122.
- Karimabadi, H., Krauss-Varban, D., Huba, J., and Vu, H. (2004). On magnetic reconnection regimes and associated three-dimensional asymmetries: Hybrid, hall-less hybrid, and hall-mhd simulations. *Journal of Geophysical Research: Space Physics*, 109(A9).
- Karimabadi, H. and Lazarian, A. (2013). Magnetic reconnection in the presence of externally driven and self-generated turbulence. *Physics of Plasmas*, 20(11):112102.
- Karimabadi, H., Roytershteyn, V., Daughton, W., and Liu, Y.-H. (2013). Recent

- evolution in the theory of magnetic reconnection and its connection with turbulence. In *Microphysics of Cosmic Plasmas*, pages 231–247. Springer.
- Kasper, J., Bale, S., Belcher, J. W., Berthomier, M., Case, A., Chandran, B., Curtis, D., Gallagher, D., Gary, S., Golub, L., et al. (2019). Alfvénic velocity spikes and rotational flows in the near-sun solar wind. *Nature*, 576(7786):228–231.
- Kasper, J., Lazarus, A., and Gary, S. (2008). Hot solar-wind helium: Direct evidence for local heating by alfvén-cyclotron dissipation. *Physical review letters*, 101(26):261103.
- Kaufmann, R. L. and Paterson, W. R. (2009). Boltzmann h function and entropy in the plasma sheet. *Journal of Geophysical Research: Space Physics*, 114(A9).
- Kim, E.-j. and Diamond, P. (2001). On turbulent reconnection. *The Astrophysical Journal*, 556(2):1052.
- Kiyani, K. H., Osman, K. T., and Chapman, S. C. (2015). Dissipation and heating in solar wind turbulence: from the macro to the micro and back again. *Philosophical transactions. Series A, Mathematical, physical, and engineering sciences*, 373(2041):20140155.
- Klein, K., Alexandrova, O., Bookbinder, J., Caprioli, D., Case, A., Chandran, B., Chen, L., Horbury, T., Jian, L., Kasper, J., et al. (2019). [plasma 2020 decadal] multipoint measurements of the solar wind: A proposed advance for studying magnetized turbulence. *arXiv preprint arXiv:1903.05740*.
- Klein, K. G., Howes, G. G., and TenBarge, J. M. (2017). Diagnosing collisionless energy transfer using field–particle correlations: Gyrokinetic turbulence. *Journal of Plasma Physics*, 83(4).
- Kliem, B., Karlicky, M., and Benz, A. O. (2000). Solar flare radio pulsations as a signature of dynamic magnetic reconnection. *arXiv preprint astro-ph/0006324*.
- Klimontovich, Y. L. (1997). Physics of collisionless plasma. *Physics-Uspekhi*, 40(1):21.

- Kolmogorov, A. N. (1941). The local structure of turbulence in incompressible viscous fluid for very large reynolds numbers. *Cr Acad. Sci. URSS*, 30:301–305.
- Kowal, G., Falceta-Gonçalves, D. A., Lazarian, A., and Vishniac, E. T. (2017). Statistics of reconnection-driven turbulence. *The Astrophysical Journal*, 838(2):91.
- Kowal, G., Lazarian, A., Vishniac, E., and Otmianowska-Mazur, K. (2009). Numerical tests of fast reconnection in weakly stochastic magnetic fields. *The Astrophysical Journal*, 700(1):63.
- Kraichnan, R. H. (1965). Inertial-range spectrum of hydromagnetic turbulence. *The Physics of Fluids*, 8(7):1385–1387.
- Krieger, A., Timothy, A., and Roelof, E. (1973). A coronal hole and its identification as the source of a high velocity solar wind stream. *Solar Physics*, 29(2):505–525.
- Lalescu, C. C., Shi, Y.-K., Eyink, G. L., Drivas, T. D., Vishniac, E. T., and Lazarian, A. (2015). Inertial-range reconnection in magnetohydrodynamic turbulence and in the solar wind. *Physical review letters*, 115(2):025001.
- Landi, S., Franci, L., Papini, E., Verdini, A., Matteini, L., and Hellinger, P. (2019). Spectral anisotropies and intermittency of plasma turbulence at ion kinetic scales. *arXiv preprint arXiv:1904.03903*.
- Lapenta, G. (2003). A new paradigm for 3d collisionless magnetic reconnection. In *Advances in Space Environment Research*, pages 167–174. Springer.
- Lapenta, G. (2012). Particle simulations of space weather. *Journal of Computational Physics*, 231(3):795–821.
- Lapenta, G., Brackbill, J., and Daughton, W. (2003). The unexpected role of the lower hybrid drift instability in magnetic reconnection in three dimensions. *Physics of plasmas*, 10(5):1577–1587.
- Lapenta, G., Krauss-Varban, D., Karimabadi, H., Huba, J., Rudakov, L., and Ricci, P. (2006). Kinetic simulations of x-line expansion in 3d reconnection. *Geophysical research letters*, 33(10):L10102.

- Lapenta, G., Markidis, S., Goldman, M. V., and Newman, D. L. (2015). Secondary reconnection sites in reconnection-generated flux ropes and reconnection fronts. *Nature Physics*, 11(8):690–695.
- Lapenta, G., Pucci, F., Goldman, M., and Newman, D. (2020). Local regimes of turbulence in 3d magnetic reconnection. *The Astrophysical Journal*, 888(2):104.
- Lazarian, A. (2006). Enhancement and suppression of heat transfer by mhd turbulence. *The Astrophysical Journal Letters*, 645(1):L25.
- Lazarian, A., Eyink, G. L., Jafari, A., Kowal, G., Li, H., Xu, S., and Vishniac, E. T. (2020). 3d turbulent reconnection: Theory, tests, and astrophysical implications. *Physics of Plasmas*, 27(1):012305.
- Lazarian, A. and Vishniac, E. T. (1999). Reconnection in a weakly stochastic field. *The Astrophysical Journal*, 517(2):700.
- Le, A., Egedal, J., Ng, J., Karimabadi, H., Scudder, J., Roytershteyn, V., Daughton, W., and Liu, Y.-H. (2014). Current sheets and pressure anisotropy in the reconnection exhaust. *Physics of Plasmas*, 21(1):012103.
- Leamon, R. J., Smith, C. W., Ness, N. F., and Wong, H. K. (1999). Dissipation range dynamics: Kinetic alfvén waves and the importance of  $\beta$  e. *Journal of Geophysical Research: Space Physics*, 104(A10):22331–22344.
- Leonardis, E., Chapman, S. C., Daughton, W., Roytershteyn, V., and Karimabadi, H. (2013). Identification of Intermittent Multifractal Turbulence in Fully Kinetic Simulations of Magnetic Reconnection. *Phys. Rev. Lett.*, 205002(May):1–5.
- Li, T. C., Howes, G. G., Klein, K. G., Liu, Y.-H., and TenBarge, J. M. (2019). Collisionless energy transfer in kinetic turbulence: field–particle correlations in fourier space. *Journal of Plasma Physics*, 85(4).
- Li, T. C., Howes, G. G., Klein, K. G., and TenBarge, J. M. (2016). Energy dissipation and landau damping in two-and three-dimensional plasma turbulence. *The Astrophysical Journal Letters*, 832(2):L24.

- Li, T. C., Liu, Y.-H., and Qi, Y. (2021). Identification of active magnetic reconnection using magnetic flux transport in plasma turbulence. *The Astrophysical Journal Letters*, 909(2):L28.
- Liang, H., Cassak, P. A., Servidio, S., Shay, M. A., Drake, J. F., Swisdak, M., Argall, M. R., Dorelli, J. C., Scime, E. E., Matthaeus, W. H., et al. (2019). Decomposition of plasma kinetic entropy into position and velocity space and the use of kinetic entropy in particle-in-cell simulations. *Physics of Plasmas*, 26(8):082903.
- Liu, Y.-H., Daughton, W., Karimabadi, H., Li, H., and Roytershteyn, V. (2013). Bifurcated structure of the electron diffusion region in three-dimensional magnetic reconnection. *Physical review letters*, 110(26):265004.
- Liu, Y.-H. and Hesse, M. (2016). Suppression of collisionless magnetic reconnection in asymmetric current sheets. *Physics of Plasmas*, 23(6):060704.
- Lotekar, A., Vasko, I., Phan, T., Bale, S., Bowen, T., Halekas, J., Artemyev, A., Khotyaintsev, Y. V., and Mozer, F. (2022). Kinetic-scale current sheets in near-sun solar wind: properties, scale-dependent features and reconnection onset. *The Astrophysical Journal*, 929(1):58.
- Lottermoser, R.-F., Scholer, M., and Matthews, A. (1998). Ion kinetic effects in magnetic reconnection: Hybrid simulations. *Journal of Geophysical Research: Space Physics*, 103(A3):4547–4559.
- Loureiro, N., Schekochihin, A., and Zocco, A. (2013). Fast collisionless reconnection and electron heating in strongly magnetized plasmas. *Physical review letters*, 111(2):025002.
- Loureiro, N. and Uzdensky, D. (2015). Magnetic reconnection: from the sweet–parker model to stochastic plasmoid chains. *Plasma Physics and Controlled Fusion*, 58(1):014021.
- Loureiro, N., Uzdensky, D., Schekochihin, A., Cowley, S., and Yousef, T. (2009). Turbulent magnetic reconnection in two dimensions. *Monthly Notices of the Royal Astronomical Society: Letters*, 399(1):L146–L150.

- Loureiro, N. F. and Boldyrev, S. (2017). Role of magnetic reconnection in magnetohydrodynamic turbulence. *Physical Review Letters*, 118(24):245101.
- Loureiro, N. F. and Boldyrev, S. (2020). Nonlinear reconnection in magnetized turbulence. *The Astrophysical Journal*, 890(1):55.
- Ma, Z. and Bhattacharjee, A. (2001). Hall magnetohydrodynamic reconnection: The geospace environment modeling challenge. *Journal of Geophysical Research: Space Physics*, 106(A3):3773–3782.
- Magara, T. (2004). A model for dynamic evolution of emerging magnetic fields in the sun. *The Astrophysical Journal*, 605(1):480.
- Maksimovic, M., Zouganelis, I., Chaufray, J.-Y., Issautier, K., Scime, E., Littleton, J., Marsch, E., McComas, D., Salem, C., Lin, R., et al. (2005). Radial evolution of the electron distribution functions in the fast solar wind between 0.3 and 1.5 au. *Journal of Geophysical Research: Space Physics*, 110(A9).
- Mallet, A. (2020). The onset of electron-only reconnection. *Journal of Plasma Physics*, 86(3):905860301.
- Mallet, A., Schekochihin, A. A., and Chandran, B. D. (2017). Disruption of alfvénic turbulence by magnetic reconnection in a collisionless plasma. *Journal of Plasma Physics*, 83(6):905830609.
- Mandt, M., Denton, R., and Drake, J. (1994). Transition to whistler mediated magnetic reconnection. *Geophysical Research Letters*, 21(1):73–76.
- Markidis, S., Camporeale, E., Burgess, D., Lapenta, G., et al. (2009). Parsek2d: An implicit parallel particle-in-cell code. In *Numerical Modeling of Space Plasma Flows: Astronom-2008*, volume 406, page 237.
- Maron, J. and Goldreich, P. (2001). Simulations of incompressible magnetohydrodynamic turbulence. *The Astrophysical Journal*, 554(2):1175.
- Marsch, E. (2006). Kinetic physics of the solar corona and solar wind. *Living Reviews in Solar Physics*, 3(1):1.

- Marsch, E., Mühlhäuser, K.-H., Schwenn, R., Rosenbauer, H., Pilipp, W., and Neubauer, F. (1982). Solar wind protons: Three-dimensional velocity distributions and derived plasma parameters measured between 0.3 and 1 au. *Journal of Geophysical Research: Space Physics*, 87(A1):52–72.
- Marsch, E. and Tu, C.-Y. (1990). Spectral and spatial evolution of compressible turbulence in the inner solar wind. *Journal of Geophysical Research: Space Physics*, 95(A8):11945–11956.
- Marsch, E., Vocks, C., and Tu, C.-Y. (2003). On ion-cyclotron-resonance heating of the corona and solar wind. *Nonlinear Processes in Geophysics*, 10(1/2):101–112.
- Maruca, B. A., Agudelo Rueda, J. A., Bandyopadhyay, R., Bianco, F. B., Chasapis, A., Chhiber, R., DeWeese, H., Matthaeus, W. H., Miles, D. M., Qudsi, R. A., et al. (2021). Magnetore: Mapping the 3-d magnetic structure of the solar wind using a large constellation of nanosatellites. *Frontiers in Astronomy and Space Sciences*, page 108.
- Matteini, L., Hellinger, P., Goldstein, B. E., Landi, S., Velli, M., and Neugebauer, M. (2013). Signatures of kinetic instabilities in the solar wind. *Journal of Geophysical Research: Space Physics*, 118(6):2771–2782.
- Matteini, L., Landi, S., Hellinger, P., Pantellini, F., Maksimovic, M., Velli, M., Goldstein, B. E., and Marsch, E. (2007). Evolution of the solar wind proton temperature anisotropy from 0.3 to 2.5 au. *Geophysical Research Letters*, 34(20).
- Matthaeus, W., Dasso, S., Weygand, J., Milano, L., Smith, C., and Kivelson, M. (2005). Spatial correlation of solar-wind turbulence from two-point measurements. *Physical review letters*, 95(23):231101.
- Matthaeus, W. and Goldstein, M. (1986). Low-frequency 1 f noise in the interplanetary magnetic field. *Physical review letters*, 57(4):495.
- Matthaeus, W. and Lamkin, S. L. (1986). Turbulent magnetic reconnection. *The Physics of fluids*, 29(8):2513–2534.

- Matthaeus, W. H., Yang, Y., Wan, M., Parashar, T. N., Bandyopadhyay, R., Chasapis, A., Pezzi, O., and Valentini, F. (2020). Pathways to dissipation in weakly collisional plasmas. *The Astrophysical Journal*, 891(1):101.
- Matthaeus, W. H., Zank, G. P., Smith, C. W., and Oughton, S. (1999). Turbulence, spatial transport, and heating of the solar wind. *Physical review letters*, 82(17):3444.
- Maz'ya, V. and Schmidt, G. (1996). On approximate approximations using gaussian kernels. *IMA Journal of Numerical Analysis*, 16(1):13–29.
- McComas, D., Bame, S., Feldman, W., Gosling, J., and Phillips, J. (1992). Solar wind halo electrons from 1–4 au. *Geophysical Research Letters*, 19(12):1291–1294.
- McComas, D., Elliott, H., Schwadron, N., Gosling, J., Skoug, R., and Goldstein, B. (2003). The three-dimensional solar wind around solar maximum. *Geophysical research letters*, 30(10).
- McManus, M. D., Bowen, T. A., Mallet, A., Chen, C. H., Chandran, B. D., Bale, S. D., Larson, D. E., de Wit, T. D., Kasper, J. C., Stevens, M., et al. (2020). Cross helicity reversals in magnetic switchbacks. *The Astrophysical Journal Supplement Series*, 246(2):67.
- Mendoza, M. and Munoz, J. (2010). Three-dimensional lattice boltzmann model for electrodynamics. *Physical Review E*, 82(5):056708.
- Meyrand, R., Galtier, S., and Kiyani, K. H. (2016). Direct evidence of the transition from weak to strong magnetohydrodynamic turbulence. *Physical review letters*, 116(10):105002.
- Mininni, P. D., Alexakis, A., and Pouquet, A. (2007). Energy transfer in hall-mhd turbulence: cascades, backscatter, and dynamo action. *Journal of plasma physics*, 73(3):377–401.
- Mistry, R., Eastwood, J., Haggerty, C., Shay, M., Phan, T., Hietala, H., and Cassak, P. (2016). Observations of hall reconnection physics far downstream of the x line. *Physical review letters*, 117(18):185102.



- Moldwin, M., Ford, S., Lepping, R., Slavin, J., and Szabo, A. (2000). Small-scale magnetic flux ropes in the solar wind. *Geophysical research letters*, 27(1):57–60.
- Moldwin, M., Phillips, J., Gosling, J., Scime, E., McComas, D., Bame, S., Balogh, A., and Forsyth, R. (1995). Ulysses observation of a noncoronal mass ejection flux rope: Evidence of interplanetary magnetic reconnection. *Journal of Geophysical Research: Space Physics*, 100(A10):19903–19910.
- Moser, A. L. and Bellan, P. M. (2012). Magnetic reconnection from a multiscale instability cascade. *Nature*, 482(7385):379–381.
- Mozer, F., Bale, S., and Phan, T. (2002). Evidence of diffusion regions at a subsolar magnetopause crossing. *Physical review letters*, 89(1):015002.
- Müller, W.-C., Biskamp, D., and Grappin, R. (2003). Statistical anisotropy of magnetohydrodynamic turbulence. *Physical Review E*, 67(6):066302.
- Muñoz, P. and Büchner, J. (2018). Kinetic turbulence in fast three-dimensional collisionless guide-field magnetic reconnection. *Physical Review E*, 98(4):043205.
- Muñoz, P., Büchner, J., and Kilian, P. (2017). Turbulent transport in 2d collisionless guide field reconnection. *Physics of Plasmas*, 24(2):022104.
- Narita, Y. (2016). Kinetic extension of critical balance to whistler turbulence. *The Astrophysical Journal*, 831(1):83.
- Narita, Y. (2018). Space–time structure and wavevector anisotropy in space plasma turbulence. *Living reviews in solar physics*, 15(1):1–48.
- Narita, Y. and Marsch, E. (2015). Kinetic slow mode in the solar wind and its possible role in turbulence dissipation and ion heating. *The Astrophysical Journal*, 805(1):24.
- Narita, Y., Roberts, O. W., Vörös, Z., and Hoshino, M. (2020). Transport ratios of the kinetic alfvén mode in space plasmas. *Frontiers in Physics*, 8:166.
- Narukage, N. and Shibata, K. (2006). Statistical analysis of reconnection inflows in solar flares observed with soho eit. *The Astrophysical Journal*, 637(2):1122.

- Nazarenko, S. V. and Schekochihin, A. A. (2011). Critical balance in magneto-hydrodynamic, rotating and stratified turbulence: towards a universal scaling conjecture. *Journal of Fluid Mechanics*, 677:134–153.
- Ng, C. and Bhattacharjee, A. (1997). Scaling of anisotropic spectra due to the weak interaction of shear-alfvén wave packets. *Physics of Plasmas*, 4(3):605–610.
- Ng, J., Hakim, A., Bhattacharjee, A., Stanier, A., and Daughton, W. (2017). Simulations of anti-parallel reconnection using a nonlocal heat flux closure. *Physics of Plasmas*, 24(8):082112.
- Ng, J., Huang, Y.-M., Hakim, A., Bhattacharjee, A., Stanier, A., Daughton, W., Wang, L., and Germaschewski, K. (2015). The island coalescence problem: Scaling of reconnection in extended fluid models including higher-order moments. *Physics of Plasmas*, 22(11):112104.
- Ni, L., Lin, J., Roussev, I. I., and Schmieder, B. (2016). Heating mechanisms in the low solar atmosphere through magnetic reconnection in current sheets. *The Astrophysical Journal*, 832(2):195.
- Nielson, K. D., Howes, G. G., and Dorland, W. (2013). Alfvén wave collisions, the fundamental building block of plasma turbulence. ii. numerical solution. *Physics of Plasmas*, 20(7):072303.
- Oughton, S., Matthaeus, W., Wan, M., and Osman, K. (2015). Anisotropy in solar wind plasma turbulence. *Philosophical Transactions of the Royal Society A: Mathematical, Physical and Engineering Sciences*, 373(2041):20140152.
- Owen, C. and Cowley, S. (1987). Simple models of time-dependent reconnection in a collision-free plasma with an application to substorms in the geomagnetic tail. *Planetary and Space Science*, 35(4):451–466.
- Papini, E., Franci, L., Landi, S., Verdini, A., Matteini, L., and Hellinger, P. (2019a). Can hall magnetohydrodynamics explain plasma turbulence at sub-ion scales? *The Astrophysical Journal*, 870(1):52.

- Papini, E., Landi, S., and Del Zanna, L. (2019b). Fast magnetic reconnection: Secondary tearing instability and role of the hall term. *The Astrophysical Journal*, 885(1):56.
- Parashar, T., Shay, M., Cassak, P., and Matthaeus, W. (2009). Kinetic dissipation and anisotropic heating in a turbulent collisionless plasma. *Physics of Plasmas*, 16(3):032310.
- Parker, E. (1957). Acceleration of cosmic rays in solar flares. *Physical Review*, 107(3):830.
- Parker, E. N. (1958). Dynamics of the interplanetary gas and magnetic fields. *The Astrophysical Journal*, 128:664.
- Parnell, C. E., Maclean, R. C., Haynes, A. L., and Galsgaard, K. (2010). 3d magnetic reconnection. *Proceedings of the International Astronomical Union*, 6(S271):227–238.
- Paschmann, G., Sonnerup, B. Ö., Papamastorakis, I., Sckopke, N., Haerendel, G., Bame, S., Asbridge, J., Gosling, J., Russell, C., and Elphic, R. (1979). Plasma acceleration at the earth’s magnetopause: Evidence for reconnection. *Nature*, 282(5736):243.
- Perez, J. C. and Boldyrev, S. (2007). On weak and strong magnetohydrodynamic turbulence. *The Astrophysical Journal Letters*, 672(1):L61.
- Perrone, D., Stansby, D., Horbury, T., and Matteini, L. (2019). Radial evolution of the solar wind in pure high-speed streams: Helios revised observations. *Monthly Notices of the royal astronomical society*, 483(3):3730–3737.
- Petschek, H. E. (1964). Magnetic field annihilation. *NASA Special Publication*, 50:425.
- Pezzi, O. (2017). Solar wind collisional heating. *Journal of Plasma Physics*, 83(3).

- Pezzi, O., Liang, H., Juno, J., Cassak, P., Vásconez, C., Sorriso-Valvo, L., Perrone, D., Servidio, S., Roytershteyn, V., TenBarge, J., et al. (2021). Dissipation measures in weakly collisional plasmas. *Monthly Notices of the Royal Astronomical Society*, 505(4):4857–4873.
- Pezzi, O., Yang, Y., Valentini, F., Servidio, S., Chasapis, A., Matthaeus, W., and Veltri, P. (2019). Energy conversion in turbulent weakly collisional plasmas: Eulerian hybrid vlasov-maxwell simulations. *Physics of Plasmas*, 26(7):072301.
- Phan, T., Bale, S., Eastwood, J., Lavraud, B., Drake, J., Oieroset, M., Shay, M., Pulupa, M., Stevens, M., MacDowall, R., et al. (2020). Parker solar probe in situ observations of magnetic reconnection exhausts during encounter 1. *The Astrophysical Journal Supplement Series*, 246(2):34.
- Phan, T., Eastwood, J. P., Shay, M., Drake, J., Sonnerup, B. Ö., Fujimoto, M., Cassak, P., Øieroset, M., Burch, J., Torbert, R., et al. (2018). Electron magnetic reconnection without ion coupling in earth’s turbulent magnetosheath. *Nature*, 557(7704):202–206.
- Phan, T., Gosling, J., and Davis, M. (2009). Prevalence of extended reconnection x-lines in the solar wind at 1 au. *Geophysical Research Letters*, 36(9):L09108.
- Phan, T., Gosling, J., Davis, M., Skoug, R., Øieroset, M., Lin, R., Lepping, R., McComas, D., Smith, C., Reme, H., et al. (2006). A magnetic reconnection x-line extending more than 390 earth radii in the solar wind. *Nature*, 439(7073):175.
- Phan, T., Lavraud, B., Halekas, J., Øieroset, M., Drake, J., Eastwood, J., Shay, M., Pyakurel, P., Bale, S., Larson, D., et al. (2021). Prevalence of magnetic reconnection in the near-sun heliospheric current sheet. *Astronomy & Astrophysics*, 650:A13.
- Pilipp, W., Miggenrieder, H., Montgomery, M., Mühlhäuser, K.-H., Rosenbauer, H., and Schwenn, R. (1987). Characteristics of electron velocity distribution functions in the solar wind derived from the helios plasma experiment. *Journal of Geophysical Research: Space Physics*, 92(A2):1075–1092.

- Platte, R. B. and Driscoll, T. A. (2005). Polynomials and potential theory for gaussian radial basis function interpolation. *SIAM Journal on Numerical Analysis*, 43(2):750–766.
- Podesta, J. (2009). Dependence of solar-wind power spectra on the direction of the local mean magnetic field. *The Astrophysical Journal*, 698(2):986.
- Podesta, J. J. (2013). Evidence of kinetic alfvén waves in the solar wind at 1 au. *Solar Physics*, 286(2):529–548.
- Podesta, J. J. and TenBarge, J. M. (2012). Scale dependence of the variance anisotropy near the proton gyroradius scale: Additional evidence for kinetic alfvén waves in the solar wind at 1 au. *Journal of Geophysical Research: Space Physics*, 117(A10):A10106.
- Pontin, D. (2011). Three-dimensional magnetic reconnection regimes: A review. *Advances in Space Research*, 47(9):1508–1522.
- Priest, E. and Démoulin, P. (1995). Three-dimensional magnetic reconnection without null points: 1. basic theory of magnetic flipping. *Journal of Geophysical Research: Space Physics*, 100(A12):23443–23463.
- Priest, E. and Forbes, T. (2007). Magnetic reconnection. *Magnetic Reconnection, by Eric Priest, Terry Forbes, Cambridge, UK: Cambridge University Press, 2007.*
- Priest, E., Hornig, G., and Pontin, D. (2003). On the nature of three-dimensional magnetic reconnection. *Journal of Geophysical Research: Space Physics*, 108(A7):1285.
- Pritchett, P. (2013). The onset of magnetic reconnection in three dimensions. *Physics of Plasmas*, 20(8):080703.
- Pritchett, P. and Coroniti, F. (2001). Kinetic simulations of 3-d reconnection and magnetotail disruptions. *Earth, planets and space*, 53(6):635–643.

- Pritchett, P. and Coroniti, F. V. (2004). Three-dimensional collisionless magnetic reconnection in the presence of a guide field. *Journal of Geophysical Research: Space Physics*, 109(A1):A01220.
- Pucci, F., Servidio, S., Sorriso-Valvo, L., Olshevsky, V., Matthaeus, W., Malara, F., Goldman, M., Newman, D., and Lapenta, G. (2017). Properties of turbulence in the reconnection exhaust: numerical simulations compared with observations. *The Astrophysical Journal*, 841(1):60.
- Pucci, F., Usami, S., Ji, H., Guo, X., Horiuchi, R., Okamura, S., Fox, W., Jara-Almonte, J., Yamada, M., and Yoo, J. (2018). Energy transfer and electron energization in collisionless magnetic reconnection for different guide-field intensities. *Physics of Plasmas*, 25(12):122111.
- Pukhov, A. (2005). Particle-in-cell codes for plasma-based particle acceleration. *Phys. Plasmas*, 12:043109.
- Rasche, V., Proksa, R., Sinkus, R., Bornert, P., and Eggers, H. (1999). Resampling of data between arbitrary grids using convolution interpolation. *IEEE transactions on medical imaging*, 18(5):385–392.
- Ricci, P., Brackbill, J., Daughton, W., and Lapenta, G. (2004a). Influence of the lower hybrid drift instability on the onset of magnetic reconnection. *Physics of plasmas*, 11(9):4489–4500.
- Ricci, P., Brackbill, J. U., Daughton, W., and Lapenta, G. (2004b). Collisionless magnetic reconnection in the presence of a guide field. *Phys. Plasmas*, 11(8):4102–4114.
- Richardson, L. F. (1926). Atmospheric diffusion shown on a distance-neighbour graph. *Proceedings of the Royal Society of London. Series A, Containing Papers of a Mathematical and Physical Character*, 110(756):709–737.
- Robert, P., Dunlop, M. W., Roux, A., and Chanteur, G. (1998). Accuracy of current density determination. *Analysis methods for multi-spacecraft data*, 398:395–418.

- Roberts, O. W., Li, X., and Li, B. (2013). Kinetic plasma turbulence in the fast solar wind measured by cluster. *The Astrophysical Journal*, 769(1):58.
- Roberts, O. W., Narita, Y., and Escoubet, C. (2017). Direct measurement of anisotropic and asymmetric wave vector spectrum in ion-scale solar wind turbulence. *The Astrophysical Journal Letters*, 851(1):L11.
- Rogers, B., Drake, J., and Shay, M. (2000). The onset of turbulence in collisionless magnetic reconnection. *Geophysical research letters*, 27(19):3157–3160.
- Romano-Díaz, E. and Van De Weygaert, R. (2007). Delaunay tessellation field estimator analysis of the psc z local universe: density field and cosmic flow. *Monthly Notices of the Royal Astronomical Society*, 382(1):2–28.
- Roytershteyn, V., Daughton, W., Karimabadi, H., and Mozer, F. (2012). Influence of the lower-hybrid drift instability on magnetic reconnection in asymmetric configurations. *Physical review letters*, 108(18):185001.
- Runov, A., Nakamura, R., Baumjohann, W., Treumann, R., Zhang, T., Volwerk, M., Vörös, Z., Balogh, A., Glaßmeier, K.-H., Klecker, B., et al. (2003). Current sheet structure near magnetic x-line observed by cluster. *Geophysical Research Letters*, 30(11).
- Salem, C. S., Howes, G., Sundkvist, D., Bale, S., Chaston, C., Chen, C., and Mozer, F. (2012). Identification of kinetic alfvén wave turbulence in the solar wind. *The Astrophysical Journal Letters*, 745(1):L9.
- Samtaney, R., Loureiro, N., Uzdensky, D., Schekochihin, A., and Cowley, S. (2009). Formation of plasmoid chains in magnetic reconnection. *Physical review letters*, 103(10):105004.
- Sato, T. and Hayashi, T. (1979). Externally driven magnetic reconnection and a powerful magnetic energy converter. *The Physics of Fluids*, 22(6):1189–1202.
- Schekochihin, A., Cowley, S., Dorland, W., Hammett, G., Howes, G. G., Quataert, E., and Tatsuno, T. (2009). Astrophysical gyrokinetics: kinetic and fluid turbulent

- cascades in magnetized weakly collisional plasmas. *The Astrophysical Journal Supplement Series*, 182(1):310.
- Schindler, K., Hesse, M., and Birn, J. (1988). General magnetic reconnection, parallel electric fields, and helicity. *Journal of Geophysical Research: Space Physics*, 93(A6):5547–5557.
- Schmitz, H. and Grauer, R. (2006). Kinetic vlasov simulations of collisionless magnetic reconnection. *Physics of plasmas*, 13(9):092309.
- Schoenberg, I. J. (1973). *Cardinal spline interpolation*. SIAM.
- Scholer, M. (1988). Magnetic flux transfer at the magnetopause based on single x line bursty reconnection. *Geophysical Research Letters*, 15(4):291–294.
- Scholer, M., Sidorenko, I., Jaroschek, C., Treumann, R., and Zeiler, A. (2003). Onset of collisionless magnetic reconnection in thin current sheets: Three-dimensional particle simulations. *Physics of Plasmas*, 10(9):3521–3527.
- Scime, E. E., Bame, S. J., Feldman, W. C., Gary, S. P., Phillips, J. L., and Balogh, A. (1994). Regulation of the solar wind electron heat flux from 1 to 5 au: Ulysses observations. *Journal of Geophysical Research: Space Physics*, 99(A12):23401–23410.
- Scudder, J. and Daughton, W. (2008). “illuminating” electron diffusion regions of collisionless magnetic reconnection using electron agyrotropy. *Journal of Geophysical Research: Space Physics*, 113(A6).
- Servidio, S., Dmitruk, P., Greco, A., Wan, M., Donato, S., Cassak, P., Shay, M., Carbone, V., and Matthaeus, W. (2011). Magnetic reconnection as an element of turbulence. *Nonlinear Processes in Geophysics*, 18(5):675–695.
- Servidio, S., Matthaeus, W., Shay, M., Cassak, P., and Dmitruk, P. (2009). Magnetic reconnection in two-dimensional magnetohydrodynamic turbulence. *Physical review letters*, 102(11):115003.



- Servidio, S., Matthaeus, W., Shay, M., Dmitruk, P., Cassak, P., and Wan, M. (2010a). Statistics of magnetic reconnection in two-dimensional magnetohydrodynamic turbulence. *Physics of Plasmas*, 17(3):032315.
- Servidio, S., Matthaeus, W. H., Shay, M. A., Dmitruk, P., Cassak, P. A., and Wan, M. (2010b). Statistics of magnetic reconnection in two-dimensional magnetohydrodynamic turbulence. *Phys. Plasmas*, 17(3):032315.
- Sharma Pyakurel, P., Shay, M., Phan, T., Matthaeus, W., Drake, J., TenBarge, J., Haggerty, C., Klein, K., Cassak, P., Parashar, T., et al. (2019). Transition from ion-coupled to electron-only reconnection: Basic physics and implications for plasma turbulence. *Physics of Plasmas*, 26(8):082307.
- Shay, M., Drake, J., Rogers, B., and Denton, R. (1999). The scaling of collisionless, magnetic reconnection for large systems. *Geophysical research letters*, 26(14):2163–2166.
- Shay, M., Drake, J., Rogers, B., and Denton, R. (2001). Alfvénic collisionless magnetic reconnection and the hall term. *Journal of Geophysical Research: Space Physics*, 106(A3):3759–3772.
- Shay, M., Drake, J., Swisdak, M., Dorland, W., and Rogers, B. (2003). Inherently three dimensional magnetic reconnection: A mechanism for bursty bulk flows? *Geophysical research letters*, 30(6).
- Shay, M., Drake, J., Swisdak, M., and Rogers, B. (2004). The scaling of embedded collisionless reconnection. *Physics of Plasmas*, 11(5):2199–2213.
- Shay, M. A. and Drake, J. F. (1998). The role of electron dissipation on the rate of collisionless magnetic reconnection. *Geophysical Research Letters*, 25(20):3759–3762.
- Shen, C., Li, X., Dunlop, M., Liu, Z., Balogh, A., Baker, D., Hapgood, M., and Wang, X. (2003). Analyses on the geometrical structure of magnetic field in the current sheet based on cluster measurements. *Journal of Geophysical Research: Space Physics*, 108(A5).

- Shen, C., Li, X., Dunlop, M., Shi, Q., Liu, Z., Lucek, E., and Chen, Z. (2007). Magnetic field rotation analysis and the applications. *Journal of Geophysical Research: Space Physics*, 112(A6).
- Smith, C. W., Vasquez, B. J., and Hollweg, J. V. (2011). Observational constraints on the role of cyclotron damping and kinetic alfvén waves in the solar wind. *The Astrophysical Journal*, 745(1):8.
- Smith, D., Ghosh, S., Dmitruk, P., and Matthaeus, W. (2004). Hall and turbulence effects on magnetic reconnection. *Geophysical research letters*, 31(2):L02805.
- Somov, B. and Titov, V. (1985). Magnetic reconnection in a high-temperature plasma of solar flares. *Solar physics*, 102(1-2):79–96.
- Somov, B. V. (2012). *Plasma Astrophysics, Part II: Reconnection and Flares*, volume 392. Springer Science & Business Media.
- Sonnerup, B. (1979). Magnetic field reconnection. *Solar system plasma physics*, pages 45–108.
- Sridhar, S. and Goldreich, P. (1994). Toward a theory of interstellar turbulence. i: Weak alfvénic turbulence. *Astrophysical Journal*, 432(2):612–621.
- Srivastava, N. and Schwenn, R. (2000). The origin of the solar wind: an overview. In *The Outer Heliosphere: Beyond the Planets*, pages 12–40.
- Stawarz, J., Eastwood, J. P., Phan, T., Gingell, I., Shay, M., Burch, J., Ergun, R., Giles, B., Gershman, D., Le Contel, O., et al. (2019). Properties of the turbulence associated with electron-only magnetic reconnection in earth’s magnetosheath. *The Astrophysical Journal Letters*, 877(2):L37.
- Stawicki, O., Gary, S. P., and Li, H. (2001). Solar wind magnetic fluctuation spectra: Dispersion versus damping. *Journal of Geophysical Research: Space Physics*, 106(A5):8273–8281.
- Strauss, H. (1988). Turbulent reconnection. *The Astrophysical Journal*, 326:412–417.

- Štverák, Š., Maksimovic, M., Trávníček, P. M., Marsch, E., Fazakerley, A. N., and Scime, E. E. (2009). Radial evolution of nonthermal electron populations in the low-latitude solar wind: Helios, cluster, and ulysses observations. *Journal of Geophysical Research: Space Physics*, 114(A5).
- Sundkvist, D., Retinò, A., Vaivads, A., and Bale, S. D. (2007). Dissipation in turbulent plasma due to reconnection in thin current sheets. *Physical review letters*, 99(2):025004.
- Sweet, P. A. (1958). 14. the neutral point theory of solar flares. In *Symposium-International Astronomical Union*, volume 6, pages 123–134. Cambridge University Press.
- Tatsuno, T., Dorland, W., Schekochihin, A., Plunk, G., Barnes, M., Cowley, S., and Howes, G. (2009). Nonlinear phase mixing and phase-space cascade of entropy in gyrokinetic plasma turbulence. *Physical review letters*, 103(1):015003.
- Taylor, G. I. (1938). The spectrum of turbulence. *Proceedings of the Royal Society of London. Series A-Mathematical and Physical Sciences*, 164(919):476–490.
- Telloni, D., Sorriso-Valvo, L., Woodham, L. D., Panasenco, O., Velli, M., Carbone, F., Zank, G. P., Bruno, R., Perrone, D., Nakanotani, M., et al. (2021). Evolution of solar wind turbulence from 0.1 to 1 au during the first parker solar probe–solar orbiter radial alignment. *The Astrophysical Journal Letters*, 912(2):L21.
- TenBarge, J. and Howes, G. (2012). Evidence of critical balance in kinetic alfvén wave turbulence simulations. *Physics of Plasmas*, 19(5):055901.
- TenBarge, J., Podesta, J., Klein, K., and Howes, G. (2012). Interpreting magnetic variance anisotropy measurements in the solar wind. *The Astrophysical Journal*, 753(2):107.
- Told, D., Cookmeyer, J., Muller, F., Astfalk, P., and Jenko, F. (2016). Comparative study of gyrokinetic, hybrid-kinetic and fully kinetic wave physics for space plasmas. *New Journal of Physics*, 18(6):065011.

- Tu, C.-Y. and Marsch, E. (1995). Mhd structures, waves and turbulence in the solar wind: Observations and theories. *Space Science Reviews*, 73(1):1–210.
- Ugai, M. (1984). Self-consistent development of fast magnetic reconnection with anomalous plasma resistivity. *Plasma physics and controlled fusion*, 26(12B):1549.
- Ugai, M. and Tsuda, T. (1977). Magnetic field-line reconnexion by localized enhancement of resistivity: Part 1. evolution in a compressible mhd fluid. *Journal of Plasma Physics*, 17(3):337–356.
- Unti, T. W. and Neugebauer, M. (1968). Alfvén waves in the solar wind. *The Physics of Fluids*, 11(3):563–568.
- Uritsky, V. M., Pouquet, A., Rosenberg, D., Mininni, P. D., and Donovan, E. (2010). Structures in magnetohydrodynamic turbulence: Detection and scaling. *Physical Review E*, 82(5):056326.
- Uzdensky, D. A. and Kulsrud, R. M. (2006). Physical origin of the quadrupole out-of-plane magnetic field in hall-magnetohydrodynamic reconnection. *Physics of Plasmas*, 13(6):062305.
- Vaivads, A., Khotyaintsev, Y., André, M., Retino, A., Buchert, S., Rogers, B., Décreau, P., Paschmann, G., and Phan, T. (2004). Structure of the magnetic reconnection diffusion region from four-spacecraft observations. *Physical review letters*, 93(10):105001.
- Vapirev, A., Lapenta, G., Divin, A., Markidis, S., Henri, P., Goldman, M., and Newman, D. (2013). Formation of a transient front structure near reconnection point in 3-d pic simulations. *Journal of Geophysical Research: Space Physics*, 118(4):1435–1449.
- Vargas Domínguez, S., MacTaggart, D., Green, L., van Driel-Gesztelyi, L., and Hood, A. W. (2012). On signatures of twisted magnetic flux tube emergence. *Solar Physics*, 278(1):33–45.

- Vasyliunas, V. M. (1975). Theoretical models of magnetic field line merging. *Reviews of Geophysics*, 13(1):303–336.
- Vech, D., Mallet, A., Klein, K. G., and Kasper, J. C. (2018). Magnetic reconnection may control the ion-scale spectral break of solar wind turbulence. *The Astrophysical Journal Letters*, 855(2):L27.
- Velli, M. and Pruneti, F. (1997). Alfvén waves in the solar corona and solar wind. *Plasma Physics and Controlled Fusion*, 39(12B):B317.
- Verscharen, D., Chen, C. H., and Wicks, R. T. (2017). On kinetic slow modes, fluid slow modes, and pressure-balanced structures in the solar wind. *The Astrophysical Journal*, 840(2):106.
- Verscharen, D., Klein, K. G., and Maruca, B. A. (2019). The multi-scale nature of the solar wind. *Living reviews in solar physics*, 16(1):1–136.
- Verscharen, D., Marsch, E., Motschmann, U., and Müller, J. (2012). Kinetic cascade beyond magnetohydrodynamics of solar wind turbulence in two-dimensional hybrid simulations. *Physics of Plasmas*, 19(2):022305.
- Verscharen, D., Parashar, T. N., Gary, S. P., and Klein, K. G. (2020). Dependence of kinetic plasma waves on ion-to-electron mass ratio and light-to-alfvén speed ratio. *Monthly Notices of the Royal Astronomical Society*, 494(2):2905–2911.
- Viall, N. M. and Borovsky, J. E. (2020). Nine outstanding questions of solar wind physics. *Journal of Geophysical Research: Space Physics*, 125(7):e2018JA026005.
- Wan, M., Matthaeus, W., Karimabadi, H., Roytershteyn, V., Shay, M., Wu, P., Daughton, W., Loring, B., and Chapman, S. C. (2012). Intermittent dissipation at kinetic scales in collisionless plasma turbulence. *Physical Review Letters*, 109(19):195001.
- Wan, M., Rappazzo, A. F., Matthaeus, W. H., Servidio, S., and Oughton, S. (2014). Dissipation and reconnection in boundary-driven reduced magnetohydrodynamics. *The Astrophysical Journal*, 797(1):63.

- Wang, L., Germaschewski, K., Hakim, A., Dong, C., Raeder, J., and Bhattacharjee, A. (2018). Electron physics in 3-d two-fluid 10-moment modeling of ganymede's magnetosphere. *Journal of Geophysical Research: Space Physics*, 123(4):2815–2830.
- Wang, L., Hakim, A. H., Bhattacharjee, A., and Germaschewski, K. (2015). Comparison of multi-fluid moment models with particle-in-cell simulations of collisionless magnetic reconnection. *Physics of Plasmas*, 22(1):012108.
- Wang, T., He, J., Alexandrova, O., Dunlop, M., and Perrone, D. (2020). Observational quantification of three-dimensional anisotropies and scalings of space plasma turbulence at kinetic scales. *The Astrophysical Journal*, 898(1):91.
- Wei, X., Cao, J., Zhou, G., Santolík, O., Rème, H., Dandouras, I., Cornilleau-Wehrlin, N., Lucek, E., Carr, C., and Fazakerley, A. (2007). Cluster observations of waves in the whistler frequency range associated with magnetic reconnection in the earth's magnetotail. *Journal of Geophysical Research: Space Physics*, 112(A10).
- Wicks, R., Horbury, T., Chen, C., and Schekochihin, A. (2010). Power and spectral index anisotropy of the entire inertial range of turbulence in the fast solar wind. *Monthly Notices of the Royal Astronomical Society: Letters*, 407(1):L31–L35.
- Wicks, R., Horbury, T., Chen, C., and Schekochihin, A. (2011). Anisotropy of imbalanced alfvénic turbulence in fast solar wind. *Physical review letters*, 106(4):045001.
- Wicks, R. T., Mallet, A., Horbury, T. S., Chen, C. H., Schekochihin, A. A., and Mitchell, J. J. (2013). Alignment and scaling of large-scale fluctuations in the solar wind. *Physical review letters*, 110(2):025003.
- Wiegmann, T. and Büchner, J. (2001). Evolution of magnetic helicity in the course of kinetic magnetic reconnection. *Nonlinear Processes in Geophysics*, 8(3):127–140.
- Wilmot-Smith, A., Priest, E., and Hornig, G. (2005). Magnetic diffusion and the motion of field lines. *Geophysical & Astrophysical Fluid Dynamics*, 99(2):177–197.

- Wygant, J., Cattell, C., Lysak, R., Song, Y., Dombek, J., McFadden, J., Mozer, F., Carlson, C., Parks, G., Lucek, E., et al. (2005). Cluster observations of an intense normal component of the electric field at a thin reconnecting current sheet in the tail and its role in the shock-like acceleration of the ion fluid into the separatrix region. *Journal of Geophysical Research: Space Physics*, 110(A9).
- Yamada, M., Kulsrud, R., and Ji, H. (2010). Magnetic reconnection. *Reviews of Modern Physics*, 82(1):603.
- Yamada, M., Yoo, J., Jara-Almonte, J., Ji, H., Kulsrud, R. M., and Myers, C. E. (2014). Conversion of magnetic energy in the magnetic reconnection layer of a laboratory plasma. *Nature communications*, 5(1):1–8.
- Yang, Y., Matthaeus, W. H., Parashar, T. N., Haggerty, C. C., Roytershteyn, V., Daughton, W., Wan, M., Shi, Y., and Chen, S. (2017). Energy transfer, pressure tensor, and heating of kinetic plasma. *Physics of Plasmas*, 24(7):072306.
- Yee, K. (1966). Numerical solution of initial boundary value problems involving maxwell’s equations in isotropic media. *IEEE Transactions on antennas and propagation*, 14(3):302–307.
- Yin, L., Winske, D., Gary, S., and Birn, J. (2001). Hybrid and hall-mhd simulations of collisionless reconnection: Dynamics of the electron pressure tensor. *Journal of Geophysical Research: Space Physics*, 106(A6):10761–10775.
- Yoo, J., Yamada, M., Ji, H., and Myers, C. E. (2013). Observation of ion acceleration and heating during collisionless magnetic reconnection in a laboratory plasma. *Physical review letters*, 110(21):215007.
- Zenitani, S., Hesse, M., Klimas, A., and Kuznetsova, M. (2011). New measure of the dissipation region in collisionless magnetic reconnection. *Physical review letters*, 106(19):195003.
- Zhdankin, V., Uzdensky, D. A., Perez, J. C., and Boldyrev, S. (2013). Statistical analysis of current sheets in three-dimensional magnetohydrodynamic turbulence. *The Astrophysical Journal*, 771(2):124.

- Zhou, M., Loureiro, N. F., and Uzdensky, D. A. (2020). Multi-scale dynamics of magnetic flux tubes and inverse magnetic energy transfer. *Journal of Plasma Physics*, 86(4).
- Zhu, B., Yan, H., Zhong, Y., Chen, J., Du, Y., Cheng, H., and Yuen, D. A. (2019a). Relativistic hpic-lbm and its application in large temporal-spatial turbulent magnetic reconnection. part ii. role of turbulence in the flux rope interaction. *Applied Mathematical Modelling*.
- Zhu, X., He, J., Verscharen, D., and Zhao, J. (2019b). Composition of wave modes in magnetosheath turbulence from sub-ion to sub-electron scales. *The Astrophysical Journal*, 878(1):48.
- Zweibel, E. G. and Yamada, M. (2009). Magnetic reconnection in astrophysical and laboratory plasmas. *Annual review of astronomy and astrophysics*, 47:291–332.
- Zweibel, E. G. and Yamada, M. (2016). Perspectives on magnetic reconnection. *Proceedings of the Royal Society A: Mathematical, Physical and Engineering Sciences*, 472(2196):20160479.